Investigation of Star Formation:

Instrumentation and Methodology

by

Todd Justin Veach

A Dissertation Presented in Partial Fulfillment
of the Requirements for the Degree
Doctor of Philosophy

Approved November 2012 by the
Graduate Supervisory Committee:

Paul Scowen, Co-Chair
Christopher Groppi, Co-Chair
Matthew Beasley
James Rhoads
Rogier Windhorst

ARIZONA STATE UNIVERSITY

December 2012

ABSTRACT

A thorough exploration of star formation necessitates observation across the electromagnetic spectrum. In particular, observations in the submillimeter and ultra-violet allow one to observe very early stage star formation and to trace the evolution from molecular cloud collapse to stellar ignition. Submillimeter observations are essential for piercing the heart of heavily obscured stellar nurseries to observe star formation in its infancy. Ultra-violet observations allow one to observe stars just after they emerge from their surrounding environment, allowing higher energy radiation to escape. To make detailed observations of early stage star formation in both spectral regimes requires state-of-the-art detector technology and instrumentation.

In this dissertation, I discuss the calibration and feasibility of detectors developed by Lawrence Berkeley National Laboratory and specially processed at the Jet Propulsion Laboratory to increase their quantum efficiency at far-ultraviolet wavelengths. A cursory treatment of the delta-doping process is presented, followed by a thorough discussion of calibration procedures developed at JPL and in the Laboratory for Astronomical and Space Instrumentation at ASU. Subsequent discussion turns to a novel design for a Modular Imager Cell forming one possible basis for construction of future large focal plane arrays. I then discuss the design, fabrication, and calibration of a sounding rocket imaging system developed using the MIC and these specially processed detectors.

Finally, I discuss one scientific application of sub-mm observations. I used data from the Heinrich Hertz Sub-millimeter Telescope and the Sub-Millimeter Array (SMA) to observe sub-millimeter transitions and continuum emission towards AFGL 2591. I tested the use of vibrationally excited HCN emission to probe the

protostellar accretion disk structure. I measured vibrationally excited HCN line ratios in order to elucidate the appropriate excitation mechanism. I find collisional excitation to be dominant, showing the emission originates in extremely dense (n$\sim 10^{11}$ cm^{-3}), warm (T$\sim$1000K) gas. Furthermore, from the line profile of the v=(0, 2^{2d}, 0) transition, I find evidence for a possible accretion disk.

DEDICATION

This tome is dedicated to my mother.

Without her love and support I would truly be lost.

ACKNOWLEDGEMENTS

I would like to thank my co-advisor Paul Scowen for his patient guidance and encouragement throughout my graduate school endeavors. His guidance truly allowed me to grow as a scientist, engineer, and person. He has always treated me like a colleague and for that I am grateful. It is upon his instruction that I will attempt to model my future interactions with graduate students and potential colleagues.

I would like to thank my co-advisor Chris Groppi, without whom my career may have been lost. Chris came along a truly changed the course of my education and there are no words strong enough to express my gratitude. Chris allowed me to fulfill a lifelong dream of traveling and working in Antarctica and for that I will be ever grateful.

I would like to thank Steve Monacos at JPL who knows more about electrical engineering than anyone I know and was willing to answer my questions no matter how busy he was or how trivial the question may have been. I would also like to thank Shouleh Nikzad and Blake Jacquot who also provided invaluable guidance during my time at JPL.

My grateful thanks are extended towards Matthew Beasley who gave me the opportunity to be a “rocket scientist” and taught me the correct way to put on latex gloves.

Friends provide an outlet for all the stress that accompanies graduate school. Steven Finkelstein, Brian Frank, Russell Ryan, Seth Cohen, Alison Loll, Caleb Wheeler, and Chelsea Allison have all provided me with friendship and support for which I will be forever grateful. I would also like to thank Four Peaks for providing the necessary atmosphere to enable groundbreaking scientific discourse.

I would like to thank Kirsten Chojnicki for the love and support she has provided me throughout our life together.

Most importantly, none of this would have been possible without the love, support, and patience of my family. My mother, to whom this dissertation is dedicated, has been a constant source of strength, support, love, and encouragement through all these years.

Zeus the dog requires a special thanks. There is no dog in the universe meant for another person more than he is for me.

TABLE OF CONTENTS

Page

LIST OF TABLES xiv

LIST OF FIGURES xv

CHAPTER

1 INTRODUCTION 1

1.1 Science Drivers 1

1.1.1 Young stellar objects (YSOs) 1

1.1.2 Disks 2

1.1.3 Outflows 2

1.1.4 Far-ultraviolet emission lines as probes of mass accretion in young stars 2

1.1.5 Feedback from Massive Stars 3

1.1.6 Extragalactic observations of Star Formation 3

1.2 Engineering Drivers 4

1.3 Star Formation 5

1.3.1 Gravitational Collapse 7

1.3.2 Protostellar Evolution 9

1.3.2.1 Classification 9

1.3.2.2 High Mass Protostellar Object 10

1.4 Charge-Coupled Device Technology 11

1.4.1 Detection 13

1.4.1.1 The Photoelectric Effect 13

1.4.2 Absorption Depth 15

1.4.3 CCD Architecture 15

1.4.4 Readout 17

1.5 Charge Transfer Efficiency 19

CHAPTER Page
1.5.1 CTE Degradation 20
1.6 Next Generation Detector Development 22
1.6.1 Large Focal Plane Arrays 22
1.6.2 Delta-doping 23
1.7 Detector Calibration: Photon Transfer Curve 24
1.7.1 Noise Regimes 26
1.7.1.1 Read Noise 26
1.7.1.2 Shot Noise 27
1.7.1.3 Quantum Yield 27
1.7.1.4 Fixed Pattern Noise 28
1.7.1.5 Camera Gain and Read Noise 28
1.7.2 Linearity 30
1.7.3 Non-linearity 30
1.7.4 Dark Current 31
1.7.5 Full Well Capacity 32
1.8 Quantum Efficiency 33
1.8.1 QE vs DQE 35
1.8.2 CCD Equation 35
2 LABORATORY FOR ASTRONOMICAL AND SPACE INSTRUMENTATION CCD CALIBRATION PROGRAM 47
2.1 Introduction 47
2.2 Motivation and Methodology 48
2.3 Detector Performance Evaluation Strategies 49
2.4 Detector Performance Evaluation Implementation 51
2.4.1 Photodiode Measurements 51
2.4.2 Operational Temperature Measurements 52

CHAPTER Page
2.4.3 Linearity Measurements 53
2.4.4 Gain and Read Noise Measurements 54
2.4.5 Quantum Efficiency Measurements 55
2.5 Detector Performance Optimization 55
2.6 Design of LASI Facility 56
2.6.1 Optical Design 56
2.6.2 Wavelength Selection 56
2.6.2.1 Optical Filters 58
2.6.3 Exposure Control 58
2.6.4 Focal Plane Illumination 59
2.6.5 Intensity Measurement and Calibration 59
2.6.6 Co-location of CCD and Photodiode 60
2.7 Environmental Considerations 60
2.7.1 Vibration Control 61
2.7.2 Stray Light Control 61
2.7.3 Thermal Control 62
2.7.4 Dewar 63
2.7.5 Temperature Measurement 65
2.7.6 Pressure Management and Measurement 67
2.7.7 Electro-Static Discharge Control 69
2.7.8 Power Conditioning 69
2.8 Electronics 70
2.8.1 Preamplifier 70
2.8.1.1 Offset Calculation 72
2.8.1.2 Gain Calculation 73
2.8.2 CCD Controller 73

CHAPTER Page
2.8.3 National Instruments PXI System 75
2.8.4 Keithley Picoammeter 75
2.9 Software 75
2.9.1 Monochromator Control 75
2.9.2 Data Acquisition 76
2.9.3 Leach Controller Software 76
2.9.4 Flexible Image Transport System 77
2.9.5 Data Processing 77
2.10 Results 77
2.10.1 Photodiode Calibration 78
2.10.1.1 Photodiode Absolute Responsivity Calibration . . 78
2.10.2 Stray Light Measurement 79
2.10.3 LBNL 1k $\times$ 1k 79
2.10.3.1 Operational Temperature 80
2.10.3.2 Gain, Read Noise, and Bias 80
2.10.3.3 Linearity and Non-linearity 80
2.10.3.4 Photon Transfer Curve 81
2.10.3.5 Quantum Efficiency 81
2.11 Discussion 81
2.11.1 Gain and Read Noise 81
2.11.2 Linearity and Residuals 83
2.11.3 Photon Transfer Curves 84
2.11.4 Quantum Efficiency 85
2.11.5 LASI Lab Shortcomings and Encountered Problems 85
2.11.5.1 Cassini Engineering Grade Detector 88
2.12 Summary 88

CHAPTER Page
2.13 Future Work . . . 89
2.13.1 Software Development . . . 89
2.13.2 Upgrades to the Calibration System . . . 89
3 MODULAR IMAGER CELL . . . 120
3.1 Motivation . . . 120
3.2 Technical Background . . . 121
3.3 Design Overview . . . 122
3.4 Driving Requirements . . . 122
3.5 Video Amplifier Design . . . 123
3.5.1 Non-inverting Amplifier Stage . . . 124
3.5.2 Inverting Amplifier Stage . . . 125
3.6 Signal Conditioning . . . 126
3.7 Two-Piece Design . . . 126
3.8 PCB Layout and Design . . . 127
3.9 Component Selection . . . 130
3.9.1 Printed Circuit Board . . . 130
3.9.2 Operational Amplifier . . . 131
3.9.3 Resistors . . . 132
3.9.4 Capacitors . . . 132
3.9.5 Connectors . . . 132
3.9.6 Board Assembly . . . 133
3.10 Cost . . . 134
3.11 Results and Discussion . . . 134
3.11.1 Mechanical Design . . . 134
3.11.2 Clock Level Filtering . . . 135
3.11.3 Amplifier Gain Settings . . . 135

CHAPTER Page
3.11.4 Bias and Offset . . . 136
3.11.5 Problems . . . 136
3.12 Summary . . . 137
3.13 Future Work . . . 137
3.13.1 Full MIC Design . . . 137
4 COLORADO HIGH-RESOLUTION ÉCHELLE STELLAR SPECTROGRAPH (CHESS) FOCAL PLANE ARRAY DEVELOPMENT . . . 150
4.1 Introduction . . . 150
4.2 CHESS Background . . . 151
4.2.1 CHESS Science . . . 151
4.2.2 Instrument Design . . . 152
4.2.3 The Échelle Grating . . . 152
4.2.4 Performance Requirements . . . 153
4.3 Detector Choice . . . 154
4.4 Environmental Control . . . 154
4.4.1 Motivation . . . 154
4.4.2 Ballistic Shock Mitigation . . . 155
4.4.3 Contamination Control . . . 155
4.5 Mechanical Design . . . 155
4.5.1 Design Overview . . . 156
4.5.2 Structural Integrity Analysis . . . 157
4.6 Cryogenic Temperature Control and Design . . . 158
4.6.1 Driving Requirements . . . 159
4.6.2 Design Overview . . . 159
4.6.3 Thermal Modelling . . . 160
4.6.3.1 Theory . . . 160

CHAPTER Page
4.6.3.2 Simulation Parameters . . . 161
4.6.3.3 Cooling: Steady State Analysis . . . 162
4.6.3.4 Cooling: Transient Analysis . . . 162
4.6.3.5 Heating: Transient Analysis . . . 163
4.6.3.6 Heating and Cooling Gradients . . . 163
4.6.3.7 Thermal Contraction . . . 164
4.7 Electronics . . . 165
4.7.1 Clock Driver Buffer Board . . . 165
4.7.1.1 Board Physical Design . . . 166
4.7.1.2 Signal Buffering . . . 167
4.7.1.3 Clock Level Filtering . . . 168
4.7.1.4 Board Results . . . 169
4.7.1.5 Design Changes and Future Work . . . 169
4.7.2 Temperature Process Control . . . 170
4.7.3 Command and Control System . . . 171
4.7.3.1 Design Overview . . . 171
4.7.3.2 Driving Requirements . . . 172
4.7.3.3 Small-Cam . . . 172
4.7.3.4 RTD . . . 173
4.7.3.5 Wiring . . . 173
4.8 Software . . . 174
4.9 Interface Control . . . 174
4.10 Discussion . . . 175
4.11 Summary . . . 176
4.12 Future Work . . . 176

CHAPTER Page
5 VIBRATIONALLY EXCITED HCN AROUND AFGL2591: A PROBE OF PROTOSTELLAR STRUCTURE 212
5.1 Introduction 212
5.2 Observations and Data Reduction 216
5.2.1 HHSMT HCN J=4→3 Observations 216
5.2.2 SMA HCN J=4→3 Observations 216
5.2.3 MIRIAD Data Reduction 218
5.2.4 Spectral Line Extraction 220
5.3 Discussion 222
5.3.1 HHSMT Data 222
5.3.2 SMA Data 223
5.3.3 Line Ratio Analysis 225
5.4 Origin of Ro-Vibrational HCN Emission 226
5.4.1 Double Peaked Emission 226
5.4.2 Filling Factor 227
5.5 Summary 229
5.6 Future Work 229
6 CONCLUSION 243
6.1 Summary 243
6.2 Toward Large Modular FPA Mass Production Implementation . . . 246
6.3 Looking Towards the Future 247
REFERENCES 251
APPENDIX A 256
APPENDIX B 258
APPENDIX C 261

LIST OF TABLES

Table Page

2.1 Small LBNL CCD Results 92

4.1 IDAN 179

4.2 SolidWorks Heat Transfer Simulation Parameters 180

5.1 Gaussian Fit Parameters 230

5.2 Energy Above Ground 231

5.3 Results (errors) calculated from gaussian fit to the HCN spectral lines. . 232

5.4 Excitation Temperatures 233

A.1 Physical Constants 257

LIST OF FIGURES

Figure Page

1.1 Protostellar Evolutionary Tracks 39

1.2 Pixel Structure 40

1.3 Three Phase CCD Layout 41

1.4 Bucket Brigade Analogy 42

1.5 Three Phase CCD Clocking Scheme 43

1.6 Delta-Doped CCD Schematic 44

1.7 Delta-Doped CCD Quantum Efficiency 45

1.8 Photon Transfer Curve (PTC) 46

2.1 CCD Calibration Schematic 93

2.2 SP-2150i Monochromator Internals 94

2.3 P-Channel Preamplifier Schematic 95

2.4 2-Channel CCD Preamplifier 96

2.5 ND-5 Series IRLabs Dewar 97

2.6 Cassini CCD and Si Photodiode 98

2.7 Co-planar Mounting Plate 99

2.8 Stray Light Control 100

2.9 Original Cold Finger for Small CCDs 101

2.10 Calibrated Photodiode Response 102

2.11 Small LBNL CCD 103

2.12 Small LBNL CCD Master Bias Frame 104

2.13 Small LBNL CCD Master Flat Field Frame 105

2.14 Small LBNL CCD Sample Object Frame 106

2.15 Small LBNL CCD Sample Reduced Object Frame 107

2.16 Small LBNL CCD Temperature Dependence 108

2.17 Small LBNL CCD Variable Gain 109

Figure Page
2.18 Small LBNL CCD Read Noise 110
2.19 Small LBNL CCD Bias Signal 111
2.20 Small LBNL CCD Linearity Exposure Time Dependence 112
2.21 Small LBNL CCD Linearity Fractional Exposure Time 113
2.22 Small LBNL CCD Linearity Residuals 114
2.23 Small LBNL CCD Photon Transfer Curves 115
2.24 Small LBNL CCD 450 nm Linearity 116
2.25 Small LBNL CCD 450 nm Non-Linearity 117
2.26 Small LBNL CCD Quantum Efficiency Variable Gain 118
2.27 Small LBNL CCD Quantum Efficiency Constant Gain 119
3.1 Non-inverting Amplifier 140
3.2 Non-inverting Amplifier PCB Layout 141
3.3 Modular Imager Cell Non-inverting Stage 142
3.4 Inverting Stage of the Amplifier 143
3.5 Inverting Amplifier PCB Layout 144
3.6 Modular Imager Cell Inverting Stage 145
3.7 Signal Conditioning of Clock Waveforms 146
3.8 MIC Inside LASI ND-5 Dewar 147
3.9 Combined Differential Output from Simulated Input 148
3.10 Zoomed Plot of Video Amplification 149
4.1 CHESS Optical System Design 181
4.2 CHESS Échelleogram 182
4.3 Overall Camera Design 183
4.4 Internals of the Dewar Design 184
4.5 Rigid Support for the Inverting Board of MIC 185
4.6 Rigid Support for the Noninverting Board of MIC 186

Figure Page
4.7 Axial Displacement of Mechanical Structure . . . 187
4.8 Orthogonal Displacement of Mechanical Structure . . . 188
4.9 Axial Displacement of PCB . . . 189
4.10 Aluminum Mounting Stage . . . 190
4.11 Aluminum Supports . . . 191
4.12 Support Arms for the G10 Cold-Head Guide . . . 192
4.13 Copper Cold-Head . . . 193
4.14 Copper Support Rod . . . 194
4.15 Machined Parts for the Imaging System . . . 195
4.16 Cold Bath and Cold-Head . . . 196
4.17 Transparent View of the Cold Finger . . . 197
4.18 Thermal Gradients Within Cooling System . . . 198
4.19 Thermal Profile: Cooling . . . 199
4.20 Thermal Profile: Heating . . . 200
4.21 Thermal Contraction of Cooling System . . . 201
4.22 Heater Control Circuit Schematic . . . 202
4.23 Heater Circuit . . . 203
4.24 Small-Cam . . . 204
4.25 RTD Control Computer . . . 205
4.26 3.5k $\times$ 3.5k LBNL Detector . . . 206
4.27 Flight Detector Output Image . . . 207
4.28 550 nm Response . . . 208
4.29 Clock Driver Buffer Board . . . 209
4.30 Lower Reset Gate Through Buffer Board . . . 210
4.31 Lower Horizontal Clock Through Buffer Board . . . 211
5.1 Selection Rules . . . 234

Figure Page
5.2 Iteration Number 235
5.3 Integrated Intensity Contours 236
5.4 Spectral Extraction Steps 237
5.5 HHSMT Spectra 238
5.6 HHSMT Spectra 239
5.7 SMA HCN v=0, v=(0,1^{1c},0), and v=(0,1^{1d},0) 240
5.8 SMA HCN v=(0,2^{0},0), v=(0,2^{2c},0), v=(0,2^{2d},0) 241
5.9 Disk Rotational Signature 242
B.1 Modular Imager Cell Schematic A 259
B.2 Modular Imager Cell Schematic B 260
C.1 Buffer Board A 262
C.2 Buffer Board B 263
C.3 Buffer Board C 264

Chapter 1

INTRODUCTION

> Any sufficiently advanced technology is indistinguishable from magic.–Arthur C. Clarke

1.1 Science Drivers

New technologies enable the exploration of a previously inaccessible parameter space, which can lead to revolutionary scientific discoveries. A comprehensive UV/optical/NIR imaging survey of Galactic star formation regions using diffraction limited high resolution imaging from very small pixel plate scales combined with a wide field of view from large focal plane arrays (FPAs) and an far-ultraviolet spectrograph would allow access to such a parameter space. Furthermore, such a survey would be essential to learning how the detailed physical processes that operate on the smaller scales interact with galactic scale astrophysical processes.

Several white papers published by Scowen et al. (2009a,b,c,d,e) and Jansen et al. (2009a,b) describe next generation missions and scientific objectives upon which those missions should be designed. Since those scientific objectives are the basis for the research in the Laboratory for Astronomical and Space Instrumentation (LASI), I will mention several here in order to lay the foundation for the technological developments upon which this dissertation is focused.

1.1.1 Young stellar objects (YSOs)

In order to assess the systemic qualities of star formation, it is crucial to observe the interactions between the gas and stars, between stars, and between disks and their environment. To do this, future technologies must be able to trace individual star, multiple star, and cluster properties in order to assess the assemblage of

various star formation products. This requires high angular resolution, sub-milli-arcsecond astrometry, and high resolution relative photometry.

1.1.2 Disks

Observations to assess the evolution of protoplanetary disks embedded within evaporating envelopes in nearby HII regions will require angular resolutions of ~ 1 AU at $\lambda \approx 200$ nm. At this resolution, it is possible to use spectral line-diagnostics to estimate photo-ionization induced mass-loss rates in irradiated propylds, which will allow for the estimation of their typical lifetimes.

1.1.3 Outflows

Jets and shocks arising from molecular clouds are likely emanating from deeply embedded protostars. By observing the spacing of ejecta within the outflow, it is possible to trace the accretion history of the source young stellar object (YSO). Furthermore, proper motion measurements of the outflows will enable the direct measurement of momentum and energy injected into the ISM by protostellar outflows. High resolution imaging of jets and outflows also allows the determination of the angular momentum and the history of interaction with nearby stellar objects.

1.1.4 Far-ultraviolet emission lines as probes of mass accretion in young stars

The far-ultraviolet (FUV) part of the spectrum allows for the observation of the hot gas (10^5 - 10^6 K) produced immediately behind the accretion shock formed from the YSO accreting material from a circumstellar accretion disk. The cooling, shocked gas which is optically thin, emits in the FUV. The luminosity of the FUV lines correlate strongly with mass accretion rate for Classical T-Tauri Stars (CTTS). Through the use of a high resolution spectrograph and stable,

high-reflectivity FUV mirror coatings, it is possible to determine the preferred modes of accretion for young low-mass stars.

1.1.5 Feedback from Massive Stars

Massive OB stars have profound influence on their environment, from destructive evaporation of molecular clouds to the creation of the heavy elements that drive evolutionary processes. High resolution imaging will allow for the quantization of feedback parameters such as ionizing fluxes, stellar wind power, elemental enrichment, and ultimately, the sphere of influence of massive stars as a function of mass and environment.

1.1.6 Extragalactic observations of Star Formation

Due to observational constraints within our own galaxy, it is difficult, if not impossible, to develop an understanding of star formation on galactic scales. One possible study is of the coherence length of star formation. If stars form independently of each other, on a global scale, then their should be no correlation between various star forming sites. However, if star formation is caused by wave propagation from one side of the galaxy to the other, then there should be a linear correlation. High resolution imaging over a large field of view corresponding to large FPAs will allow for the determination of clustering of extragalactic star formation.

True advances in most, if not all, of the aforementioned scientific endeavors requires diffraction limited high resolution imaging from very small pixel plate scales combined with a wide field of view from large FPAs. Ultimately, to support these science programs, one must develop the technology capable of constructing and calibrating large FPAs that are flight rated for space while simultaneously minimizing risk and cost, and maximizing scientific throughput.

1.2 Engineering Drivers

Engineering requirements for comprehensive UV/O/NIR wide field imaging surveys using large focal plane arrays are defined by the wavelength regime of observation, the form factor and pitch of the detectors, the overall size of the array or field of view of the camera, the seam size between the detectors, the detector clocking rate, the noise characteristics and the operational temperature of the detectors. The infrastructure must also be developed and be ready for implementation to mitigate the risk associated with integration and testing. Furthermore, the development of a low power, low noise, and low mass modular design for detector control, readout, and mechanical support is a necessity. This development would allow individual detectors to be tested and easily removed as needed, once integrated into the focal plane assembly, with a minimum of impact on any neighboring detectors (Scowen et al., 2009b).

Performing emission line surveys requires a suite of narrowband and continuum filters to separate out ionization structures at shock fronts. The use of orthogonally arranged detectors abutted together with small seams and even smaller pixels allows for high resolution with very little dithering of exposures required, which maximizes observing efficiency and minimizes the observing time. The detector clocking rate determines the time it takes to extract the data from the detector with faster clocking allowing for faster readout. However, as a consequence of clocking the data out of the array quickly, the intrinsic design of the detector causes an increase in the noise level from the movement of electrons through the readout amplifier on the CCD. Efficient observational strategy must be developed to balance noise with read time without degrading the science return.

According to Scowen et al. (2009b), in order for the the development of large focal plane arrays technologically and fiscally feasible, the following requirements must be met and associated technologies must be developed:

- Easy mass production through streamlining and shortening the production period of the individual detectors comprising the large focal plane arrays.
- Increased production yield of the scientific grade detectors in order to mitigate the calibration and characterization time scales.
- An effective method for abutting the detectors while minimizing seam and maintaining coplanarity.
- The technology to reduce the operational temperature of the detector easily, efficiently, and inexpensively in order to achieve the highest fidelity data products.
- The development of detector readout and control systems that are low power, low mass, and low noise, such as a modular imager cell, for use in the finite resource environment of space missions.

The development of a facility capable of addressing some of the aforementioned technological endeavors is a critical step in the development of large focal plane arrays that will eventually address the underlying astrophysics controlling the evolution of the baryonic matter in the universe.

1.3 Star Formation

Early stages of star formation have observational signatures across the electromagnetic spectrum. The collapse of a molecular cloud into a protostar is best observed in wavelengths longer than optical, such as submillimeter (submm) and infrared (IR), in order to peer through the clouds of gas and dust enshrouding

the protostar. The onset of hydrogen fusion is best observed in near-infrared (NIR) and optical (O) wavelengths in order to assess the effect of core hydrogen burning on the enshrouding gas cloud as it is heated. Eventual escape from the enshrouding cloud reveals the young stellar object (YSO), which is now easily observable in the optical and ultraviolet (UV) where the radiation emanating from the star continues to shape the surrounding environment. Observations of the aforementioned stages of stellar evolution are essential to understanding the astrophysical processes that govern star formation.

Star formation begins with molecular cloud formation within the Interstellar Medium (ISM). These molecular clouds are comprised of cold (10 – 20 K) molecular hydrogen (H_2) and carbon monoxide (CO), have densities on the order of 10^{2-3} particles/cm^{-3}, and have typical diameters of 1000 AU. Clumping of the gas within the molecular cloud causes the molecular cloud to fragment under gravity to form cores that have densities on the order of 10^6 particles/cm^{-3} and temperatures around (10 – 100 K). The temperature rises a little, but only at the core where the majority of the mass is concentrated. The densest of the cores with densities 20 times greater and diameters 10^7 times smaller collapse to form protostars.

The collapse is governed by the interplay of thermal kinetic energy and gravitational potential energy related through the virial theorem. As the dense cores collapse to form protostars, the temperature within the gas rises to 10^6 K at the center and $\sim$ 3000 K in the surrounding material. From here, the protostar continues to evolve through a T-Tauri phase, named after the first star of this type observed. During the T-Tauri phase, spin and pressure gradients channel accretion material from the envelope into a spinning disk. As time passes, material from the accretion disk is funneled onto the protostar while supersonic jets and outflows

attempt to conserve angular momentum by expelling material into the ISM. When enough mass has been funneled onto the protostar, the energy afforded through gravitational potential and the associated increase in temperature and density becomes great enough to overcome the repulsive force of two hydrogen nuclei to trigger hydrogen fusion within the core. From here, the YSO continues to expel mass until hydrostatic equilibrium is reached and the star arrives on the main sequence where it will continue to burn hydrogen in its core for millions to billions of years, depending on the initial mass.

1.3.1 Gravitational Collapse

Gravitational collapse occurs when thermal kinetic energy within the gravitationally bound clump of gas can no longer support against the force of gravity. Gravitational forces will overwhelm kinetic forces when the total mass is greater than the Jean's mass, which is the critical mass a gravitationally bound clump can have and remain stable against gravitational collapse.

The Virial theorem says that for a system in equilibrium, the total energy available is equal to 1/2 the potential energy. The total energy is also equal to the kinetic energy plus the potential energy. So, according to the Virial theorem, 2K+U=0. If the kinetic and potential energies are given by:

$$K = \frac{3}{2} N k_B T \tag{1.1}$$

$$U = -\frac{3}{5} \frac{GM^2}{R} \tag{1.2}$$

then collapse will occur when:

$$3 N k_B T < \frac{3}{5} \frac{GM^2}{R} \tag{1.3}$$

By substituting for N and R and assuming a spherical distribution of constant density mass, the Jean's mass can be written as:

$$M_J = \left(\frac{3}{4\pi\rho_0}\right)^{1/2} \left(\frac{5k_BT}{G\mu m_H}\right)^{3/2} \tag{1.4}$$

where μ is the mean molecular weight of the particles within the gas, ρ_0 is the initial density, k_B is Boltzmann's constant, m_H is the mass of the hydrogen atom, and T is the kinetic temperature of the gas (Carroll & Ostlie, 1996). The critical radius for collapse, known as the Jean's length, can also be expressed by assuming a spherically symmetric distribution of mass with uniform density:

$$R_J = \sqrt{\frac{15k_BT}{4\pi G\mu m_H\rho_0}} \tag{1.5}$$

If the radius of the cloud is larger than the Jean's length or has a mass greater than the Jean's mass, then the cloud will be unstable against gravitational collapse.

The minimum time over which the cloud will gravitationally collapse in known as the free-fall time scale:

$$t_{ff} = \sqrt{\frac{3\pi}{32G\rho_0}} \tag{1.6}$$

and is dependent only on the density of the initial cloud, again assuming a spherically symmetric distribution. The free-fall timescale is independent of the initial radius of the sphere.

These equations provide only estimates for the minimum collapse mass, radius, and timescales for an isothermally collapsing sphere. In this analysis, it was assumed that the radiation escaping during the collapse did not interact with the collapsing material, creating an isothermal collapse. A more rigorous treatment would involve the inclusion of angular momentum transport, magnetic field pressure support, and the inclusion of the density gradients in the collapse process.

A simplification for the Jean's mass in terms of solar mass, $M_\odot$, is given by:

$$M_J \approx 18 M_\odot T^{3/2} n^{-1/2} \tag{1.7}$$

Since hydrogen nuclei are almost exclusively bound in H_2 within a molecular cloud and $n \approx n(H_2) + n(He)$, then the density is given by $\rho = \mu_n m_H n$ where the mean molecular weight, $\mu_n = 2.29$, in a fully molecular cloud with 25% by mass helium and n is the number density per cubic centimeter. The coefficient can range from 18 - 90 based upon the definition of n (Evans, 1999).

1.3.2 Protostellar Evolution

The brief synopsis of stellar evolution described in Section 1.3 provides the general principles and stages of the formation of main sequence stars. Low-mass stars (0.8 - 4.0$M_\odot$) evolve very slowly, requiring 10^6 - 10^7 years to reach the main sequence. Due to convection, the surface temperature of the protostar remains relatively constant, so the luminosity decreases as gravitational collapse proceeds. This is shown as a downward motion in the H-R diagram (Figure 1.1). After a time, the gravitational collapse causes the internal temperature of the star to increase such that the interior becomes ionized. At the point when the occurs, radiative transport becomes dominant over convective transport, causing the surface temperature and luminosity to increase. This is shown as the upward bend in the H-R diagram. Eventually, the interior temperature becomes hot enough for fusion to begin ($\sim 10^{6-7}$ K), providing enough heat and pressure to stop gravitational contraction. The star then falls onto the main sequence.

1.3.2.1 Classification

Protostars are classified by the amount of infrared radiation excess in their spectral energy distribution (SED) and the peak of their SED. There are four classes

defined: Class 0, Class I, Class II, and Class III. The spectral energy distribution of Class 0 protostars peaks in the far infrared to sub-millimeter and are undetected at wavelengths less than 10 μm (Barsony, 1994). The mass of the core is much less than the mass of the surrounding envelope. The bulk of the stellar mass has yet to be assembled and they have strong bipolar outflows. Class I are slightly more evolved protostars with their peak in the mid infrared and a mass of the YSO greater than the mass of the envelope.

Classes II and III avail themselves of the possibility of optical detection. Class II is the classical T-Tauri star (CTTS) where the temperatures are $\sim$1000 - 2500 K and the peak of their SED is in the near-infrared. In this phase, the YSO is still encircled by an accretion disk and the YSO is now visible in the optical. The mass of the disk is now on the order of 1% solar. According to Li & Hu (1998), these CTTS are characterized by strong optical emission lines, ultraviolet and infrared excesses.

Finally, Class III protostars are the most evolved with their SED peaks close to optical. Class III are also known as weak lined T-Tauri stars (Barsony, 1994) and are believed to be relatively devoid of circumstellar material (Li & Hu, 1998). The temperature has increased to $\sim$3000 K and the disk mass is now less than the mass of Jupiter.

1.3.2.2 High Mass Protostellar Object

The above description corresponds nicely to the evolution of low-mass protostellar candidates. High mass protostars follow a slightly different evolutionary chain. For protostars about $4M_{\odot}$, the protostar contracts and heats more rapidly than the low-mass protostars, allowing hydrogen burning to begin earlier. As a result, the luminosity quickly stabilizes at nearly its final value, while the surface temperature continues to increase as gravitational collapse continues. It appears on the

HR-diagram (Figure 1.1) that the massive stars move horizontally. Eventually, the pressure built up from burning interior to the surface of the star will counteract the gravitational collapse and the star will fall upon the main sequence.

A high mass protostellar object (HMPO) is considered the precursor to the formation of high mass stars. They are characterized by high luminosities ($> 10^4$ $L_\odot$), dense ($> 10^6$ cm^{-3}) and warm (> 100 K) molecular gas, and strong dust emission. They have little to no free-free emission at centimeter wavelengths from ionized gas and and have yet to develop an ultracompact HII region (Sridharan et al., 2002). They are typically Class 0/I and have little to no emission in short-ward of the FIR or even sub-millimeter. An example is AFGL 2591, which is discussed in Chapter 5.

Observations of a high mass protostellar objects in the submm in conjunction with FUV/UV/O/NIR observations could provide valuable insight into the formation of the accretion disk and the excitation mechanisms within.

1.4 Charge-Coupled Device Technology

The charge-coupled device (CCD) was invented by William S. Boyle and George E. Smith at Bell Telephone Laboratories as a solid state memory storage device in 1969 (Boyle & Smith, 1970).While the application as a memory storage device never took hold, it was realized the CCD was sensitive in incident radiation and could be used as in imaging device. With that realization, a revolution took place in the world of research, commercial, and personal imaging. The applications and use of CCDs were so widespread and ubiquitous, from astronomy to medical imaging to personal cameras, that Boyle and Smith received the Nobel Prize in Physics[1] for their invention in 2009.

[1]Copywrite The Nobel Foundation

The first astronomical use of the CCD occurred in the late 1970s. Since then, they have become the dominant detector of choice for optical photons at professional observatories. They work via the photo-electric effect and are far more sensitive to incoming photons than the human eye or photographic film. Their popularity arises from their ability to integrate over long periods of time, a high dynamic range, a linear response to radiation from ultra-violet to optical to near-infrared radiation, a high quantum efficiency, low mass, reliable rigidity, excellent noise characteristics, and low power consumption (Kitchin, 2003). In an astronomical context, the ccd provides good spatial resolution, allowing for the detection of very faint objects and high photometric precision, which allows for precise measurements of fluxes and magnitudes of astronomical targets.

In order to generate an astronomical image, the CCD must detect incoming photons. In order to turn these incident photons into an image, the CCD must perform four primary functions: charge generation, charge collection, charge transfer and charge measurement. Charge generation is the ability of the CCD to generate an electric charge from an incoming photon. Charge collection is the ability of the CCD to store and authentically recreate the charge distribution caused by the charge generation process. Charge collection depends upon the size of the detector, the full well capacity, and the ability to mitigate charge diffusion. Charge transfer is the ability of the CCD to accurately transfer charge out of the detector. Finally, charge measurement is the detection and measurement of the charge collected in each pixel. This is accomplished by dumping the charge onto a small capacitor that is connected to an output amplifier that converts the charge to an output voltage proportional to the transferred charge (Janesick, 2001). The output amplifier voltage is then read out and converted to a digital number (DN) using external analog-to-digital electronics. The digital numbers are then

converted into an two-dimensional image by a computer where each pixel in the image corresponds to the magnitude of the digital number.

1.4.1 Detection

The basic detection mechanism in the conversion of incident light into photoelectrons is through the photoelectric effect (Section 1.4.1.1). When photons of appropriate energy incident upon the detector are absorbed, the photon interacts with the substrate by liberating an electron from the valence band into the conduction band, generating an electron-hole (e-h) pair. The liberated electrons become trapped in the depletion region within the pixel by voltages applied using sub-pixel size electrodes attached to each pixel (Section 1.4.3). The electrons are held in place by a large positive voltage on the center electrode and accumulate until their total number is read out by charge-coupling the detecting electrodes to a single readout electrode (Kitchin, 2003) Section 1.4.4 provides further detail on the readout process.

1.4.1.1 The Photoelectric Effect

The photoelectric effect (Einstein, 1905) governs the operation of the CCD. When photons of an appropriate energy are incident upon a metallic surface, electrons are liberated from the surface, leaving behind a hole, creating and electron hole (e-h) pair. The appropriate energy corresponds to the band-gap energy of the material, in this case, silicon (Si), which is the energy required to liberate an electron from the valence band into the conduction band. For Si, the band-gap energy is $\sim$1.14 electron-Volts (eV) (Janesick, 2007). The maximum wavelength of interaction for Si is:

$$\lambda = \frac{12390}{E(\text{eV})}\ [\text{Å}] \tag{1.8}$$

where equation (1.8) is the simplified form of wavelength dependence on incident energy. Equation (1.8) then allows for the calculation of the longest wavelength that will interact with a Si-based detector that has a band-gap energy of 1.14 eV:

$$\lambda = \frac{12390}{1.14}\ [\text{Å}]$$

$$\lambda = 10868\ [\text{Å}]$$

$$\lambda \approx 1.1\ [\mu\text{m}]$$

Wavelengths longer than $\sim 1.1\ \mu$m will typically pass through the detector without interaction. Wavelengths shorter than $\sim 1.1\ \mu$m will generate a single electron-hole pair for wavelengths up to 3000 Å. Beyond 3000 Å, which corresponds to higher energies, multiple electron-hole pairs are generated for each incident photon. Furthermore, for wavelengths longer than ~1240 Å, corresponding to energies above 10 eV, the number of electron-hole pairs generated can be calculated from:

$$\eta_i = \frac{E(\text{eV})}{E_{e-h}}\ [electrons(e^-)/photon] \tag{1.9}$$

where η_i is the quantum yield and E_{e-h} is the energy required to generate an electron-hole pair, which is 3.65 eV/e$^-$ for Si at room temperature (Janesick, 2001). For Lyman-α (1216 Å) the quantum yield is 2.74 electrons. Knowing the exact number of electron-hole pairs created at specific wavelengths is essential to measuring the absolute quantum efficiency (QE) of a detector for wavelengths outside the visible range. Further discussion on quantum yield is given in Section 1.7.1.

1.4.2 Absorption Depth

Photons incident upon the CCD interact differently depending on their wavelength. Shorter wavelength photons are absorbed nearer to the surface of the CCD than longer wavelength photons. The short wavelength photons may not even make it to the depletion region in a front-side illuminated device due to absorption or reflection by the poly-silicon gate structures. Longer wavelength photons are absorbed much deeper within the substrate where the gate potential is rather weak, leading to possible migration into the neighboring pixel along the column or underneath the channel stops that separate the columns into the neighboring row. Even longer wavelength photons will pass through the substrate without interacting. The thickness of the detector will determine the wavelengths of interaction, with thicker detectors being more sensitive to longer wavelengths than thin detectors. The absorption depth has implications for the CCD architecture.

1.4.3 CCD Architecture

The active photosensitive material of CCDs is typically silicon. The CCD is constructed of an orthogonal two-dimensional array of coupled metal-oxide-semiconductor (MOS) (or metal-insulator-semiconductor (MIS)) capacitors arranged on a silicon substrate with three electrodes attached to each. A single element of the array is known as a pixel. Figure 1.2 shows a three dimensional view of the structure of a typical CCD pixel. The majority of modern scientific grade pixels are buried channel, where charge packets are confined to a potential well that lies beneath the surface of the CCD. Electrodes are attached to poly-silicon gates which are deposited upon a layer of silicon-dioxide, SiO_2, which acts as a dielectric. Below the SiO_2 is the n-channel depletion region. Below sits the buried-channel, or potential well, between potential barrier channel

stops on either side designed to prevent charge spillover into neighboring pixels. All of this rests within a p-type silicon substrate. The term MOS comes from the arrangement of the metal gates on top of a dielectric oxide on top of the silicon semiconductor substrate.

The terms p-type and n-type are used to describe the charge excess, the type of majority charge carriers, and subsequently, the type of dopant introduced into the silicon substrate. In a p-type silicon, the dopant is typically boron, which is an acceptor atom, and the majority charge carriers are positively charged "holes." Since the excess number of free holes forms a positive charge, the semi-conductors are known as p-type. In n-type silicon, the dopant is a donor atom, such as phosphorus and the charge carriers are electrons. N-type silicon is known as negatively charged since there are an excess number of free electrons.

The architecture for a typical three-phase CCD, showing the arrangement of pixels in rows and columns, is shown in Figure 1.3. The columns are typically defined as the vertical structures within the CCD and the rows are the horizontal structures. The term three-phase arises from the readout requiring only three potentials to clock the charge out of the device. By sequentially manipulating the potential at each phase, the charge within the pixel columns can be clocked into an extra row of pixels, known as the serial register, at the end of each column. This is known as parallel charge transfer because all the parallel columns are shifted at the same time. The charge in the serial register is then clocked one-by-one to a sense capacitor and subsequently to the output register.

The depletion region of the CCD is directly below the oxide layer and is created by the application of either a high positive or negative potential. In a p-type CCD, a large positive potential is applied to the gate electrode, causing the majority carriers (holes) to be driven away from the Si-SiO_2 interface, leaving

behind a region “depleted” of mobile charge carriers. The number of holes driven away is equal to the number of positive charges on the gate electrode. The depletion region is non-conductive and acts as an insulator with a capacitance proportional to depletion region depth. By manipulating the potential applied to the gate electrode one can affect the size of the depletion region and consequently the number of photo-electrons that can be collected. In an n-type CCD, the potential applied to the gate electrode is negative.

In designing a CCD, the thickness of the detector must also be taken into account because the thickness also determines the wavelengths of interaction. Thicker detectors will increase the probability of interaction with a longer wavelength photon, at the cost of increased interaction with undesirable particles, such as cosmic rays. Thin detectors have increased response to shorter wavelengths and have lower interaction probability with cosmic rays. Further discussion on thin detectors is presented in Section 1.8.

1.4.4 Readout

Three-phase CCD readout is most easily described with an analogy to a “bucket brigade.” Figure 1.4 shows a parallel bucket array that is exposed to raindrops for a fixed amount of time. After the integration time is complete, the first row will be shifted and dumped into the serial array of buckets. The serial array of buckets will then be dumped into a calibrated measuring container. After the entire serial array has been measured, the next parallel row is dumped into the serial array and the process is repeated until all of the buckets are empty.

Fugure 1.5 shows what happens to a pixel in terms of gate voltages. During integration, the middle voltage, Φ_2, is held at a high potential, while Φ_1 and Φ_3 are held low, so the generated photo-electrons will be driven into the depletion region within the pixel and held there. At the end of integration, when clocking

begins, Φ_3 is brought to high potential in order to allow the photo-electrons to diffuse. Next, Φ_2 is brought low to trap the charges within Φ_3. Next, Φ_1 is brought high and Φ_3 remains high, allowing the charge to transfer to the neighboring pixel. At the end of the column, the charge is dumped into an extra row of pixels known as the serial register. The serial register is then clocked in a similar fashion until all of the charge has been dumped from the serial register onto a capacitor, or "sense node," connected to an on-chip output metal-oxide-semiconductor field-effect transistor (MOSFET) amplifier. The amplifier converts the charge to an output voltage which can then be measured by external readout circuitry. This process is repeated until all of the charge within the array is read out.

Ideally, every photo-electron generated within the substrate of the CCD is measured by the output amplifier. The charge-transfer efficiency (CTE) defines the maximum amount of generated photo-electrons that can be transferred to the output amplifier. CTE values $> 99.9999\%$ are typical for modern CCDs. Further discussion of CTE is in Section 1.5. In addition to the generated photo-electrons being read out of the detector, spurious noise sources introduce themselves into the signal chain. These noise sources consist of read noise, shot noise, fixed pattern noise, full well noise, and dark current. These noise sources are discussed in Section 1.7.1 and Section 1.7.4.

Consideration of these noise sources motivated the design for the LASI facility. Typically, one can exert control over the read noise, fixed pattern noise, and the dark current generated in the detector. Shot noise is the statistical noise intrinsic to the arrival of photons at the detector and is not a controllable noise source. The full well noise is determined by the fabrication of the device and is typically only controllable at the CCD fabrication level. The read noise can be minimized by using low noise readout electronics, short cable lengths, and proper

power conditioning. Some fixed pattern noise can be minimized by developing a system free from light leaks, specular reflections, and appropriately designed readout architecture. In addition, the fixed pattern noise can be effectively removed from the final data product by flat fielding. Control over the dark current is exerted by cooling the detector to cryogenic temperatures, effectively slowing the random thermal motions of the electrons within the substrate. Modern astronomical CCDs have dark currents on the order of 0.01 electrons/pixel/hour at < 175 K.

1.5 Charge Transfer Efficiency

Charge transfer efficiency is a measure of the ability of the device to transfer charge from one pixel to the next and is defined as the ratio of charge transferred from the target pixel to the initial charge stored in the target pixel (Janesick, 2001). During transfer operations, charge is lost due to defects in the silicon lattice, or charge "traps" as they are known, which remove and retain some fraction of the charge, disallowing complete transfer.

CTE is computationally defined as charge transfer inefficiency (CTI), which is the fraction of charge left behind in a single pixel transfer:

$$\mathrm{CTI} = (1 - \mathrm{CTE}) \tag{1.10}$$

For an m×n pixel CCD with serial CTE (C_s) and parallel CTE (C_p), the percentage of photo-electrons that arrive at the output amplifier is given by:

$$CTE = \left(C_p^n\right)\left(C_s^m\right) \times 100\ [\%] \tag{1.11}$$

If n_{e^-} is number of photo-electrons (total charge) in the final pixel, then the number of electrons that will arrive at the amplifier is given by (Jansen, 2006):

$$n'_{e^-} = (n_{e^-})\left(C_p^n\right)\left(C_s^m\right) \tag{1.12}$$

The charge lost, l_{e^-}, is then given by:

$$l_{e^-} = n_{e^-} - n'_{e^-} \tag{1.13}$$

$$l_{e^-} = n_{e^-} \left(1 - \left(C_p^n\right)\left(C_s^m\right)\right) \tag{1.14}$$

The charge that is left behind during an inefficient transfer will not necessarily be lost. It may join the charge transferred from the next pixel in that column becoming indistinguishable from the charge of the next pixel and subsequently transferred out of the detector (Jansen, 2006).

1.5.1 CTE Degradation

Detectors subject to prolonged exposure to ionizing radiation, such as those used in the Wide-Field Camera 3 (WFC3) (Dressel, 2011) on the Hubble Space Telescope (HST) will experience a decrease in CTE over time. This occurs because cosmic rays, which are mainly relativistic protons, interact with the detectors causing permanent physical damage to the substrate. This physical damage can also manifest as charge traps. The effects can be minimized by using p-channel detectors, which are more radiation tolerant than n-channel detectors.

The charge carriers in p-channel devices are the holes in the e-h pair left behind from the interaction of a photon with the substrate. When a proton strikes the detector and passes through, it leaves behind a trail of electrons within the bulk substrate. Since the holes are the charge carriers, the electrons generated from this interaction are ignored during the charge transfer and are left to freely recombine within the substrate.

Aside from changing detectors, according to Janesick (2001) and Giavalisco (2003), the mitigation of CTE degradation is based upon the idea that if the charge traps are kept filled with charge, they are less likely to trap additional

charge from transmitting packets moved through them during the charge transfer operation. Two possible methods discussed are charge injection (CI) and pre/post flash (PF).

Charge injection involves the manipulation of the output transfer gate and output summing well gate within the detector to electronically deposit charge into the pixels (Janesick, 2001). Charge can be injected before or after exposure in all or only select pixel locations. In the case of WFC3, charge is injected in rows across the device at every tenth horizontal row (Bushouse et al., 2011). When the device is read out, the injected charge then fills the traps, making them "passive", i.e. incapable of additional charge trapping from passing sources. Since passivity has a limited duration, the spacing between horizontally injected rows must be such that throughout the read, the charge traps remain "passive" (Stiavelli et al., 2001).

In the case of PF, charge is deposited by photons emitted using an appropriate source, such as a lamp either before or after an exposure is taken. The average amount of charge generated is controlled through the exposure time and the intensity of the light source (Giavalisco, 2003).

The difference between the two methods comes down to the noise properties. The noise in PF is controlled by Poisson statistics, since the flashing is intrinsically a Poisson process. The noise associated with CI is related to the accuracy of the electronics. As long as the total amount of charge required to mitigate CTE losses is small, PF is the desired design solution because of the design simplicity. However, if the electronics are stable and charge can be injected accurately, CI is the better alternative (Giavalisco, 2003).

1.6 Next Generation Detector Development

The development of new detector technology is necessary to enable the creation of more efficient, more cost effective, and less risky large format focal plane arrays. The current state of large focal plane arrays, along with a suggested solution to ameliorate scaling problems with building large focal plane arrays, is discussed below. A detector technological advance, delta-doping, is also presented as a solution to address detector efficiency problems at shorter wavelengths.

1.6.1 Large Focal Plane Arrays

The 95-Megapixel Kepler Focal Plane Array Assembly (FPAA) is the current state-of-the-art FPA in space (Philbrick et al., 2004). The FPAA is comprised of 46 CCDs, of which 42 are for science and four provide fine guidance control. The 42 science CCDs are arranged as 21 CCD modules, with each module housing two 2k $\times$ 1k pixel detectors. Behind the FPA lies an electronics rack providing the bias, clocks, and pre-amplification of the CCD video output. Cooling is done via heat pipes and a passive radiator pointed away from the Sun. This setup is a massive load for the overall Kepler power and mechanical system, drawing 7 W and weighing 57 kg. If this system were to be deployed for future mission concepts consisting of FPAs on the order of 540 CCDs, such as the Star Formation Camera (SFC) (Scowen et al., 2009d), the power requirement would be upwards of 90 W and the mass upwards of 741 kg, assuming a linear relationship. The mass of the FPA alone would be a significant driver in mission cost and could push any proposal beyond the scope of what is financially feasible.

Wide-Field Camera 3 (WFC3) on the Hubble Space Telescope is a state-of-the-art focal plane array and is made of two 4k $\times$ 2k CCDs nearly abutted to make a single 4k $\times$ 4k focal plane array with a field of view of .002 square

degrees. The field of view of WFC3 is small when compared to Kepler (105 square degrees) and future mission concepts like the SFC (22 square degrees), (Scowen et al., 2009d) but the resolution is diffraction limited. The limitation with this approach is the small field of view, requiring extensive observation time in order to complete large areal surveys, which subsequently drives the mission costs upwards and limits the overall effectiveness of the observatory.

Ground based technology like the MOSAIC-1.1 imager at KPNO is comprised of an 8k $\times$ 8k pixel mosaic of 2k $\times$ 4k pixel CCDs (Schweiker et al., 2011). The Large Binocular Camera (LBC) at the Large Binocular Telescope is also composed of four 2k $\times$ 4k CCDs (Pedichini et al., 2003) mounted to a single CCD platform. The single platform mosaics are difficult, costly, and time-consuming to repair. In the future, the Large Synoptic Survey Telescope (LSST) will have a 3.2-gigapixel FPA comprised of 189, 4k $\times$ 4k, CCDs with 10 μm pixels for a 9 $(^{\circ})^2$ field of view (FOV). The FPA will be tiled with 3 $\times$ 3 detector "rafts" with all of the associated readout and control electronics within the footprint of the "raft" (LSST Science Collaboration et al., 2009). While these "rafts" are inherently modular, forming a single 144-Megapixel array on their own, they are still very large and therefore prohibitive for space missions where mass, volume, and power are at a premium.

A solution to the above problems is the development of modular imager cells using embedded controllers to ameliorate the power, mass, and cost for the large format CCD focal plane arrays.

1.6.2 Delta-doping

Short wavelength FUV-NUV radiation is absorbed just below the surface of a pixel in a silicon CCD, which generates a charge carrier that could possibly recombine instead of being detected. This lends itself to very low quantum efficiency for a

typical CCD (Figure 1.6). A possible solution to increase the efficiency at the aforementioned wavelengths is to alter the band structure of the silicon substrate through a process known as delta-doping.

Delta-doping, developed at the Jet Propulsion Laboratory (JPL), (Hoenk et al., 1992) and (Nikzad et al., 2000) is a process by which a thin layer ($\sim$few 10's of angstroms) of highly doped silicon is grown on the back surface of a CCD, providing an ideal electronic potential near the CCD back surface by modifying the band structure and subsequently increasing the internal quantum efficiency of the silicon to the reflection limit (Hoenk et al., 1992; Janesick, 2001) across the responsive bandpass (Figure 1.6). Typical dopants are boron (for n-channel devices) or antimony (for p-channel devices).

By delta-doping the detectors and applying a significant substrate potential, on the order of 40 - 80 V for some devices, an electron that would typically recombine is forced into the collection region within the pixel. Collecting the photo-generated electron instead of letting it recombine increases the quantum efficiency. Because the detector substrate upon which the delta-doping process is typically performed are thick ($\sim$ 150 - 300 μm) the detectors have enhanced response across the spectrum from 1000 - 11500 Å. Furthermore, due to the delta-doping process, the most enhanced response is in the FUV to NUV, where the QE is driven above 30% from $\sim$1000 - 1200 Å (Figure 1.7). In order to understand the effects of delta-doping, it is important to fully calibrate the detectors.

1.7 Detector Calibration: Photon Transfer Curve

The photon transfer curve (PTC) (Figure 1.8) is probably the single most important calibration curve one can create when working with camera systems and detectors. The PTC is also easy to construct consisting of only a plot of log(noise) on the y-axis versus log(signal) on the x-axis. The units are typically digital

number (DN), but the PTC can also be expressed in terms of electrons, as long as the gain for the system has already been determined. By evaluating the PTC, one can determine the linearity, full well depth, read noise, gain, and dark current associated with a detector.

To construct the PTC, one selects a region of interest on the detector, subtracts the offset value from each pixel attained from the overscan region, and calculates the standard deviation and mean signal for those pixels. The following formalism defines the construction of the standard PTC:

$$S(\mathrm{DN}) = \frac{\sum_{i=1}^{n_{\mathrm{PIX}}} \mathrm{DN}_i}{n_{\mathrm{PIX}}} - S_{OFFSET}(DN) \tag{1.15}$$

$$\sigma_{\mathrm{TOTAL}}(\mathrm{DN}) = \left\{ \frac{\sum_{i=1}^{n_{\mathrm{PIX}}} \left[S_i(\mathrm{DN}) - S(\mathrm{DN})\right]^2}{n_{\mathrm{PIX}}} \right\}^{1/2} \tag{1.16}$$

where $S(\mathrm{DN})$ is the average signal level, DN_i is the raw signal of the ith raw pixel, n_{PIX} is the number of pixels contained in the subarray, $S_{OFFSET}(DN)$ is the ADC offset level, typically obtained by averaging the overscan region of an exposure, $\sigma_{\mathrm{TOTAL}}(\mathrm{DN})$ is the total noise (read, shot, and FPN) plotted in Figure 1.8, and $S_i(\mathrm{DN})$ is the raw signal of the ith raw pixel without offset. When choosing a region of interest, it is best to select as many pixels as possible because the measurement accuracy is proportional to the square root of the number of pixels (Janesick, 2007).

The PTC has four identified regimes within its structure: the read noise dominated regime, the shot-noise dominated regime, the pixel fixed pattern noise regime (FPN), and the full well noise regime. These different regimes are defined by their change in slope with respect to the neighboring section of the PTC. Figure 1.8 shows graphically the contribution to the photon transfer curve of each noise regime. The read noise dominated regime has a slope of 0 and is representative of noise associated with extracting the charge from the detector and is approximately

fixed for every readout of the detector. After the read noise, the shot-noise dominated regime takes over as the illumination level increases. The shot noise regime has a slope of 1/2 because it is correlated with the arrival of photons to the detector (Section 1.7.1.2). The FPN regime has a slope of 1 because the signal and FPN scale together as the illumination level is increased. Finally, the full well noise regime begins when the slope starts to deviate significantly from a dependence on the increase in light level. Full well corresponds to a slope of infinity, which is representative of pixel saturation (Janesick, 2001).

1.7.1 Noise Regimes

Characterization of detector noise properties is essential to proper calibration. Below I discuss the typical noise properties of the detectors that can be determined from the photon transfer curve.

1.7.1.1 Read Noise

According to Janesick (2007), the read noise is defined as any noise source that is not a function of signal and sets a noise floor upon the device. A signal cannot be measured lower than the read noise. The physical size of the on-chip amplifier, the integrated circuit construction, the temperature of the amplifier, and the sensitivity all contribute to the read noise for a CCD. Furthermore, readout speed of the external readout electronics also contributes to read noise because the rate at which currents flow through the on-chip amplifier can cause thermal swings in the amplifier temperature, affecting the read noise level. Higher temperatures through the amplifier may cause thermally generated electrons to enter the data stream. Generally speaking, slower readout speeds lead to a lower read noise floor, but at the expense of an increased camera duty cycle (Howell, 2006).

Readout noise, which I define here to be the noise associated with the external readout electronics, consists of two inseparable components. The first is the conversion of analog signal to a digital number, which is not perfectly repeatable. Since we used a predefined readout architecture, we were unable to correct for analog-to-conversion (ADC) conversion errors. The second component is composed of the spurious signals generated in the readout electronics and test architecture. This second noise source is what we attempted to mitigate within our laboratory set-up.

1.7.1.2 Shot Noise

Shot noise is fundamentally connected to the way photons spatially arrive on a detector. The standard deviation of the number of photon interactions per pixel is called the photon shot noise (Janesick, 2007). This statistical regime obeys a classical Poisson probability distribution which describes the probability that an event will occur in a given length of time as long as it can be counted, occurrences are independent, the frequency of occurrence during the time period is known. The Poission distribution can be shown to be:

$$p_i = \frac{P_{\mathrm{I}}^i}{i!} e^{-P_{\mathrm{I}}} \tag{1.17}$$

where p_i is the probability that there are i interactions per pixel, and $\mathrm{P_I}$ is the number of interacting photons per pixel. The signal shot noise is then given by:

$$\sigma_{\mathrm{SHOT}} = \eta_i \left(P_{\mathrm{I}}\right)^{1/2} [DN] \tag{1.18}$$

$$\sigma_{\mathrm{SHOT}} = \left(\eta_i S\right)^{1/2} [DN] \tag{1.19}$$

where S is the average signal (DN) and η_i is the quantum yield ($\mathrm{e^-}$/photon).

1.7.1.3 Quantum Yield

The quantum yield, η_i, is an important parameter when calculating the quantum efficiency of a detector. The quantum yield is defined as the number of

electron-hole pairs generated per photon incident upon the detector. For silicon, the quantum yield is unity for incident radiation from $\approx$ 3000 Å to 1.1 μm. This means that for every incident photon, a single electron-hole pair will be generated. This spectral region covers the optical and near-infrared spectrum. At wavelengths shorter than 3000 Å, the quantum yield is greater than 1, meaning that for every incident photon, multiple electron-hole pairs can be created. If the quantum yield is not taken into account when calculating the quantum efficiency of a detector, greater than 100% QE is possible.

1.7.1.4 Fixed Pattern Noise

Fixed pattern noise becomes dominant for high levels of illumination and is defined as:

$$\sigma_{\mathrm{FPN}} = P_{\mathrm{N}} S \left[rms\ e^{-} \right] \tag{1.20}$$

where P_{N} is the FPN quality factor, which is approximately 0.01 (1%) for CCD systems (Janesick, 2007). FPN present in every image generated by a camera system and is proportional to the amount of light incident upon the detector and the efficiency with which the pixels collect charge. Not all pixels will collect charge uniformly and will thus produce structure apparent in the output image. This structure is known as "fixed" because it is the same for all illuminated exposures, only varying in intensity. FPN is also dependent on the camera system because structure from internal reflections and dust on the detector or camera optics will also show up as FPN. While FPN is a problem in every camera system, it can be effectively eliminated through flat-fielding.

1.7.1.5 Camera Gain and Read Noise

Knowledge of the two factors camera gain, G, and read noise, R, are essential to accurate calibration of CCDs and development of the PTC. The camera gain is

used to convert from analog-to-digital units (ADU), or digital number (DN), which are camera units, to electrons, which are physical units. The read noise describes the minimum signal level, or noise floor, one can measure with the CCD. The read noise is present in every image and is independent of exposure time.

According to Janesick (2001), camera gain can be calculated using evenly illuminated flat frames and bias frames. A flat frame is one in which the illumination pattern is fairly uniform and within the shot-noise dominated regime of the photon transfer curve such that the image obeys Poisson statistics. A bias frame is a zero-length dark exposure that is meant to measure only read noise. The Janesick method involves comparing the differences between flat frames and bias frames. By comparing the differences between images, we can eliminate large-scale variations in signal levels and pixel-to-pixel sensitivity variation that would make our gain estimate uncertain. According to Howell (2006), who breaks down the Janesick method, we can use the following equations to calculate the camera gain constant and read noise:

$$\text{Gain} = \frac{(\bar{F}_1 + \bar{F}_2) - (\bar{B}_1 + \bar{B}_2)}{\sigma^2_{F_1 - F_2} - \sigma^2_{B_1 - B_2}} [\text{e}^-/\text{DN}] \tag{1.21}$$

where $\sigma^2_{F_1 - F_2}$ is the variance of a difference flat frame where both flat frames are approximately equal in illumination and $\sigma^2_{B_1 - B_2}$ is the variance of a difference bias frame. The read noise is then given by:

$$R = \frac{G \cdot \sigma_{B_1 - B_2}}{\sqrt{2}} [\text{e}^-] \tag{1.22}$$

The same equations can be used to calculate gain using different pairs of flat field images at different illuminations and plotting the difference in the sum of the means versus the variance in the difference. The slope of this plot corresponds to the gain.

A third way to determine camera gain, as long as the data is shot-noise limited, is to plot the variance of the signal versus the signal on linear graph. The slope of the graph corresponds to the gain and the form is given by:

$$\sigma_{\mathrm{SHOT}(DN)} = \left[\frac{S(DN)}{G_{\mathrm{ADC}(e^-/DN)}}\right]^{1/2} \tag{1.23}$$

$$\sigma_{\mathrm{SHOT}(e^-)} = \left[S(DN)G_{\mathrm{ADC}}(e^-/DN)\right]^{1/2} \tag{1.24}$$

1.7.2 Linearity

CCDs should respond linearly to incident optical radiation until saturation is reached for illumination levels above the shot noise regime. Linearity as it pertains to the LASI facility CCD calibration program is the measurement of the response of the detector, at a given wavelength, for increasing exposure time. By increasing the exposure time and maintaining a constant source of illumination, the signal detected by the CCD can be measured and correlated with exposure time. The exposure time is increased until saturation is reached. Linearity can be determined by developing the photon transfer curve mentioned in Section 1.7 or by plotting the output signal (DN) versus the exposure time.

1.7.3 Non-linearity

At the end of the photon transfer curve, when the device reaches full well saturation, the slope of the PTC turns from 1, which is the slope in the fixed-pattern noise regime, to ∞. At this point, individual pixels within the detector can no longer contain their electrons and the electrons begin to enter into neighboring pixels, causing effects such as blooming which appears in images as one or more bright streaks leading away from the saturated pixel. As full well is approached, either by a long integration times or imaging a bright source, one must adjust the observational mode. In order to combat device non-linearity, one typically integrates on the target for shorter periods of time and co-adds the

images. By co-adding multiple shorter exposures, one increases the noise in the final image, subsequently decreasing the signal-to-noise ratio (SNR), by $\sqrt{N}$, where N is the number of frames. The best SNR achievable is for a single long exposure, but due to cosmic rays, the typical exposure on an astronomical target can be no more than 45 minutes.

1.7.4 Dark Current

The dark current within the detector is the signal generated due to the random thermal motions of the electrons with the substrate. Accordingly, the dark current is sensitive to the temperature of the device. Since the dark current arises from random thermal motion of electrons, it is governed by Poisson statistics. If the temperature is high enough, electrons will be freed from the valence band into the conduction band, and collected in the pixel well. When the device is read out, these "thermal" electrons become part of the signal, indistinguishable from electrons generated from the interaction of the substrate with incident photons (Howell, 2006). The dark current follows an analytical equation, whose full derivation is shown in Janesick (2001):

$$D_R = 2.5 \times 10^{15} P_s D_{FM} T^{1.5} e^{-E_g/(2k_B T)} \ [\mathrm{e}^-/pixel/sec] \tag{1.25}$$

where P_s is the pixel area (cm^{-2}), D_{FM} is the "dark current figure of merit" at 300 K (nA/cm^2), and E_g is the band-gap energy (eV) which also varies as a function of temperature. For silicon:

$$E_g = 1.1557 - \frac{7.021 \times 10^{-4} T^2}{1108 + T} \ [\mathrm{eV}] \tag{1.26}$$

As one can see, the dark current increases with increased temperature. In order to mitigate the effects of dark current, typically some form of cooling is employed, such as liquid cryogens or thermo-electric coolers. Typical dark rates for scientific grade devices at operational temperature are $\sim$0.02 e^-/pixel/hr.

The most prevalent liquid cryogen used in CCD operation is liquid nitrogen (LN_2), which has a temperature of 77 K. However, the CCD will begin to stop working at liquid nitrogen temperatures because of the physical limit known as carrier "freeze-out." According to Janesick (2001), freeze-out occurs when the low temperatures cause the dopant atoms to recombine rather than exist in the lattice structure in an ionized state. Donors used in processing CCDs have approximately the same ionization energy requirements. Since this energy becomes large when compared to k_BT at 77 K, the donors cease to ionize. Furthermore, the resistivity at low temperatures of the polysilicon gates increase enormously, resulting in clocking problems. In typical operation, a heater is employed close to the detector in order to maintain the temperature of the detector well above the freeze-out temperature within safe operational ranges.

In practice, to correct science frames for the effects of dark current, one takes "extra" exposures that are of the same length as the science exposures, but with the zero illumination. These images are termed dark exposures and are subtracted from the science frames.

1.7.5 Full Well Capacity

The maximum amount of charge that can be stored within a given pixel during an integration is known as the pixel full well capacity or full well depth. The full well capacity is the number of electrons a pixel can hold before reaching saturation. The FWD can be found by plotting the PTC referenced in Section 1.7. The point where the slope of the PTC changes drastically from the slope of the FPN regime defines where saturation has been reached. Mathematically, the slope at full well saturation is infinity. The FWD for modern CCDs can range from 140,000 to 200,000 electrons.

The full well depth is affected by several factors associated with the CCD design. The physical size of the pixels limits the amount of charge the pixel can hold, with less voluminous pixels unable to store the same quantity of charge as their larger brethren, on average. Charge diffusion within the Si substrate also limits the full well capacity. Voltages applied to pixels during integration are set to hold a collected charge in the pixel within which it was collected. However, situations can arise in which the pixel can wander, or "diffuse," into the neighboring pixel. Such a situation occurs within devices that are front-side illuminated and have geometrically long pixels that are much deeper than their areal extent. Electrons produced by long wavelength photons are captured near the bottom of the pixel, far from the potential well, setting up a situation where the deep potential well is merely a "dip", allowing the electron to diffuse into a neighboring pixel (Howell, 2006). Finally, the type of silicon with which the CCD is fabricated affects the ability of charges to diffuse into neighboring pixels. High-resistivity, or high-ρ, substrate has a crystal lattice structure that confines electrons more tightly to their collection sites.

1.8 Quantum Efficiency

The quantum efficiency (QE) is the ability of the semiconductor to produce electrons from incident photons (Janesick, 2007). It is the ratio of actual number of photons that are detected to the number of incident photons.

QE (electrons/incident photon) is defined as:

$$\mathrm{QE} = \eta_i \mathrm{QE}_I \tag{1.27}$$

$$\mathrm{QE}_I = \frac{P_I}{P} \tag{1.28}$$

where η_i is again the quantum yield, QE_I is the interacting quantum efficiency, P is the average number of incident photons/pixel, and P_I is the average number of interacting photons/pixel. From these equations, we can see that the QE can be

greater than one due to the quantum yield, but QE_I will always be less than unity. QE_I provides a figure of merit to describe how well the sensor manufacturer has allowed incident photons to interact with the semiconductor (Janesick, 2007). This second measure of quantum efficiency is the one we primarily reference in the LASI facility.

The final quantum efficiency for a camera system is determined by measuring the response of the CCD and calibrated photodiode and calculating the QE through the relationship (Janesick, 2007):

$$QE = \frac{A_D S(DN) G_{ADC}(e^-/DN) QE_D}{P_A S_D t_I} \tag{1.29}$$

$$QE_D = \frac{12390 R_e}{\lambda} \tag{1.30}$$

where A_D is the active area of a photodiode (cm^2), QE_D is the quantum efficiency of a photodiode, P_A is the pixel area (cm^2), S_D is the current generated by the photodiode (e^-/sec), t_I is the exposure or integration time, G_{ADC} is the gain (Section 1.7.1.5), and R_e is the calibrated photodiode responsivity, defined as the ratio of electrical output to optical input and typically expressed in terms of amps per watt (A/W) and is provided by the manufacturer.

A photodiode is an illumination sensitive p-n junction operated in reverse bias. When light is incident upon the photosensitive surface, a proportional reverse current flows. The responsivity is a function of wavelength of incident radiation and the band-gap of the material of which the photodetector is made (Janesick, 2001).

Modern techniques to increase the quantum efficiency of the detector include thinning the device and illuminating the device from the "backside." Thinning the device allows for an enhanced response to short wavelength radiation because the photons are absorbed closer to the Si-SiO_2 interface where the

potential well is maximum. However, this has a negative side effect in that longer wavelength photons can more easily pass through the device without interaction. By backside illuminating the device, the front-side circuitry is no longer blocking incident radiation, allowing for the enhanced probability of absorption of an incident photon.

1.8.1 QE vs DQE

Detective quantum efficiency (DQE) is a measure of the square of the ratio of the output signal-to-noise ratio to the input signal-to-noise ratio (Kitchin, 2003). The DQE is the measurement of the quantum efficiency for an equivalent virtual detector. Calculation of the the DQE allows one to compare the efficiency of different detection methods. An extensive treatment is given by Zanella (2002). The functional form is given by:

$$DQE = \frac{SNR_o^2}{SNR_i^2} \tag{1.31}$$

(1.32)

The terms DQE and QE are commonly interchanged in the literature without regard for which term is correct, which leads to published results that are difficult to interpret. When one is speaking of a CCD, one should quote the quantum efficiency, which is an intrinsic property of the detector. When one is speaking of a camera system, one can either quote the QE or DQE, but one must be explicit as to the definition of each. The only way to combat this plague across the literature is explicit explanation for whether QE or DQE was measured.

1.8.2 CCD Equation

For observations of astronomical targets, one can typically quantify the performance of a CCD using the “CCD Equation.” The CCD equation relates

the signal from the source, to the noise generated during the observation. More formally, the CCD equation is used to calculate the signal-to-noise (SNR or S/N) (Howell, 2006):

$$\text{SNR} = \frac{S_*}{\sqrt{S_* + n_{pix}\left(1 + \frac{n_{pix}}{n_B}\right)\left(S_s + S_D + S_R^2 + G^2\sigma_f^2\right)}} \tag{1.33}$$

where the "signal" term, S_*, is the total number of photons collected from an object of interest and can come from one or more pixels within an astronomical image. The "noise" terms in equation (1.34) correspond to the square roots of the source signal (S_*), the number of pixels under consideration (n_{pix}), the dark current per pixel (S_D), the signal from the sky per pixel (S_S), the total number of electrons per pixel resulting from the read noise, $\left(S_R^2\right)$, the number of pixels corresponding to the sky background (n_B), and the error introduced by the digitization noise within the typical ADC $(G^2\sigma_f^2)$. According to Howell (2006), σ_f^2 is 0.289, but the specific value is likely dependent on the system configuration.

For use in laboratory, one can neglect the source of noise from the background because the typical data collection involves taking only flat fields, in which the entire array should be evenly illuminated and signal is the background. Rewriting the CCD equation:

$$\text{SNR} = \frac{S_*}{\sqrt{S_* + n_{pix}\left(S_D + S_R^2 + G^2\sigma_f^2\right)}} \tag{1.34}$$

The dark current, defined in Section 1.7.4 increases linearly with integration time, t, such that the total dark signal is the integration time multiplied by the dark rate, D_R, which is typically expressed in electrons/pixel/second or electrons/pixel/hour:

$$S_D = t * D_R \; [e^-] \tag{1.35}$$

However, during laboratory testing, the dark current is typically so low compared to the flat field images that the contribution is negligible.

The read noise, as defined in Section 1.7.1.5, exists in every image taken and is independent of exposure time. Since the read noise does not obey Poisson statistics, it adds linearly to the noise term in the CCD equation. The final term in the CCD equation dealing with the digitization noise in the ADC, also adds linearly. However, for laboratory testing, the read noise is negligible when compared to the flat field level and can be ignored.

Since the arrival of individual photons to the detector is random, the noise associated with the arrival obeys Poisson statistics and the error is given by $\sqrt{S_*}$. If one assumes the read noise, dark current, and digitization noise to be negligible, which is a valid assumption for laboratory testing, the SNR is given by:

$$\text{SNR} = \frac{S_*}{\sqrt{S_*}} \; [e^-] \tag{1.36}$$

$$\text{SNR} = \sqrt{S_*} \; [e^-] \tag{1.37}$$

$$\text{SNR} = (G_{ADC} S_*)^{1/2} \; [DN] \tag{1.38}$$

where in the last equation, the SNR is determined with respect to the digital number. The last two equations presented above are of interest in typical calibration facilities where the light levels are typically high when compared to astronomical observations.

In the following chapters, I present results on the development of a laboratory for the calibration and characterization of large format CCD detectors that could possibly populate large focal plane arrays. I also present results on the development of a modular imager cell designed to bring video signal pre-amplification and clock level filtering in close proximity to the output amplifier on the CCD. The modular imager cell is a possible first building block to

the development of large focal plane arrays for future space missions. I also present the development of an imaging system for a suborbital sounding rocket mission based upon the the modular imager cell and next generation detector technology. The final topic is a scientific endeavor into the study of molecular line emission at sub-millimeter wavelengths from hydrogen-cyanide (HCN) around AFGL 2591, a massive protostellar object.

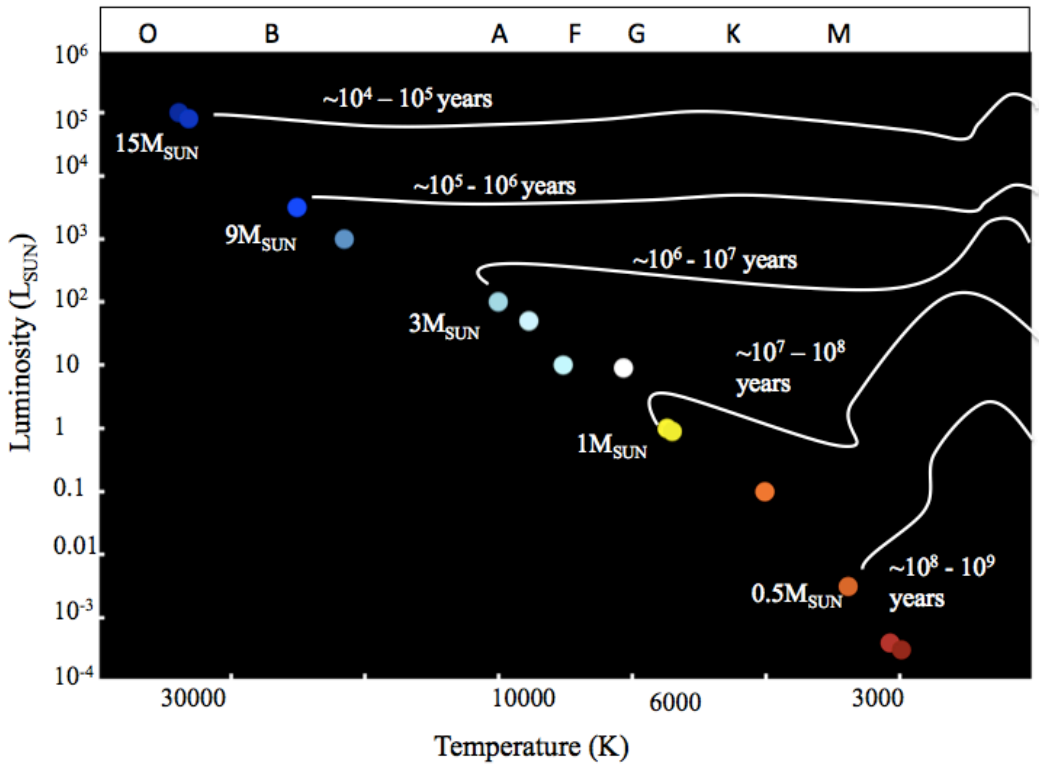

Figure 1.1: H-R diagram for evolution of various $M_{\odot}$ protostars. Larger protostars evolve to the main sequence significantly faster than smaller protostars. Based on an image generated by Prof. Dale Gary of the New Jersey Institute of Technology.

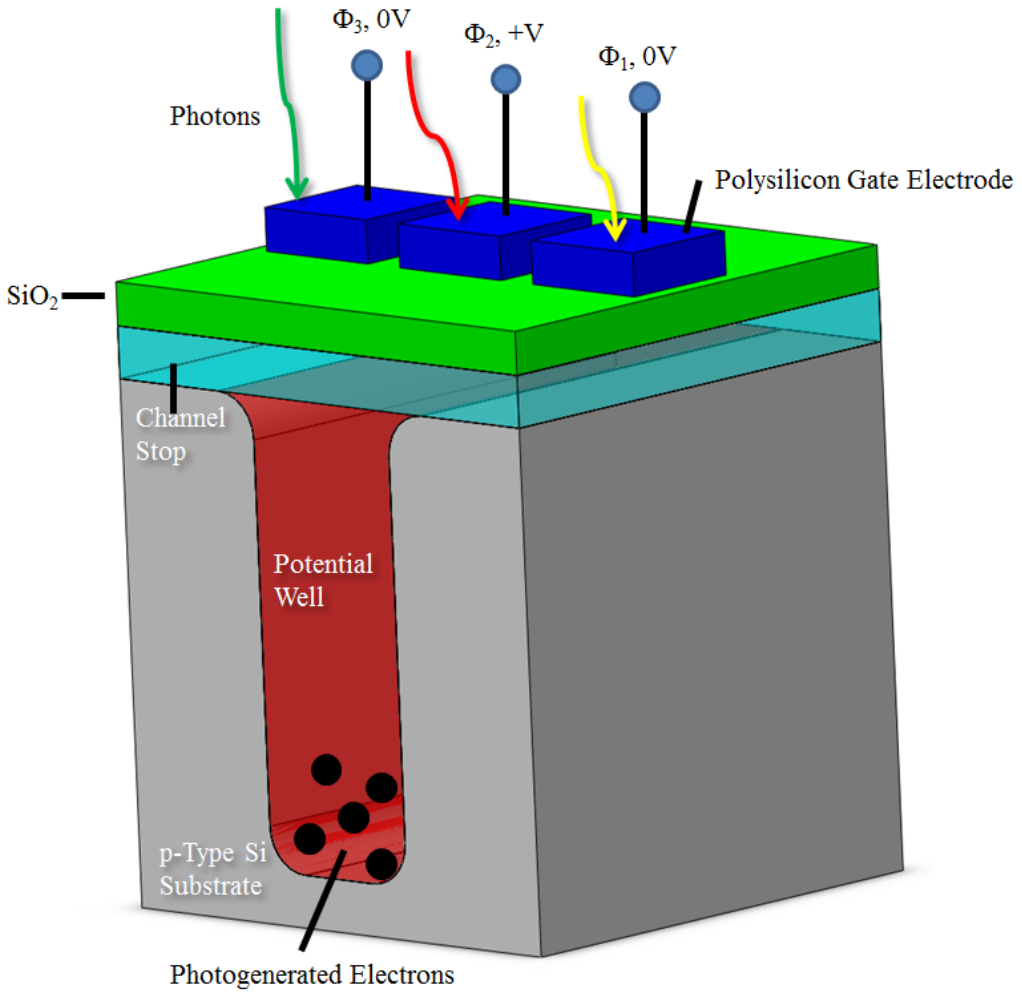

Figure 1.2: The structure of a pixel in a front illuminated CCD. The pixel has three poly-silicon gate electrodes attached in order to clock the charge out of the pixel.

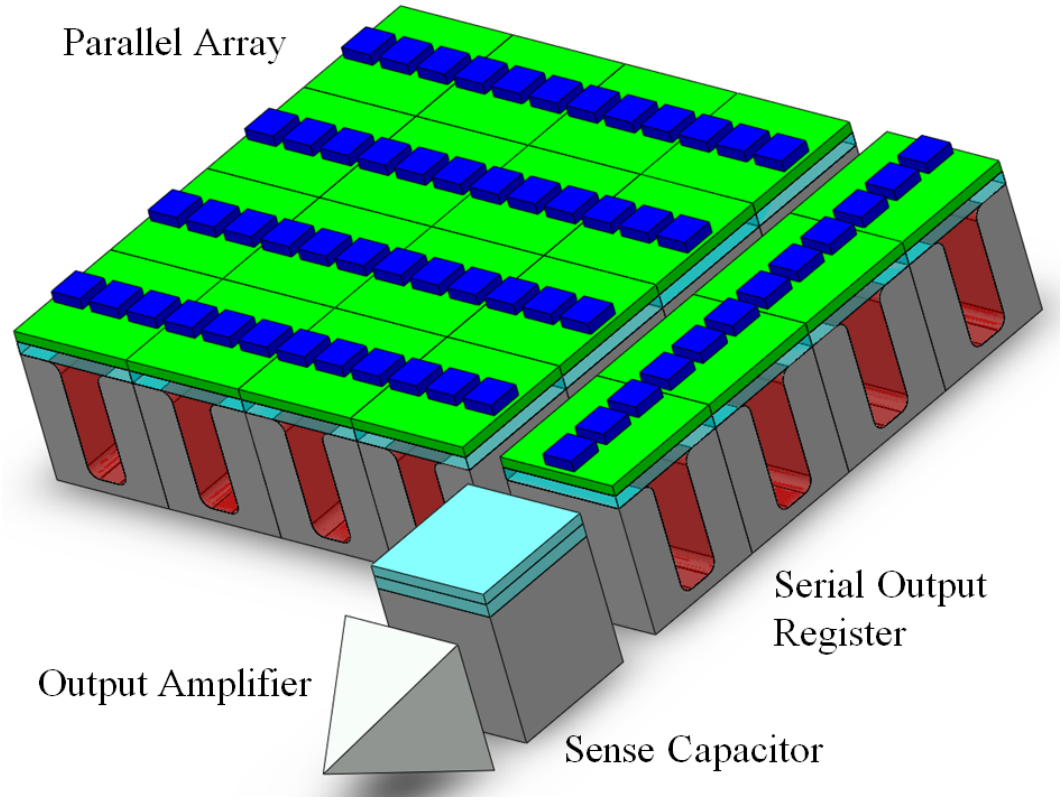

Figure 1.3: Three Phase CCD mechanical layout. The device is manufactured on a silicon substrate with three electrodes attached to every pixel for charge extraction. Image is based on Mackay (1986).

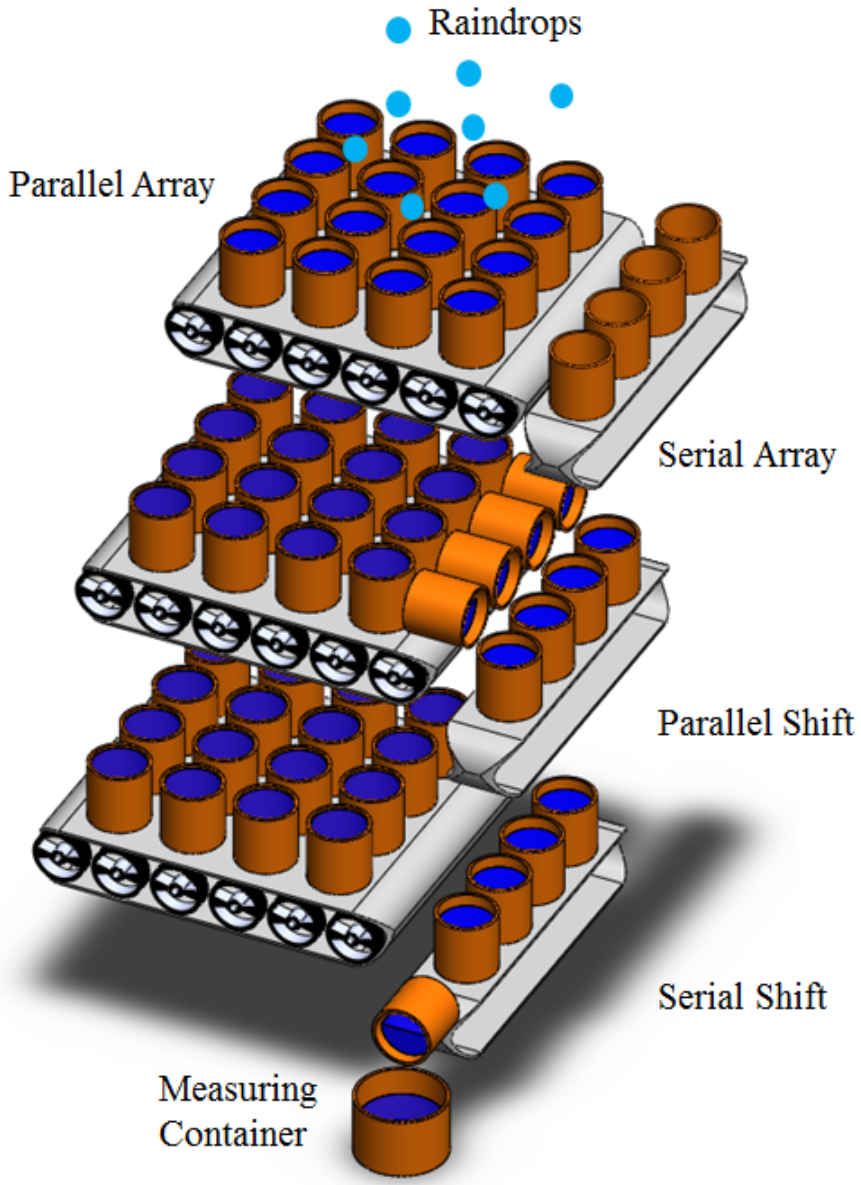

Figure 1.4: A simple bucket-brigade analogy for charge-transfer for the three-phase CCD clocking scheme. Pixels catching photons are like buckets catching raindrops. After the buckets are full, the belts move the buckets along a parallel path to dump the water into the serial bucket belt. The serial buckets are then dumped into a calibrated measuring container, such as barrel. When all the buckets on the serial belt have been dumped into the barrel and measured, the parallel buckets dump the next rows of buckets into the corresponding buckets on the serial belt until all the buckets have been emptied. This process repeats until all the buckets have been emptied. Image based on figure in Jansen (2006).

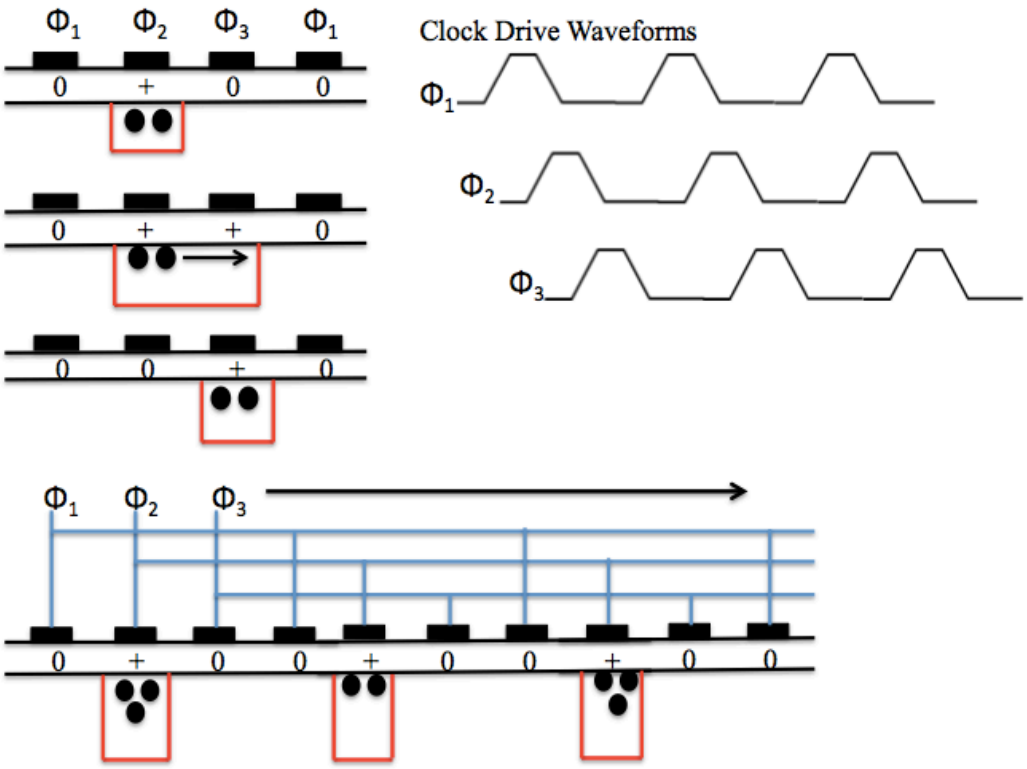

Figure 1.5: Charge-transfer in three-phase CCD clocking scheme. Adapted from Mackay (1986).

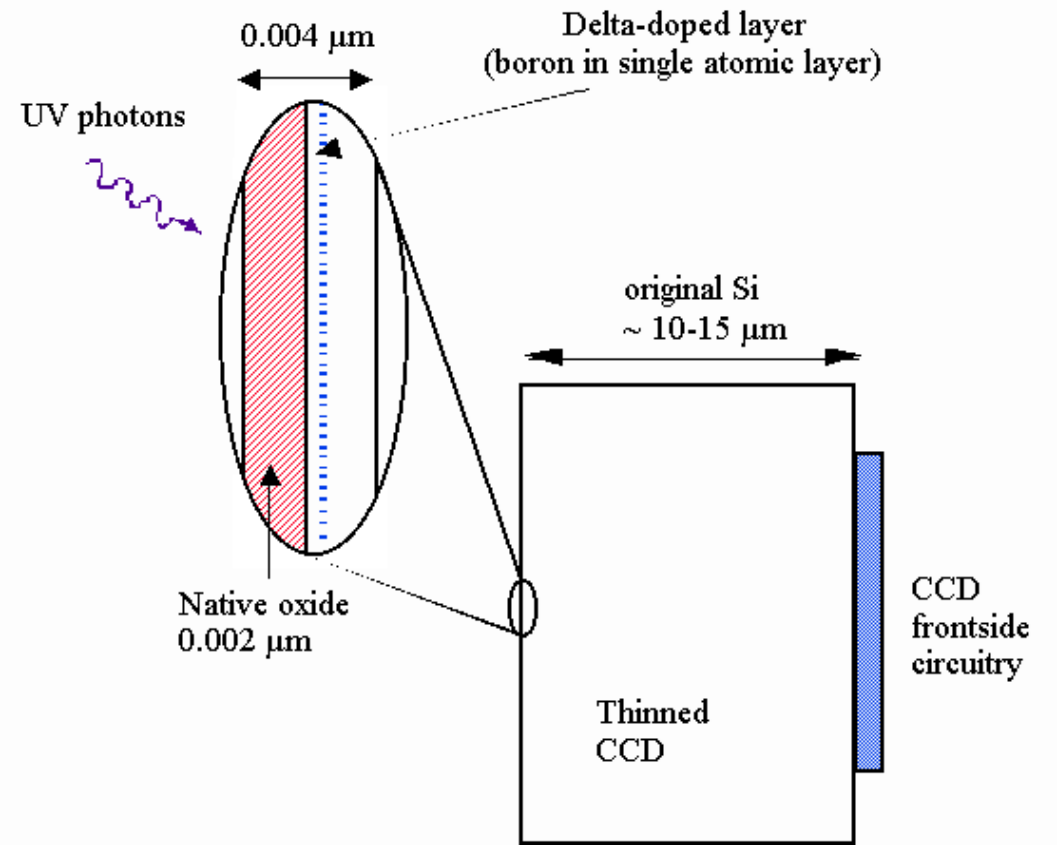

Figure 1.6: Cross-section schematic of a delta-doped CCD. The epitaxially grown delta-doped layer on the back surface of a thinned CCD places a high density of dopant atoms approximately 0.5 nm below the silicon epilayer surface and is protected by an oxide overlayer. (Nikzad et al., 2000; Janesick, 2001)

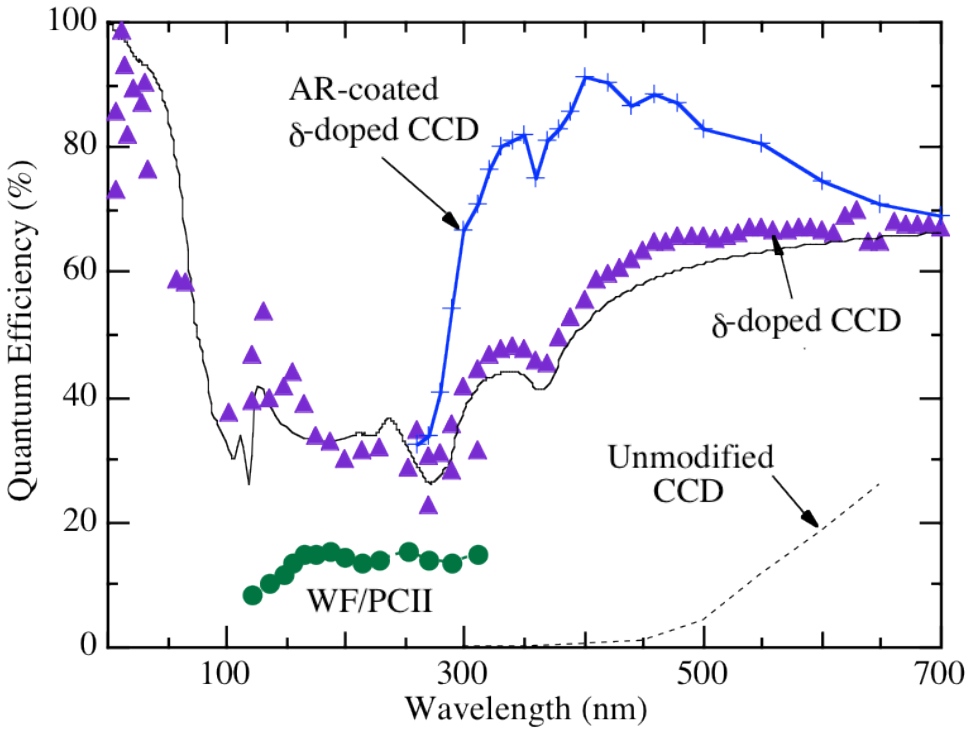

Figure 1.7: Quantum efficiency curves for an unmodified 1024 $\times$ 1024 CCD, a delta-doped device, and a delta-doped anti-reflection coated device. The solid line is the transmittance of silicon with a 20 Å layer of oxide, which corresponds to the maximum quantum efficiency possible without the addition of anti-reflection coatings. (Nikzad et al., 2000; Janesick, 2001)

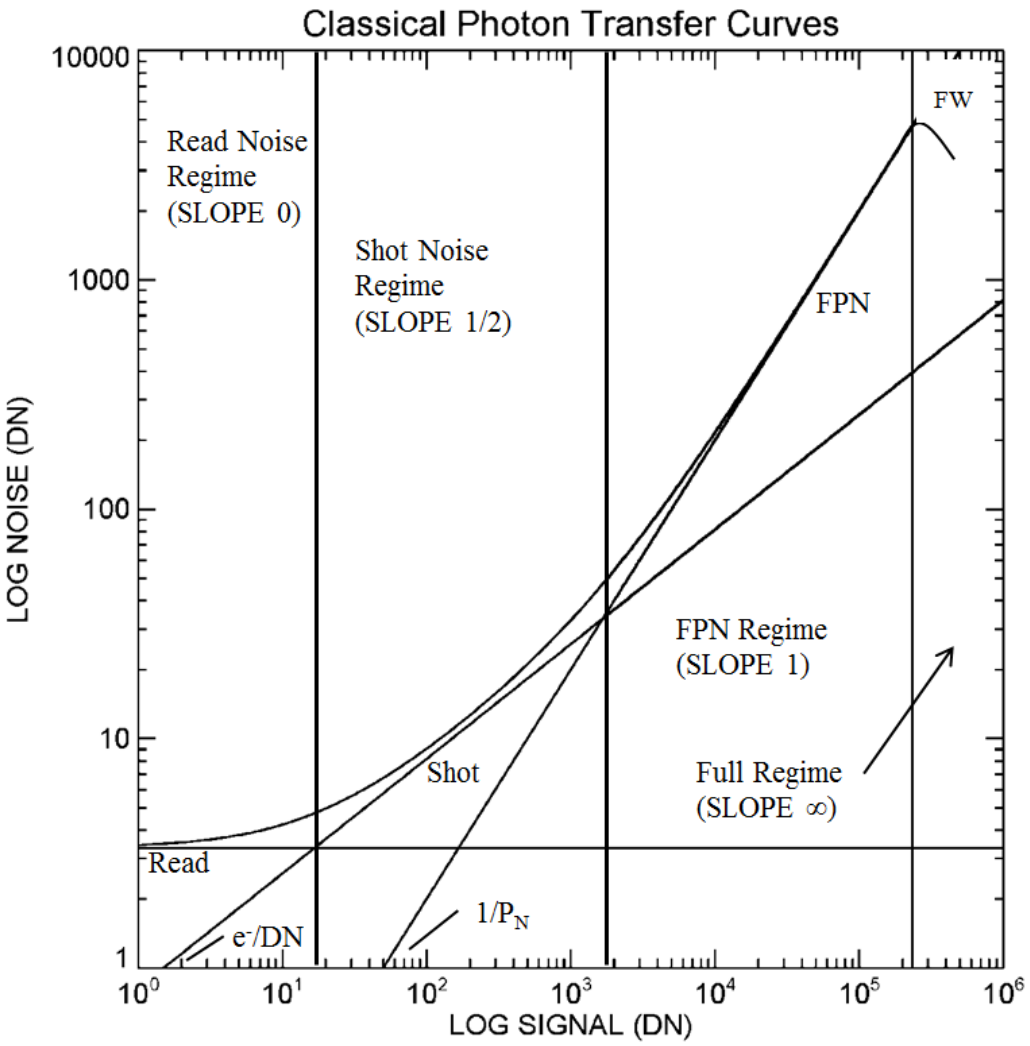

Figure 1.8: Simulated photon transfer curve. The read noise line has a slope of 0. The shot noise has a slope of 0.5. Fixed pattern noise has a slope of 1. Full well has a slope of infinity. The gain is given as the intersection of the shot noise curve with the signal axis in units of e^1/DN. The value for the FPN is shown as $1/P_N$. The total noise is the curve given by the sum of the individual curves.

Chapter 2

LABORATORY FOR ASTRONOMICAL AND SPACE INSTRUMENTATION CCD CALIBRATION PROGRAM

In this chapter I present the design, development, and results from the establishment of the Laboratory for Astronomical and Space Instrumentation facility at Arizona State University, a CCD calibration lab. LASI was instituted to mitigate the risk and minimize the cost associated with the development of large focal plane arrays for future space missions by providing a facility with the capability for rapid detector characterization. This chapter also lays the theoretical and practical framework for the hardware development discussed in Chapters 3 and 4.

If large focal plane arrays, like the Star Formation Camera (SFC) instrument concept (Scowen et al., 2009d), consisting of twin 270 CCD focal planes, each with an areal extent on the sky of 285 sq arcmin, are going to become a reality, then it is going to be necessary to develop the technology and strategically plan the methodology required to calibrate four times the number of CCDs at the current rate of serial detector calibration, approximately four per month. It would take approximately 40 years to calibrate that number of CCDs which is prohibitive in both time and cost. The solution proposed here is to develop a calibration lab to learn the methodology for rapid, cost-effective detector calibration. Furthermore, a calibration facility would provide training for the next generation of scientists and engineers.

2.1 Introduction

"In order to understand the performance limits and calibration requirements of an instrument, it is necessary to have an understanding of the nature of the detector array, its key performance parameters, and the way these are defined and

measured" (Hopkinson et al., 2004). I would add that in order to understand the science I am interested in investigating, not only do I need a complete understanding of the instrumentation used in the collection of the data, such as detectors, telescopes, and optical elements but also the uncertainty in noise contributed by the detector system.

2.2 Motivation and Methodology

The motivation to develop a CCD calibration lab at ASU was born from the notion that future space missions are going to require large focal plane arrays to achieve their science objectives. For these large focal plane arrays (FPAs), many detectors will need to be calibrated efficiently and quickly in order to minimize financial and temporal cost.

Through the development of a CCD calibration program in the LASI facility, ASU will be well positioned to propose mission concept designs like the High-Orbit Ultraviolet-Visible Satellite (HORUS) (Scowen et al., 2010) or the Star Formation Observatory (SFO) (Scowen et al., 2008) that will require the calibration of large numbers of detectors. The FPAs will be populated with with a number of detectors great enough to provide diffraction limited resolution from a 2.4 m telescope mirror across a large areal field. As part of the mission concepts, ASU will address the technology required to mosaic hundreds of large format CCD detectors to create a single FPA.

In preparation for the development of unprecedented large FPAs, ASU will use its CCD calibration facility, in collaboration with the Jet Propulsion Laboratory (JPL), to streamline the scientific grade detector selection process. Typical scientific grade detectors have a relatively low yield rate with common rates as low as $\sim$25%, meaning 1-in-4 detectors produced is of acceptable quality.

The goals of the LASI facility are:

- To investigate the methodology behind the calibration of ultra-violet/ optical/ near-infrared imagers.
- To demonstrate the LASI lab production of full calibration data for a given detector similar to the calibration data produced at already established detector calibration facilities, such as the facility of our colleagues at JPL.
- To develop calibration methodology and techniques to streamline the detector calibration process.
- To determine the feasibility of using large format detectors in the development of future large focal plane arrays.

Due to the sheer volume of effort that has to be invested to complete this process, the methodology and calibration strategies developed must be scalable effectively and inexpensively for any number of detectors. The penultimate goal of the LASI facility is to provide fully calibrated data for various detectors in preparation for their use in the development of future large focal plane arrays.

This chapter begins with CCD performance evaluation strategies and the techniques required to understand and optimize their performance. Those baselines for optimal performance were used to generate the design specifications for the LASI. I will then describe the LASI design in more detail, give results from a delta-doped CCD calibrated in the LASI, and suggest future modifications to streamline the detector calibration process for large volume operation.

2.3 Detector Performance Evaluation Strategies

In order to properly develop a program for detector calibration, one must first lay the foundation for the definition of evaluation measures for CCD calibration.

According to Janesick (2001), CCD calibration can be divided into three categories: CCD performance, CCD camera performance, and CCD camera calibration.

CCD performance is related to the ability of the detector to convert incident photons into electrons. CCD performance curves can be supplied by the manufacturers and are typically used to assist the customer in making design choices. Such curves relate to the four CCD operational categories defined by Janesick (2001): charge generation, charge collection, charge transfer, and charge measurement. Examples of CCD performance curves include the photon transfer curve, which allow the user to investigate the pixel-to-pixel variations, amount of charge a pixel can store, the likelihood of turning a photon into an electron, and additional electrons added to the signal during detector readout; the quantum efficiency transfer curve, which is a measure of detected photons to incident photons; and the dark current transfer curve, which is sensitive to temperature variation, which allows the user to determine the optimum operational temperature for the CCD.

The CCD camera performance curves are used to optimize operation of the detector. For example, these carves can be used to optimize the gate voltages within the transistors, the dc bias levels, camera gain, etc. The primary curve used is again the PTC, which allows one to investigate signal processing, clock wave shaping, well capacity, and sensitivity.

CCD camera calibration curves are the final step in characterizing the detector, after one has measured the detector performance and subsequently fully optimized the detector. The camera calibration curves can still be used to calibrate off-the-shelf camera systems that have already been optimized despite not having access to detector performance data provided by the manufacturer or vendor. The

PTC, the QE transfer curve, and the linearity transfer curve are the most typical curves used to investigate camera calibration.

Necessarily, there is crossover between the three categories when using the PTC or QE curves, but the LASI facility is primarily focused on the CCD performance curves and the the CCD camera performance curves.

2.4 Detector Performance Evaluation Implementation

Calibration procedure for detectors have been discussed at length in Janesick (2001); Hopkinson et al. (2004); Howell (2006); and Janesick (2007). Here we discuss details from those aforementioned sources along with specific calibration techniques developed for the LASI facility.

2.4.1 Photodiode Measurements

System calibration begins with measurement of the LASI facility photodiode response as a function of wavelength and subsequent comparison of the results with the absolute responsivity calibration provided by the National Institute of Standards and Technology (NIST) (Section 2.6.5, Figure 2.10). A photodiode converts incident radiation to a photocurrent. The absolute responsivity, in conjunction with the measured photocurrent, is used to calculate the absolute quantum efficiency of the CCD (see Section 2.10.1).

In the LASI facility, I measured the relative response of the photodiode to incident illumination. I then multiplied this by the QE of the photodiode, assuming the QE curve supplied by NIST was accurate, to generate a response curve similar to the NIST supplied absolute responsivity curve. I do not have the capability to measure the absolute responsivity in the lab because I do not have an appropriate light source, which is why I measured only the relative response. Section 2.10.1.1 offers a discussion of how the absolute responsivity would be measured.

Detector calibration begins with visual inspection and certification by looking for broken wire bonds and superficial surface defects. It is essential to ensure the detector is free from physical defects that could interfere with further calibration.

2.4.2 Operational Temperature Measurements

Due to the random thermal motions of the electrons within a CCD, the response of the device has a strong dependence on operational temperature. Section 1.7.4 provides further detail on the generation of the "dark" photocurrent. In order to suppress the random thermal motions of the electrons within the substrate, and subsequently reduce the dark current, one would cool the detector to cryogenic temperatures. In practice one cools the detector, via an LN_2 cooling system or mechanical cryo-cooler, such as a Cryotiger[1], in discrete temperature steps. Ideally, at each temperature step, the temperature is held constant and the detector integrates in total darkness, allowing the random thermal motions of the electrons in the substrate to populate the depletion regions of the pixels. The detector is then read out.

In the original configuration of the LASI facility, it was not possible to hold the temperature of the detector constant at any temperature other than the operational temperature because there was not enough heat flux within the vacuum space to effectively balance the cooling rate. Instead I measured a proxy for the dark current to determine the optimum operational temperature.

In order to find the optimum operational temperature, I counted the number of saturated pixels in an image made from two-minute integrations as the detector cooled. I measured the initial and final temperature at the beginning and end of the integration period and averaged them together to get a single value, T_{ave}. This

[1] www.brooks.com

value was then assigned to be the temperature for that integration period. This process was repeated until the number of saturated pixels reached a minimum (Figure 2.16). The upper limit of the operational temperature corresponded to the temperature at which the number of saturated pixels was at a minimum, meaning that for a fixed integration time of two minutes, the detector was no longer generating enough charge from the random thermal motion of the electrons within the substrate to be detected above the bias level. The lowest operational temperature limit is defined as the "freeze-out" temperature, which is 142 K for the devices tested in the LASI facility (Blake Jacqout, private communication), but can vary based upon the type of CCD being calibrated.

2.4.3 Linearity Measurements

Linearity, and conversely, nonlinearity, are measurements of the camera gain, and are expected to be constant as a function of time (Janesick, 2001). Since a silicon based detector has a linear response to incident radiation from $\sim$350 nm to $\sim 1.1\mu$m, meaning an indecent photon generates a single election-hole pair, a plot of average signal, S(DN), versus exposure time, t(s), should have a slope equal to unity (Figure 2.24). When plotted on a log-log plot, the functional form of the response is given by:

$$S(DN) = C\,(t_e)^{\gamma} \tag{2.1}$$

where C is a proportionality constant and γ is the measure of the linearity of the device (a truly linear detector would have a $\gamma = 1.0$).

We can also calculate the "linearity residuals" using the equation:

$$LR = 100\left(1 - \frac{S_M(DN)/t_{eM}}{S(DN)/t_e}\right)\ [\%] \tag{2.2}$$

where LR is the percentage linearity residual at a specific signal level. The variables S and t_e are the individual measured signal and exposure times and

similarly S_M and t_{eM} are the median signal and corresponding exposure time. An ideally designed camera system will have a linearity residual of less than $\pm 1.0\%$

As the device approaches saturation, one can see from Figure 2.21 that the measured signal appears to reach a maximum value of $\sim$38800 DN, which is defined to be the full well capacity. This process is repeated for various values of wavelength in order to determine the linearity and linearity residuals with respect to wavelength.

2.4.4 Gain and Read Noise Measurements

Gain and read noise measurements were made by following the procedures outlined in Janesick (2001) and described here in Section 1.7.1.5. Gain and read noise are ideally calculated using equation (1.21) by taking a pair of equally illuminated flat field images and pairs of bias frames, which account for the readout noise in the camera system. This is the minimum amount of data needed to successfully measure the gain and read noise.

The approach adopted in the LASI facility is more robust. I generated $\sim$8 evenly illuminated flat field images at wavelengths from 450 - 950 nm with SNR $>$ 200. I then generated 125 bias frames. For each of the bias frames, I calculated every possible combination for the sum of the averages and the squared standard deviation of the difference. This led to greater than 15,500 combinations. I also repeated this process for each wavelength measured. Then, using equation (1.21), I calculated the difference in the sum of the average flat and the sum of the average bias frames and then divided by the difference in the squared standard deviations of the difference frames. These calculations produced arrays of values for gain and read noise for every combination of bias and flat frame. For the final gain and read noise value for the entire detector, I extracted the median value. The mean values were compromised due to large outliers from some frame combinations. The

median can be successfully used for replacement of the mean because for significantly large Poisson distributed data, the median and the mean should be similar. The final gain table is shown in Table 2.1. A discussion of the gain calculations appears in section 2.11.1.

2.4.5 Quantum Efficiency Measurements

Quantum efficiency was calculated by collecting a variety of flat field images from 450 - 950 nm. The mean of the net signal within each image was used in combination with the photocurrent generated by the photodiode and other CCD properties mentioned in Section 1.8 to create a quantum efficiency plot against wavelength (Figure 2.26). The net signal was determined by subtracting a median combined bias frame comprised of all 125 generated bias frames. Following equation (1.29), I calculated the quantum efficiencies shown in Table 2.1.

2.5 Detector Performance Optimization

The performance optimization of the CCD is described in detail by Janesick (2001). The basic procedure for optimization is to adjust the clock voltages in order from the horizontal clocks, to the output amplifier clocks, to the vertical clocks, back to the horizontal clocks, back to the vertical clocks, and then eventually to the output drain level. The effects of adjusting the above parameters can be measured using a photon transfer curve.

Another method for detector characterization is to “guess and check.” This method involves first adjusting the clock voltages and clock timings then analyzing the output images and measuring the SNR using the CCD equation or generating a photon transfer curve. The shape of the PTC will assist in determining if the parameter adjustment was successful. This method may not be as accurate as above, but should still provide voltage and clock levels within the safe operating window.

2.6 Design of LASI Facility

The LASI facility is designed to perform detailed characterization of detectors from the near-UV to the near-IR. Detailed characterization includes evaluating the quality of arrays by comprehensive evaluation of QE from 350 - 1100 nm, noise, stability, linearity, dark current, gain, read noise, well capacity, well-depth, and flat-field uniformity. The significance of this work is to provide essential calibration products to enable the pushing of the QE of the detectors up above 80% at the blue and red edges of the silicon response in order to dramatically improve the efficiency of the detectors for space-based survey work as envisioned in the SFO mission concept.

2.6.1 Optical Design

In this section, I describe the optical design of the calibration system by "following the photons" from emission to detection. The first stage in the optical design is the light source, which is 24 V/250 W tungsten-halogen light-bulb. The broadband emission from the light-bulb is collimated and sent into the monochromator for wavelength selection (section 2.6.2). After wavelength selection, the beam passes through a shutter used for integration time definition (section 2.6.3) and enters the collimation stage for transfer of light to the detector and photodiode (section 2.6.4). The goal for focal plane illumination was an evenly illuminated focal plane. The final step in the optical train is illumination of the co-located CCD and photodiode in image plane (section 2.6.6).

2.6.2 Wavelength Selection

In order to measure the quantum efficiency of our detectors, we use a combination monochromator/spectrograph for wavelength selection. The LASI facility uses an

Acton[2] SP2150i monochromator in conjunction with a TDS-420 250 W broadband light source.

The SP2150i features an astigmatism-corrected optical system, dual indexable gratings, and interchangeable grating turrets. The configuration of the monochromator is a Czerny-Turner (CZ), consisting of two concave mirrors and a turret housing two diffraction gratings. The first mirror functions to collimate the incoming light source. The second mirror focuses the dispersed light from the grating through the exit slit. The turret houses two gratings that have blaze angles of 300 nm and 500 nm respectively and are both ruled at 1200 grooves/mm. The wavelength accuracy of the 1200 grooves/mm grating is ± 0.25 nm and the wavelength repeatability is ± 0.05 nm.The grating blazed at 300 nm is used for calibration from 250 - 400 nm and the 500 nm blazed grating is used for calibration from 350 - 1100 nm. Further specifications are detailed in the SP-2150i user manual (PIActon, 2003).

Calibration below 250 nm is prohibitive in the LASI facility due to the lack of a sufficient vacuum chamber or purge system. For calibration from 91.2 nm to 250 nm, an experimental calibration system should be entirely enclosed within a vacuum chamber in order to mitigate atmospheric contaminants, such as hydrocarbons and water vapor, from deposition on the detector surface. If a vacuum system is not available, then a Helium purge system would also suffice. The ionization energy of a Helium atom is 54.4 eV, corresponding to a wavelength of 22.8 nm, which is well below the minimum wavelength of the calibration range. The vacuum or purge system is also intended to prevent the possible interaction of higher energy photons from the light source with atmospheric particles.

[2]www.princetoninstruments.com

2.6.2.1 Optical Filters

The lab is equipped with a set of Johnson (Johnson, 1963) UBVRI calibration filters. The filters provide for the calibration of the monochromator and can be used to eliminate out of band transmission when testing other filters. Narrow (0.4 nm) laser line filters at 500.0 and 656.2 nm allow for calibration of the monochromator for wavelength selection accuracy. This calibration is done by sweeping the monochromator through the filter bandpass and determining the location of the peak. The peak should occur at the central wavelength of the narrowband laser line filter. Data from four or five narrowband filters spanning the entire range of the monochromator spectral calibration regime would allow the fit of a function, typically linear, that describes the offset from the peaks of each filter as a function of wavelength.

2.6.3 Exposure Control

In order to control the exposure time, I installed a CVIMellesgriot 25.4 mm clear aperture 04IES211 5-blade iris-design shutter[3] at the exit slit of the monochromator. The shutter requires a 12 V_{dc} drive to activate the shutter actuation solenoid. The voltage remains high as long as the shutter is open. A bi-stable shutter, where voltage is only applied to actuate the shutter, could have also been used, but this design option was not initially explored for the LASI facility. The supplied shutter controller allows for TTL control of exposure timse from $\sim$0.02 s to "open." Furthermore, the TTL control allows for easy interface to a digital or analog control system. A TTL signal can be sent to the shutter from the Leach controller software in order to set the exposure time (Section 2.8.2). An added benefit is that the Leach controller interface also adds the exposure time to

[3] www.cvimellesgriot.com

the output header of the Flexible Image Transport System (FITS) image file (Wells et al., 1981). Section 2.9 has description of the FITS format.

2.6.4 Focal Plane Illumination

As shown in Figure 2.1, the transfer optics used to illuminate the focal plane are a flat mirror and an off-axis parabola (OAP). The flat mirror is a $1''$ diameter UV-enhanced protected aluminum round mirror manufactured by Thorlabs[4]. The UV-enhanced mirror has greater than 75% reflection from 0.250 μm to 18 μm. The flat mirror is placed at the focal point of the exit slit of the monochromator at a 45° angle, $2.35''$ from a $2''$ electroformed nickel mirror off-axis parabola manufactured by CVIMellesgriot that serves as the collimating mirror. The electroformed nickel mirror has greater than 60% reflection from 0.250 μm to 18 μm. The mirror figure of the OAP is that of a full parabola that has been sectioned to have a focal length of $2.35''$.

2.6.5 Intensity Measurement and Calibration

In order to perform the measurements mentioned in section 2.4.1 we adopted the use of an s2281 photodiode manufactured by Hamamatsu[5] and calibrated by the NIST. The s2281 photodiode is a silicon substrate photosensor sealed in a metal package with a BNC connector with an active area of 100 mm^2. The BNC connector on the back of the photodiode is connected via a coaxial cable to a model 6485 Keithley Picoammeter[6] used to measure the photodiode current. Extensive calibration was performed on the photodiode and is discussed in section 2.10.1. An instrument description of the picoammeter is provided in section 2.8.4.

[4] www.thorlabs.com
[5] www.hamamatsu.com
[6] www.keithley.com

2.6.6 Co-location of CCD and Photodiode

The optical design in the LASI facility has a unique feature: the CCD and photodiode are in the same image plane (Figure 2.6). Placing the CCD and photodiode in the same physical plane seemed like the logical design choice to increase overall system throughput and efficiency by cutting overall quantum efficiency calibration time in half. A typical calibration lab would take the measurements of the photodiode and CCD in separate physical locations, swap the locations, then retake the same measurements, which requires twice as much time as the LASI facility.

The LASI method is superior because it requires less handling of the detector and photodiode, does not require correction factors to account for the CCD and photodiode location, and cuts the overall calibration time by a least a factor of two. One drawback to this method is the requirement that the collimated beam must have an evenly illuminated diameter larger than the physical separation of the CCD and photodiode, possibly requiring large collimation optics. If a radial gradient exists across the interacting surface of the beam, then the measured photocurrent will also have a gradient with respect to the CCD, leading to inaccurate QE calculations.

2.7 Environmental Considerations

In order to perform carefully calibrated experimental measurements, one must have careful control of the environmental conditions in the experimental apparatus. In this section, I describe the environmental control strategies I employed in the lab.

2.7.1 Vibration Control

Optical calibration requires a stable platform to ensure experimental repeatability over the course of a day, a week, or months of operation. In order to provide said stable platform, we used a Newport Optics[7] vibration isolation breadboard table. The optical breadboard table is 6 ft long $\times$ 4 ft wide $\times$ 8" thick and stands 48" off the ground. For mounting optical components, the breadboard has a 1" square grid of 1/4-20 threaded holes covering the entire surface area except a 1" thick border. The considerable mass of this table provides vibration mitigation and an extremely stable platform for optical alignment.

2.7.2 Stray Light Control

In order to ensure accurate calibration of the detectors, I designed a method by which we could control the stray light and specular reflections incident upon the detector. In order to execute a modicum of control, I developed a "light-tight" cover for the optical bench, within which the calibration measurements were performed (Figure 2.8). The design and fabrication was done by the Arizona State University Mechanical Instrument Shop[8].

The enclosure is fabricated from T-6061 aluminum and has been black-anodized to reduce specular reflections. The approximate dimensions of the black enclosure are 6 ft long $\times$ 4 ft wide $\times$ 1.25 ft high. The enclosure bolts to the optical table using 1/4-20 screws on all four sides. There are two ports in one side for light-tight cable feed-through. There are five doors to the inside of the enclosure that enable access without requiring the total removal of the enclosure. There is also an access port on the top of the enclosure to allow for ease of access

[7] www.newport.com/

[8] www.physics.asu.edu/shops/mechanical

when refilling the LN_2 in the cryogenic dewar (Section 2.7.4). However, during calibration, it was determined the box was not as light-tight as it was designed to be and required "gaffer's tape" to cover the seams.

2.7.3 Thermal Control

High-quality scientific measurements require cooling the detector to minimize the dark current (Section 1.7.4). Cryogenic measurements of CCDs require particular attention to the vacuum conditions in order to avoid buildup on condensation or ice on the detector surface (Jacquot et al., 2011). In order to cool the detector to the temperature range we employ, 143 K - 173 K, and prevent condensation from forming on the detector due to the decrease in the vapor pressure of H_2O with temperature (Jacquot et al., 2011), I installed the detector inside a dewar evacuated to 10^{-6} Torr, which is a pressure 10^6 times lower than atmospheric pressure at sea level, which is termed "high vacuum." High vacuum is defined as a point in which the mean free path is greater than the size of the dewar. The number of particles at 10^{-6} Torr and at 300 K is $\sim 10^{16}$ m^{-3} with the mean free path of $\sim$1 km. The mean free path decreases to $\sim$200 m as the temperature of the cold plate inside the dewar is lowered to 77 K, the boil-off temperature of LN_2, but the dewar is still under high vacuum since the mean free path is larger than the dewar size.

At 5×10^{-6} Torr, the temperature at which ice begins to form is $\sim$ 183 K (Jacquot et al., 2011). While ice forming on the detector surface is extremely detrimental to calibration measurements at wavelengths shorter than 3000 Å, in the vacuum-UV, it has little effect on calibration measurements at wavelengths greater than 4000 Å. In order to mitigate the effects of ice condensation, one should attempt a vacuum greater than 10^{-9} Torr, which also allows characterization of the detectors in the vacuum-UV all the way to down 145 K, just above the 142 K "freeze-out" temperature of the LBNL detector.

In the LASI facility, cooling the detector is accomplished via a mechanical connection of the cold plate to the backside of the detector. The backside of the detector is typically bonded to an aluminum nitride substrate (AlN) for rigidity and thermal conductivity. The mechanical connection is made with the cold finger shown in Figure 2.9. The cold finger is made of oxygen free high thermal conductivity (OFHC) copper. OFHC cooper is also known as alloy-101 copper. The outer cylinder of the cold finger slips over the insert and is supported by a stainless steel spring that provides the contact pressure to the back of the CCD during thermal cycling. The outside of the inner cylinder is coated with a thin layer of thermal grease (Apiezion N[9]) in order to ensure good thermal conductivity. The inner cylinder is bolted to the Dewar cold plate using vented 4-40 socket head cap screws.

2.7.4 Dewar

The dewar we use in the LASI lab is a liquid cryogen (LN_2) Infrared Laboratories (IRLabs) ND-5[10]. The dewar is shown in Figure 2.5. The dewar has a $5''$ cold plate, or work surface, and a $4.25''$ diameter fused silica window for transmission of radiation in the UV/O/NIR. The dewar was specially designed to have an extra long neck for accessibility and dual radiation shields for an extended hold time of 36 hours at 77 K and 10^{-6} Torr, which is 12 hours past the standard hold time for the ND-5 series dewars. However, a 12 hour hold time only applies to an empty dewar. Typical hold time in the lab while using a fully populated dewar was $\sim$20 hours.

The dewar cold plate is gold-coated and tapped with $1/4''$ deep 4-40 holes on a $.500''$ grid. The gold coating has been applied to prevent tarnish and enhance

[9] www.apiezon.com
[10] www.infraredlaboratories.com/

thermal contact with mounted equipment. The tapped grid is for mechanically mounting components to the cold surface.

The dewar has an activated charcoal "getter" continuer that bolts directly to the cryogenic work surface. The getter assists the vacuum by absorbing the contaminants from within the dewar at cryogenic temperature. When the dewar is removed from the vacuum pump, the materials inside the workspace will begin to outgas and release trapped volatiles into the vacuum space. The activated charcoal absorbs those outgassing products, protecting the guard vacuum. The charcoal requires cryogenic temperatures to activate and is therefore ineffective at room temperature. For this reason, it is good practice to leave the dewar on the vacuum pump while filling with liquid nitrogen until the charcoal cools. Once the charcoal cools, it can absorb the outgas products. However, it is also essential to limit exposure of the charcoal to atmosphere as it will absorb water vapor, reducing its performance. To restore performance, the charcoal should be vacuum baked for 8-12 hours at 473 K.

Proper maintenance of the dewar is required to ensure long-term stability and reliability. All components to be placed into the vacuum space should be clean and grease-free and also free of trapped air pockets which can result in "virtual" leaks which may spoil the vacuum. All fasteners used within the dewar should be vented. High quality silicon vacuum grease should be applied to all o-rings prior to assembly. It is also recommended by IRLabs to "bake-out" the dewar and all components that will be in the vacuum space. Typical "bake-out" involves extended pumping with the vacuum system and heating the dewar either internally, by introducing hot water into the LN_2 reservoir, or externally with a heat gun or heater strips. Prior to delivery, the dewar was baked at 339 K for 24 hours.

All materials within the dewar should be "baked" at high enough temperatures to allow hydrocarbons and water to completely outgas from the material (IRLabs, 2004).

Metals going inside the vacuum space should be cleaned via sonic agitation for 30 minutes or more followed by 5/5 minutes of acetone/IPA sonication and a vacuum "bake-out" at 393 K or higher for 18 - 48 hours. Any organics entering the system (PCBs, wires, o-rings, etc.) should experience similar treatment, except for the acetone bath. Any organics introduced into the vacuum space must be carefully controlled because hydrocarbons outgassing from the materials will irrevocably contaminate the surfaces of the vacuum (Jacquot et al., 2011).

For the electrical connections within the dewar, two Detoronics hermetically sealed 55-pin solder cup connectors[11] serve as the interface between the evacuated space and the external environment. The hermetic, meaning "airtight", seal is accomplished by using a glass seal between the electrical contacts. The glass prevents the atmosphere from penetrating through the spaces between the electrical contacts, thus preserving the vacuum. I wired the connectors, using phosphor-bronze wire, with all of the appropriate connections necessary to operate the CCD installed inside the dewar and read the video signal from the dewar. Phosphor-bronze wire has a lower thermal conductivity than standard copper wire and serves to maximize dewar hold time.

2.7.5 Temperature Measurement

The temperature is measured using two Lakeshore DT-414 silicon diodes[12] mounted in copper housings and attached to the cold plate and cold finger inside the dewar. The silicon diodes were chosen for their repeatability, wide-temperature

[11] www.detoronics.com
[12] www.lakeshore.com

response, and predictable thermal response. All silicon diodes follow the same predictable calibration curve and therefore can be used interchangeably with each other. Both diodes are wired in a four-wire configuration in order to achieve the most accurate measurement for the temperature. Four-wire configuration involves the use of a current source in conjunction with a voltage measurement circuit. The use of a four-wire connection avoids introducing current/resistive drops in the voltage sensing pair, since the drops translate into temperature measurement errors.

A Lakeshore Model 321-01 temperature controller is used to control the temperature. According to the user manual (LakeShore, 2004):

> The control software in the Model 321 compares the measured value of the control sensor to the desired control setpoint and acts with three term proportional-integral-derivative (PID) function to minimize the difference. The ramping feature permits the user to set the rate that the setpoint increases or decreases when the setpoint is changed. If this feature is combined with the zone feature, the user could do a ramp through all 10 zones from $\approx$2 K to room temperature by only changing the setpoint. The controller will change the PID and heater range settings as the temperature setpoint passes through the different zones. Two heater ranges, with the high providing 25 Watts and the low 2.5 Watts, accommodate a variety of cryogenic cooling systems. The power output of the Model 321 is a quiet, variable DC current to ensure as little noise coupling as possible between the heater and experiment.

PID control involves measuring the present, summing the errors, and predicting the future. The PID process is one of closed loop feedback control

typically used in industrial process control. The proportional controller calculates a term proportional to the error in the system, then a term proportional to the integral of the error, and a term promotional to the derivative of the error. A transfer function involving all three of these terms determines the control process. The proportional control reduces the rise time of a closed loop. The integral control will eliminate steady-state error but slow down transient response. The derivative term increases stability by reducing overshoot and improving transient response[13].

2.7.6 Pressure Management and Measurement

In order to bring the pressure from atmospheric to high vacuum for testing, we use the Varian Mini-Task KF-40 compact pumping system[14] which houses a Varian Turbo-V81 MacroTorr© turbomolecular pump backed by a 10 liter/min diaphragm pump. The turbo-pump has a base pressure of 3.75×10^{-8} Torr with a pumping speed of H_2 gas of $\sim$ 36 liters/second. In a turbomolecular pump, a rapidly spinning turbine hits gas molecules from the pump inlet to the outlet exhaust (Moore, 2009). This is a mechanical process involving the transfer of momentum from the rotating blades to the molecules within the vacuum space, physically moving the particles towards the exhaust.

Pressure is measured using a MicroPirani™ pressure transducer in combination with an HPS™ series A900[15] vacuum sensor system from MKS Instruments. The MicroPirani™ is based on a unique solid state sensor designed for measuring thermal conductivity, has a wide measurement range from atmospheric to 1×10^{-5} Torr, with a very high measurement accuracy, very small dead volume, and excellent stability to changes in ambient temperature. Furthermore, the MicroPirani™ measuring circuit provides a 0-10 V nonlinear

[13] www.ctms.engin.umich.edu/
[14] www.home.agilent.com
[15] www.mkinst.com

analog output signal the can be read-in using the National Instruments hardware in the lab and converted to pressure using the equation:

$$P = \frac{1}{C_0 + (C_1 V + C_2 V^2 + C_3 V^3 + C_6 V^6)^{-1}} \; [mbar] \tag{2.3}$$

where the constants vary based on the gas inside the dewar. For air, $C_0 = -.0278168$, $C_1 = 0.1371869$, $C_2 = 0.0602274$, $C_3 = 0.0148662$, and $C_6 = 0.0000121$.

The process followed in order to bring the vacuum space to operational pressure is as follows: First, I closed off the vacuum valve located at the inlet to the dewar and pumped out the transfer hoses. This process typically took less than two minutes and typically reached a pressure reading of 10^{-5} Torr, which is the lower limit of measurement for the pressure transducer. Second, I slowly opened the valve to the vacuum space and allowed the displayed pressure on the PDR900 series controller to rise by two orders of magnitude. While working with the system, it is audible when the turbo pump engages and when it is stressed from too great a pressure differential between its inlet and outlet exhaust ports. I would open the valve slowly every couple of minutes until the turbo started to slow below its maximum rotational speed and wait. Once the turbo was again spinning at its maximum rotational speed, we then proceeded to open the valve a little more and repeat the procedure until the valve to the vacuum space was fully open. We followed this very slow "pump and release" process in order to mitigate the strain on the turbo pump and bring the pressure down to experimental levels in a safe and consistent manner. This process could take anywhere from 30 to 60 minutes, depending on how fast I felt it safe to evacuate the dewar for any particular experiment.

2.7.7 Electro-Static Discharge Control

Working with next generation detectors requires careful consideration for dealing with electro-static discharge, (ESD). Improper ESD control can result in electronic parts being shocked, resulting in failed parts, intermittent failures, reduced performance, and decreased reliability. Furthermore, since the detectors being calibrated in the LASI facility are baseline detectors for future space missions, one has to ensure no damage is done before flight because in-flight repair is impossible.

ESD is the sudden transfer of of static charge between bodies at different charge potentials caused by near contact or induced by an electric field. On a dry day ($< 30\%$ humidity), the human body can build a 25 kV static potential difference resulting in a visible 1 cm spark that would destroy even the most robust equipment.

In order to mitigate ESD damage from human interaction with electronic components, we follow the procedures outlined in the JPL Electrostatic Discharge Control Program documentation (JPL, 2005). We employed the use of wrist and foot grounding straps, ESD (grounding) mats, ESD lab coats, and ESD-safe tools.

The optical benches were also grounded to the main building ground using thick 12-gauge stranded copper wire. Large wire was chosen to allow an extremely low resistive path for the ESD to travel.

2.7.8 Power Conditioning

During the course of detector calibration, we found the wall main power to have significant amounts of high and low frequency noise along with the 60 Hz AC signal. I was able to see the amplitude of the noise was approximately $\pm 20\%$ of

the 110 V wall power, causing the wall power to have a peak voltage greater than 130 V. With this much variation, I felt power conditioning should be employed in order to remove the variations. In order to remove the noise, we purchased several Tripp-Lite[16] power conditioners with battery backup capabilities, to ensure safe operation in the event of a power surge or power outage. However, we failed to purchase the power conditioning equipment prior to irreparable damage of one of our detectors which was caused by a power spike in the main power line (Section 2.11.5).

2.8 Electronics

The electronics description will "follow the electrons" from the output amplifier on the CCD to the FITS file generated at the control computer.

2.8.1 Preamplifier

In order to provide a signal to the CCD array controller and minimize strain on the CCD output amplifiers, a preamplifier was fabricated based upon the design shown in Figure 2.3, which was developed at JPL based on an earlier design by Lawrence Berkeley National Laboratory for the LBNL detectors. The amplifier is designed as a two-stage differential amplifier. The first stage is a non-inverting stage with a gain of +2 or +4 depending on jumper configuration. The second stage is an inverting stage with a gain of -1. The amplifier can be used as a single-ended or differential amplifier, depending on where the user interacts with the video signal. The user can adjust the gain and offset using the two potentiometers provided. The gain is adjustable from $1\times$ to $\sim 10\times$ using the 10k Ω potentiometer, R_6, while the offset is adjustable from 0 to $\sim$ -7.5 V using R11, which is 20k Ω. The gain circuit also has a jumper, J_2, that allows the user to remove the gain circuit completely from the amplifier feedback chain.

[16] www.tripplite.com

For the fabricated design used in the LASI facility, potentiometer R_6 was removed and replaced with a 2k Ω resistor in order to fix the maximum possible gain to +4 in order to mitigate the possibility of ADC saturation in the controller.

In single-ended operation, the video signal from the CCD is passed through the non-inverting amplifier circuit directly to the CCD array controller. The offset and gain can be adjusted in relation to the input signal. If the user wants to operate in single-ended mode, then the video signal should be taken from subminiature-A (SMA) connector, J_6. In differential operation, the video signal is passed through a non-inverting amplifier and the output from the non-inverting amplifier is passed through an inverting amplifier stage after which both the non-inverted and inverted amplified video signals are provided to the array controller. The gain and offset are only adjustable at the non-inverting stage. The offset, in this case, adjusts the difference between the non-inverting and inverting waveforms delivered to the array controller. It does not adjust the difference from zero, which is the bias level. The design choice to employ the signal manipulation only at the non-inverting stage is to minimize the possibility of introducing spurious noise or offsets to the inverting and non-inverting waveforms before their introduction to the array controller.

The heart of the amplifier design is the AD829 operational amplifier from Analog Devices[17]. The AD829 was selected for its extremely low noise floor ($1.7\frac{nV}{\sqrt{Hz}}$ input voltage noise), high slew rate ($230\ \frac{\mathrm{V}}{\mu\mathrm{s}}$ slew rate), and unity gain stability. The noise floor determines the amount of noise picked up when using the amplifier. The slew rate determines the maximum rate of change of the output voltage through the op-amp. Unity gain stability ensures the op-amp will not oscillate for matched input and feedback resistance. The amplifier only draws

[17] www.analog.com

5 milliamp supply current per amplifier (at $\pm$5 or $\pm$15 V), which is useful for low power applications. Finally, the op amp has an extremely fast settling time (90 ns), which is useful for high-speed data conversion.

Figure 2.3 shows a schematic of the differential preamplifier. Figure 2.4 is a picture of the two-channel differential preamplifier fabricated by myself and used both at ASU and JPL. Each differential channel is identical, providing a robust cross-checking mechanism. Output from the video amplifier on the CCD is input to the preamplifier via a coaxial cable. The coaxial cable shields the video signal from external interference. The video signal then passes through a dc blocking capacitor, to remove the dc offset, which is approximately -18 V for the the LBNL delta-doped CCD. After the dc component is removed from the signal chain, the oscillatory waveform data passes through the first stage of the preamplifier where the gain and offset can be adjusted. The amplified non-inverted waveform is then passed through a unity gain inverting amplifier stage. The outputs at both stages are then passed through attenuation resistors to the output SMA connections which are then delivered to the array controller using coaxial cables.

2.8.1.1 Offset Calculation

The total range for the voltage offset, or bias, is given by:

$$V_b = \frac{R_3}{R_4} V_{input} \tag{2.4}$$

giving an available range of offset voltage correction of 0 - -7.5 V for the non-inverting circuit. However, the full possible rail-to-rail range is covered because the offset is fed into the inverting amplifier, which then has a range of 0 - +7.5 V, giving a total range of $\pm$15 V. The goal of the offset circuit is to balance the differential waveforms around a common voltage. The absolute range is unimportant as long as it is large enough to allow for an equally balanced circuit.

2.8.1.2 Gain Calculation

The gain for the non-inverting stage is simply that of a two resistor element non-inverting amplifier:

$$\mathrm{A_V} = \left(1 + \frac{R_5 + R_6}{R_3}\right) \tag{2.5}$$

where the lower and upper limits of gain are 1 and 10. The gain value is not important as long as the overall V_{pp} of the video signal is less than the limit of the ADC in the controller, which is ± 5 V for the CCD controller in the LASI facility.

For the inverting stage, the gain is given by a simple relationship between the feedback resistor and input resistor:

$$\mathrm{A_V} = -\frac{\mathrm{R}_f}{\mathrm{R}_{in}} \tag{2.6}$$

$$\mathrm{A_V} = -\frac{\mathrm{R_8}}{\mathrm{R_7}} \tag{2.7}$$

where R_f is the feedback resistor and R_{in} is the input load resistance. The designed output gain of the inverting amplifier is -1. The inverting amplifier is designed to match the gain of the non-inverting amplifier.

2.8.2 CCD Controller

An Astronomical Research Cameras (ARC)[18] controller ("Leach" controller) (Leach, 1994) is the standard controller used at many astronomical observatories so it was an obvious choice for use in the LASI facility. The controller in the LASI facility is the GENIII model, meaning the third generation of the design. The controllers are designed to be universal, allowing for the operation of various CCD and infrared arrays by simply changing the Motorola digital signal processor (DSP[19]) code used to program the controller. The controller provides power, clock

[18] www.astro-cam.com
[19] Motorola (1996)

level translation, correlated-double sampling video acquisition, gain adjustment, and FITS image generation. The systems are configurable to read any number of CCDs just by increasing the number of video input cards to the controller and editing the DSP control code.

The gain and CCD gate voltages are defined via software in the Leach controller by programming the appropriate voltage level in the DSP code. Clock level translations, required to read out the CCD, are also defined within the user specified DSP code. Input video signals are delivered to the video acquisition board within the controller either directly (single-ended) from the CCD or differentially using a preamplifier. The user must select the input configuration to the board by changing a set of jumpers within the controller. The operation in the LASI facility is differential, in order to provide the best signal-to-noise input for analog-to-digital conversion on the video board.

Correlated-double sampling (CDS) is used to process CCD video signals. The purpose of using CDS is to achieve optimum signal-to-noise performance. The CDS process is used to remove the offset level by measuring the video signal twice, once at at reference voltage after pixel reset and and once at the signal voltage. The reference voltage is then removed from the pixel voltage at the end of the integration. Extensive treatment of the CDS process is presented in Janesick (2001).

The Leach controller is communicated with via a personal computer running either Windows, UNIX, or Mac OSX. A peripheral component interconnect (PCI) or PCI-express card installed into the host computer communicates via fiber-optic with an interface card installed in the Leach controller. All drivers are provided by the manufacturer. A description of the software interface is provided in Section 2.9.

2.8.3 National Instruments PXI System

The LASI facility has a National Instruments (NI) data acquisition and hardware control system. The system is comprised of an PXI-8336 communication system for remote pc control, a PXI-6221 multifunction 16-Bit, 250,000 samples/second, data acquisition (DAQ) system with 16 analog inputs, and a PXI-6534 for digital I/O. The PXI-6221 DAQ is used to record the pressure as a function of time during dewar evacuation.

2.8.4 Keithley Picoammeter

Current from the photodiode is measured using a model 6485 picoammeter. The picoammeter can measure current from $\pm$20 fA to $\pm$21 mA, has an analog output, and can be externally controlled via serial RS-232 or General Purpose Interface Bus (GPIB) communication. The user manual (Keithley, 2001) provides the detailed specifications. One important concept of operation of the picoammeter is to allow the device to warm up for an hour before attempting to measure current.

2.9 Software

An explicit effort has been made to ensure that the software design for the LASI facility makes use of software for both Windows and UNIX environments.

2.9.1 Monochromator Control

The monochromator (Section 2.6.2) is provided with Princeton Instruments proprietary SpectraPro software to allow for wavelength selection and monochromator communication. The communication interface is either serial RS-232 or universal serial bus (USB). The software is written for the Windows environment. Princeton instruments also provides a device driver application

interface (API) that end users can employ to develop their own interfaces using LabVIEW[20], C++, or even Python[21].

The SpectraPro software provides a graphical user interface in which the user can enter the wavelength of interest, switch between diffraction gratings, and adjust the operational parameters of the monochromator. The software also provides an interface for scripting commands.

2.9.2 Data Acquisition

Data acquisition software for the pressure gauge was written in LabVIEW. The pressure gauge provides an analog output, which is connected to an analog input in the NI PXI-6221 DAQ. The voltage levels are then converted to pressure measurement following equation 2.3.

Proprietary ExcelLinx[22] add-in software for Microsoft Excel developed by Keithley provides an easily accessible remote user interface and data acquisition for the picoammeter.

2.9.3 Leach Controller Software

The Leach controller can be commanded using either Voodoo or Owl[23], which are Java based programs written specifically for the controllers produced by Astronomical Research Cameras, or C++, Python, Java, or LabVIEW depending on the user preference. The software used for control of the controller in the LASI facility is Voodoo. Voodoo allows the user to set the operational parameters for the CCD array in a simple Java interface. The software will also generate the output FITS file for analysis. The manufacturer also provides an API that the user can implement to develop their own interface software.

[20] www.ni.com/labview
[21] www.python.org
[22] www.keithley.com
[23] www.astro-cam.com

2.9.4 *Flexible Image Transport System*

FITS files are the standard data format for the astronomical research community. An extensive discussion is provided in Jansen (2006). The FITS data format allow the user to manipulate the image information and tag the file using a "header" which stores pertinent image acquisition data, such as exposure time, the size of the array, and what processing has already been applied to the array. FITS files are cross-operating-system accessible and should be the standard input to any astronomical analysis software.

2.9.5 *Data Processing*

After generation of the array FITS files by the Leach controller software and subsequent acquisition by the interface computer, the images were analyzed using reduction software written in interactive data language (IDL)[24]. The data reduction software written in IDL provides correction for read noise, dark current, and fixed pattern noise from the object frame according to Janesick (2001); Howell (2006); Jansen (2006); and Janesick (2007). This software analysis package was also provided to JPL collaborators for analysis of data acquired in their CCD calibration laboratory. Software was also written to automatically generate quantum efficiency plots based upon bias exposures, flat field exposures, and the photodiode current measured CCD focal plane.

2.10 Results

A next generation 1k $\times$ 1k delta-doped LBNL CCD was calibrated in the LASI facility. Here I present the results of the calibration, followed by an interpretation of the results.

[24] www.exelisvis.com/idl/

2.10.1 Photodiode Calibration

The LASI facility photodiode was calibrated at NIST (Figure 2.10). The calibration was confirmed in the LASI facility. The top two curves in Figure 2.10 are the photodiode quantum efficiency and absolute responsivity, provided by NIST. The bottom curve is the measured relative response of the photodiode multiplied by the provided quantum efficiency. The photodiode response follows the same general shape with the peak at ∼1000 nm and decreasing on either side. Absolute responsivity measurements in the LASI lab are not possible due the design of the light source.

2.10.1.1 Photodiode Absolute Responsivity Calibration

In order to make absolute responsivity measurements, a system capable of measuring the QE of a photodiode is required. To measure the photodiode QE, a calibrated light source with an adjustable power supply is necessary in order to quantify the number of incident photons per second per wavelength.

$$\#_{incident\ photons} = \frac{Power(W)}{E(J)}\ [photons/second] \tag{2.8}$$

From the current measured through the photodiode, the number of photo-electrons generated is given by:

$$S_{\mathrm{D}} = \frac{I_d}{q}\ [e^-/second] \tag{2.9}$$

From those two values the quantum yield for the diode can be calculated:

$$QE_D = \frac{\#_{incident\ photons}}{S_{\mathrm{D}}}\ [photons/e^-] \tag{2.10}$$

The responsivity is then calculated:

$$R_e = \frac{QE_D \lambda(\mu m)}{12390}\ [A/W] \tag{2.11}$$

2.10.2 Stray Light Measurement

After construction of the dark enclosure, we tested the photodiode to ensure that the enclosure was in fact dark. This test was run by simply measuring the quiescent current from the photodiode with the room lights on and then again with the room lights off. Initially, we found that the dark enclosure was not strictly as dark as it should have been. We found a 13% percent difference in the response of the photodiode when the lights were off versus when the lights were on. Had the dark hood functioned like it was supposed to, there should have been closer to a zero percent difference between light-on and light-off measurements. I solved this problem using "gaffer's tape" to cover all the seams and joints on the enclosure to eliminate any stray room light from entering the box. This tape was chosen for its matte black appearance in order to avoid adding a source of specular reflection. After taping all the seams and taping over the bolts, I measured only a 0.5% difference, which was acceptable.

2.10.3 LBNL 1k $\times$ 1k

A delta-doped engineering grade 1k $\times$ 1k LBNL CCD (Figure 2.11) was provided to the LASI facility by JPL for calibration. Engineering grade means that there may be clock shorts or cosmetic defects that make the device unsuitable for scientific operations, but usable for characterization of the calibration facility. Nominal operational data for clock, transistor, and substrate voltages were provided by JPL. Nominal clock timings were also provided. These initial parameters were set within the Leach controller software and the detector installed inside the dewar. The results of the calibration are presented here. Importance of note is that the power supply for the light source was kept constant for all measurements.

2.10.3.1 Operational Temperature

Figure 2.16 shows the temperature dependence of the CCD. The plot is of the number of saturated pixels as a function of temperature. The optimum operational temperature can be read from this plot as the point at which the number of saturated pixels is no longer changing. I find the upper limit of the operational temperature to be $\sim$155 K.

2.10.3.2 Gain, Read Noise, and Bias

Figure 2.17 shows the gain of the device as a function of wavelength. The average gain across the bandpass is $1.10 \pm 0.14 e^{-}$/DN. The gain was set to 1.0 within the Leach controller software. The measured value of gain was within the error of the gain set within the control software.

Figure 2.18 shows the read noise as a function of wavelength. The read noise is constant across the entire calibration spectrum. The black curve that shows the extreme variations is determined using equation (1.21). The average value for read noise across the calibration bandpass is 302 DN.

Figure 2.19 shows the offset, or bias, signal measured in the Leach controller as a function of frame. This is the signal from a zero exposure and includes the signal and noise introduced into the system by the readout electronics. Hundreds of frames were taken, but only a small portion of the data is shown here. The average value is $\sim$27000 DN.

2.10.3.3 Linearity and Non-linearity

Figures 2.20 - 2.25 show the linearity and non-linearity, as measured using residuals, of the detector as functions of wavelength and time. The detector should respond linearly across the entire calibration bandpass. The linearity residuals are

a measure of the non-linearity of the device. Table 2.1 presents the values for linearity measurements and calculations.

Figures 2.24 and 2.25 are the linearity response for the detector at 450nm. These response curves were plotted separately because of their deviation from the rest of the data set. The dashed line corresponds to full well saturation, $\sim$38860 DN. The two solid lines correspond to the FPN and shot-noise regimes.

2.10.3.4 Photon Transfer Curve

Figure 2.23 shows the photon transfer curves calculated for the detector from 600 - 900 nm. The horizontal dot-dashed line corresponds to the read noise regime and has a value of $10^{2.48}$ DN. The vertical dashed line corresponds to full-well saturation and has a value of $10^{4.58}$. The slanted line corresponds to a slope of 0.97 ± 0.02 which delineates the linear response regime of the detector.

2.10.3.5 Quantum Efficiency

Figures 2.26 and 2.27 and Table 2.1 present the calculated quantum efficiency of the detector. Figure 2.26 assumes a variable gain from 450 - 925 nm. Figure 2.27 assumes the average value for gain given in section 2.10.3.2. The table presents values assuming an average value for gain.

2.11 Discussion

Discussion of the results from the calibration of the LBNL 1k $\times$ 1k delta-doped detector are presented below.

2.11.1 Gain and Read Noise

The plots of the gain and read noise show that the gain of the detector changes as a function of wavelength. This is likely a feature of the testing procedure and less an actual feature of the device. However, according to quantum efficiency measurements, detector response does depend on wavelength. The best way to

measure the gain would have been to generate flat fields at every wavelength for sufficiently long exposure times to be within the linear regime but away from the nonlinear regime of the calibration system. Another excellent approach is to measure the gain using flat fields developed from broad band illumination. According to equation 1.21 the gain should be linear across the optical/NIR spectral regime as long as the average signal in the flat frames and the variance in the flat frames remain relatively constant. However, the average gain did fall within error of the gain set within the Leach controller software.

The gain of the data for 450 nm is far lower than the gain for the rest of the data except for 600 nm. This is because the shorter exposure times for the flat fields I took at 450 nm were not long enough to be within the linear response regime of the CCD. From Figure 2.25, it is apparent that at 450 nm, the device has a greater than 1% non-linearity for exposure times up to 40 seconds. The exposure time I used for flat integration at 450 nm was 20 seconds, where the device still experiences $\sim$5% non-linearity. At extremely short exposure times, the device response is still in the shot noise regime, which is clearly seen from Figure 2.25. The point at which the curve has a slope of $\sim$0.5, corresponds to the shot noise regime and is delineated by a linear fit on the plot. In order to achieve better results, I would integrate for times that fall within the linear regime, which is greater than 50 seconds but less than 90 seconds.

The read noise of the device is quite stable across the spectral bandpass, which is to be expected. Since the read noise is quantified using bias frames, there should be no dependence with respect to wavelength. There is however a slight upturn near 450 nm, the source of which is likely a warm CCD. The measurements taken at 450 nm were the first measurements of the day and the temperature of the detector may not have equilibrated to cryogenic operational temperature. Figure

2.19 shows the bias as a function of frame. This plot is just a sampling of the bias exposures taken in the LASI lab over the course of the LBNL CCD calibration. From the plot, one can see the average bias level is $\sim$27000 DN and is stable for frames taken weeks apart.

The bias level is high as a result of the detector presenting very large negative values to the dual-slope integrator (DSI) within the Leach controller after going through the preamp. The bias level had to be set high in order to ensure the (DSI) would accurately integrate the signal. In all likelihood, this limited the dynamic range of the detector calibration system, which is typically quoted as the log of the full well depth divided by the read noise,in decibels:

$$dB = 20log\frac{FWD}{S_R} \tag{2.12}$$

The full dynamic range possible for these detectors could have been increased had I set the gain within the Leach controller to a value greater than 1.

2.11.2 Linearity and Residuals

The data shown in Figures 2.20 - 2.25 were taken at a constant illumination level from a broadband tungsten-halogen light-bulb at the source of the monochromator. The light-bulb input power is adjustable from 0 - 250 W. For these calibration tests, the input power on the light source was set to 50%. Figure 2.20 shows that for a constant input power, the CCD response reaches saturation faster at longer wavelengths. This is likely a combination of two effects: (1) the tungsten-halogen halogen light bulb emits more radiation at longer wavelengths, even for a constant input power, and (2) the device is actually more responsive at longer wavelengths. Figure 2.21 shows that, within error, the response of the device across the entire spectral range of interest is linear with the $\gamma \approx 1$ of equation (2.1) all the way to

saturation. This was an expected result. One of the benefits of using CCDs for astronomical imaging is their linear response to optical radiation.

Figure 2.22 shows the non-linearity residuals as a function of fractional exposure time to saturation. From $\sim$50% saturation onward, the device deviates less than $\pm$1% until $\sim$90% where the non-linearity effects of approaching full well start to influence the data. This plots allows us to determine at what level of full well capacity the detector should be operated in order to be within the linear response regime. Looking at the outer envelope of the data, one can see that the greatest linearity residuals occur for the longest wavelengths. The longer wavelengths also had the shortest exposure times, possibly leading to effects from shutter shading.

Figures 2.24 and 2.25 are the response of the CCD to illumination at 450 nm. This looks like a classical photon transfer curve even though the axes are not the standard log(N) versus log(S). Linear fits to the data show that at extremely short exposure times, the data has a slope of $\sim$.50, which is defined as the shot noise regime, and a slope of $\sim$1, which is the fixed pattern noise regime.

2.11.3 Photon Transfer Curves

The PTC shown in Figure 2.23 demonstrates the power of the PTC when used for analysis. The read noise, shot noise, and fixed pattern noise regimes are clearly seen in the plot. The measured value for read noise and full well depth are exactly in agreement with Figure 2.21. The slope of the linear portion of the curve is also in agreement with the gamma values calculated from the linearity plots. The PTCs from 600 - 900 nm all fall along the same line with the same slope, further confirming the linear nature of the detection of incident radiation by CCDs.

2.11.4 Quantum Efficiency

When compared to Figure 1.7, which is the response of a delta-doped CCD measured at JPL, one can see the QE is approximately 60% in that case whereas the QE measured here is approximately 40%. One can also see the delta-doped CCD shows an increased response in the red when compared with the blue, similar to Figure 1.7.

2.11.5 LASI Lab Shortcomings and Encountered Problems

Overall, the LASI facility provided an excellent setting for calibration of the detector. Most of the hardware in the lab was usable in some respect or another. I was able to measure several important data products for the calibration of CCDs, such as the QE, linearity, gain, and read noise. The vacuum system was excellently sized of our cryogenic dewar and the thermal control system was able to maintain the operational temperature of the detector to ± 1 K. The software interface control of the picoammeter and monochromator provided sufficient customizability such that the development of "in-house" software was not required.

There were, however, some shortcomings in the facility. The pressure gauge would only measure pressures to 10^{-5} Torr. Ideally, I we would be able to measure the pressure within the dewar all the way to the base pressure of the turbopump, which would have required a different type of gauge, such as cold cathode ion gauge. The light-tight enclosure fabricated to eliminate specular reflections could have been better designed. I assisted in the design of the enclosure early in my graduate career before I was well versed in mechanical design and had to rely heavily on the ASU machine shop for their expertise. While the design was based mainly on my specifications, I believe it would have served the purpose within the LASI facility better had it been larger and more easily

accessible. The original design of the enclosure did not allow for access to all portions of the optical bench, which necessitated me crawling inside the enclosure. I am too large to fit comfortably inside the light box and got myself temporarily stuck inside on several occasions. Future designs do not have to be large enough for one standard graduate student to fit within, but they must be better designed to allow for easy access to all sectors of the optical bench.

The wall power to the facility was not filtered or cleaned and noise along the 60 Hz main was observable in the images read out from the detectors. This led to the absolute destruction of a detector during calibration. I was calibrating the detector referenced in Section 2.10 when all of a sudden the upper video amplifier showed a strange behavior. The waveforms measured at the video channel no longer had the typical three-level shape. They appeared to have fully saturated pixel levels, which meant that either the entire CCD was dead or just the had a single blown output amplifier. Luckily, half the CCD was still functional so calibration could continue. However, two months later, the other video output amplifier was also blown by a voltage spike on the power main. Needless to say, power conditioners were installed soon after the last incident. Power conditioners were not installed after the first incident because the root cause was not determined until after the second amplifier was destroyed. The destruction of both amplifiers was attributed to faulty building power.

The biggest problems were with the Leach controller. The initial installation of the PCI control card into the control computer had communication problems with the Leach controller. The issues were related to the driver software not being loaded correctly and the start-up sequence of the computer not allocating enough memory for the images. Furthermore, after the communication issues were corrected, readout from the Leach controller showed spurious periodic peaks of

illumination in the output images. These peaks were periodic, formed what looked like a diamond shape, and occurred in the the same place in every image. They were present in the data products with or without the installation of a detector into the cryostat. It turns out that they were caused by an improperly written Windows XP driver. The solution presented by Bob Leach, of ARC, was to install the Leach controller PCI communication card and the communication software to a Linux machine. I followed these instructions and installed the software to a machine running Linux and used that machine as the lab calibration machine, which solved the problem.

The ADC circuit on the video board in the Leach controller only had a ± 5 V range meaning any signal amplified through the preamplifier had to have an amplitude no larger than ± 5 V. This presented a problem as the preamplifier was designed to provide a gain from 1 to 10 times and the video signal had a range of ± 5 V about the dc offset. If the gain were set too high on the preamplifier, then the ADC would saturate before full well capacity is reached, leading to non-linearity in the ADC. The ADC ± 5 V limit was not known before the design of the preamplifier circuit, hence the lack of correction of the enormous gain stage available in the original preamplifier.

The software for the Leach controller also presented some interesting challenges. The DSP code would only compile easily on a Windows machine because the compiler existed only for windows. This forced my operation of the Leach controller using two computers, a Linux machine for array control and readout, and a Windows machine for controller code compilation. This made data collection tedious. Thankfully, this problem can be addressed by using the WineHQ[25] tool set to run the DSP compiler on a Linux machine. Also, the drivers

[25] www.winehq.org

have been rewritten since the inception of the LASI facility, allowing the Leach controller to properly process the video data under the Windows environment.

2.11.5.1 Cassini Engineering Grade Detector

The initial lab setup was configured using an engineering-grade flight spare CCD from the Cassini mission (Figure 2.6). The CCD is divided into four quadrants, Only two of the quadrants are usable for imaging. The other two are coated to block incident radiation, which gives the checkerboard-like appearance. After designing the system around the Cassini device, which involved wiring the dewar, designing the cold finger and CCD support structure, and installing everything into the dewar, I was unable to image with the device. I checked all of the operational parameters such as clock levels and temperature and found no flaws in either. I then visually inspected the device and saw the device was missing wire bonds. From this, since I was unable to move charge through the device, I determined the device to be dead. Since it was an engineering-grade device, there was no guarantee it would work properly

2.12 Summary

I set out to develop and design a large format detector calibration lab and calibrate a detector within the calibration lab. I was able to develop a fully functional CCD calibration lab and generate data products for a single LBNL delta-doped 1k $\times$ 1k CCD. In the current configuration of the LASI facility, the cryogenic dewar has been modified to allow the operation of the modular imager cell discussed in Chapter 3. The cold finger has been redesigned to provide better contact with the detector so as to allow better thermal control of the imagers. The Leach controller and all associated readout electronics and operational software are available on the lab computer. A new clock signal buffer board to allow the use of long clock-drive cable runs without affecting the shape of the waveform at the CCD has also been

developed and is discussed in Chapter 4. The LASI facility is now a fully operational CCD feasibility evaluation and calibration laboratory.

2.13 Future Work

In order for the LASI facility to enter into the next generation of detector calibration, a few upgrades are in order.

2.13.1 Software Development

Future work in the LASI facility involves the development of software to fully automate the CCD calibration and data collection procedure. By automating the software, it is possible to collect data and generate the appropriate calibration curves faster and more efficiently than the current configuration, thereby increasing the yield rate for detector calibration. This endeavor would likely involve the development of an over-arching control interface, such as LabVIEW, which has instrument drivers already available for all the hardware in the lab. The user would then develop modules to control the different aspects of calibration such as wavelength selection, temperature control, pressure measurement, current measurement, detector control and finally, image acquisition. The software could also provide an easy user interface with buttons that allow the user to automatically generate a PTC or calculate the gain and read noise. This automation software should be accessible enough that any first or second-year graduate student could use the software to calibrate a detector.

2.13.2 Upgrades to the Calibration System

There are also several mechanical upgrades that I recommend for the LASI facility. I recommend the addition of a computer controlled dial for the TDS-420 light source. This will allow the software mentioned in the previous paragraph the ability to adjust the output from the light source. During a calibration run, the light source is typically held at a constant percentage of total output. With the addition

of a computer-controlled mechanism to the light source, one could more easily maintain equivalent exposures levels across the relevant spectral region, allowing for longer exposure times thus eliminating effects introduced from the shutter opening and closing. Along with the computer control of the light source, I recommend the addition of a deuterium light source which will provide a continuous spectrum into the FUV to approximately 112 nm.

I also recommend the addition of an integrating sphere into the calibration system for CCD calibration at wavelengths greater than 350 nm. At FUV wavelengths, there exist no coatings that will provide uniform diffusion of the incident radiation. The integrating sphere serves to preserve the intensity of the input radiation while eliminating all phase information, thereby creating a diffuse source of uniform intensity.

I recommend the addition of a vacuum system or a helium purge system that would allow for the calibration of the detectors well into the vacuum UV. Along with that recommendation, I strongly recommend the purchase of a larger cryogenic dewar to allow for parallel processing of multiple CCDs. This new dewar would necessarily have to be cooled via a liquid cryogen free cooling system, such as the Brooks Polycold PCC compact cooler, which has the ability to cool to 74 K which is well below the operational temperature of the CCDs. The Brooks PCC compact cooler can be controlled via a software interface, allowing the user to adjust the cooling within the software program mentioned above. Another advantage of the cryogen free cooling systems is the turn-around time between calibration. The user does not have to wait for the liquid cryogen to evaporate from inside the dewar before switching out detectors for a new calibration run.

If the LASI facility is going to participate in the calibration of the large number of detectors required to populate the FPAs of proposed future space missions, then a system designed to calibrate multiple CCDs at a time is a necessity. This would involve either the purchase of a new series of Leach controllers or the in-house development of a detector controller that could handle at least four large format detector arrays at a time. This may also require the development of new packaging methods for mounting the CCDs and creating the "rafts" that would form the building blocks large focal plane arrays.

Table 2.1: Results from the calibration of the 1k×1k LBNL delta-doped CCD. QE_1 corresponds to a variable gain. QE_1 corresponds to the average of the variable gain table (1.10 ± 0.14).

Wavelength (nm)	Linearity Measure $(t_e)^\gamma$ ($\pm$0.010)	Gain (e^-/ADU) ($\pm$0.140)	Read Noise (ADU) ($\pm$2)	QE_1 (%)	QE_2 (%)
450	0.967	0.454	315	7.8 (5.4)	24.1 (13.1)
500	1.026	0.678	301	39.7 (1.5)	34.0 (1.3)
550	0.977	1.256	300	37.1 (5.2)	25.2 (8.4)
600	0.991	0.501	309	41.4 (0.9)	25.2 (8.4)
625	0.972	0.714	306	17.3 (1.2)	37.2 (2.7)
650	0.991	0.829	306	37.1 (2.1)	32.9 (3.2)
675	0.990	0.958	300	39.1 (3.0)	32.6 (2.6)
775	0.972	1.614	300	56.4 (1.6)	36.4 (1.1)
800	0.969	1.711	300	52.7 (2.4)	38.1 (1.7)
875	0.947	1.524	295	43.6 (3.7)	37.9 (3.2)
900	0.958	1.665	298	38.3 (3.9)	32.5 (3.4)
925	0.974	1.275	299	37.1 (2.4)	31.7 (2.1)

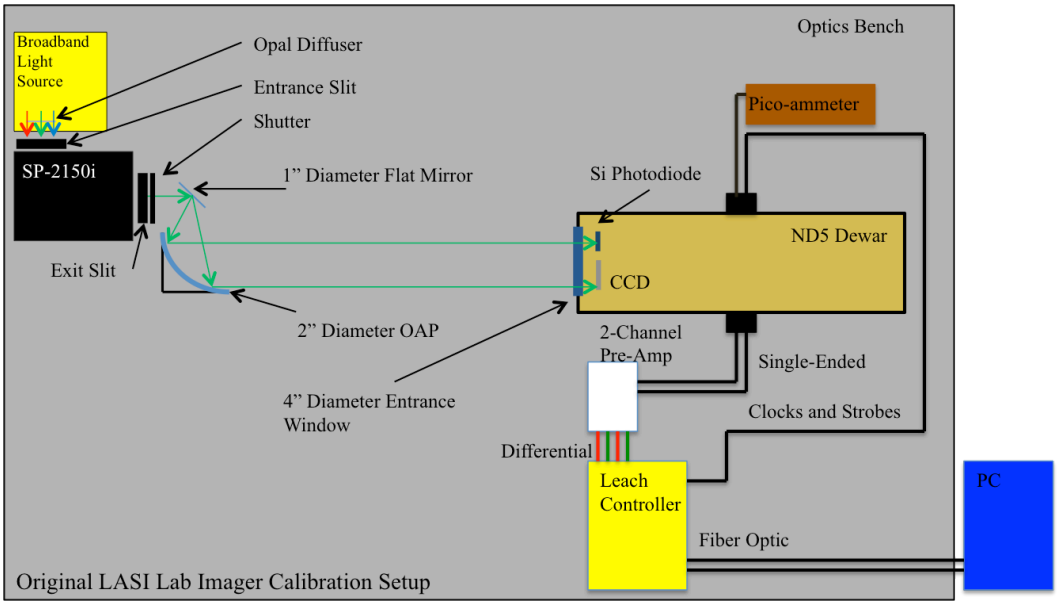

Figure 2.1: Schematic layout of the original CCD calibration setup in the Laboratory for Astronomical and Space Instrumentation (LASI).

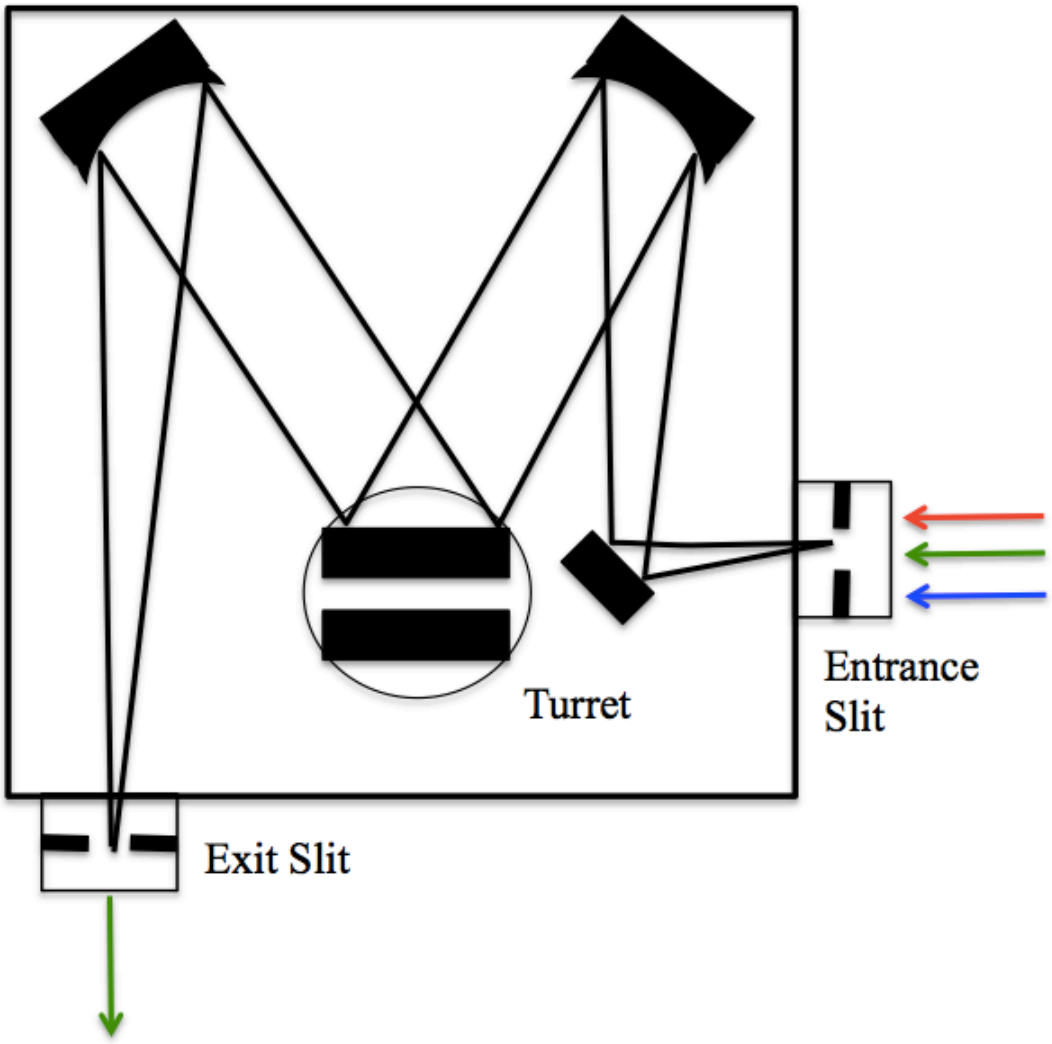

Figure 2.2: Internals of the SP-2150i monochromator. Adapted from the manual (PIActon, 2003). The entrance slit limits the amount of power into the monochromator and the exit slit limits the free spectral range. The rotating grating turret supports two gratings that are indexible within the monochromator controller software. Both slits are adjustable to a maximum width of 3.0μm.

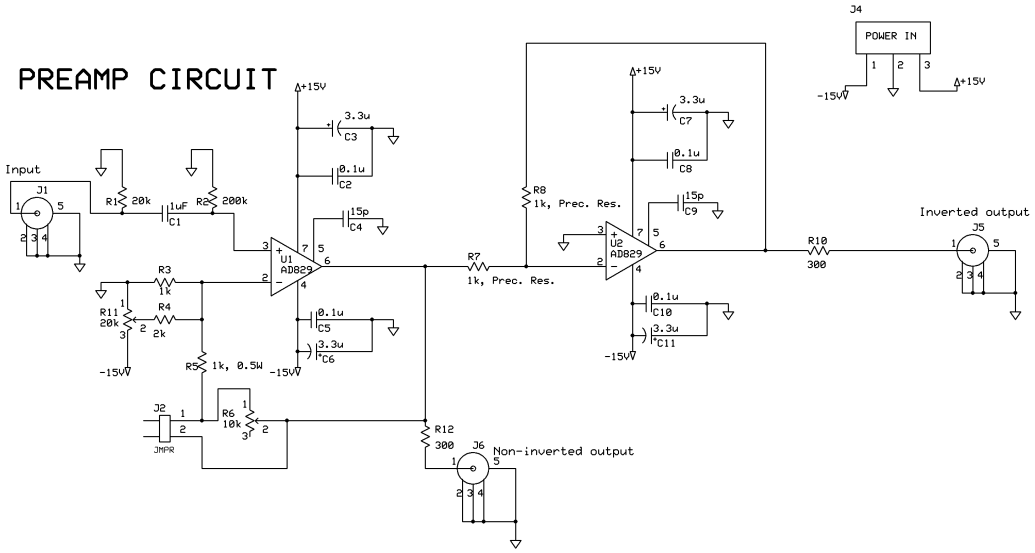

Figure 2.3: Differential preamplifier with adjustable gain from $1\times$ to $10\times$ and bias offset from -7.5 to +7.5 V. (Credit LBNL and JPL)

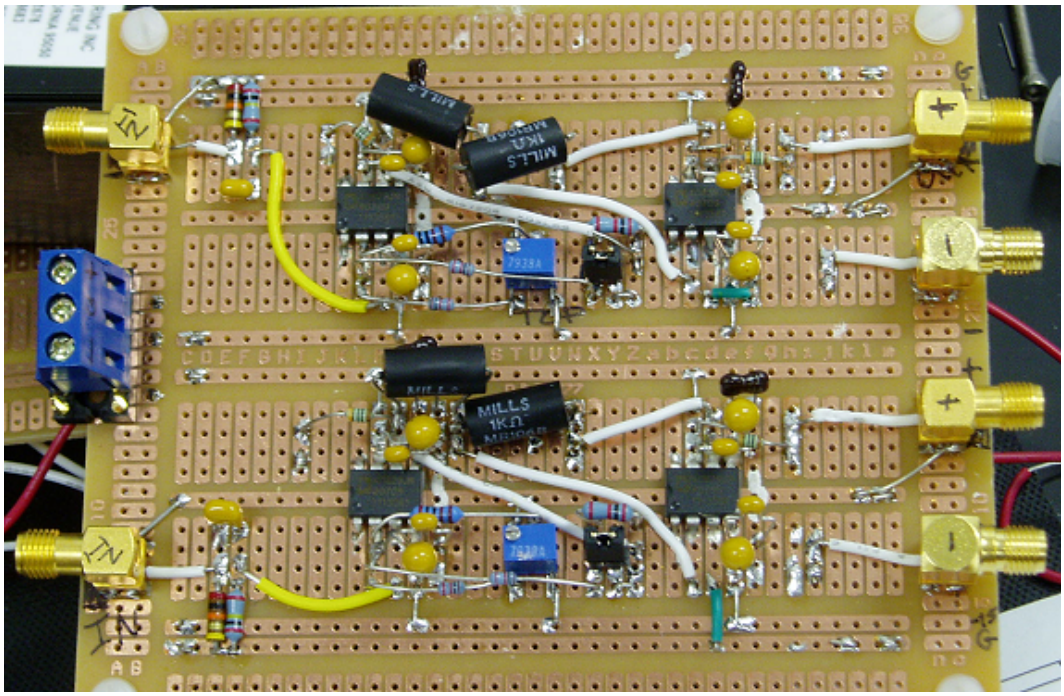

Figure 2.4: Original 2-channel differential preamplifier with adjustable gain from $1\times$ to $20\times$.

Figure 2.5: LASI facility CCD calibration dewar body shown disassembled.

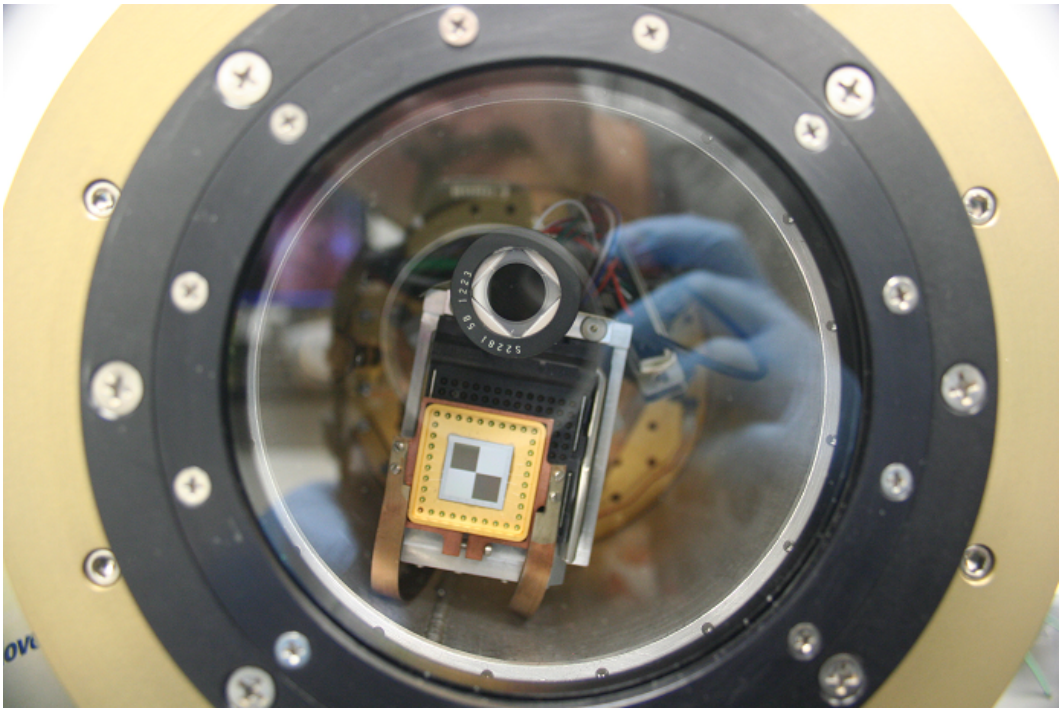

Figure 2.6: Co-planar arrangement of the CCD and Si photodiode.

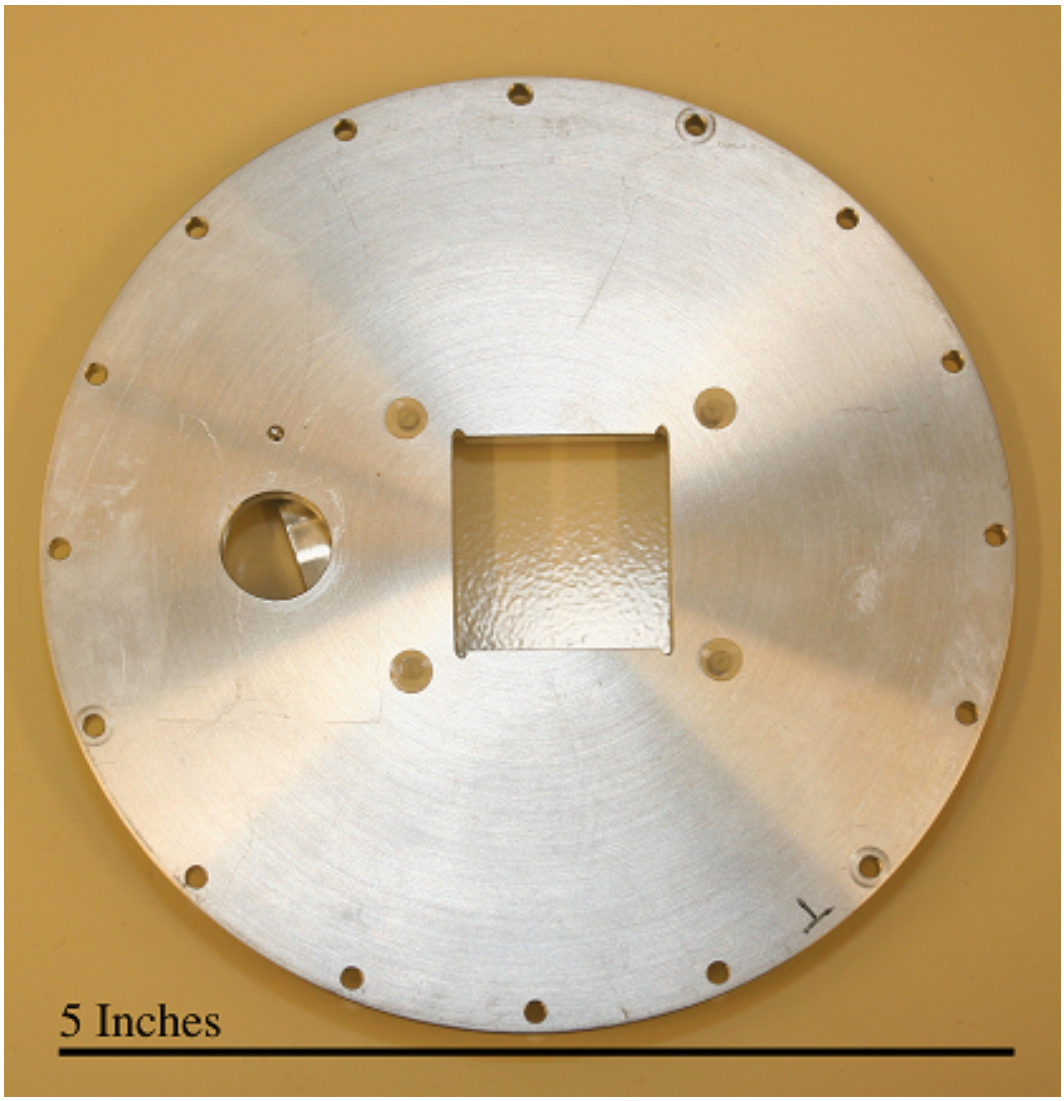

Figure 2.7: The mounting plate is 0.125 inches thick and made of Al6061. The small round hole is for mounting the photodiode. The large square cutout is to allow pass through of the cold finger for thermal contact with CCD.

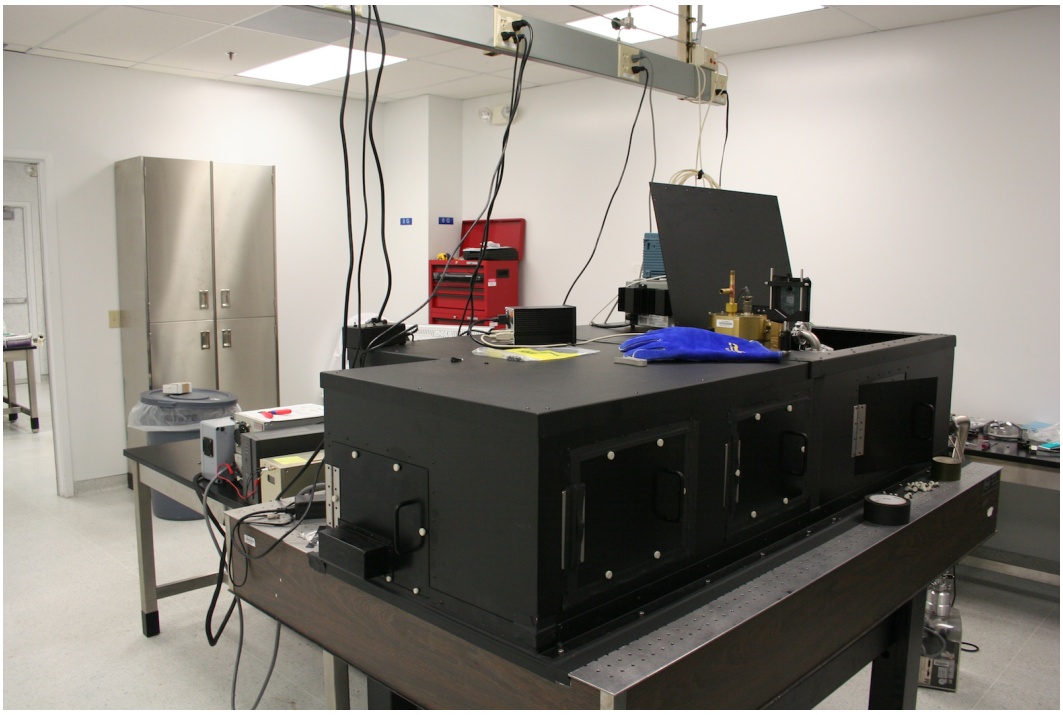

Figure 2.8: Black enclosure designed to reduce specular reflections within the LASI calibration facility.

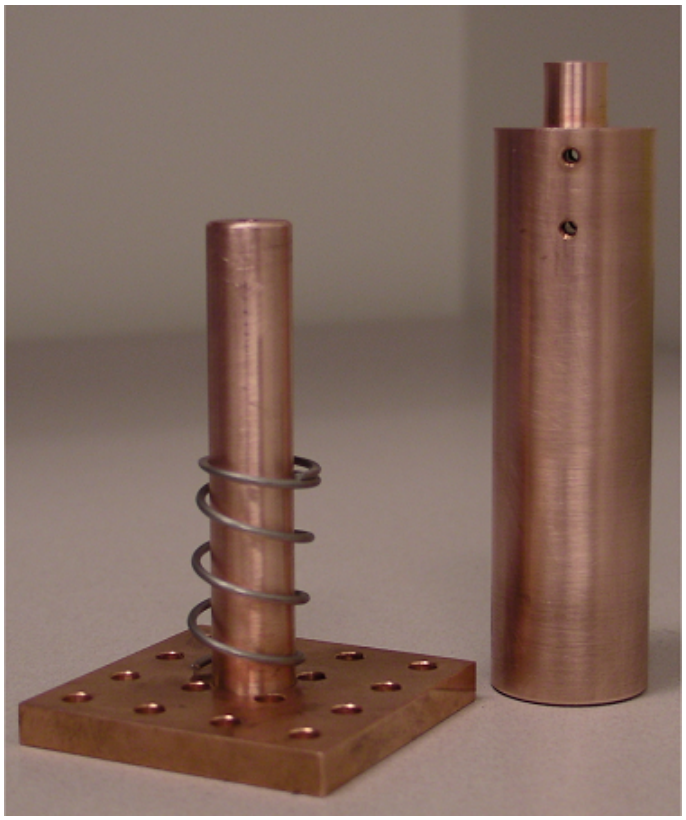

Figure 2.9: The original cold finger designed for CCD operational temperature control.

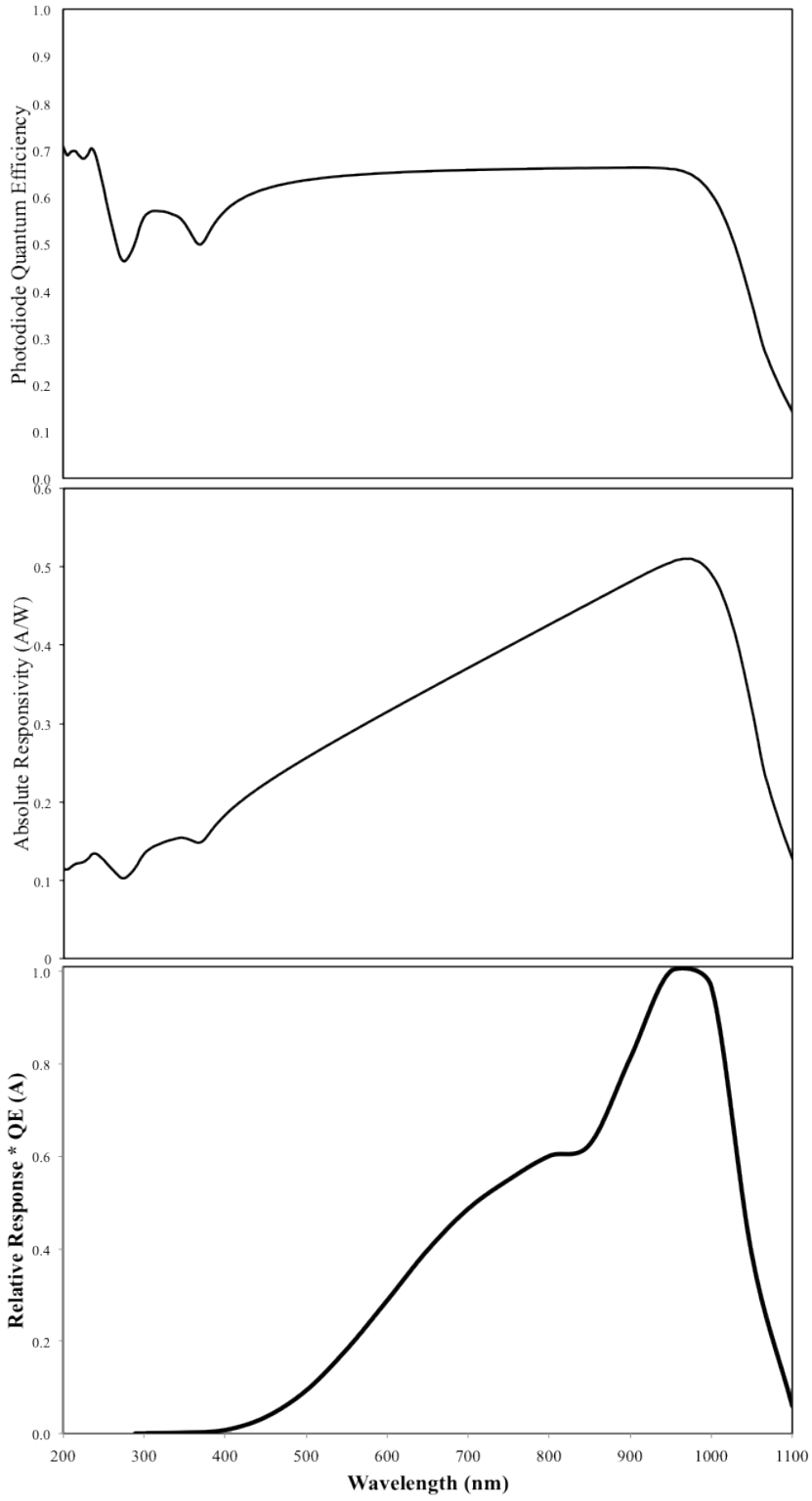

Figure 2.10: The top two curves correspond to the supplied data from NIST. The bottom curve is the relative response of the Si photodiode measured in the LASI facility assuming the QE from NIST is accurate.

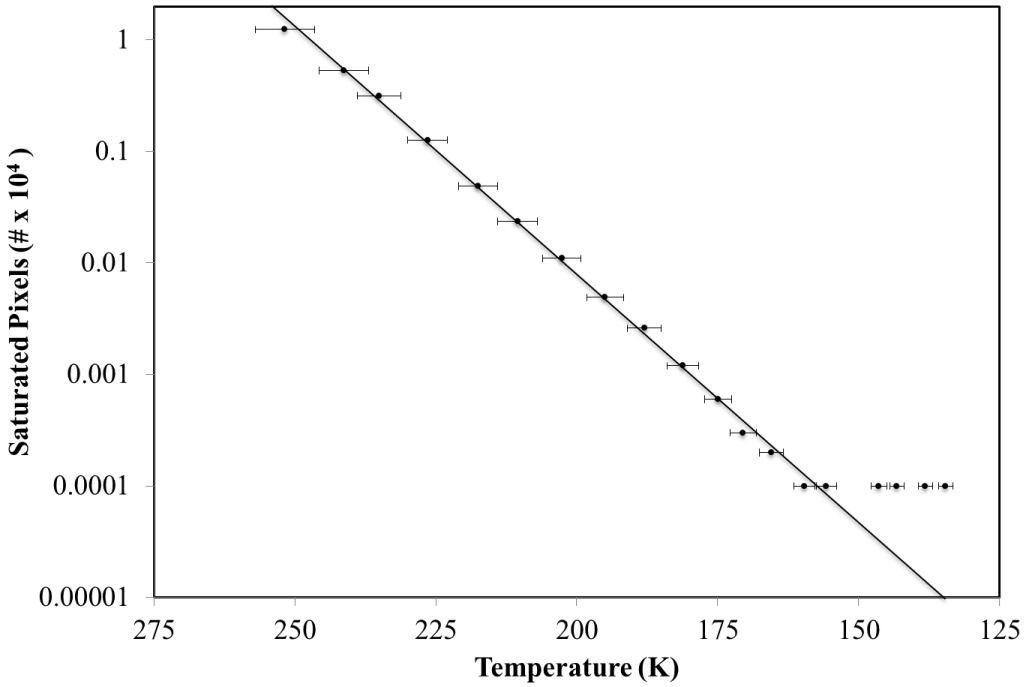

Figure 2.11: The 1k $\times$ 1k CCD calibrated in the LASI facility. The detector is delta-doped.

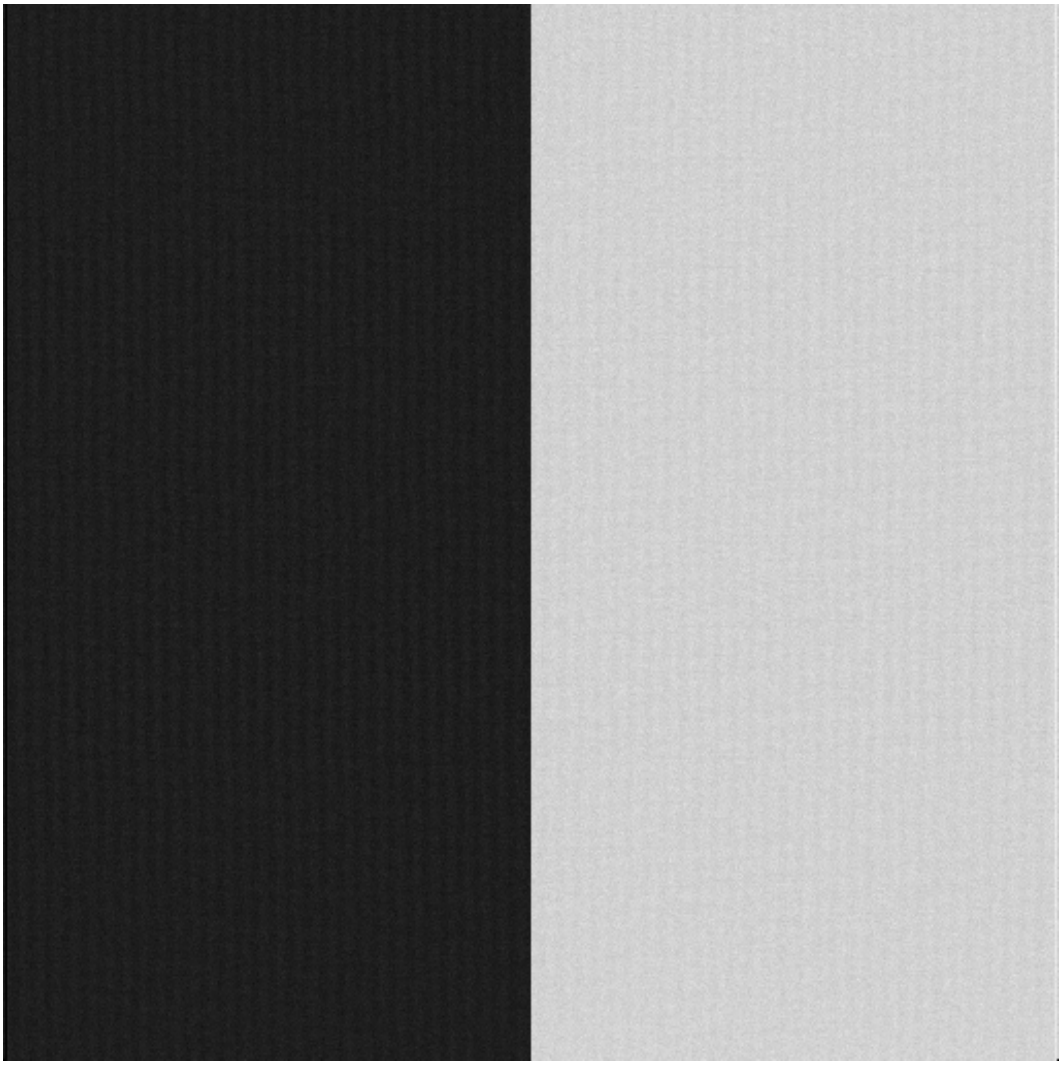

Figure 2.12: Master bias frame for the small LBNL CCD and Leach controller created by averaging 15 individual exposures. The mean signal level on the left half of the image is $\sim$23500 DN and the right is $\sim$25700 DN.

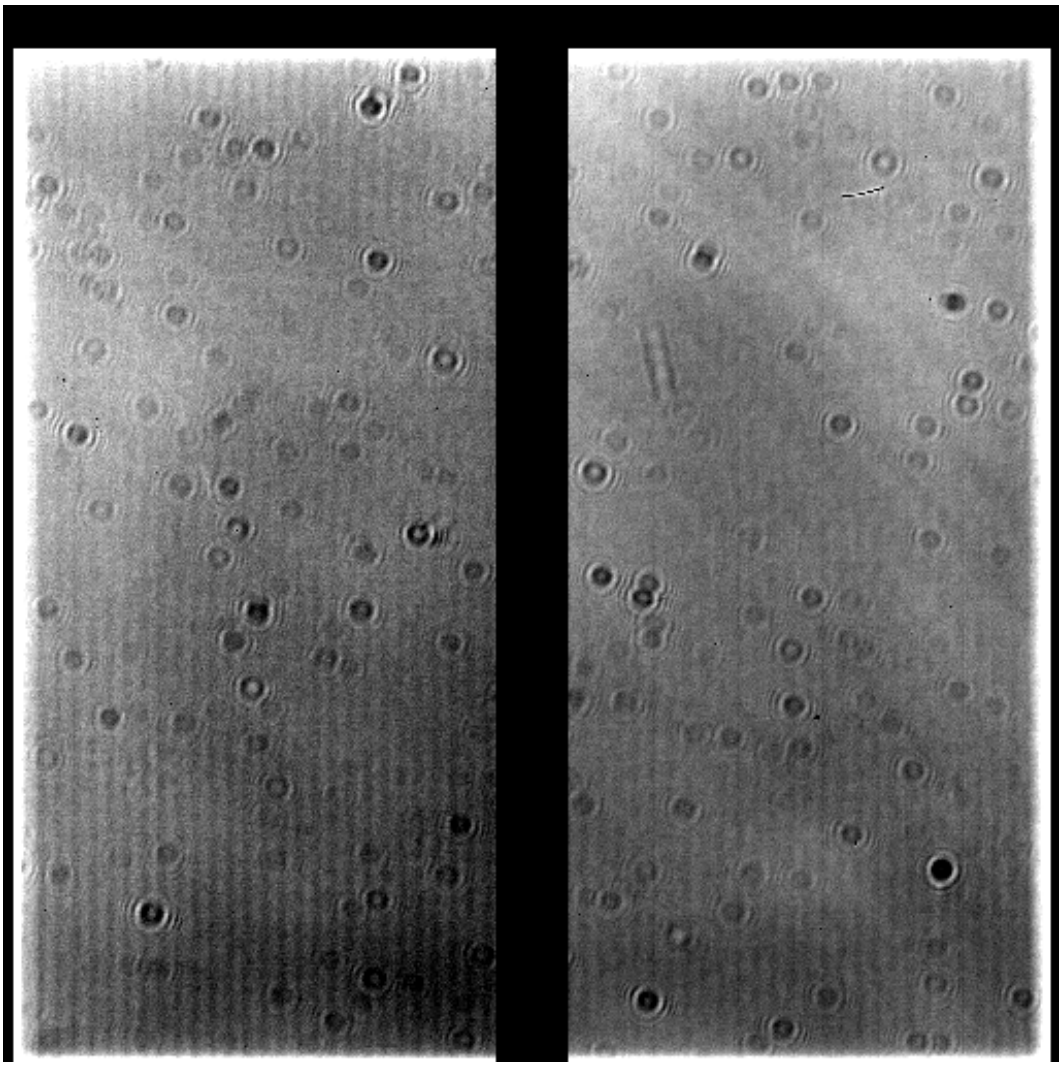

Figure 2.13: Average combined flat field frame for the small LBNL CCD. The frame has been normalized.

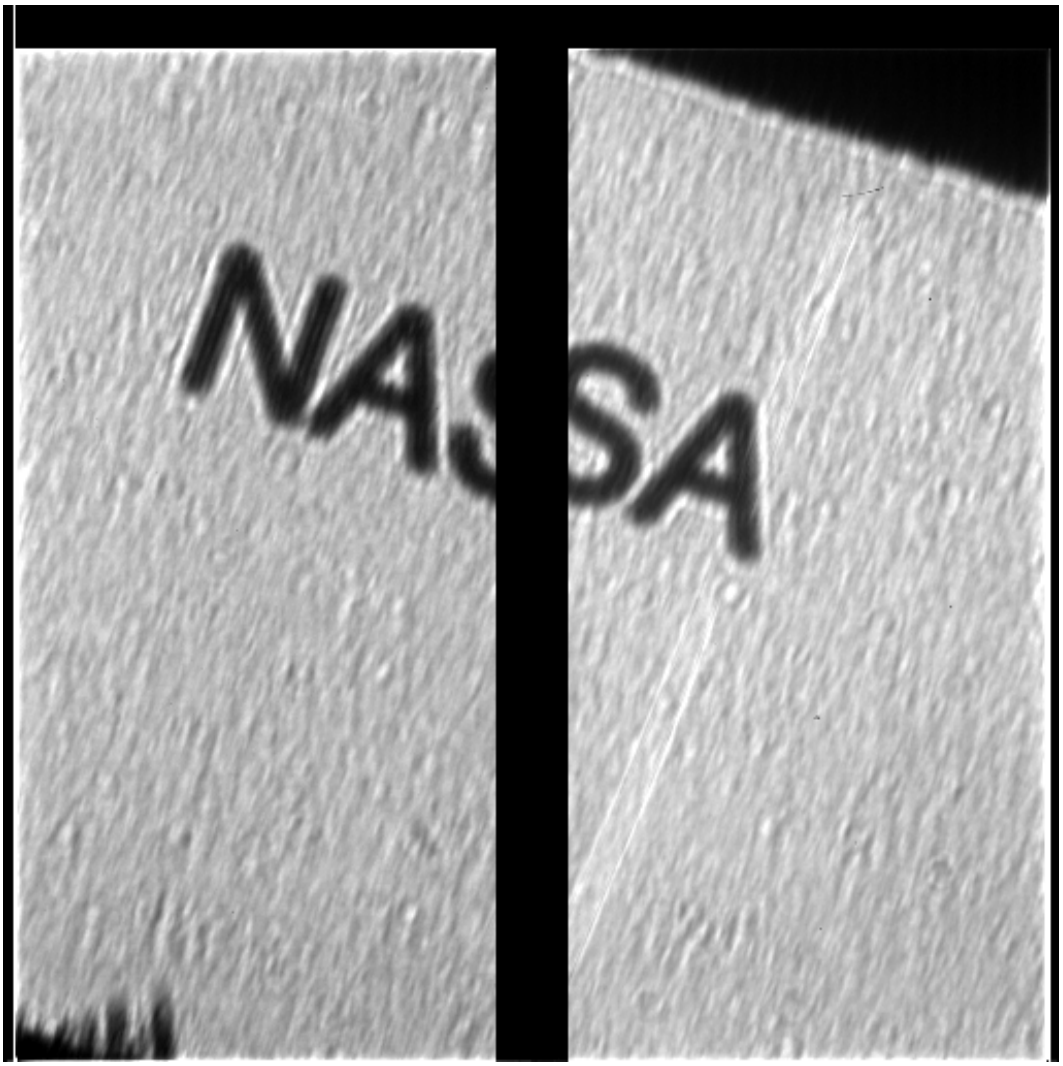

Figure 2.14: Sample object frame for the small LBNL CCD. The mean signal level is ∼57000 DN.

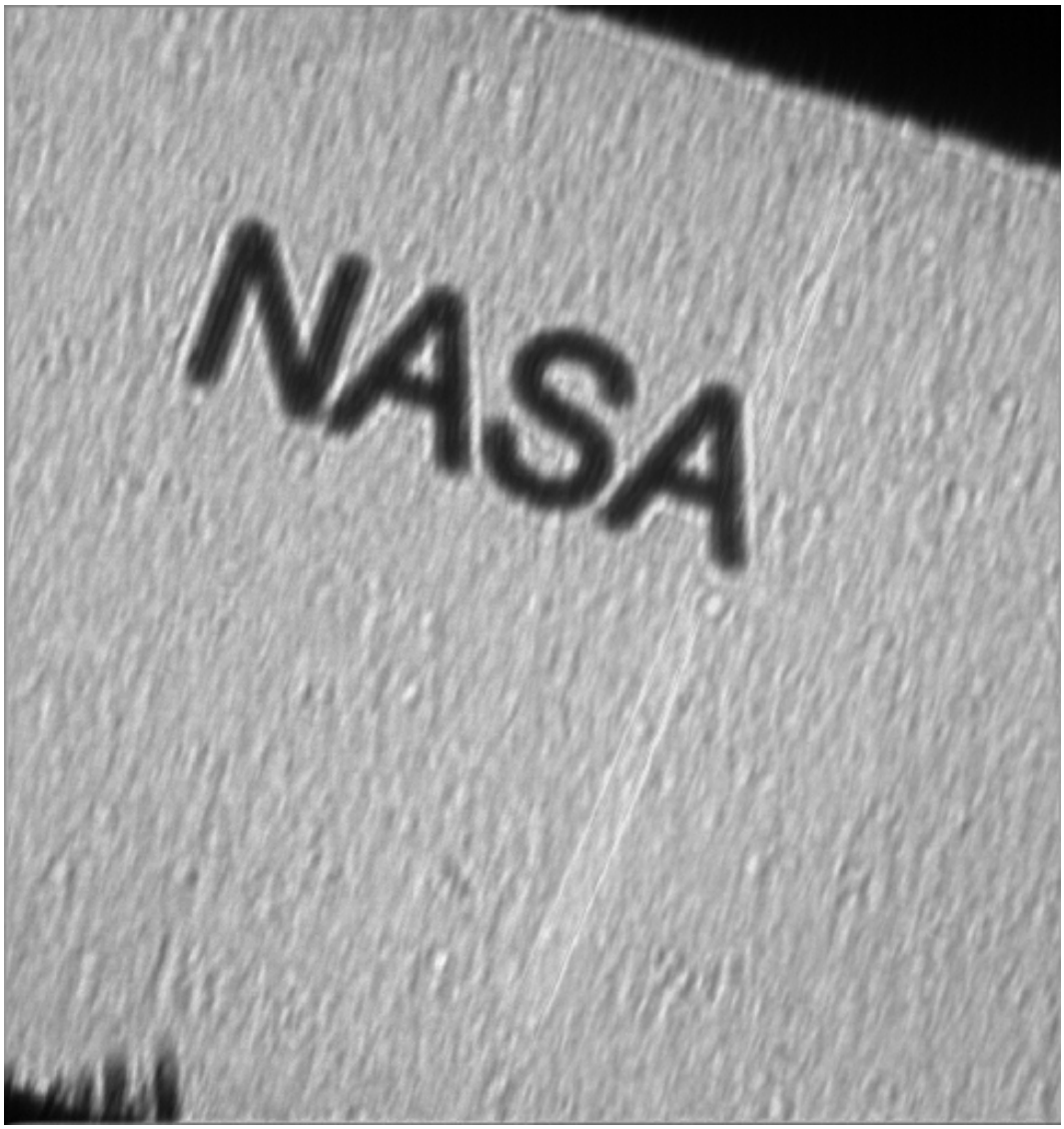

Figure 2.15: Sample reduced object frame that has been corrected for flat field variations and read noise for the small LBNL CCD. The mean signal level is $\sim$32400 DN.

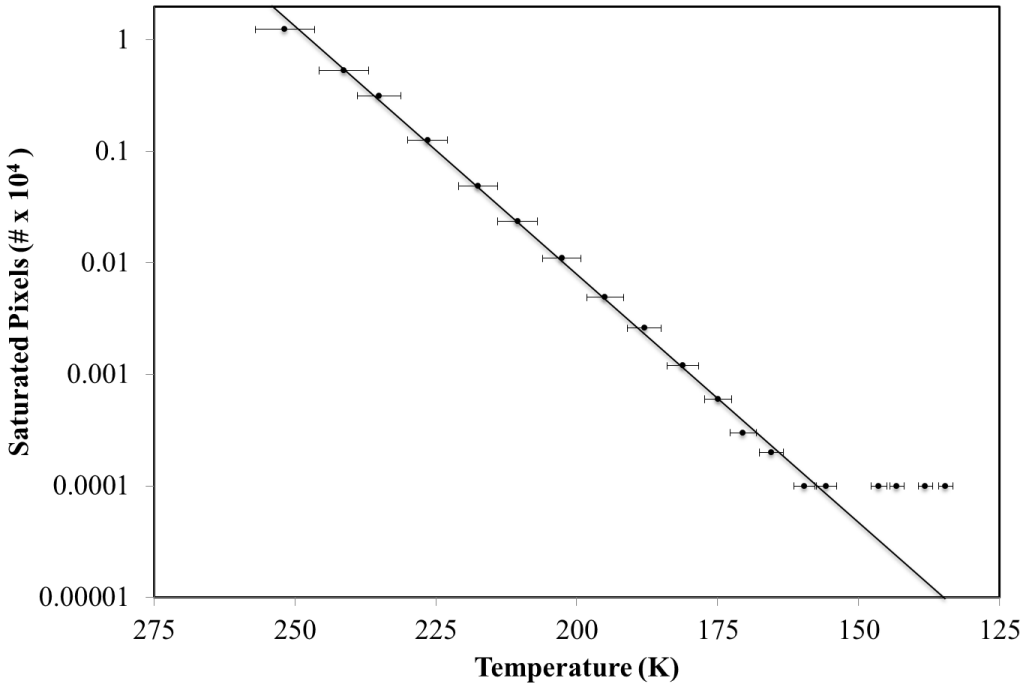

Figure 2.16: This plot shows the number of saturated pixels as a function of temperature for the small LBNL device tested in the LASI facility.

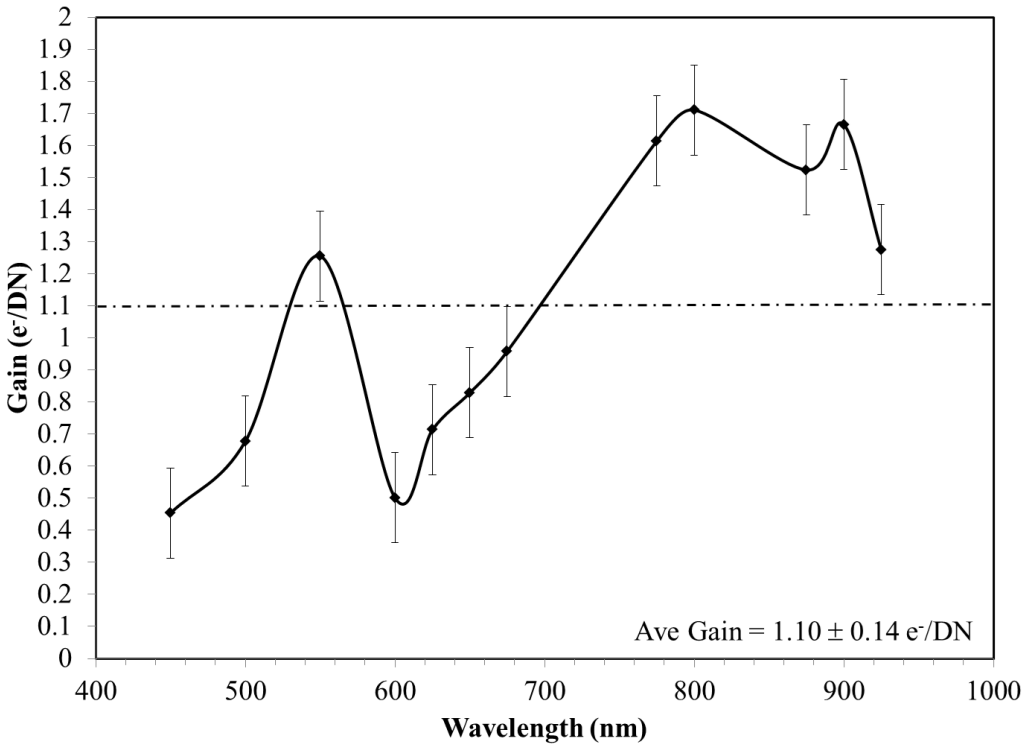

Figure 2.17: This is a plot of the gain measured for the delta-doped 1k $\times$ 1k LBNL CCD.

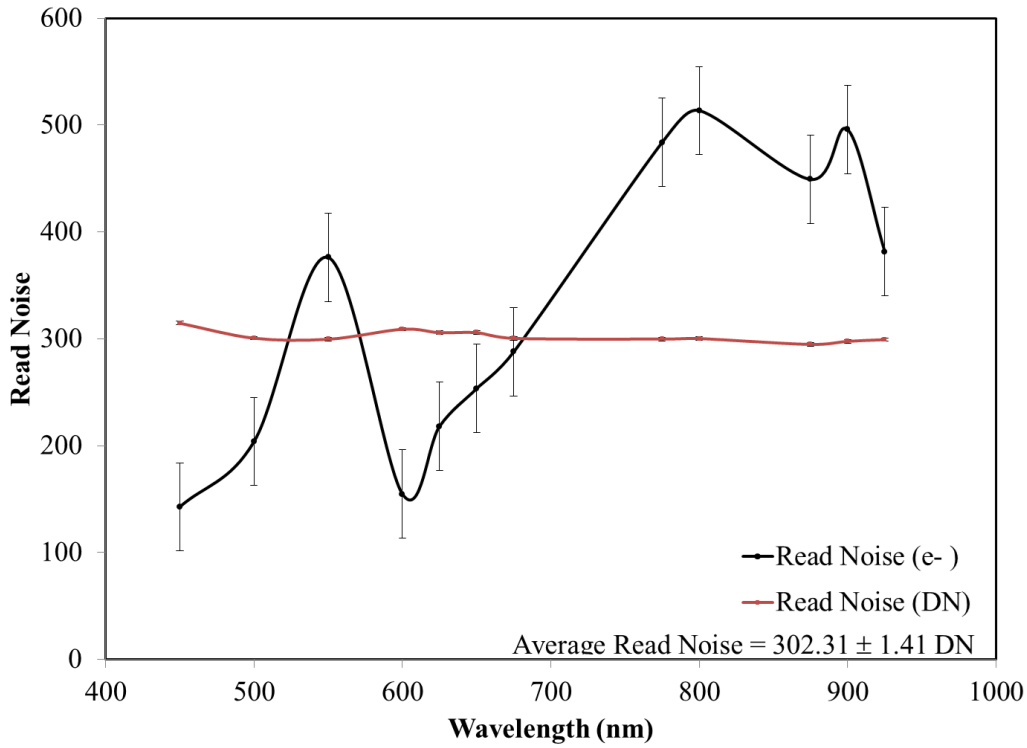

Figure 2.18: Plot of the read noise as a function of wavelength. The read noise should be constant across the optical spectrum.

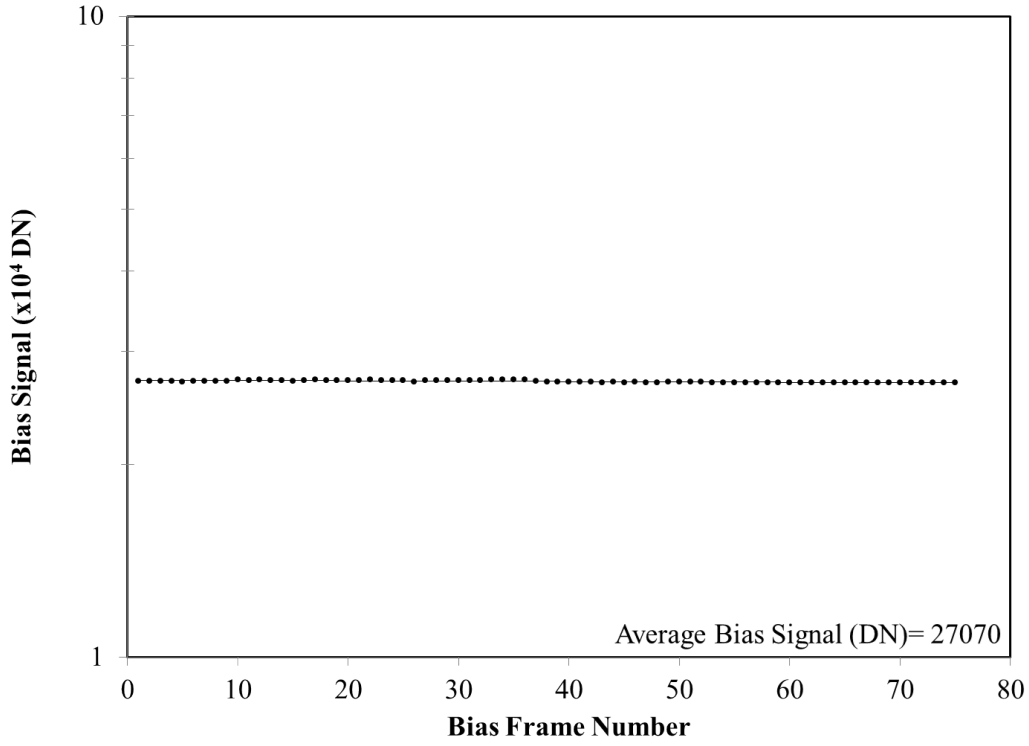

Figure 2.19: Bias signal from the Leach controller and small LBNL CCD. The detector was present negative values to the dual-slope integrator leading to spurious data. The bias was raised to ensure the values presented were positive. Ito fix this problem without adjusting the bias, I should have changed the gain setting within the Leach controller software. However, the device was destroyed by a power spike before further data could be taken.

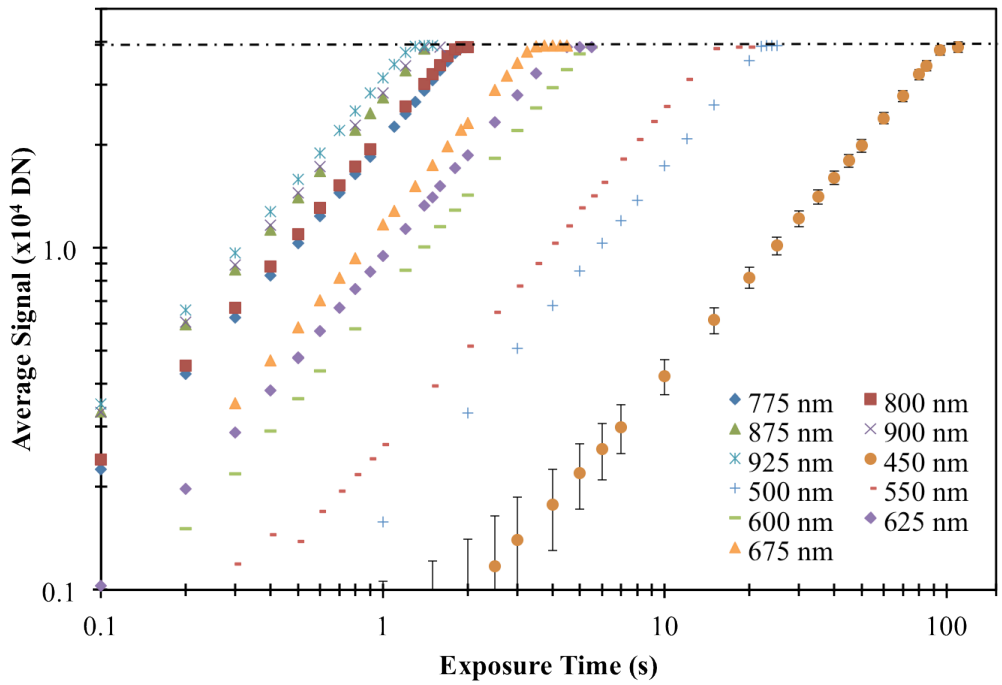

Figure 2.20: This plot shows the average signal as a function of exposure time for flat field illumination of the small LBNL device. The maximum value is 38860 DN. Error bars are 1σ.

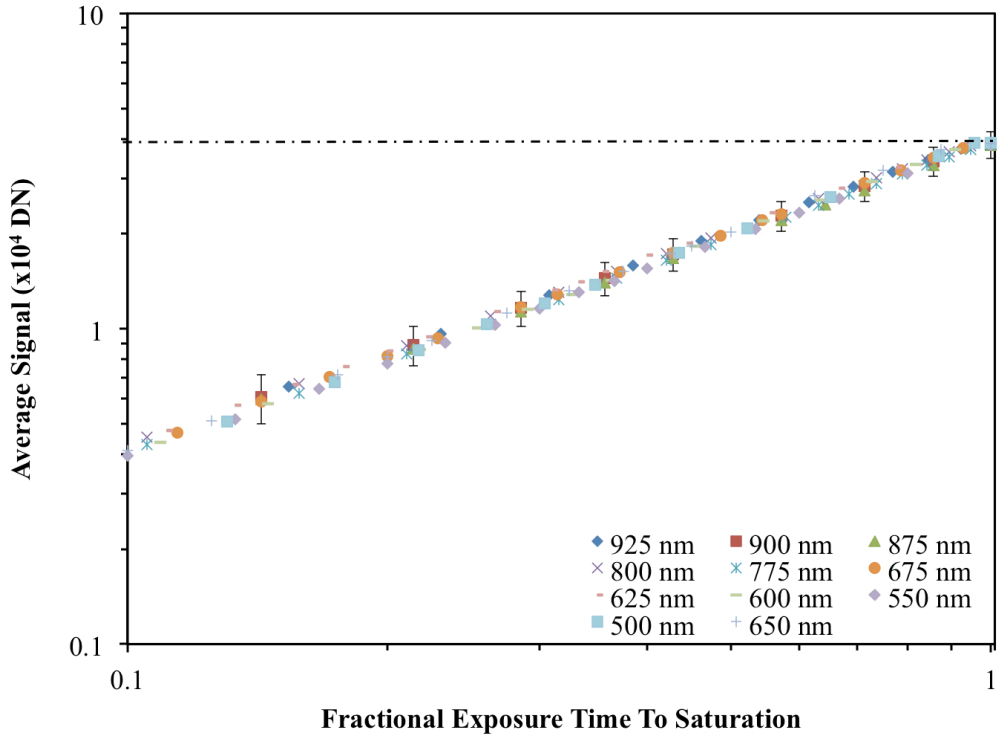

Figure 2.21: This plot shows the average signal as a function of fractional exposure time to saturation for flat field illumination of the small LBNL device. The maximum value is 38860 DN. Error bars are 1σ.

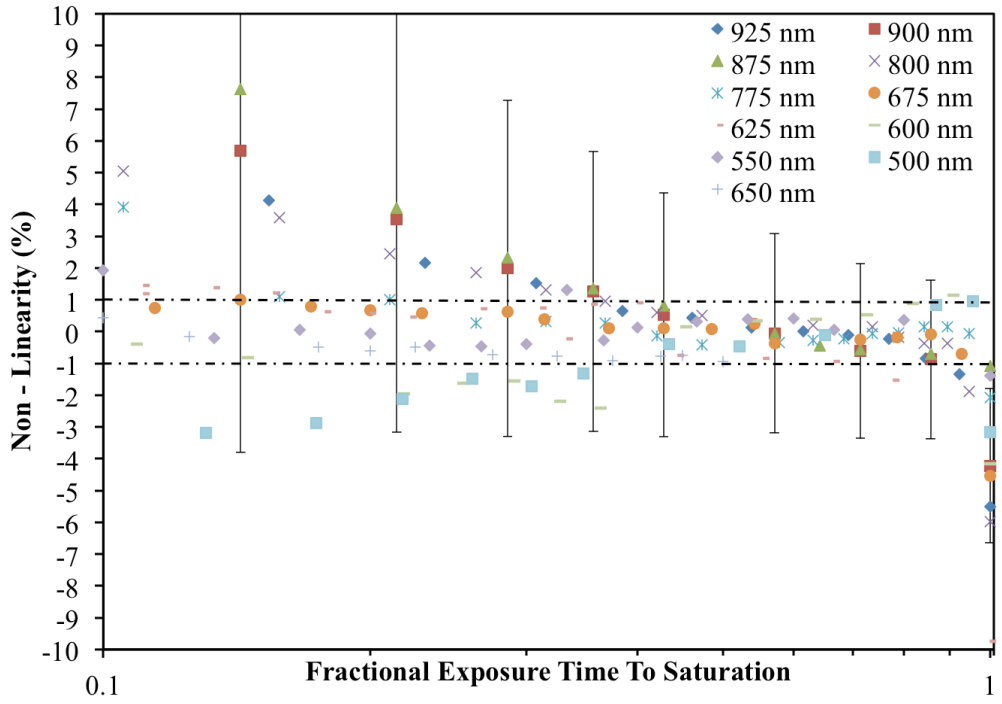

Figure 2.22: This plot shows the percent non-linearity of the LBNL device for fractional exposure time to saturation. The errors have been propagated and correspond roughly to 1σ. The values are as expected with the largest errors at the farthest points of non-linearity. The device is linear for all wavelengths from 50% - 85% of saturation.

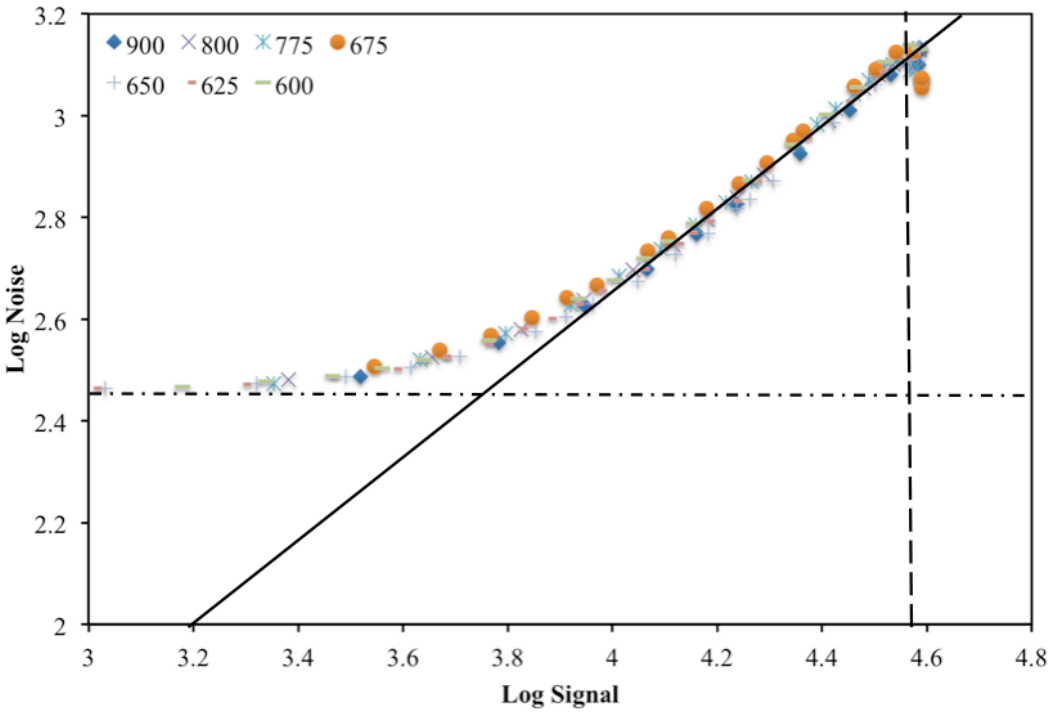

Figure 2.23: Wavelengths presented here correspond to the red end of the spectrum from 600 - 900 nm. The horizontal dot-dashed line corresponds to the read noise regime and has a value of $10^{2.48}$ DN. The vertical dashed line corresponds to full-well saturation and has a value of $10^{4.58}$. The slanted line corresponds to a slope of 0.97 ± 0.02 which is the FPN regime.

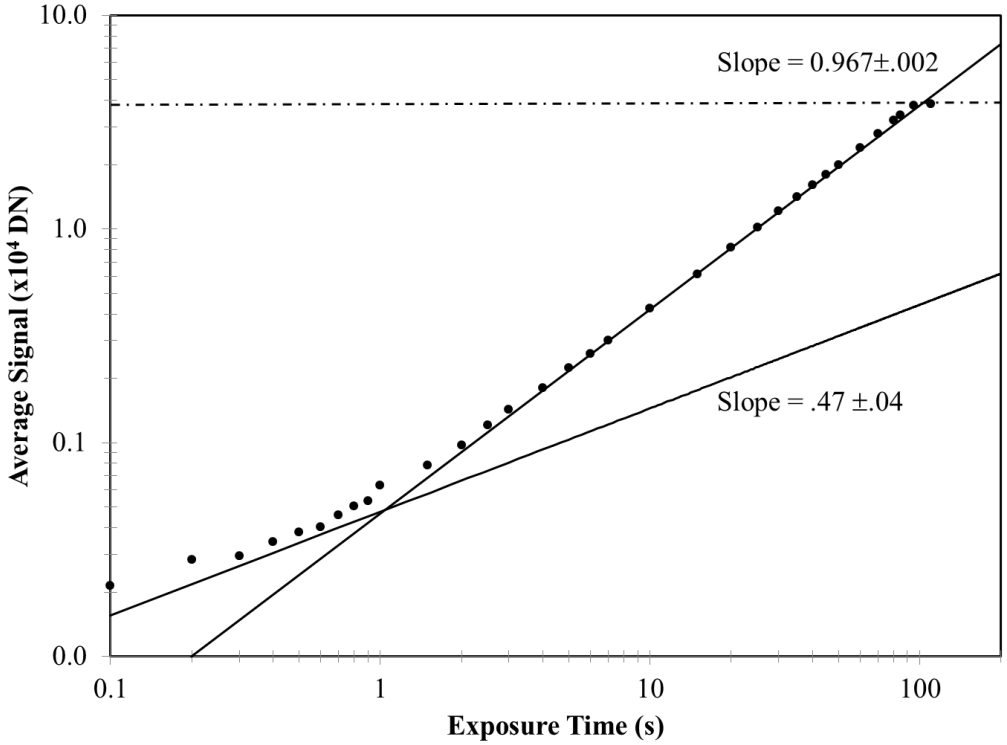

Figure 2.24: This plot shows the average signal as a function of exposure time for 450 nm flat field illumination of the small LBNL device tested in the LASI facility. Notice that this plot is a nearly perfect photon transfer curve. One can see the shot noise regime, the linear regime, and full well saturation.

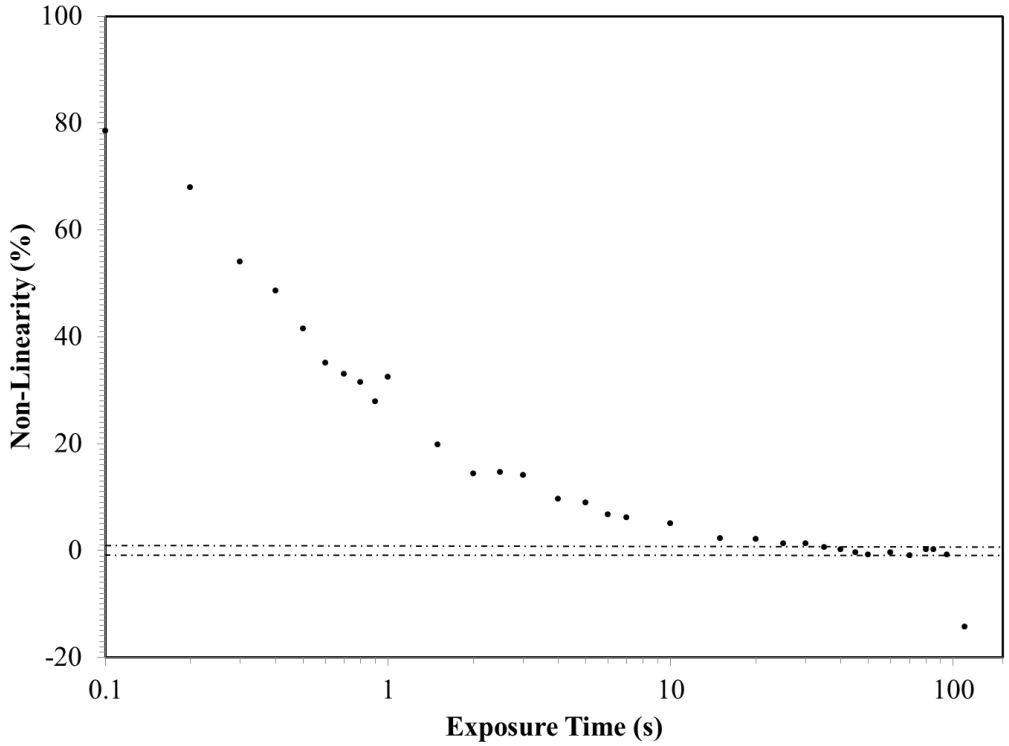

Figure 2.25: This plot shows the percent non-linearity as a function of exposure time for 450 nm flat field illumination of the small LBNL device tested in the LASI facility. The curve is as expected because we were strongly in the non-linear regime for $\sim$55% of the data collected.

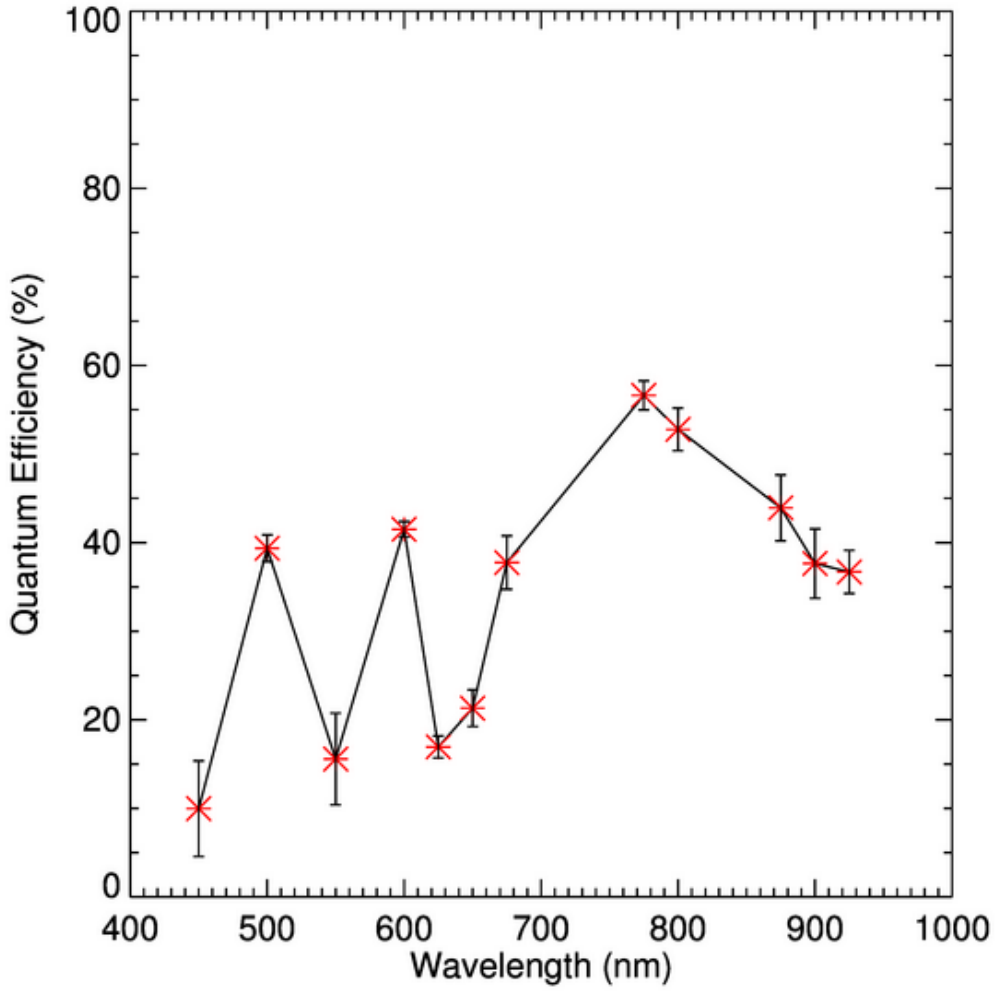

Figure 2.26: Quantum Efficiency of the small LBNL device tested in the LASI facility with the gain varied by lambda. The errors are the 1σ errors corresponding to the deviations in the average gain table.

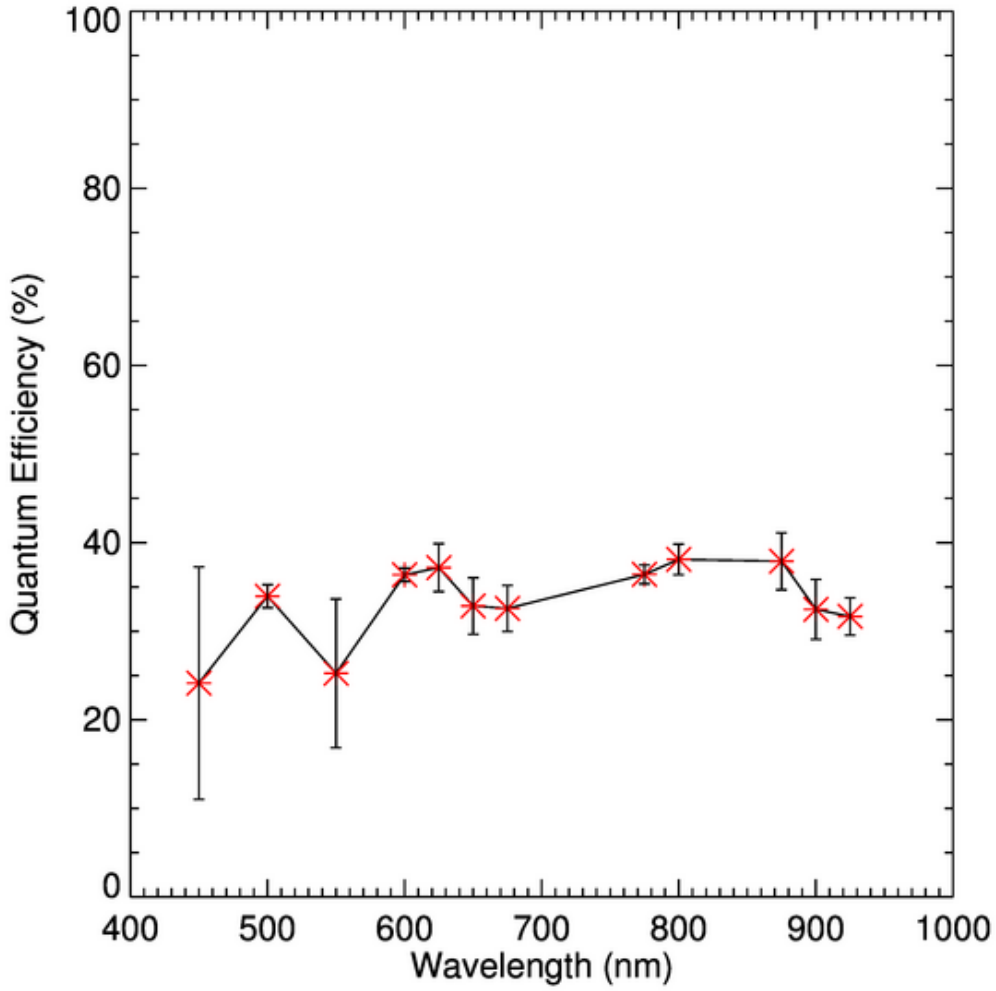

Figure 2.27: Quantum Efficiency of the small LBNL device tested in the LASI facility with a constant gain of 1.10 $\pm$0.14 electrons/DN, which is the average of the variable gain table.

Chapter 3

MODULAR IMAGER CELL

3.1 Motivation

The development of new technologies for astronomical observations hinges on discovering the answer to fundamental questions about the evolution of matter, both baryonic and dark, in the Universe. Several open questions whose answers would provide a change to our fundamental understanding of the universe are:

- What is the effect supernovae have on their surrounding environment?
- Is star formation a triggered process and what is the trigger mechanism?
- What is the formation mechanism for the large-scale structure of the Universe?
- How do planetary systems form and evolve?
- Do observed planetary systems contain the necessary ingredients to support life?

Studies of these research questions would benefit greatly from high angular resolution and large areal coverage. High angular resolution would allow for the observation of distinct ionization stages at the leading edges of shock fronts and possible imaging of protoplanetary disks and systems. Large areal coverage would drastically increase the observing efficiency of large scale survey missions and further allow for enhanced understanding of stellar interactions on a global scale.

Future mission studies will be expecting Hubble-class resolution and extremely wide areal coverage in order to provide the best science return per investment dollar. The only way to combine high resolution imaging with wide areal coverage is to design large FPAs with very small pixel plate scales. The

design and construction of a modular imager cell (MIC) using embedded controllers to ameliorate the power, mass, and cost for the large format CCD focal plane arrays, can provide a robust, low-risk, high-reward solution to mitigate possible mission failures by providing a way to assemble large FPAs using a modular "plug and play" solution. By placing the detector and the associated readout electronics on a single module, one can easily remove and replace any single module without adversely affecting other detectors in the FPA.

In this Chapter, I present a prototype design and results for an MIC for use with a delta-doped LBNL 3.5k $\times$ 3.5k CCD. This prototype design is comprised of the CCD preamplification circuitry and CCD control voltage filtering circuitry and is currently scheduled for flight in an upcoming sub-orbital rocket payload (Chapter 4).

3.2 Technical Background

When CCDs were first introduced in a laboratory setting, they required racks of power supplies and function generators commensurate with the number of clocks, strobes, and bias levels for control (Tom Elliot, private conversation). Subsequent technology moved to dedicated logic systems and control switches (Gunn et al., 1998) on large numbers of printed circuit boards, such as the 207 circuit boards used in the Sloan Digital Sky Survey photometric camera, which uses a mosaic of 30, 2k $\times$ 2k pixel detectors mounted to a single platform for its FPA. Current technology typically involves the clocking and data readout be done using an external controller, such as the Leach or MONSOON controllers (Leach, 1994, 1995; Daly & Buchholz, 2004), which are small form-factor user-programmable DSP based control systems with a high-level user command input and command interpreter that provide the digital timing and analog video signal readout. This final approach is the most robust and cost-effective method currently available.

3.3 Design Overview

The MIC concept for use in large FPAs is relatively straightforward. The MIC accepts high-level user input from an FPA controller (PC) and provides the necessary clocks and strobes with associated level translation to the detector, reads the video data from the detector, converts it to a digital number, and subsequently transmits the data back to the FPA controller. Furthermore, unlike large monolithic arrays, the modular imager cell concept allows one to remove and replace a module without adversely affecting other modules in the FPA, thereby allowing for easier testing and calibration during the design stages and troubleshooting during science operation.

3.4 Driving Requirements

The MIC requirements are to provide:

- Preamplification of the video signal.
- Faithful reproduction and conditioning of the CCD drive clocks.
- Mechanical support for the CCD.

For the purposes of the LASI facility (Chapter 2) and sounding rocket flight (Chapter 4), the MIC has to work in an evacuated environment at ambient temperature. Proximity is a significant issue when dealing with analog signal transmission and is especially significant when dealing with CCD video signals and drive clocks. I therefore chose to place the preamplifier within the MIC as close as physically possible to the CCD in order to provide a lower noise floor to the detector and detector controller, leading to better overall performance.

3.5 Video Amplifier Design

Figure 3.3 shows the design for the non-inverting stage of the MIC and an example CCD picture frame package from JPL. The flight CCD was not installed at the time the picture was taken in order to ensure the MIC was functioning properly before installing the detector, so as to avoid damaging the CCD, which is extremely susceptible to ESD.

The original preamplifier design for this detector is defined in Chapter 2. The design split the single-ended output from the video amplifier on the CCD into a differential output with a non-inverted and inverted video signal that served as inputs to the video board ADC in Leach controller. The design had a potentiometer allowing for adjustable gain at both the non-inverting and inverting stages as well as another potentiometer at the non-inverting stage feedback network allowing the user to adjust the bias in order to trim offset voltage to zero. The design had an adjustable gain from 1 to 10, which was found to be unnecessary during the re-design of the preamplification circuitry (Section 2.8.1).

The original design was modified by ASU and JPL, but followed a similar principle by using a two-stage amplification circuit. The two-stage amplifier splits the single-ended input from the on chip CCD video amplifier into two differential signals for input to the Leach controller; a non-inverted signal (Figure 3.1) and an inverted signal (Figure 3.4). The Leach controller also accepts single-ended inputs and the MIC to has been designed to accommodate both modes of operation. Neither the non-inverting nor inverting amplifier stages have adjustable gain, as had the previous preamplifier model. This design choice was made because after extensive testing of the LBNL CCDs at JPL and in the LASI facility, we found the intrinsic peak-to-peak voltage of the single-ended video signal was large enough

for measurement by the Leach controller video processing circuitry. In fact, in all cases where we used the preamplifier, we needed to attenuate the response from the preamplifier circuit in order to avoid exceeding the ± 5 V acceptable range of the Leach controller ADC input.

If needed, the preamplifier can be reconfigured to have adjustable gain only at the non-inverting input stage, similar to the design in Chapter 2, making the system easier to configure and calibrate in comparison to a system with multiple adjustable gain stages. In a two-stage gain system where both stages were independently adjustable, difficulties would arise in the analysis of the detector readout. On the other hand, a secondary adjustable gain stage would provide more flexibility if it is required.

3.5.1 Non-inverting Amplifier Stage

The non-inverting amplifier stage of the MIC is shown in Figures 3.1 and3.3. A non-inverting amplifier, designed with an operational amplifier (op-amp), has the input signal applied directly to the non-inverting terminal on the op-amp. A portion of the output signal is sent through a feedback resistor, R_f, back to the inverting input of the op amp. This feedback exists to sample the output signal and correct the input signal for variation. According to one of the "golden rules" of op amps, the op amp will do whatever is necessary to to make the voltage difference between the two inputs zero, so V_{in} will be seen at the inverting input (Horowitz & Hill, 1989). This further implies the output signal of the amplifier remains in phase with the input signal. Since the design for the MIC is essentially identical to the design from section 2.8.1, the gain is given as in equation 2.5 with the appropriate substitutions for resistance.

On the positive input to the amplifier, there exists $R_L = 20$k, which serves as the load resistor for the CCD amplifier. The output amplifiers on the LBNL

devices, according to their data sheet, expect to see a 20k load resistance for proper operation. The capacitor and resistor following the load resistor serve to ac-couple the input signal while creating a 3db-frequency of ~ 0.8Hz. By ac-coupling the signal, we create a high-pass filter and remove the -18V DC offset that is output from the amplifier channels (LBNL data sheet) and leave behind the oscillatory signal that contains the ac portion of the pixel data (Figure 3.7).

For the feedback loop, the feedback resistor, R_f, is equal to 1k Ω and the gain resistor, R_g, is equal to 100k Ω giving a gain of $A_V = +1.01$ (see Equation 2.5). which is directly in the center of the ADC range for the typical ± 1 V video waveform. The bias network is used to equilibrate the differential output voltage for all four on chip amplifiers. During single-ended operation, the bias network is used to equilibrate the four amplifier channels to the same potential. Calculations for the bias network follow Equation 2.4.

3.5.2 Inverting Amplifier Stage

The inverting amplifier stage (Figures 3.4 and 3.6) provides half an inverted differential signal to the differential video input on the Leach controller. An inverting amplifier, designed with an operational amplifier (op-amp), has the input signal applied directly through an input resistor, R_{in}, to the inverting terminal on the op-amp. Then a portion of the output signal is fed through a "feedback resistor", R_f, back to the input, at a location between R_{in} and the inverting op-amp input. The use of "negative feedback", so termed because the feedback signal is fed into the inverting input, increases gain stability in the amplifier and improves linearity. Because this is an inverting amplifier, the output signal of the amplifier is 180° out of phase with the input signal and the ideal closed loop voltage gain is given by equation 2.6. The designed output gain of the inverting amplifier is given as, $A_V = -1.00$.

3.6 Signal Conditioning

According to the Supernova Acceleration Probe (SNAP) CCD Imager Technical Manual (Bebek, 2006) the source follower transistor DC voltage rails required for operation necessarily need different capacitive filters. The transistor drain voltage, V_{dd}, requires a 1 μF, 25V capacitor to the P+ guard ring. The output signal, V_{out}, requires a 20 kΩ load resistor to P+ and a 1 μF, 25V capacitor to signal processing, to serve as a DC blocking filter. The substrate depletion voltage, V_{DC}, requires a 100 nF, 100 V capacitor to P+. The P+ guard ring serves as the ground to which all signals are referenced.

During testing at JPL, it was found that the higher speed clock drive signals experienced an unknown capacitive pickup, possibly from the cable lengths, room electromagnetic interference (EMI), or induced capacitance from the Leach controller. We installed RC low pass filters in the JPL test setup on all of the horizontal clocks where R = 100 Ω for all clocks and C = 1000 pF or 330 pF, depending on the clock. The associated cutoff frequencies are 1.6 and 4.8 MHz for the summing wells and horizontal clocks, respectively. As a first iteration, these filters are also installed in the MIC.

For all of the amplifier circuits, we installed 0.1 and 3.3 μF decoupling capacitors across the power planes to filter high and low frequency noise on the power. The capacitors shunt the ac noise to ground in order to prevent the noise from interfering with the rest of the circuit.

3.7 Two-Piece Design

Our MIC design incorporates a two-piece modular system, composed of separate printed circuit boards (PCBs) for the non-inverting and inverting stages of the differential amplifier. Since the Leach controller can be configured to accept either

single-ended or differential video input signals, the two-piece design allows us to independently test each stage for fidelity. Both single-ended input and differential inputs have benefits to the overall camera calibration system. Single-ended inputs are easier to wire, configure, and program in the Leach controller, but suffer from a higher noise floor. Also, single-ended inputs mirror the actual output from the detector video amplifiers and can be directly fed into the Leach controller. The unity gain buffer stage mentioned in section 3.5 serves to balance the single-ended output to the input signal from the CCD video amplifier.

Differential signals, on the other hand, are more accurate because they allow for common mode noise rejection and a lower noise floor. The differential signal is comprised of an inverted signal and a non-inverted signal from the MIC fed into the Leach controller. Differential connections require more wiring and careful handling of the signal chain to ensure the path lengths for both the non-inverted signal and the inverted signal are the same. By maintaining strict control of the path lengths, we can reject noise that is common to both differential transmission lines and the video signal op-amps. The bias network mentioned in section 3.5 serves to balance the non-inverted and inverted signals to each other and not the input signal.

Finally, all of the components comprising both amplifiers would not fit on a single PCB, which forced the development of a two-piece system.

3.8 PCB Layout and Design

The combination surface mount through-hole PCBs were designed using ExpressPCB[1] design software. The schematics were designed using their proprietary PCB layout software. The full schematics are presented in appendix B. Figures 3.1 - 3.6 show the trace layout and partial schematics for the amplifiers.

[1] © 2012, ExpressPCB

The non-inverting board (Figure 3.3) is circular in shape with a section removed from the center to allow the pass through of a CCD cold finger. This is not an ideal design choice, but given the "picture frame" mounting package for the detector, the only way to contact the detector for cooling is from the back-side. The PCB material is lead-free four layer FR-4 board with a split power plane to provide $\pm$15 V for operation of the AD829 amplifiers. "Lead-free" is a manufacturing designation corresponding to the amount of lead content in the solder pads. The boards are manufactured using lead-free processes, which makes them safer, but has the negative side effect of requiring higher solder temperatures, increasing the possibility of damaging sensitive circuit components.

The inverting board (Figure 3.6) is rectangular and much smaller than the non-inverting PCB board. The size and shape of this board was dictated by the pricing scheme set forth by ExpressPCB. If the boards were designed to fit within an exact $2.5''$ by $3.8''$ rectangle, then one could order three for a single price. I designed the inverting stage and found it to fit easily within these dimensional specifications. The inverting board accepts the non-inverted signal from the non-inverting board and processes it through a unity gain buffer. All eight signals are then read from the inverting board and passed to the Leach controller.

Since the clock signals are square waves, we can calculate the the theoretical maximum root mean square (RMS) power dissipated through the resistive components in the circuit. This allows for the choice of appropriately sized resistors. The formula for calculating the RMS power dissipated in a resistive component is given by:

$$< \mathrm{P} >= d * \frac{(\Delta V)^2}{\mathrm{R}} \tag{3.1}$$

$$d \approx \frac{2 * \tau}{T} \tag{3.2}$$

where d, the duty cycle, is the pulse duration divided by the frequency of pulses, ΔV is the change in potential, and R is the resistance. Here we will approximate the duty cycle by τ, which is the RC time-constant through the filters. Given the two types of low-pass filters mentioned in section 3.6, we calculate the maximum power dissipated by the 100 Ω resistors to be 20 mW at 100 kHz. Since the power dissipated is quite small, low power resistors can be used in the design. I chose to use 0.25 W (250 mW) resistors in the filtering circuits because they are physically large enough to manipulate with ease when developing surface mount boards. Smaller resistors are an excellent solution when trying to maximize board space, but they are difficult to handle when assembling the board by hand.

Large 100 μF electrolytic bypass capacitors across the power planes provide filtering of unwanted noise on the power supplies by serving to decouple the ac transients induced within the circuit from the dc power planes. One of the inner planes serves as a ground plane. Both sides of the PCB are populated with components, with the top of the PCB housing the video amplification circuitry and the bottom providing the clock level filtering circuitry. This was done to keep the two signal chains separate, with the input chain on the bottom and the output chain on the top.

Board traces were routed in order to avoid inductance and capacitive pickup. The traces were kept as short as possible and there were no right angles in any of the traces. The traces above and below the board were not run directly in parallel in order to avoid building unintentional capacitance.

This was my first attempt at designing a surface mount PCB so I maintained some of the through-hole components for comfort, familiarity, and robustness. I had an understanding of the through-hole design process and wanted to limit the possible design issues from using too many surface mount components

too soon. Future designs will eliminate all through-hole components to allow for rapid prototyping and assembly.

3.9 Component Selection

Here I will describe the design choices in detail. The components for the MIC were chosen to meet military specification, for use in the sounding rocket flight, to allow the best possible operation of the MIC at flight altitude, and to allow for operation within a vacuum environment, since the MIC is designed to work within the dewar in close proximity to the detector.

3.9.1 Printed Circuit Board

In total, five PCBs were ordered from ExpressPCB: two non-inverting amplifier boards and three inverting amplifier boards. This choice was made because ExpressPCB set certain pricing limits based upon the number and size of boards ordered. The inverting boards were $\sim$\$100 for three, which was the least-expensive option. The non-inverting boards, because of their size and design, were $\sim$\$400 for two boards.

In order to mitigate costs, we chose to use FR-4 circuit board for the MIC PCB. Typically, one would not use FR-4 within a vacuum due to the outgassing of the PCB, which doesn't meet NASA outgassing specifications[2] without proper preparation. In order to meet the two main NASA outgassing criteria: 1) a maximum total mass loss (TML) of 1.0% and 2) maximum collected volatile condensable material (CVCM) of 0.10% (Campbell & Marriott, 1987), we baked the PCB board in a vacuum chamber at $\sim$20% below atmospheric pressure and a temperature of 113° C for 96 hours. We chose a temperature above the boiling point of water but below the melting point of the PCB (140° C) in order to remove the water from the PCB. Ideally, I would have baked the PCB at 99.9999% below

[2] http://outgassing.nasa.gov

atmospheric (10^{-6} Torr) and at 125° C for only 18 hours in order to facilitate full water vapor and hydrocarbon release from the PCB. However, the vacuum chamber to which I had access did not reach the appropriate pressures and temperatures.

The second preparation made to the PCB in order to meet NASA outgassing requirements is to conformal coat the PCB with low outgassing materials. The coating of choice is Arathane 5750[3] which has low outgassing properties at vacuum and serves as an electrical insulator, limiting the possibility of shorts during MIC operation. The coating also serves as good thermal conductor. The conformal coating treatment will be applied before the MIC is launched in Colorado High-Resolution Echelle Stellar Spectrograph (CHESS) (see Chapter 4).

3.9.2 Operational Amplifier

Multiple design choices were not explored here because the AD829 was shown to work at LBNL, JPL, and the LASI facility (see Chapter 2). Changing the design mid-stream would go against Occam's razor and the NASA method of "tried-and-true" engineering. The original through-hole design (see Chapter 2) used 8-pin plastic dual inline package (PDIP) amplifiers. In this design, we chose to use 8-pin small-outline integrated circuit (SOIC) surface mount components in order to conserve space and fit all four non-inverting amplifier channels and their associated electronics on a single PCB board . Using the smaller SOIC design allows for future versions of the MIC to be small enough to fit within the footprint of the detector and still provide the necessary amplification and signal conditioning.

[3]http://www.spolymers.com/

3.9.3 Resistors

The resistors are composed mostly of surface mount components with a small number of through-hole components where surface mount components were unsuitable. The 20 kΩ potentiometers for the bias stages are through-hole components. The resistors are SMT0805 ($0.079'' \times 0.049''$) and SMT1206 ($0.13'' \times 0.063''$) sizes. The feedback resistor is the larger of the sizes while the rest of the resistors are smaller sizes. The choice of surface mount components was essential to the future use of the MIC in large focal plane arrays.

3.9.4 Capacitors

The use of appropriate capacitors is essential to proper operation of the MIC. The amplifier decoupling capacitors and the filter capacitors are tantalum-electrolytic for their high operational temperature range (- 55°C to 125°C), stability, and long lifetime. We explored the possibility of aluminum-electrolytic capacitors but determined the instability and size of the aluminum electrolytic capacitors to be unsuitable for our applications. The decoupling capacitors are through-hole elements with 35 V ratings. The filter capacitors are SMT402 and SMT0805 sizes, also with 35 V ratings, except for the V_{sub} filter capacitor, which has a rating of 100 V. It's important to pay attention to voltage ratings with capacitors because catastrophic failure can occur if the rated voltage is exceeded. Furthermore, the through-hole capacitors used here are polarized, which means they have a preferential direction for current flow. If proper polarization isn't adhered to, the capacitor would likely also suffer catastrophic failure.

3.9.5 Connectors

The initial design had SMA connectors for connecting the video signals from the non-inverting board to the inverting board. SMA connectors were chosen in order

to use coaxial cable as the video transmission cable. Coaxial cable has an inner conductor surrounded by a flexible insulating layer surrounded by a metallic shield, which typically serves as the ground connection. The metallic shield and dielectric serve to keep the external electric and magnetic fields from interfering with transmitted signal. After testing the boards, it was determined that soldering the video signals from the non-inverting board to the inverting board was a more robust solution.

The PCB headers and electrical connectors are Tyco[4] Micro-D 51-pin connectors. These connectors were chosen because of their vacuum compatibility, small size, and number of terminations.

The CCD is held in place by two custom zero-insertion force (ZIF) sockets manufactured by TACTIC Electronics[5]. The design for the ZIF sockets were developed at JPL and for use in the calibration experiments and MIC design. The ZIF sockets are fastened to the MIC by four 0-80 screws and the soldered electrical connections on the PCB. The ZIF sockets allow the installation of the CCD without using any force that may break or bend the detector. The ZIF socket has a lever that, when closed, locks the CCD in place.

3.9.6 Board Assembly

Both PCBs were assembled over the course of a single week in the LASI facility. This was my first effort at assembling surface mount components on a PCB board so very careful attention was paid to the process. Since I purchased three inverting boards, I assembled one of those first to account for mistakes and to learn the process of surface mount assembly. The LASI lab is equipped with a hot-plate that can be used for solder reflow, which is the act of heating the solder to allow it to

[4] www.te.com
[5] www.tacticelectronics.com

flow. When cooled, the solder then forms an electrical and mechanical connection between the component and the PCB board. I followed a typical solder reflow profile by slowly raising the temperature of the hot plate to 500K in 5 minutes, maintaining that temperature for 120 seconds, or until the solder started to flow, which was typically shorter than 120 seconds, and then turning the temperature all the way down and removing the PCB from the hot plate. The solder solidified within a few seconds affixing the surface mount components to the board. After the installation of all the surface mount components, I soldered the through-hole components using a standard soldering iron and lead-free solder.

3.10 Cost

Six boards were manufactured at a cost of approximately $500.00 with the components used for board assembly costing an additional $2000 for a total cost of $2500. This is an extremely low cost design when one considers the typical cost of a single detector which can run upwards of $100,000 depending on the user selected options. For each detector to have an associated MIC, the added cost would only be 2.5% the detector cost, which falls within the “noise” for many space missions.

3.11 Results and Discussion

The MIC as described in this chapter works as it was intended. It provides clock level filtering and differential video signal for input to the Leach controller for readout.

3.11.1 Mechanical Design

This design for the MIC non-inverting CCD support interface board has an outer diameter of $\sim 5''$. This board is to be installed in the flight dewar discussed in Chapter 4, which has an inner diameter slightly less than 5 inches. This meant I

had to grind away the edge of the PCB using a Dremel[6]. I tested the board before and after this manipulation and found no problems. The inverting board had no mechanical issues.

3.11.2 Clock Level Filtering

Figure 3.7 shows the results of the filtering circuitry on a single 83 kHz clock on the MIC. As one can see in the figure, the clock edge transitions are sharper, the clock levels are faithfully reproduced, and the SNR increases from 30 at the input to 35 at the output. The transitions occur approximately 0.01 μs later after passing through the filtering circuit, but all the waveforms experience the same shift, so this is inconsequential to the overall operation of the array.

3.11.3 Amplifier Gain Settings

The non-inverting and inverting stages were designed to have a gain of 1.01 and -1.00, respectively. When the gain was calculated from an 80 kHz square wave serving as a simulation for the video signal (Figures 3.9 and 3.10), the gain at the first stage was found to be $\sim$1.25, not 1.01. This was not surprising as ideal gain of 1.01 was for an unattenuated output signal. In the MIC design, every output channel is equipped with an 300 Ω attenuation resistor, which influences the gain calculation. The gain is now approximately calculated by 1+300 Ω /1000 Ω $\times C$ where C is related to the ideal gain of the amplifier stage. The gain of the inverting stage was identical to the gain of the non-inverting stage.

Figure 3.9 shows a single channel on the MIC. The input "video" signal ranges from $V_{min} = -1.07 \pm 0.07$ V to $V_{max} = 1.17 \pm 0.08$ V. The output amplified differential "video" signal ranges from $V_{min} = -2.86 \pm 0.23$ V to $V_{max} = 2.93 \pm 0.24$ V. The overall gain in this system is 2.57 which falls well within the ADC limits of $\pm$5 V for an input video signal from the LBNL device of

[6]www.dremel.com

$\pm$1.0V max. However, by adjusting the value of the 300Ω attenuation resistor, the gain can be reduced if necessary. All four video channels show the same response. The SNR for the input is $\sim$15.0 while the SNR for the amplified stage is $\sim$12.4.

3.11.4 Bias and Offset

The potentiometer in the non-inverting amplifier circuit sets the bias with respect to two separate quantities, depending on the mode of operation. In single-ended operation, the potentiometer would try to balance the input signal from the CCD and the and output signal to the Leach controller. In differential operation, the potentiometer sets the offset between the non-inverted and inverted signals, with no regard for the input signal. Using the differential mode, I was able to adjust the offset between the non-inverted and inverted signals to be within $\pm$0.025V of each other.

3.11.5 Problems

The physical size of the non-inverting stage is a problem for the sounding rocket dewar design. Since the MIC was designed to be flown inside the sounding rocket dewar mentioned in Chapter 4, the outer diameter of the PCB should have been dictated by the inner diameter of the dewar. However, since the development of the MIC was prior to the development of the sounding rocket dewar, the MIC had to be altered to fit within the dewar dimensions.

Figure 3.6 shows two "oops" wires on the inverting PCB. The original traces had connected the output amplifiers to the voltage rail, which is not ideal for proper operation. To fix this, I simply cut the traces and soldered two wires to the correct locations. Figure 3.5 shows the corrected PCB layout.

3.12 Summary

This chapter presented the design and testing results for a first-generation MIC. I found the MIC to provide an amplification of the video signal of $\sim$2.6 with only a slight decrease in the SNR. Overall, the MIC was a successfully designed, fabricated, and tested as an amplifier and signal conditioner. The design of the MIC has been published in the International Society for Optical Engineering (SPIE) conference proceedings.

3.13 Future Work

In order to bring the full MIC to actuality, the system will need to designed around a DSP based Field Programmable Gate Array (FPGA) control system that incorporates the analog readout electronics and digital control signals into a single module that is spatially located within the detector footprint. A design in which the electronics fit within the detector footprint provides the compactness that will allow the construction of future large FPAs with minimal seams between the detectors. I intend to continue working on this project in the future.

3.13.1 Full MIC Design

To design and build an MIC module and demonstrate readout using embedded control, the following developmental aspects would need to be addressed: electrical interface, mechanical interface, and thermal isolation and design.

The electrical interface consists of a further subset of tasks such as: (1) development of the standalone embedded FPGA platform to provide communication between the detector and a remote host; (2) development of a PCB detector interface card to perform level-translation of clocks and strobes and analog to digital conversion of pixel data for digital input/output (I/O) operation; (3) development of custom flex cables using phosphor bronze conductors; (4) the

development of the host/backplane interface and application to provide high-level control to the MIC and display/store the video signal; and (5) detector selection. The text will focus on interfacing with a CCD as the detector, but the MIC concept allows for CCDs, CMOS devices, or Hybrid type arrays as the imaging element.

The detailed MIC electrical design includes the PCB detector interface card and a FPGA with low voltage differential signal (LVDS) communication, all of which provide the MICs digital control and analog readout. The PCB detector interface card will hold the analog components and include preamplifiers to buffer the output video signals, an analog signal processing chip to perform CDS operations, buffer circuitry for the CCD strobe lines, circuitry for gain adjustment, circuitry to provide pixel bias levels, and finally, circuity to provide analog-to-digital conversion.

The FPGA components include a command interpreter to provide communication from the high-level user interface to the CCD, transceivers for interface to the MIC host controller, control clocking, and CCD pixel readout logic from the ADC. Furthermore, the user will be able to provide device configuration information, such as exposure time and readout mode, as a high-level command, which is subsequently interpreted at the MIC command interpreter and relayed to the device. The FPGA will be highly software configurable, thus making the system more robust and more widely usable for various detector types, such as CCD, CMOS, or even hybrid type arrays.

The electronics will have to be vacuum compatible and thermally stable, a design that necessitates the manufacture of PCBs out of polyimide or Kapton and wiring out of low thermally conductive wire, such as phosphor bronze. The electronics must individually draw little power if they are to be the building blocks

for future NASA space missions. A preliminary baseline design suggests a nominal 0.5 W power draw using modern low power circuitry.

The mechanical interface consists of: (1) the interface between the detector and a rigid mount made of a material providing thermal and mechanical support, such as invar capable of keeping the detector head cold while maintaining the readout electronics at a stable hotter temperature; (2) the interface between the detector and the control PCBs; (3) the interface between the invar mount and the surrounding mosaic; (4) the interface of the PCBs within the MIC to the backplane electronics; and (5) the interface between the MIC and other MICs located within the FPA. Finally, the MIC would have to be suitably packaged for space flight, which entails low mass and volume.

Thermal design considerations include: (1) the isolation of the detector from the hotter co-mounted MIC electronics, using custom flex cables made of phosphor bronze conductors; and (2) the maintenance of an optimal operating temperature, typically a brisk 173 K or lower, to limit noise from the detector that would subsequently degrade performance.

The final design consideration is the development of a host application to control the MICs and read pixel data for storage and display at a user console. This component requires the development of high-level command software for control and implementing low-level protocol for communication with the MIC local controller. The software will be targeted for use on a personal computer (PC).

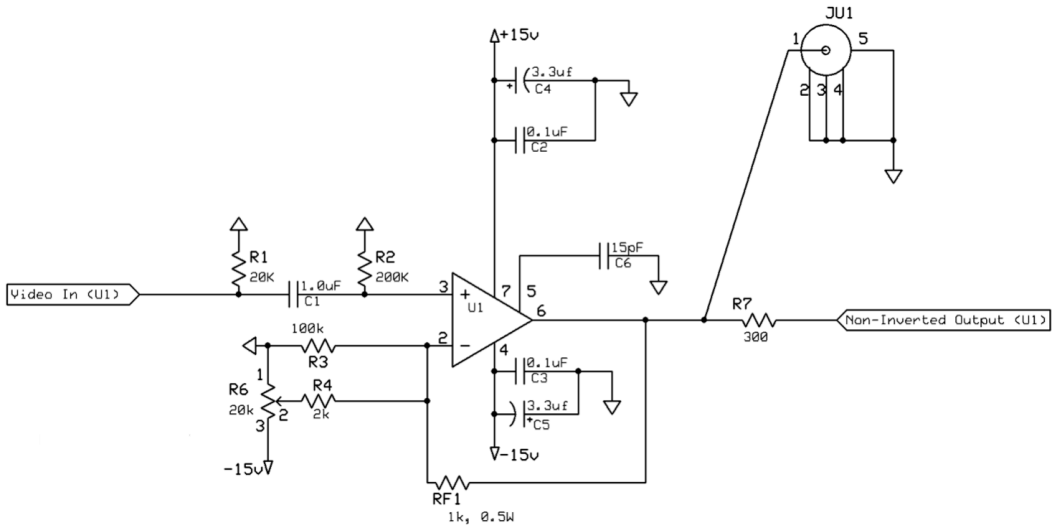

Figure 3.1: Noninverting amplifier design used to drive the video signal from the CCD into the Leach controller. This is only the first stage of a differential amplifier and rests on the PCB closest to the CCD. R1 serves as the load resistance to the video amplifier on the imager. R4 limits the current to R6. R6 allows the user to adjust the offset, or bias level of the amplifier.

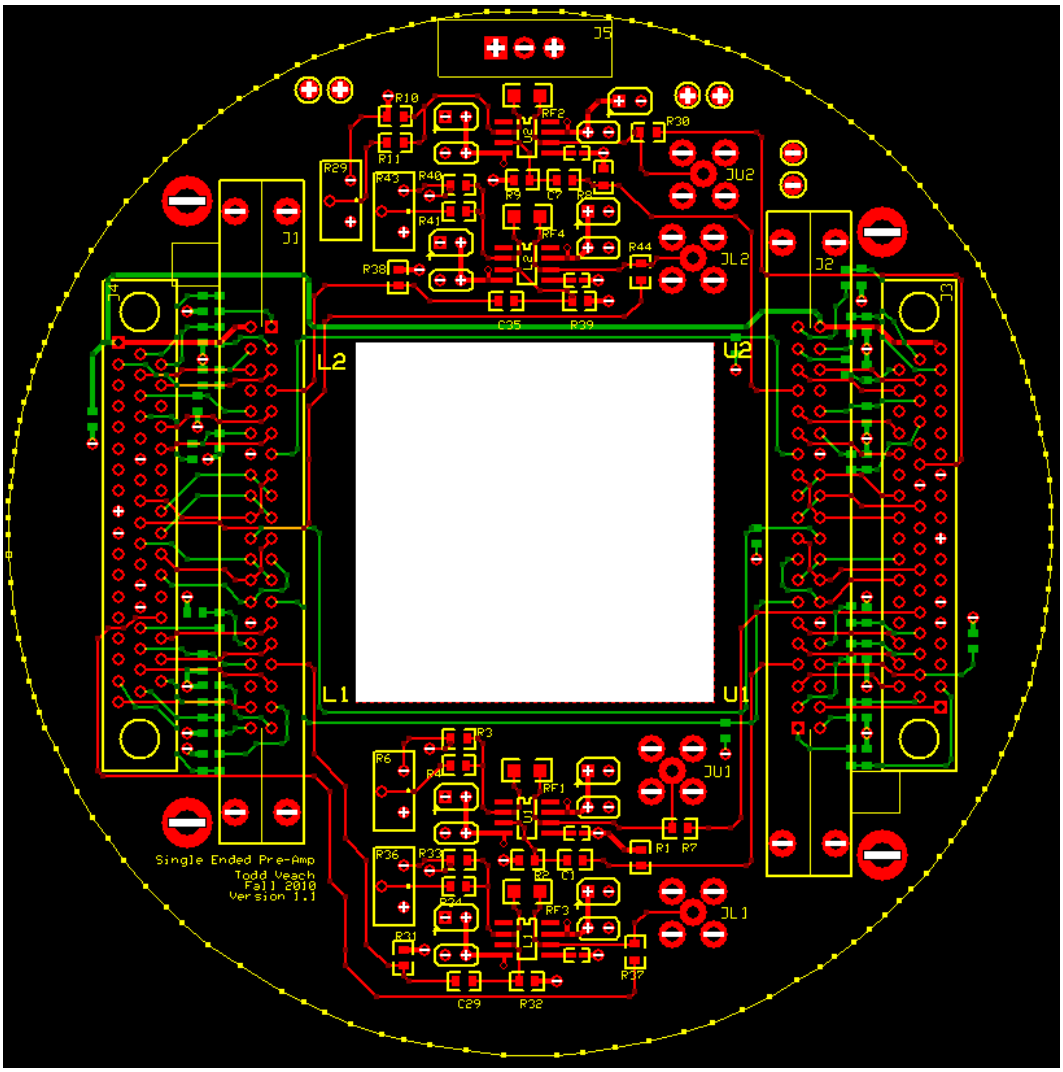

Figure 3.2: Color Layout of the noninverting PCB board. The blank section in the center is for the feedthrough of a cold-finger.

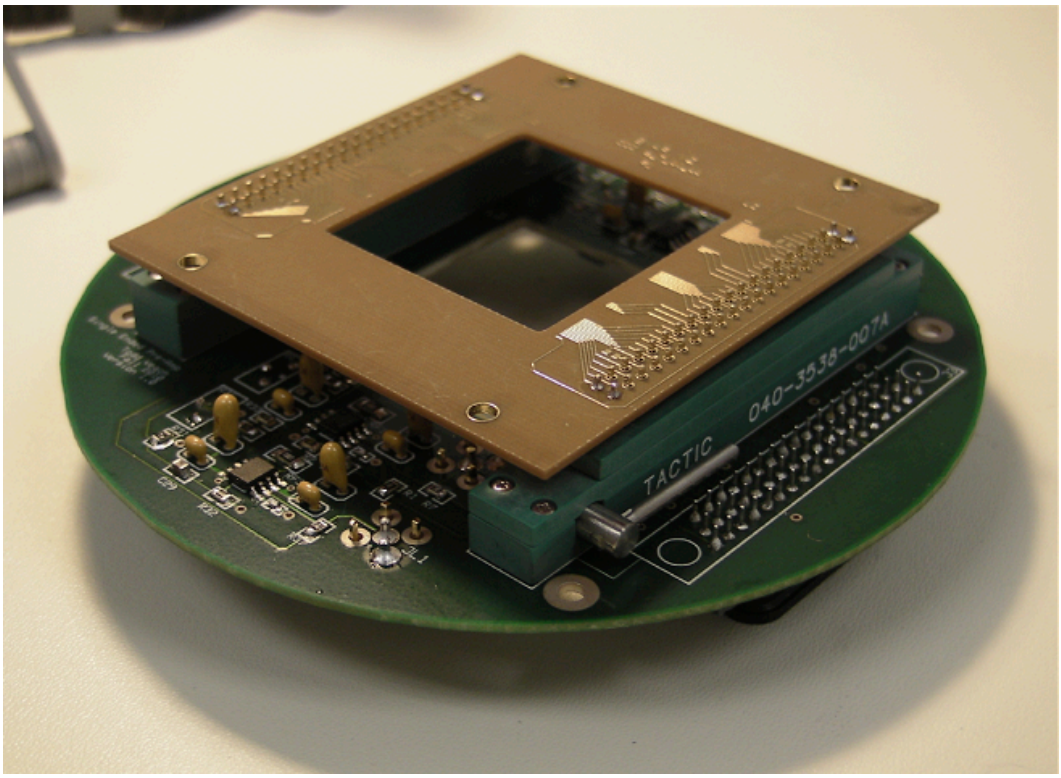

Figure 3.3: First stage of the MIC with a CCD picture frame package for fit. This stage provides inverting video signal amplification and clock level filtering. The detector was developed by Lawrence Berkeley National Laboratory for the Supernova Acceleration Probe.

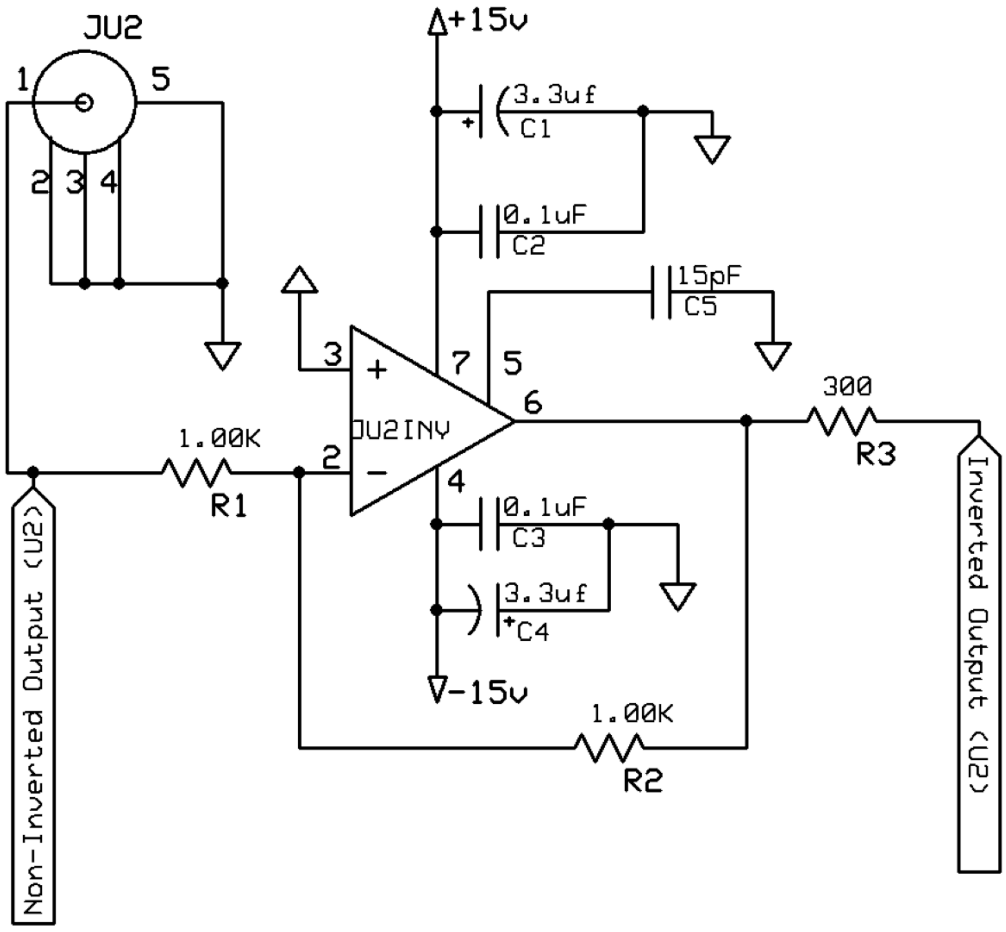

Figure 3.4: Inverting stage of the amplifier design used to drive the video signal from the CCD into the Leach controller. This is the second stage of the differential amplifier and rests on a secondary PCB. The input to this stage is the output from the noninverting stage.

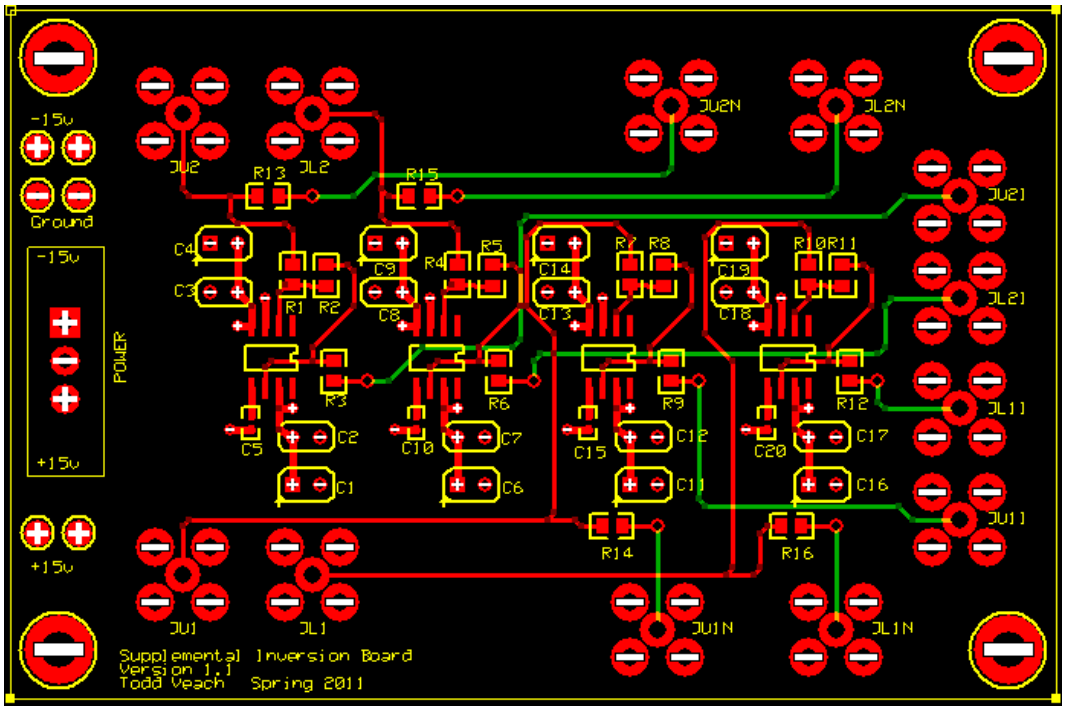

Figure 3.5: Color Layout of the PCB.

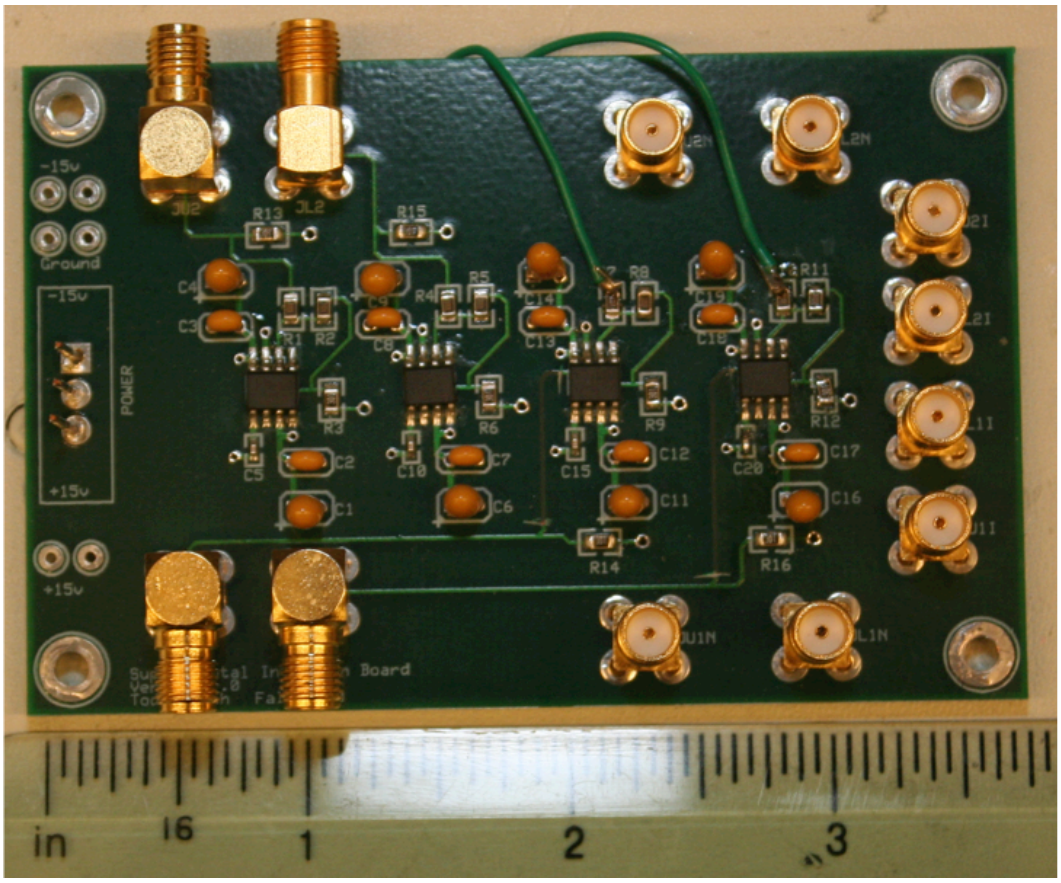

Figure 3.6: This is the inverting PCB board for the MIC. The amplifiers lie along the split in the power plane. Signal input is on the left, output is on the right.

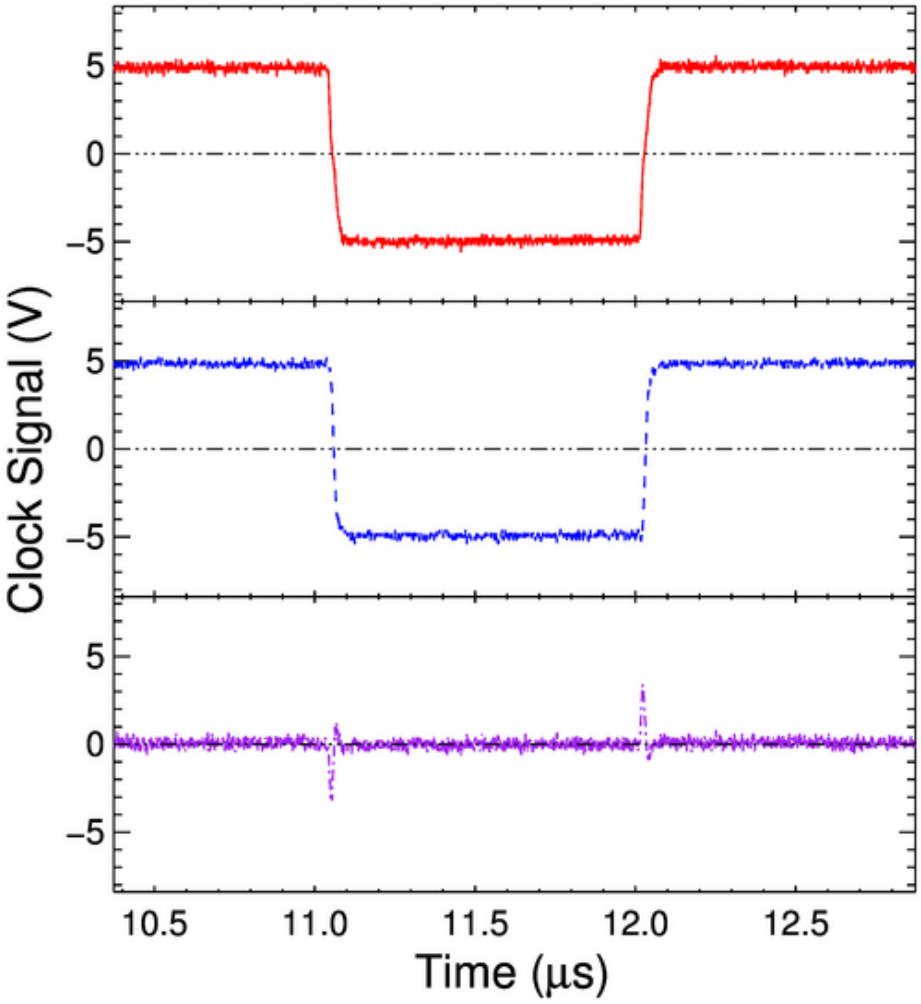

Figure 3.7: Top: Single pulse of an 83 kHz serial clock measured at the SmallCam output. Middle: Serial clock measured at the CCD pin after traversing the MIC filtering circuit. Bottom: Difference. Notice the sharper transition through the MIC. The SNR increases from 30 to 35 through the filtering circuit.

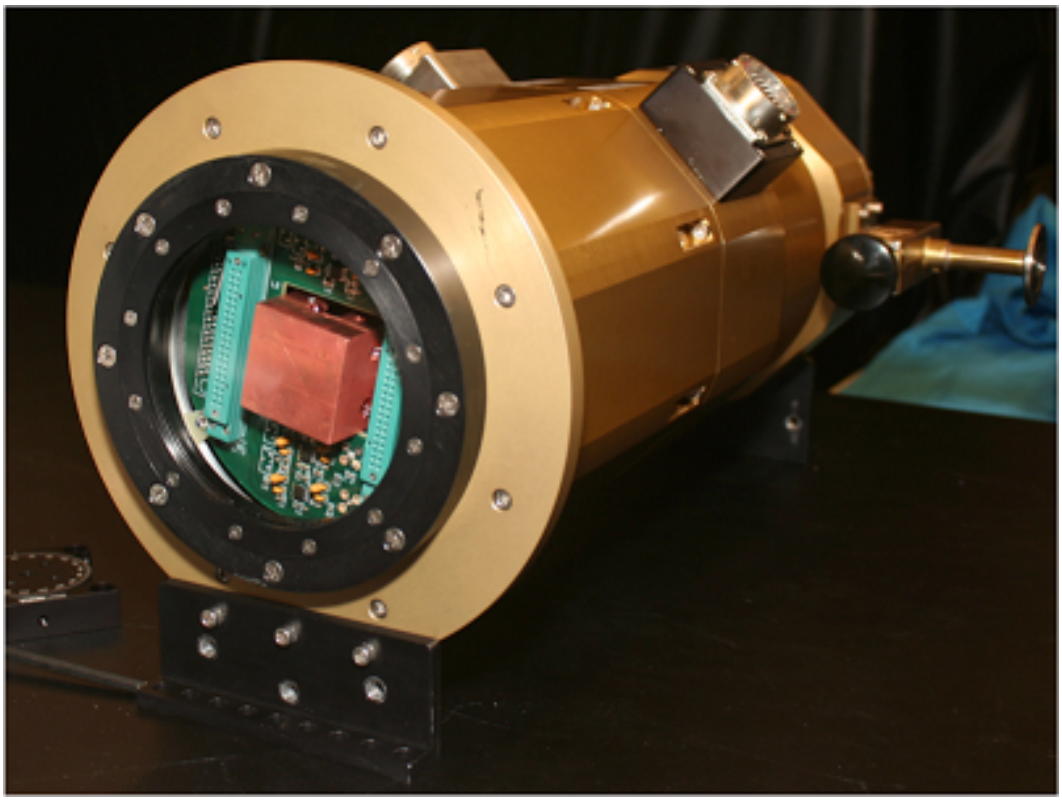

Figure 3.8: Here is an angle view of the MIC inside the cryogenic test dewar for lab calibration and testing. The dewar is the same IRLabs ND-5 dewar referenced in Chapter 2. Modifications have been made to accommodate the increased number of signal wires. This dewar has been configured for testing of the MIC before installation into the flight dewar referenced in Chapter 4.

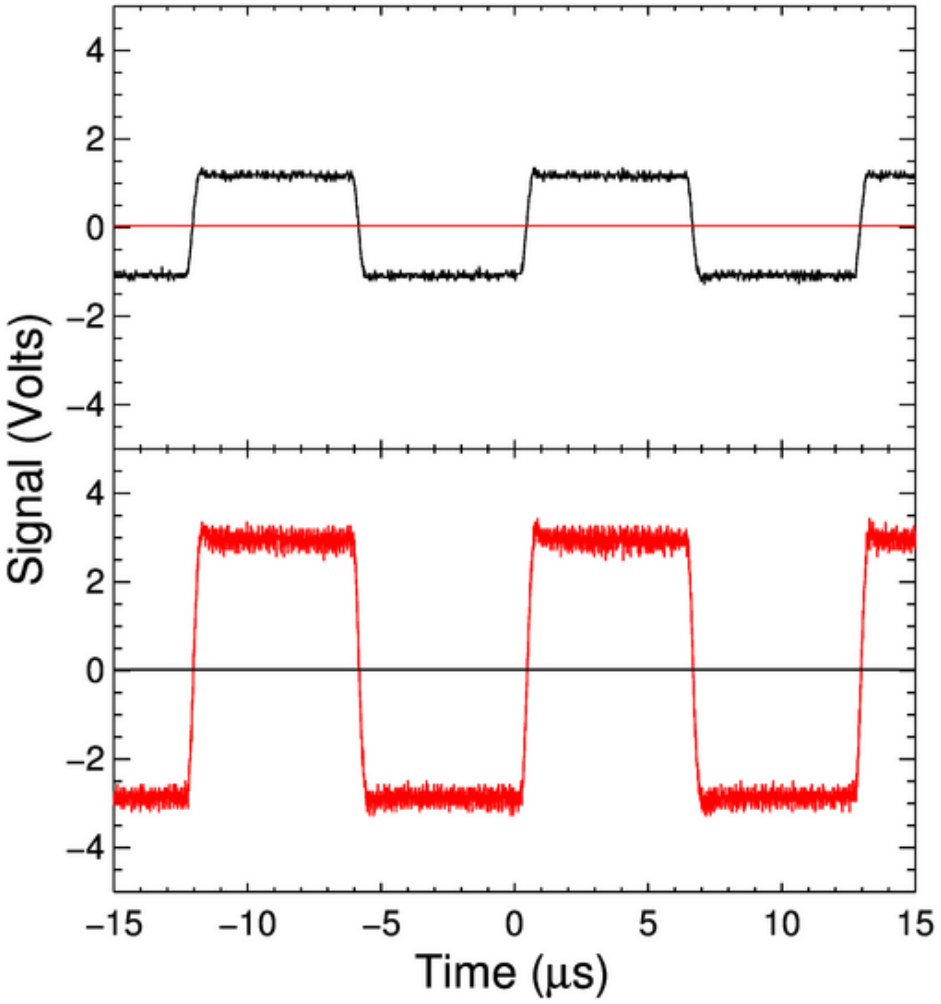

Figure 3.9: The upper square wave is an 80 kHz signal meant to simulate the output from the CCD amplifier into the MIC pre-amplifier circuitry. The bottom signal is the combined differential signal from the MIC that the Leach controller differential video inputs should see.

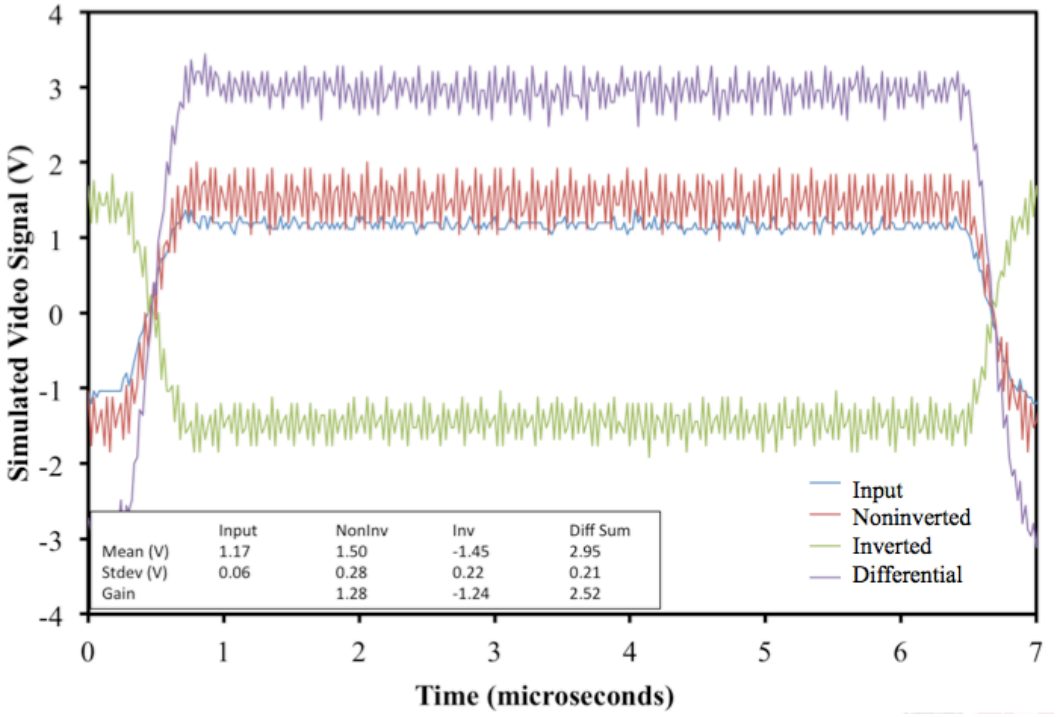

Figure 3.10: Zoomed view of the video amplification provided by the MIC. The input is the blue waveform. The noninverted and inverted waveforms are shown along with the differential signal. The box within the image contains measurement comparisons along the flat portion of the curves.

Chapter 4

COLORADO HIGH-RESOLUTION ÉCHELLE STELLAR SPECTROGRAPH (CHESS) FOCAL PLANE ARRAY DEVELOPMENT

4.1 Introduction

I present the design and system calibration results from the fabrication of a CCD based imaging system designed using a modified modular imager cell (Chapter 3) used in an ultraviolet sounding rocket mission. The design of this low-cost camera around an MIC provides a working test of the delta-doping process on a 3.5k square large format p-channel CCD aboard a sounding rocket, thus increasing the technology readiness level (TRL) level of delta-doping technology, the CCD, and the MIC. At the heart of the imaging system is the MIC, which provides clock level filtering of the CCD control signals and differential video pre-amplification for input to the detector controller. Further, the MIC provides a ground plane in close proximity to the detector, which is another method to attempt the limiting of noise generated by the system.

As shown in figure 4.3, the imaging system appears to be a half-enclosed, self-contained assembly, composed of sub-assemblies that are integral to the imaging system. The functional design of the cryostat is to support the FPA during its 800-second sounding rocket flight. The vacuum housing provides the environment necessary for cryogenic operation of the detector at 155 K. Structural support and thermal control systems, within the vacuum vessel, maintain a suitable operating environment and isolate the detector from external loads.

The majority of the control electronics are located external to the dewar with ultra-high vacuum rated feed-throughs providing the electrical connections. Thermal control is provided via an external controller attached to a non-inverting operational amplifier circuit and a MOSFET switch that provides 50 W of power

to maintain the temperature at 155 K. The heating is balanced via an LN_2 cooling system, which is comprised of a close cycle liquid nitrogen loop and a copper block serving as a thermal mass.

Detailed design parameters for the imaging system subsystems are described below along with the driving requirements and consequent design features. The camera design results in an imaging system that meets the performance requirements to provide detection of the CHESS échellogram from $1100 - 1600$ Å while demonstrating new technologies that will be crucial for future astronomical missions with UV spectroscopic capability and large FPAs. Furthermore, the research completed here also lays the groundwork for future sounding rocket detector systems.

4.2 CHESS Background

CHESS is a rocket-borne far-ultraviolet (FUV) instrument designed to provide R> 150,000 spectroscopy from 100 - 160 nm with photon-limited sensitivity. It will be launched on a Black Brant IX sounding rocket provided by the NASA sounding rocket program.

4.2.1 CHESS Science

CHESS has multiple defined science goals but I will focus on the high-resolution studies of the local interstellar medium (LISM) as it pertains to detailed studies of the atomic-to-molecular transition in the LISM.

According to K. France (2012), CHESS will provide unprecedented measurements of the atomic-to-molecular transition in the LISM. CHESS should be able to sample translucent clouds surrounding protoplanetary disks for H_2 and CO absorption in the ultraviolet. The CHESS bandpass contains the 100 - 160 nm absorption lines of H_2 as well as bands of CO shortward of 151 nm. With the high

resolution from CHESS, it is possible to resolve the rotational structure of CO, which is essential to determining its column density.

4.2.2 Instrument Design

> CHESS is comprised of a mechanical collimator, lithographically ruled échelle grating, holographically ruled cross-disperser, and an FUV detector system. The spectrograph, detector, and supporting electronics are packaged into a standard 17.26″ rocket skin provided by Wallops Flight Facility (WFF). The payload is pumped down to operating pressures of 10^{-5-6} Torr, and the detector system shares a common vacuum with the CHESS spectrograph. The payload vacuum is monitored with a gauge mounted on the electronics bulkhead to ensure that the operating pressure has been reached prior to detector operation. When the WFF shutter door opens during ascent, the payload is passively evacuated quickly. The CHESS field-of view is $\sim 1^{\circ}$, placing a restriction on nearby hot stars. Instrument pointing is monitored during flight by the use of an integrated, aft-looking aspect camera that is mounted to the space frame. (K. France, 2012)

4.2.3 The Échelle Grating

An échelle grating is useful in applications where a high throughput and high angular dispersion are required in a compact package. Échelle gratings are typically used in high diffraction orders with high resolution ($R \approx 10^5$), causing order overlap. In order to combat order overlap, the échelle should be used in conjunction with a cross-dispersing element to separate the orders into a two-dimensional plane. Once the spectrum has been dispersed into a two-dimensional plane, detection lends itself nicely to two-dimensional arrays,

such as CCDs.

According to K. France (2012),

> The CHESS échelle is lithographically ruled, exploiting developments in silicon wafer fabrication pioneered for the semiconductor industry. The lithographically-ruled gratings have low scatter, comparable to holographic gratings. The ability to combine high efficiency and low scatter at FUV wavelengths is a powerful tool for future spectroscopic missions. Unlike standard diffraction gratings, which have grooves blazed at an angle, these grooves are cut into square troughs using a photo-resist method. The light is diffracted, scatter is reduced, and efficiency is increased by the use of corner cube reflection.

Figures 4.1 and 4.2 show the CHESS optical system design and the spot diagram for the échelle. The spot diagram (Figure 4.2) shows the total dispersion of the echellogram to be $\sim 4000 \times 4000$ μm, which will fit comfortably inside the typical CCD. Further discussion of the detailed design of the CHESS instrument can be found in K. France (2012).

4.2.4 Performance Requirements

The overarching performance requirement that concerns the development of the imaging system for the CHESS mission is a detector that is sensitive from $1100 - 1600$ Å. The CHESS instrument also requires a fixed pixel architecture, such as that of the CCD, in order to obtain high SNR spectra. These requirements led to the selection of a delta-doped CCD. The selection of the delta-doped CCD then led to the design requirements for the imaging system. Individual design requirements are listed in their respective sections below.

4.3 Detector Choice

The detector at the heart of the imaging system is a 3.5k $\times$ 3.5k large-format p-channel CCD (see Figure 4.26) that has been specially processed through delta-doping (Chapter 2, Section 1.6.2). This detector was chosen to provide a strong response across the relevant band-pass and a large collection area upon which the échellogram can land. The device has 12 μm pixels, is 300 μm thick, and requires a very high substrate bias voltage (40 - 80 V) in order to fully engage the depletion region. Because the device is thick, it is also highly responsive to long wavelength photons near the Si cutoff at 1.1 μm.

4.4 Environmental Control

As mentioned in Chapter 1, the CCDs are required to be operated at cryogenic temperatures in order to mitigate the dark current. As such, I designed a cryogenic dewar to easily mate with the CHESS sounding rocket payload for flight. During the data acquisition period of the flight, preservation of life for the CCD is essential to the dewar design.

4.4.1 Motivation

The main requirements for the dewar design are ultra-high vacuum (10^{-7} Torr) (UHV) compatibility and compatibility with the overall structure of the sounding rocket. The dewar must fit within the sounding rocket skin. In order to meet the vacuum requirement and minimize the cost, the dewar is designed from stainless steel conflat components which are commercially available off the shelf (COTS). The use of COTS components is typically a reliable method to reduce mission cost while still providing most of the necessary function. A downside of COTS component use is the possible lack of end-user customization, which could lead to a loss of generality and some of the necessary function. During the design phase, it

is essential to determine if COTS components will suffice or if custom fabricated components are required to provide all of the required functionality. The most typical solution combines both COTS and end-user designed custom components.

4.4.2 Ballistic Shock Mitigation

A rocket flight is not a comfortable ride, with axial forces in excess of 10 g's and radial forces in excess of 2 g's possible. Obviously this would cause tremendous stress on any mechanical system which is why mitigation of this shock is vitally important to the health and survival of any instrument. In order to mitigate the shock, the support structure of the dewar is made of aerospace-grade materials, such as aluminum alloys 2024 and 7075, that have been used in similar environments and therefore have strong operational heritage. The threads for all fasteners have Heli-coil inserts to prevent loosening during flight and are torqued to the maximum specification.

4.4.3 Contamination Control

All components are chemically cleaned and gloves are worn at all times during assembly and testing. The entire instrument is baked in a vacuum oven in order to remove contaminants. Assembly within a class-10,000 or better clean room also provides mitigation of contamination from the deposition of atmospheric particles. The clean room specification corresponds to the maximum number of 0.5μm particles per cubic foot.

4.5 Mechanical Design

The rocket camera is designed to be as inexpensive as possible. I used SolidWorks[1] to perform 3D solid modeling of the structure before fabrication. I went through 23 numbered design iterations before the design was finalized.

[1] © 2012 Dassault Systèmes SolidWorks Corp.

4.5.1 Design Overview

The dewar, Figure 4.4, is required to provide an interface to the sounding rocket UHV vacuum system while maintaining a stable platform for the detector and thermal control system. The dewar is comprised of a 6.75″ diameter conflat nipple with 6.75″ diameter conflat ends and is 6.75″ long. The length of the dewar is a coincidence of the design. I wanted the dewar to be long enough to house the structural components of the imaging system, but small enough to fit easily in the sounding rocket. One end is open for mating with the rocket while the other end has the liquid nitrogen feed-throughs for the cooling system. The sealed end conflat also provides a rigid support base for the CCD, MIC, and cooling system. Pave Technologies[2] electrical connectors are welded through the side of the dewar.

The mechanical design was modeled using SolidWorks. All stainless steel conflat components, the LN_2 feed-through, and the half nipples were purchased from Kurt J. Lesker Company[3]. The nipple that makes up the main dewar walls was purchased from MDC Vacuum[4]. I kept the design as simple as possible in order to minimize the cost of fabrication. This dewar for the rocket flight is not suitable for standalone bench testing. I have designed an adapter plate to mate the 6.75″ conflat ends to an ND5 series cryogenic dewar from IR Labs[5] for bench-top testing of the system.

Figure 4.4 and 4.6 show the internals of the dewar. The non-inverting stage of the MIC is held in place by four, 1″ 4-40 threaded female-male standoffs that mate with a aluminum, alloy 7075-T6, mounting stage (Figure 4.10) that rests near the MIC and the CCD. This mounting stage provides an intermediate rigid

[2] www.pavetechnologyco.com
[3] www.lesker.com
[4] www.mdc-vacuum.com
[5] www.irlabs.com

platform and allows for easier assembly of the flight dewar. The standoffs are made of stainless steel and are fastened into the mounting platform via a 4-40 thread at the base. The base is then supported by four, 3.855″ Al 7075-T6 rods tapped 1/4-20 on one end and threaded 8-32 on the other (Figure 4.11). The support rods also have two flats with small through holes in order to provide a surface that can be used for torquing the support rod with a wrench. The holes are large enough to allow a hex key to be inserted, providing an additional method for tightening the support rods.

The MIC is thermally and electrically isolated from the outside world and the cold bath via G10 fiberglass mounting feet (see Figure 4.16 and 4.15. G10 is a rigid fiberglass safe for use in cryogenic and evacuated environments. Figure 4.5 shows the inverting PCB support structure. Figure 4.6 shows the mounting position and method used to ensure rigidity during flight. The inverted stage of the MIC is bolted to the conflat base and the intermediate support stage mentioned above. Six points of contact, four at the base and two at the top, ensure structural rigidity, when combined with the larger support structure.

All fasteners and mounting hardware are vented 18-8 stainless steel nickel-plated socket-head cap screws. All tapped holes are threaded with Heli-coils for maximum rigidity and strength. All the machined parts are shown in Figures 4.10 -4.15.

4.5.2 Structural Integrity Analysis

Using the SolidWorks simulation tools, I modeled the effects on the structural integrity of a 10-g load and a 100-g load in both axial and orthogonal directions to the CCD interfacial surface. Figures 4.7, 4.8, and 4.9 show the resultant displacement of 10-g forces in axial and orthogonal directions to the CCD.

The deformation of the support structure in the axial direction under a 10-g load assuming all components are bonded, which is the ideal case, is ~ 0.34 μm away from the cold finger interface to the CCD. Under a 100-g load, the deformation is ~ 3.4 μm. Deformation simulated orthogonally to the axial component is calculated parallel and perpendicular to the inversion board support structure. The deformation along the perpendicular axis is ~ 6.7 μm. Along the parallel axis the deformation is ~ 4.0 μm. Under the 100-g load, the perpendicular and parallel deformations are ~ 70 μm and ~ 40 μm. All deformations under a 10-g load are smaller than the size of a pixel and will have no effect on the operation of the instrument during flight.

The PCB deformation was also calculated using the SolidWorks simulation tools. The deformation for the PCB is calculated to be ~ 7 μm axially and $\sim 4-10$ μm orthogonally. The thickness of the PCB material is 1.6 mm implying the deformation is $\sim 0.4\%$ of the overall thickness. Such a small deformation will not influence the overall function of the MIC.

From the aforementioned analysis, I determined that the imaging system be mounted along the axial direction of the CHESS instrument in order to minimize the deformation of the PCB and the support structure of the instrument during flight.

4.6 Cryogenic Temperature Control and Design

In order for the CCDs to function optimally, they must be cooled to cryogenic operational temperatures. Cooling the CCDs minimizes the dark current while maintaining full carrier mobility, as long as the temperature remains above the charge carrier "freeze-out" temperature. The CCD chosen for this imaging system is a large-format 3.5k by 3.5k delta-doped LBNL detector whose operational temperature range is from 145 to 175 K, depending on the level of dark current the

observations can tolerate. For extremely bright sources imaged using systems with high throughout, the dark current at 175 K is likely tolerable. For systems where the throughput is low or the background very faint, lower operational temperatures are desired. For operation of the detector for the CHESS mission, the detector is cooled to 155 K (-118 °C), which is found from testing in the LASI facility to be the optimum temperature to minimize the dark current.

4.6.1 Driving Requirements

The main requirements for this subsystem were to provide the appropriate operational temperature for the duration of the science portion of the sounding rocket flight, which is 800-seconds. However, it was requested I not fly any closed cycle cooling systems that required gasses, such as J-T Coolers, G-M coolers, or Stirling coolers, or any LN_2 systems. Since the flight time is short and I was given permission to allow for a pull-away system, I opted for a simple cold bath system, in which a thermal mass is cooled, in this case OFHC Copper, with a closed-cycle liquid nitrogen loop which is warmed throughout the duration of the flight using a heater system, all the while ensuring the operational temperature of the detector is within the operational temperature range listed above.

4.6.2 Design Overview

While the rocket is on the launch pad, using a simple pull-away system, liquid nitrogen is pumped through the LN_2 feed-through in a closed-loop created by welding a stainless steel loop to the ends of the feed-through within the vacuum space. The loop is then clamped between two OFHC copper blocks that serve as a cold bath to provide a stable cooling platform for the detector. The cold bath, which is a large thermal mass of $\sim$5.0 kg, is affixed to the conflat base via thermally isolating G10 supports. A smaller copper block, which is forced into thermal contact with the aluminum nitride backing at the back of the CCD using a

copper support rod, serves as the "cold-head." The aluminum nitride bonded to the CCD provides structural support and a thermally conductive interface to the cooling system. Around the cold-head, there is a G10 fiberglass guide square that limits radial motion while providing thermal isolation from neighboring components. The G10 guide square is mounted to the intermediate rigid mounting stage via four Al7075-T6 supports that are grooved to fit tightly (0.01 cm clearance) around the edges of G10. Finally, the cold-head is thermally strapped to the cold bath using 1/32″ copper strips that are fastened with vented screws and vibration mitigating washers to ensure stable thermal contact as the temperature of the system varies and protect from the high vibration environment associated with the rocket flight.

4.6.3 Thermal Modelling

The modeling of thermal transport was completed using the SolidWorks simulation tools. Analysis was performed to model the conductive and radiative heat transport within the cooling system. Convection was ignored because the cooling system exists in vacuo. In this section, I discuss the thermal analysis performed on the copper block cold bath to ensure it would properly cool the detector. I find that the coold-head in contact with the CCD provides a stable cooling platform for the duration of the sounding rocket flight as long as the cold bath is cooled until launch.

4.6.3.1 Theory

The three possible mechanics of heat transport are convection, conduction, and radiation. Convection is the transfer of heat through the bulk motion of a fluid. Conduction is heat transfer due to the interactions between the atoms and molecules of a material. Thermal radiation is the transfer of heat due to the intrinsic temperature of the material. All bodies emit radiation as long as their

temperature is above absolute zero. Radiation and conduction can both occur in vacuo much more efficiently than convection and as such, were the focus of the simulations.

4.6.3.2 Simulation Parameters

The data generated in Figures 4.19 and 4.20 were obtained by setting the initial temperature of the system to 310 K, which is an approximation for the temperature of the launch site during the summer. The model was allowed to have conductive and radiative heat transfer contributions. The SolidWorks simulation tools model the heat transfer by conduction and radiation using the heat transfer equations:

$$Q_{conduction} = -KA\frac{dT}{dx} \tag{4.1}$$

$$Q_{radiation} = \varepsilon\sigma A(T_s^4 - T_a^4) \tag{4.2}$$

where the radiation equation is just the Stefan-Boltzmann Law modified for a grey-body with emissivity, ε. K is the thermal conductivity (W/m °C), and A is the heat transfer area.

The simulation works by creating a mesh-grid across the solid model. At the intersections of the different mesh cells are the nodes where the heat transfer equations are solved. The mesh size determines the fidelity of the results and duration to convergence for the simulation. In order to balance fidelity with length of simulation, I chose a medium grit mesh with 14394 nodes covering the copper surfaces. This allowed for a solver rate of $\sim$2.5 minutes per simulation increment. The simulations for the cooling and heating of the copper block were run separately with the final output from the cooling solution used as the input to the heating solution. The simulation parameters are shown in Table 4.2.

4.6.3.3 Cooling: Steady State Analysis

Thermal analysis begins with the calculation of the steady state solution. The steady state solution sets up the boundary conditions for transient analysis in the solver. Two cooling scenarios were explored:

1. Cooling the system with the two 25 W heaters in the cold-head at full power.
2. Cooling the system with the two 25 W heaters in the cold-head at half power.

The steady state solution for final temperature at the CCD interface was 142.5 K scenario one and 112 K for scenario two. The second steady state solution is too cold for proper operation of the detector. Subsequent transient analysis used only simulations based on full power for both heaters.

4.6.3.4 Cooling: Transient Analysis

With the steady state solution established, I modeled the transient response of the cooling system in order to determine the length of time until the interface with the CCD was at the CCD operational temperature. Using 10 seconds as the time increment over a duration of 2000 seconds, the simulation took about 8 hours to complete. Figure 4.19 shows the cooling curves of the copper cold-head CCD interface and the cold-bath as a function of time. The top two curves represent the cooling of the cold head at the backside of the CCD. Both heaters are at full power (25 W each) for the entire cooldown period. The green curve is the thermal profile for heaters at half power (12.5 W each). The CCD cold-head interface reaches an equilibrium temperature of 142 K after about 15 minutes using both heaters on full power the entire time. The cold mass, shown in the bottom two curves, reaches an equilibrium temperature of $\sim$80 K. Simulations were also explored for the half-power heating scenario for future reference only.

4.6.3.5 Heating: Transient Analysis

I was not concerned with the steady state solution for heating the copper blocks and concerned myself only with transient analysis. This choice was made because of the short duration of the rocket flight. After completing the transient analysis, this assumption was confirmed to be acceptable because the heating curves did not reach a steady state before the 800-second duration of the rocket flight.

For heating, I explored three different scenarios:

1. Both heaters at full power.
2. Both heaters at half power,
3. Both heaters off.

These are both extreme cases and the middle solution. All other cases will fall between these two extremes. Figure 4.20 shows the heating as a function of time and power to the heaters. In scenario one, with the heaters at full power, the device warms up past 193 K in $\approx$ 800s which is the duration of the flight. In this scenario, the heating rate is $\sim 0.06 K/second$. Over the course of a typical 20 second exposure, which is a reasonable exposure time for a bright source over a wide field of view, the temperature of the array would rise $\sim$1 K. Scenarios two and three allow the detector to get too cold for proper operation and are therefore explored no further.

4.6.3.6 Heating and Cooling Gradients

Figure 4.18 shows the thermal gradients within the cooling system for a single time step during the transient analysis. The figure on the left is the gradient of temperature. It is of note that the colder temperatures are flowing from the fill

tubes to the CCD interface. At the interface between the G10 and copper there is very little thermal flux, further confirming the decisions to use the G10 as a thermally isolating material.

The figure on the right shows the heat flux within the system. The sources of heat are the two heaters and the CCD, which the plot clearly shows. The heat is flowing from the heater and CCD to the cold LN_2 fill tubes. These gradients are the conductive gradients. There is very little heat flowing from the stainless tubes to outside the dewar. As in the previous plot, the G10 standoffs impart very little heat to the system, shown by the inability of the vectors to penetrate between the surfaces.

4.6.3.7 Thermal Contraction

I also felt it necessary to calculate the contraction of the copper block at cryogenic temperature (see Figure 4.21). Linear thermal expansion is given by:

$$\alpha = \frac{\Delta l / l}{\Delta T} \tag{4.3}$$

where α is the thermal coefficient for thermal expansion, which for copper is $10 - 24 \times 10^{-6}/K$ over the range of temperatures involved in this analysis. As the extreme case, I used $24 \times 10^{-6}/K$. I used the simulation tools provided in SolidWorks to calculate the displacement of the copper block at operational temperature. The interface to the CCD was held at 145 K while the large thermal mass was held at 77 K. All surfaces in the model were bonded together, which is an ideal solution, but quickly solvable using the simulation program. SolidWorks performs volumetric analysis, but I was only concerned with the linear component along the CCD axis. After running the simulations, I found the axial displacement at the CCD interface to be ~ 0.6mm directed away from the CCD interface

towards the base of the camera system. The orthogonal displacements were an order of magnitude smaller.

The ~ 0.6mm deflection away from the detector could cause problems with proper operation of the detector. In order to mitigate possible problems associated with this deflection, the copper rod which currently supports the cold finger could be made of Invar or stainless steel, which have lower coefficients of thermal expansion (CTE) when compared to copper. Invar is the material of choice because it has the one of the lowest CTEs when compared to other conductive materials used at cryogenic temperatures. Also, the copper rod will likely need to support a "spring" made of stacked Bellville disc washers that will absorb the vibration from launch and minimize the deflection of the copper cold head from the detector interface as the copper block cools down. By stacking the Bellville washers appropriately and using washers of differing spring constants, it is possible to mitigate the development of any fundamental frequencies leading to resonant oscillatory modes during flight, where the rumble frequencies are less than 200 Hz.

4.7 Electronics

The electronics described below are only those pertaining to the development of the imaging system and communication with the CHESS control computer.

4.7.1 Clock Driver Buffer Board

During the course of analysis, at JPL, of the LBNL CCD selected for use in this imaging system, it was found that the device suffered from saturation along the columns (see Figure 4.27) and periodic horizontal and vertical structure in the image frame. This structure is postulated to have been caused by noise in the clock driver lines from long cable runs or capacitive coupling between clock driver lines. Some of the noise might be from "hot pixels" causing blooming along the columns, but it was impossibly to reliably separate the noise sources. It was

postulated that these unwanted structures could be removed via the addition of an extra clock drive buffer board in the signal chain that could perform the tasks of filtering of the unwanted noise in the clocking waveforms and buffering the signals from the Leach controller before entering the CCD. I describe the board design, the two tasks required of the the board, and subsequent analysis.

4.7.1.1 Board Physical Design

The buffer board is a standard thickness (1.6 mm) four-layer FR-4 PCB designed using the ExpressPCB software. There is a $\pm$15 V split power plane with a full ground plane on the inner two layers while the outer two layers are populated with the board components and signal traces. The physical dimensions of the board are 6.90 $\times$ 3.55 inches. There are six 0.125$''$ holes. Four of the mounting holes correspond exactly to the mounting hole pattern for a PCI/104 card. This design choice was made because this board was designed for future expansion into PC/104 component systems. The board has two right-angle DB-37 pin headers, one female and one male, for I/O. The DB-37 pin headers were chosen to provide an exact match to the output connectors from the Small-Cam. All of the components are surface mount except the 100 μF bypass capacitors, the power supply connector, and the output resistors to the CCD.

The input signal traces all run along the top plane of the PCB. Best effort was made to keep the traces as short as possible to prevent undesired capacitive pickup. In an ideal design, the spacing between the traces would be greater than 3 times the trace width (0.015$''$), to minimize capacitive coupling, but there was not enough space on the PCB to maintain such spacing without increasing the PCB size to unreasonable dimensions. While this is a non-ideal solution, the filter at the input to the buffer circuit should filter the unwanted signals. The output signal traces all run along the underside of the PCB. Again, best effort was made to keep

the traces as short as possible. The spacing between traces is larger to mitigate capacitive coupling and inductance. The wide 0.025″ traces provide a low resistance high-current path for dc-voltage continuity.

There are 18 buffer amplifiers arranged along the split-line between the two halves of the power plane to provide easy access for powering the amplifiers. The 18 buffers correspond to each of the drive signals for the CCD: two sets of parallel (vertical) and serial (horizontal) clocks along with the transfer gate, summing well, and reset gate. Full schematics are given in appendix C.

4.7.1.2 Signal Buffering

A buffer amplifier is an non-inverting unity gain amplifier that serves retransmit the input signal from one circuit to a second circuit without any amplification or phase change. The buffer also serves to decouple the two circuits, meaning the buffer prevents the second circuit from interfering with the first circuit. Since the voltage signal is unchanged, this buffer is also known as a voltage follower, meaning the output voltage follows the input voltage.

The operational amplifier chosen for all of the buffer circuits is the AD826 from analog devices. It is a dual, high-speed voltage-feedback amplifier. The key AD826 performance features are a 350 V/μs slew rate, 50 mA output current per amplifier, the ability to drive unlimited capacitive loads, and operation with a supply voltage of $\pm$15 V, which is the same supply voltage as the MIC (see Chapter 3).

The amplifier maintains a slew rate greater than 320V/μs across a wide operational temperature range, -60° C to + 125° C, making it an excellent choice for the rocket flight. The slew rate determines how fast the amplifier output can respond to changes on the amplifier input as is defined typically with respect to a

sine wave. A sine wave of frequency f (Hz) and an amplitude of A (V) requires a minimum slew rate of $2\pi Af$ V/s (Horowitz & Hill, 1989). As a crude estimation, the horizontal clock speed for the slow readout of the LBNL detector is $\sim$30 kHz with a maximum peak-to-peak voltage of $\sim$10 V, leading to a minimum slew rate of $\sim$10 V/μs. For the fast readout mode of the LBNL detector a slew rate of $\sim$30 V/μs is required. The AD826 offers a minimum 10$\times$ larger slew rate, allowing for faithful reproduction of the input signal for a wide range of clock driver frequencies.

A more faithful analysis comes from Blake (2003) where the slew rate for a square wave is derived. For a square wave, the maximum edge rate of change of a square wave with a rise time, t_r and peak-to-peak voltage of V_{pp} is:

$$max\left(\frac{dV_{OUT}(t)}{t}\right) \approx \frac{0.8V_{pp}}{t_r} \tag{4.4}$$

Rearranging, I find that for 30 ns rise times and a 10 V_{pp}, the minimum slew rate required is 266V/μs, which is still below the minimum slew rate of $\sim$320 V/μs for the AD826 across the entire operational temperature range.

The 50 mA supply current and the ability to drive unlimited capacitive loads are important because the capacitance introduced by the CCD is typically unknown. By allowing for a circuit that will drive any capacitance, one can mitigate possible problems that arise when operating the detector.

4.7.1.3 Clock Level Filtering

Clock level filtering is accomplished via tunable RC low-pass filters placed at the input to the buffer amplifiers. This was done in order allow the adjustment of the transient response of the clock line regardless of the loading from the CCD with the only caveat being that the op-amp have enough current drive to handle the load capacitance. The RC filters are tunable through the use of a potentiometer, whose

value is set based upon the range of frequencies one wishes to eliminate. The final value for resistance should be set through testing of the buffer board within the calibration setup. There also exist jumpers that allow the user to remove the filter from the circuit. Currently, the RC circuits have 330 pF capacitors and 1000 pF capacitors for filtering. The potentiometers are either 1k Ω or 10k Ω depending on the level of filtering required. These component values were chosen from testing at JPL and may not be sufficient values for the Small-Cam. Further analysis is required to determine the best values for R and C to provide filtering for the input to the clock levels.

An option for a resistor is placed at the op-amp outputs in order to eliminate gain peaking for highly capacitive loads (Blake, 2003). Gain peaking can occurs when working with an uncompensated capacitive load. The operational amplifier can be modeled by an LC circuit. If the load capacitance is large enough, the output resistor cannot effectively dampen the LC resonance, causing the gain to peak. The output resistor should be able too be shorted in the case where there is no gain peaking observed.

4.7.1.4 Board Results

The board was found to faithfully reproduce the input signals over a distance of at least 20 m, determined by using two 10 m, 37-pin cables from the Small-Cam to the buffer board (Figures 4.30 and 4.31).

4.7.1.5 Design Changes and Future Work

Before the buffer board is ready for use, the capactive loading from the CCD and CCD controller should be determined through laboratory analysis. From there, the values for the input RC filter should be set. These values will change based on the laboratory setup. I would also recommend the design change of putting a jumper

around the output resistors, allowing the user to effectively remove them from the output circuit.

For future work, I would recommend developing a buffer board with a programmable RC circuit using a programmable resistor and a capacitance latter and multiplexer with an inter-integrated circuit (I^2C) or serial peripheral interface (SPI) for communication. An (I^2C) or SPI converter would then be used to plumb the board into a USB port of a personal computer for control.

4.7.2 Temperature Process Control

The thermal control system uses an auto-tuning PID controller, a power op-amp controlled heater circuit that uses a MOSFET switch, a cold bath, and a cold-head in order to maintain the operational temperature (Figure 4.16). The cold bath and cold-head lie within the ultra high vacuum while the PID controller and heater control circuit lie external to the UHV.

The temperature controller is a CNi32, 1/32 DIN controller from Omega Engineering Inc[6]. The controller takes as input the temperature from a type-T thermocouple, which is suitable for measurement from 73 to 600 K. A thermocouple consists of two-alloys joined together at one end and open at the other. Changes in the temperature at the joined end induces an emf between the other ends. As the temperature increases, the output from the emf increase, though not necessarily linearly. The induced emf from the thermocouple is -6 - 20 mV over the full operating range. The emf is then converted to a range from 0 - 10 V inside the temperature controller and reprocessed as an analog output voltage.

The analog output is fed into a non-inverting amplifier with a gain of +2. After passing though the first amplifier, the signal is passed buffer amplifier

[6]www.omega.com

designed to activate a MOSFET switch that allows current (up to 1 A) to flow through the 25 W heaters that is proportional to the input analog voltage (see Figure 4.22). Using this heater control circuit, the temperature of the CCD is controllable to within $\pm$ 2° of 155 K. Figure 4.24 shows the PCB board with the non-inverting amplifier circuit and MOSFET. The connecting wires are on the underside of the board.

Located on the same board as the heater control circuit is a power switching circuit that operates via a TTL input or manual actuation of the switch. The power switching circuit uses a Darlington pair with a high gain in order to switch the control circuit using a digital control signal from the controlling computer. The purpose of the Darlington pair is to amplify weak signals. I over engineered this circuit to ensure the power switching would work correctly for extremely weak signals and allow for complete switching of the relay.

I also developed a power supply to provide the $\pm$15 V for the MIC. The power module is a Recom RS3-2415D. It supplies 100 mA per output and has remote on/off for TTL control. The switching frequency is 200 kHz so I designed an output filter across the power supplies in order to remove the switching frequency. I also designed the remote on/off switch based upon the data sheet (Recom, 2010).

4.7.3 Command and Control System

The command and control system is designed to interface the Small-Cam with the instrument control computer (ICC) and the ICC with the flight computer.

4.7.3.1 Design Overview

In order provide detector array control, we used a Leach (Leach, 1995) controller, specifically the Small-Cam, which is a smaller PC104/e version. It provides the

exact same functionality as its larger brethren, but in a nice compact package, perfect for fitting into the fuselage of a sounding rocket. The Leach controller also requires an interface card and we chose the PCIe/104 express interface card. We could also run the Small-Cam with a standard PCExpress or PCI card, but that would typically require flying a large desktop computer, which is obviously untenable. The control computer, on the other hand, is a small PCIe/104 from RTD Embedded Technologies, Inc.[7]. This computer has heritage on multiple rocket missions and provides the functionality needed to command the Leach controller and communicate with CHESS control system.

4.7.3.2 Driving Requirements

The main requirements for the control system were compactness and robustness for use on the sounding rocket. The PCIe/104 interface and small form factor meets both requirements. The control computer also had to accommodate a PCIe/104 Leach controller interface card and the RTD computer does provide such an interface. Furthermore, the control computer must run either Windows or Linux, with CentOS[8] being the preferred operating system for the Small-Cam. Ultimately, the Small-Cam detector controller set the majority of the requirements for the control computer. The interface of the ICC to the flight computer must also be robust.

4.7.3.3 Small-Cam

The next generation Leach controller (see Section 2.8.2) is the Small-Cam controller, Figure 4.25. This compact system is identical to the larger system, only physically smaller. The Small-Cam is designed to be universal, allowing the operation of various CCD and IR arrays by changing the Motorola DSP code used

[7] www.rtd.com/
[8] www.centos.org

to program the controller. The controller provides the appropriate level translations based upon a user specified DSP program and will read the video output from 4 output amplifiers on the CCD. The Small-Cam provides three-phase CCD control, has a high-speed fiber optic communication link, and works off a 12 V dc power supply requiring 30 W of power. The system is compact allowing for simple integration into a sounding rocket fuselage.

4.7.3.4 RTD

The flight control computer is an Intel[9] Core 2 Duo 1.2 GHZ computer designed by RTD Embedded Technologies, Inc. The important specifications are listed in Table 4.1. The computer was chosen to provide enough computing power and have sufficient RAM for on-the-fly data reduction and enough storage space for data storage until after the rocket is recovered. The storage disks are necessarily solid state for robustness on a sounding rocket flight and for use in low gravity. Spinning disks have been known to fail on sounding rocket flights. The control system also has watchdog circuitry for monitoring its health, analog I/O, and digital I/O for further system monitoring or control. Communication can either be through serial port or Ethernet, with Ethernet being preferred. The wide DC power supply is also essential for use on a sounding rocket, as the BUS power provided by the batteries on rocket is 28 V.

4.7.3.5 Wiring

All of the camera connections are made using 26-gauge Tefzel insulated wire. The video signals are transmitted on twisted pair wire and the control signals are transmitted on shielded twisted pair wire in order to limit capacitive pickup from the cables. The PCB headers and electrical connectors are Tyco[10] Micro-D 51-pin

[9] www.intel.com
[10] www.te.com

connectors. These connectors were chosen because of their vacuum compatibility, small size, and number of terminations. Further, the connections are locking, ensuring a rigid connection that will survive a sounding rocket launch and subsequent flight. The connectors to the external environment are Pave Technologies 55-pin connectors mounted on 2.75″ diameter conflat flanges mounted to half nipples that are welded through the sides of the dewar at a 90° angle. The Pave connectors were chosen for their Neoprene vacuum seal providing pressure isolation in high vibration environments, such as a sounding rocket flight.

4.8 Software

The software for control of the Small-Cam by the ICC is written to access the API directly from C++ or Python. The native graphical interface program, Owl3, which is a Java based program, is not used for flight, but is used for preflight lab calibration.

The command sequencing during flight for the instrument control computer (ICC) begins with the initialization of the RTD heartbeat, or watchdog circuit, then initialization of the detector control software, then the detector, then the exposure control sequencing. The exposure control sequencing is designed as 3 or 4 predefined routines offering different exposure times and exposure numbers. The selection of the control sequence is determined through analysis of several postage stamps taken at the beginning of flight. The postage stamps are then communicated to the flight computer for ground truth. Based on the results, the user is allowed to select one of the predefined exposure control sequences.

4.9 Interface Control

The ICC computer interfaces with the Small-Cam via a fiber optic communication link, that provides 12.5 Mpixel/second data transfer rate. The ICC computer will

interface to the CHESS control electronics via Ethernet, USB, or serial port. Ultimately, this system is designed to be stand-alone and will only communicate with the CHESS control electronics to transfer data, as a backup, or to be issued simple pre-defined exposure sequencing commands. The flight computer will only communicate with the ICC through a TTL signal in order tell the the ICC to power on, to register the health of the ICC, to communicate the pre-defined exposure control sequences to the ICC, and to pull the data files from the ICC for telemeter to the ground station.

4.10 Discussion

The detector was preliminarily tested at JPL and was found to be linearly responsive to 550 nm illumination but with significant streaking and banding (Figure 4.27). Streaking and banding is not desirable, especially for spectroscopic studies, where the streaking and banding can be coincide with emission or absorption features. However, it is postulated that the streaking and banding can be mitigated with changes to the CCD drive clocks and their associated voltage levels.

This new camera system is essential to providing the necessary test of the LBNL delta-doped detectors in a relevant operational environment in hopes of raising the technology readiness level. The possible selection of these detectors to comprise large focal plane arrays in future space missions is greatly enhanced by raising the TRL of the detectors and the delta-doping process. NASA is a risk-averse institution that typically requires technology demonstration in a relevant environment before the technology can be used for long-duration space missions. A sounding rocket platform provides the necessary qualifying environment.

4.11 Summary

I have developed an imaging system for a sounding rocket based upon a modular imager cell and a next generation delta-doped detector. The design is modular and can be adapted for other detectors on future sounding rocket flights, with only minor modifications to the PCB layout. The design is low-cost, not including the detector, which makes the design an excellent starting point for future imaging systems. The design is also robust and provides the necessary thermal, mechanical, and electrical support for ensuring the proper operation of the large format delta-doped detector, the MIC, and for survival of the detector throughout the data acquisition phase. This imaging system is ideal for capturing the echellogram from the CHESS payload across the entire interested bandpass. This work has been published in the International Society for Optical Engineering (SPIE) conference proceedings, which are peer-reviewed. I will also receive authorship on future scientific and technical publications related to the CHESS rocket using this imaging system.

4.12 Future Work

Assembly, Integration, and Testing (AI&T) is still required in order to reach the the launch pad.

Assembly involves preparing the dewar for flight readiness. The parts have already been machined and are ready for assembly (Figures 4.10 - 4.15). The components must be chemically cleaned and thermally sanitized prior to assembly in order to limit hydrocarbon contamination. The dewar cannot be operated as a stand-alone instrument and must be integrated with a vacuum system for evacuation.

After dewar assembly, it will be mated to the focal plane of the CHESS instrument. The CHESS instrument will provide the evacuation required to operate the detectors. Mating with CHESS should be a smooth process as the entire assembly has already been mated using 3D-modeling software.

After assembly, the dewar and its control systems must be integrated into the CHESS instrument. Integration involves the synthesis of the separate instrument systems into a single operational unit. The following steps are involved:

- The power systems for the rocket camera must be integrated into the CHESS flight system.
- The ICC must be interfaced with Small-Cam the flight computer.
- Data from the detector needs to be available on both the ICC and flight computers.
- The thermal control system for the dewar must be integrated into the CHESS instrument configuration.
- Interface controls must be developed for the ICC and Small-Cam and flight computer.
- Testing protocols must be developed in order to avoid damaging the detector.

After successful integration, the CHESS instrument will be tested according to protocols developed during the integration phase. The detector and MIC will be tested for operation at cryogenic temperatures and evacuated pressures while mated with the CHESS instrument. The detector will be calibrated from $1100 - 1600$ Å according to protocols developed in Chapter 2. The calibration will not only determine the flight viability of the detector but will also provide valuable

calibration products from a wavelength regime inaccessible to the LASI facility. By using this calibration information along with calibration information obtained in the LASI facility, quantum efficiency can be calculated from 1100 - 11000Å providing an unparalleled calibration data set for an LBNL delta-doped device.

Table 4.1: IDAN Parameters

CPU	IDAN-CMA22MVD1200HR-2048
Form Factor	PCI/104-Express
Operating System	CentOS 5.5
Storage	4GB + 32GB SSD
Specifications	14aDIO, 8aAIO, 15.8 W, 4 Serial, 8 USB, 2GB SDRAM, Gig. E
Operating Temperature	-40 to +85°C
Supply Voltage	8∼36 Volts DC

Table 4.2: SolidWorks heat transfer simulation parameters. Columns 1 and 2 correspond to cooling of the system. Columns 3, 4, and 5 correspond to the system warming.

Simulation Number	1	2	1	2	3
Fill Temperature (K)	77	77	0	0	0
Initial Temperature (K)	310	310	142.5	142.5	142.5
Heater Power (W)	25, 25	12.5, 12.5	25, 25	12.5, 12.5	0,0
CCD Power (W)	1	1	1	1	1
Radiative Emissivity	0.05	0.05	0.05	0.05	0.05
Convection (W/m^2K)	0.1	0.1	0.0	0.0	0.0
Nodes	14394	14394	14394	14394	14394
Time (s)	2000	2000	1200	1200	2000
Increment (s)	10	200	60	60	10
Type	Cool	Cool	Warm	Warm	Warm

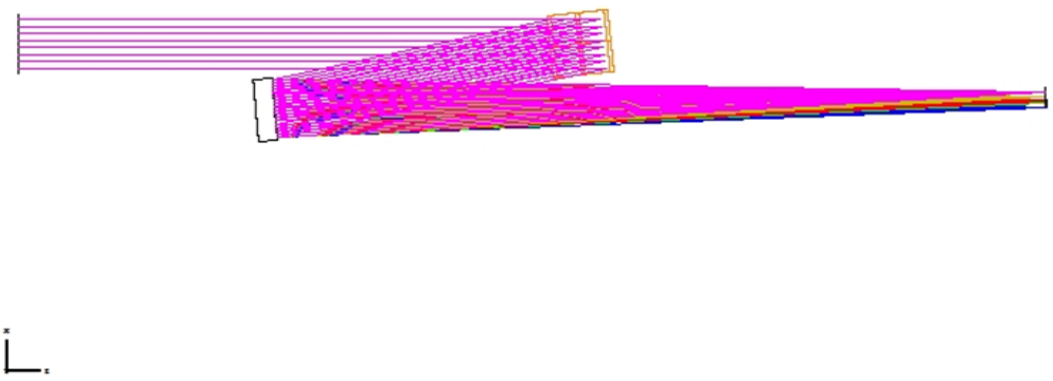

Figure 4.1: Shown is the ray trace of the CHESS optical system. The colors correspond to the échelleogram. Light enters from the left side of the image, interact with the échelle and cross-disperser, which transforms the input into a 2D-spectrum which is imaged by the LBNL detector at the focal plane. Image credit: Dr. Matthew Beasley from the University of Colorado Boulder.

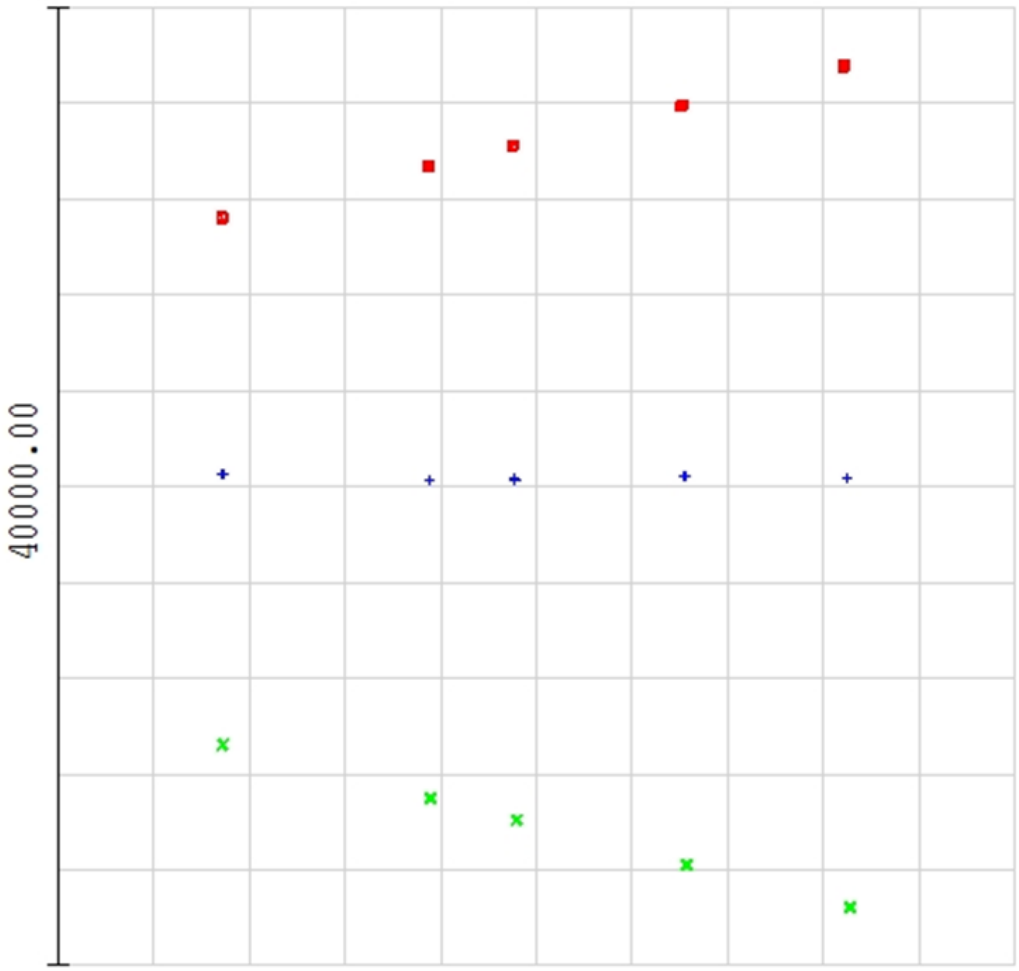

Figure 4.2: CHESS échelleogram at the focal plane. Units are in μm. Image credit: Dr. Matthew Beasley from the University of Colorado Boulder.

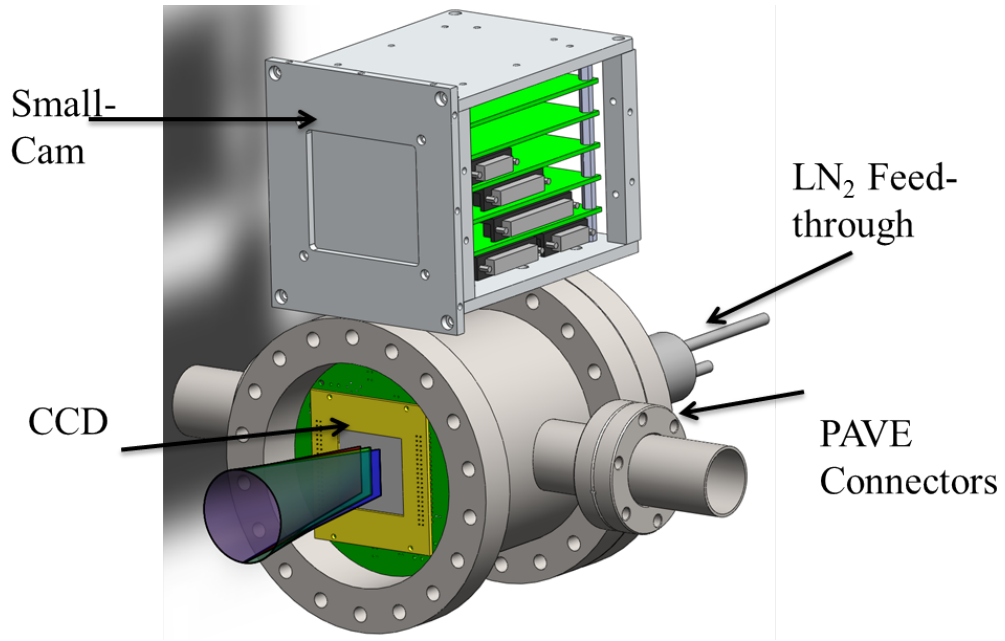

Figure 4.3: Overall imaging system design. Light comes in at the front of the camera, electrical connections are through the sides, and the cryogenics are at the rear.

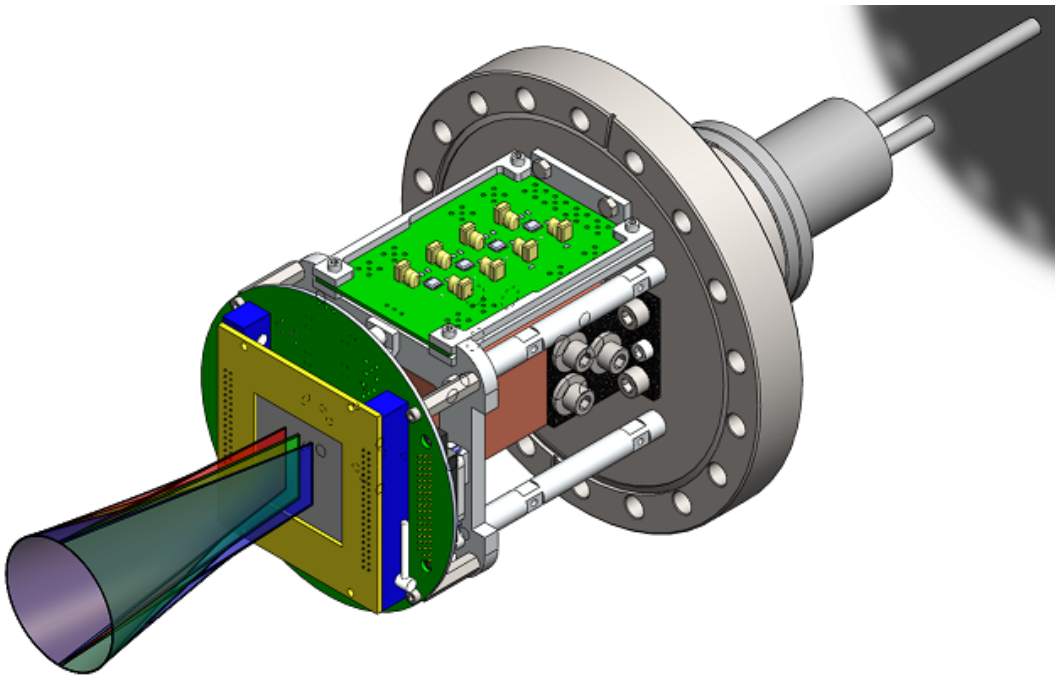

Figure 4.4: Shown are the dewar internals. The LN_2 fill tubes protrude from the back and allow for the closed-loop cycling of LN_2 in order to cool a $\sim$5.0 kg OFHC copper cold bath that is attached to a copper cold-head that provides the thermal interface to the CCD.

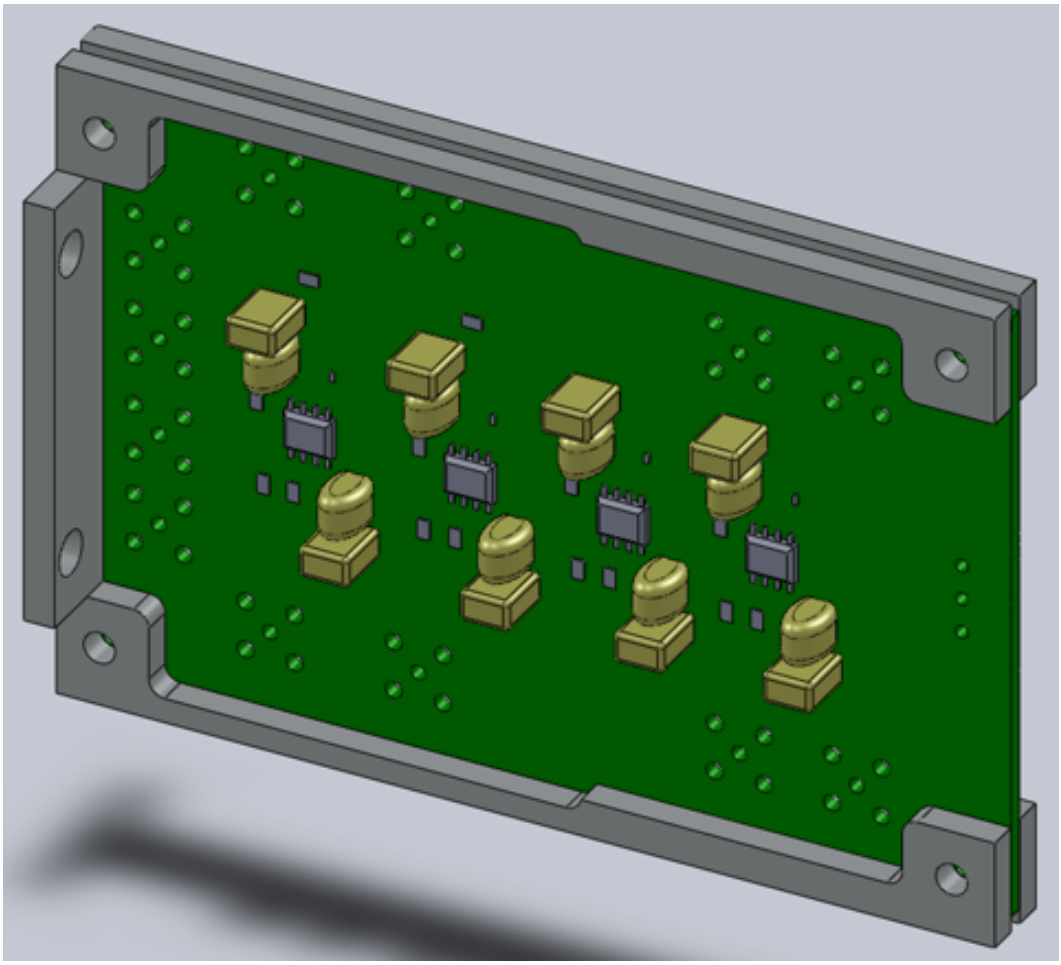

Figure 4.5: MIC inversion board with rigid Al7075-T6 support clamp to prevent motion during flight. The support for the inverting board also serves to support the overall structure of the dewar structure.

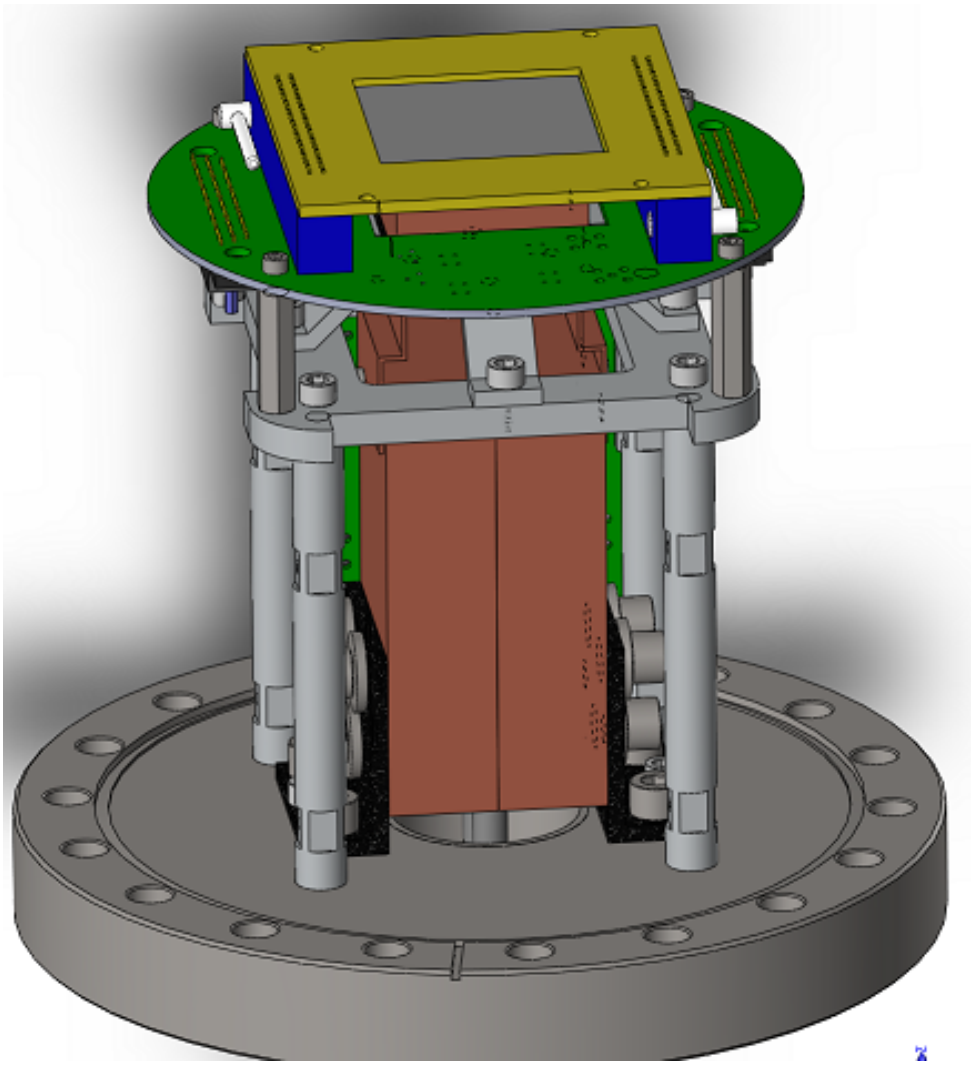

Figure 4.6: The noninverting board of the MIC is supported by Al7075-T6 support rods that are mounted to a conflat stage. The intermediate support stage is made of Al7075-T6. The ZIF sockets are shown as the blue components. The Tyco micro-d connectors are on the underside of the noninverting MIC board. The fasteners have been supressed for clarity.

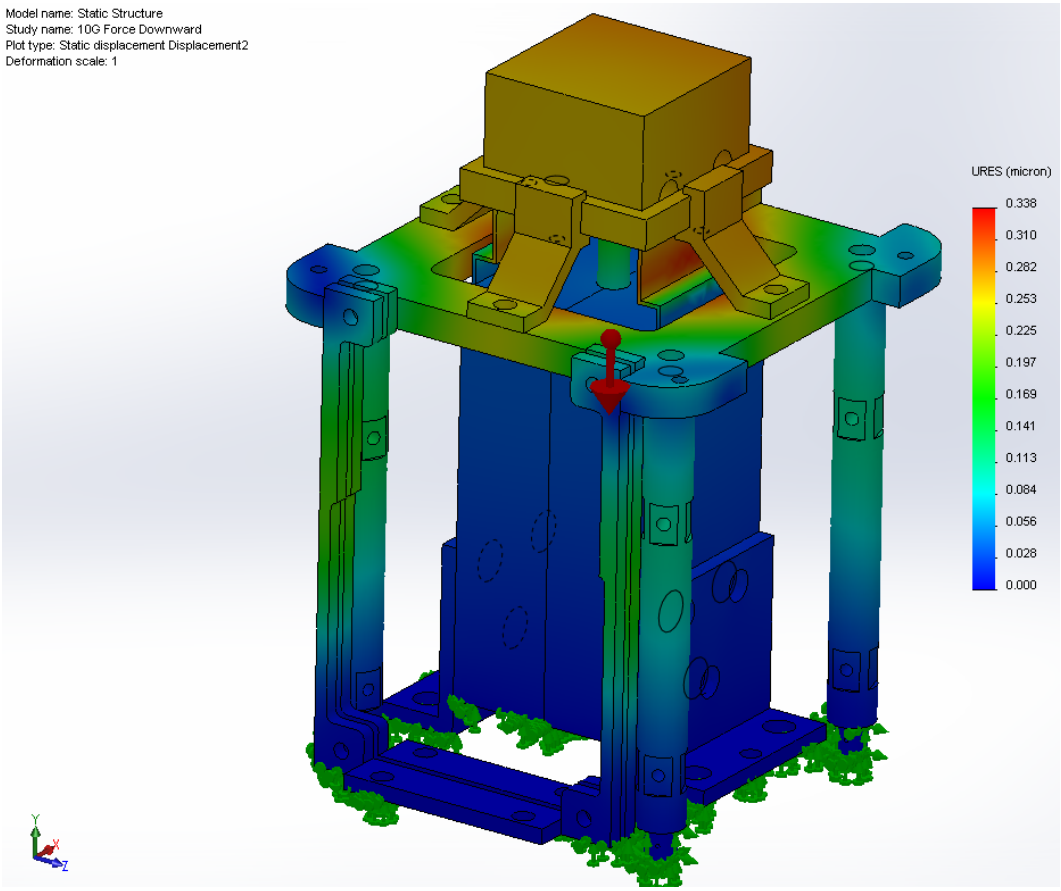

Figure 4.7: Simulated deformation of the CCD support structure to a 10-g axial load. The maximum vertical displacement is less than .4 μm, which is 30 times smaller than a pixel in the detector.

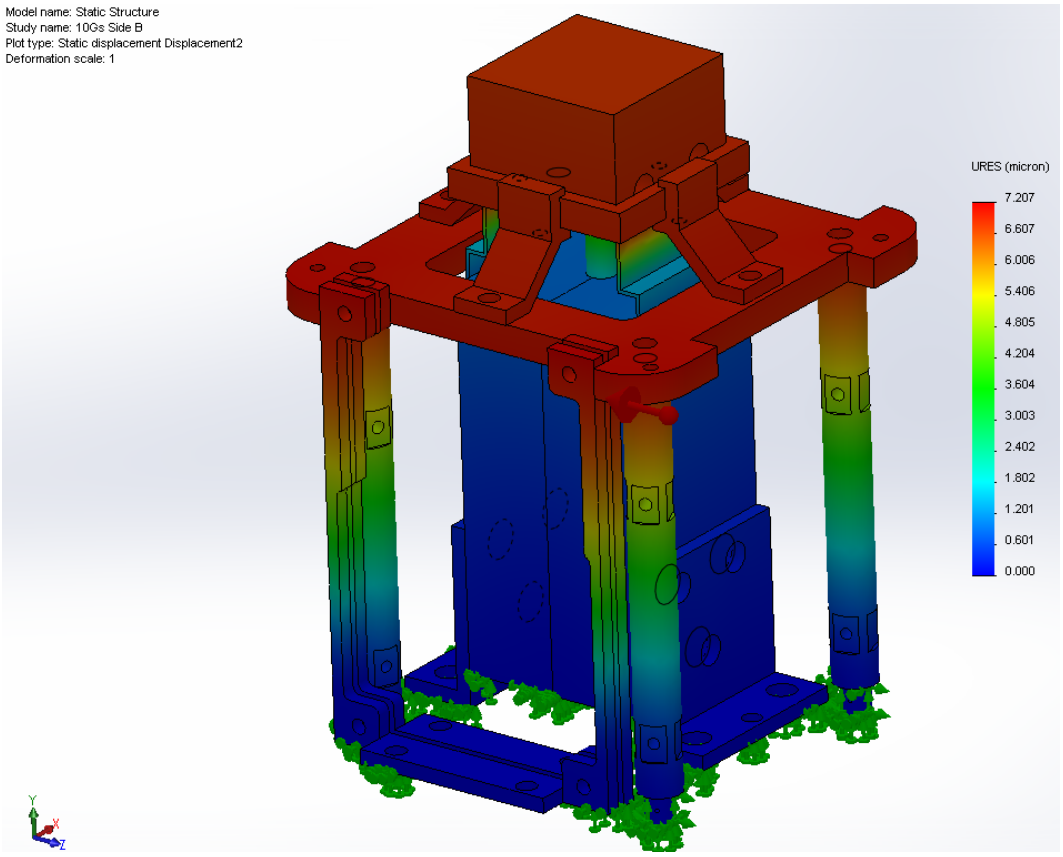

Figure 4.8: Simulated deformation of the CCD support structure to a 10-g orthogonal load perpendicular to the inverting board support structure. The maximum displacement in the orthogonal plane is approximately 7 μm

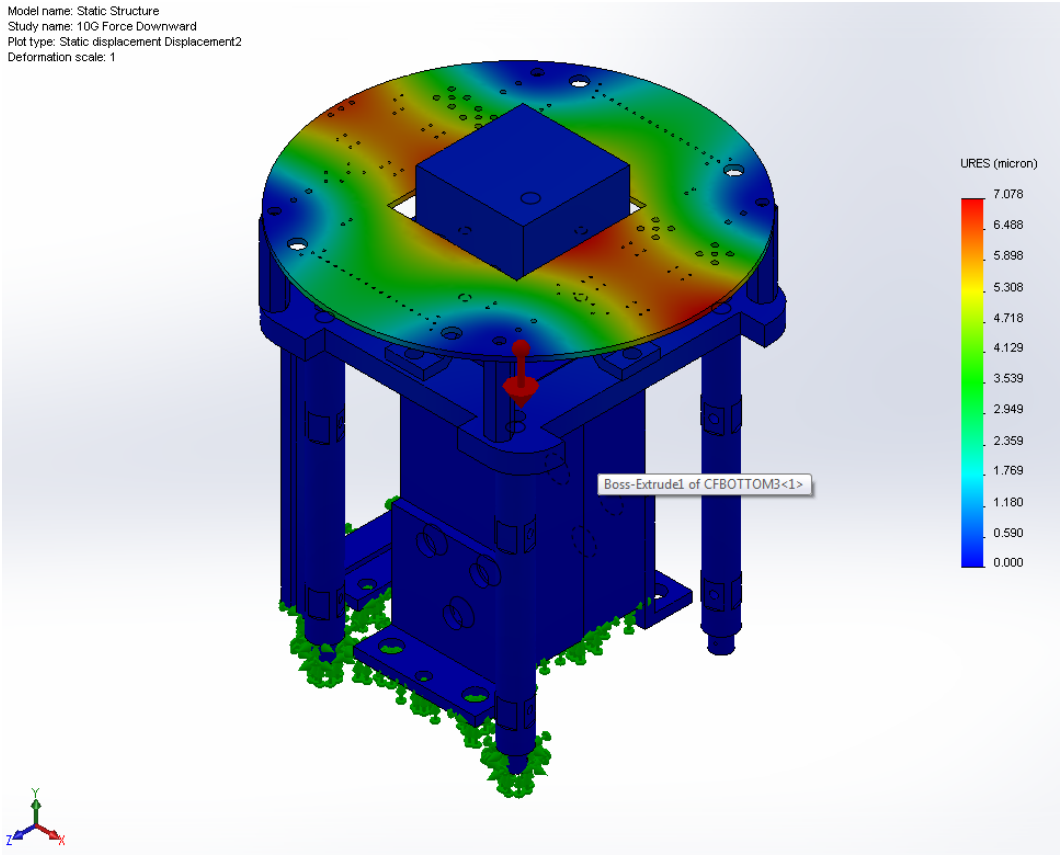

Figure 4.9: Simulated PCB displacement. The maximum value is $\sim 7\mu$m.

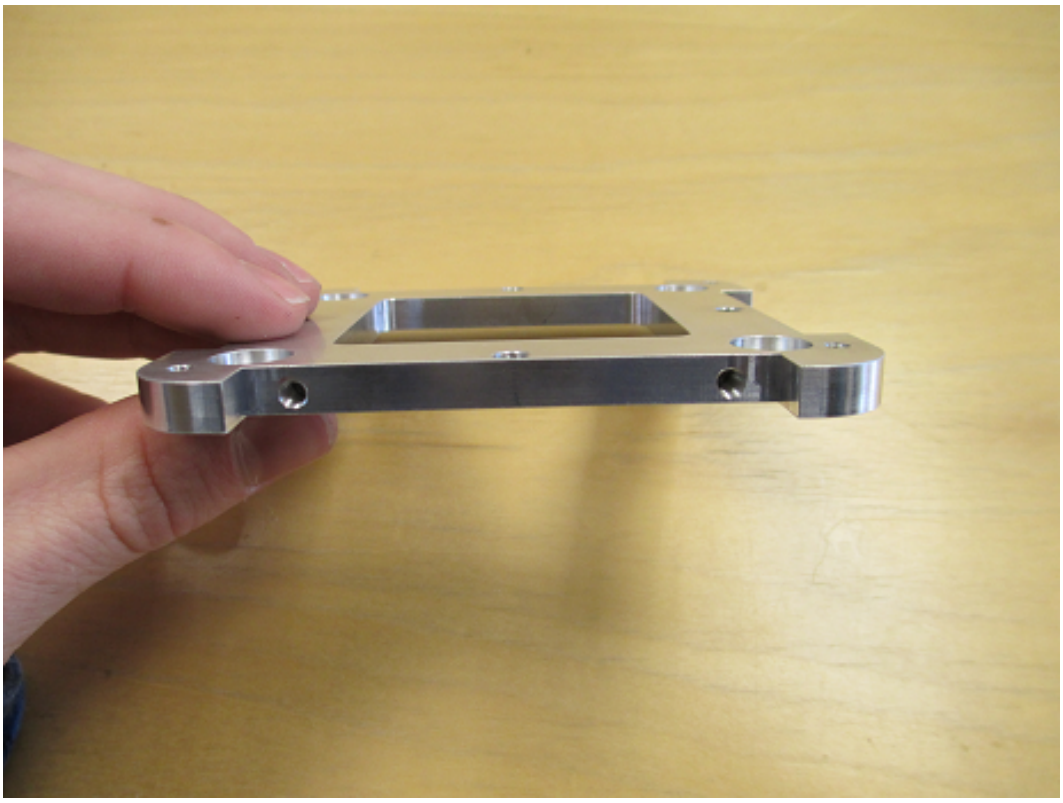

Figure 4.10: Side-view of the intermediate support stage. The two tapped holes in the side are for mounting the inverting pcb board support structure.

Figure 4.11: The Al7075-T6 aluminum support rods for maintaining rigidity throughout the rocket flight. The threaded end mates with the conflat mounting stage and the tapped end mates with the aluminum mounting stage.

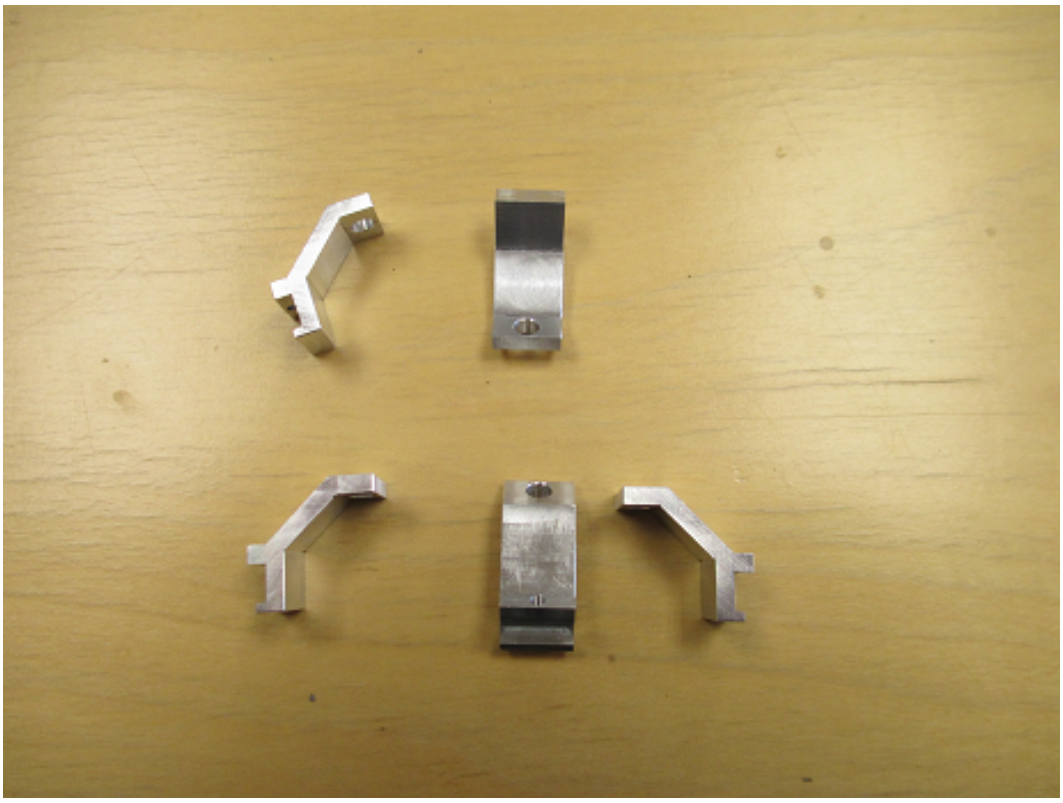

Figure 4.12: The support arms mate with the aluminum support stage to provide rigid support for the G10 guide square.

Figure 4.13: Copper cold-head interface to the CCD. The quarter-inch holes on the sides are for the heaters. The quarter-inch hole in the base is for the copper rod guide pin. The small 4-40 holes are for mating the cold strap.

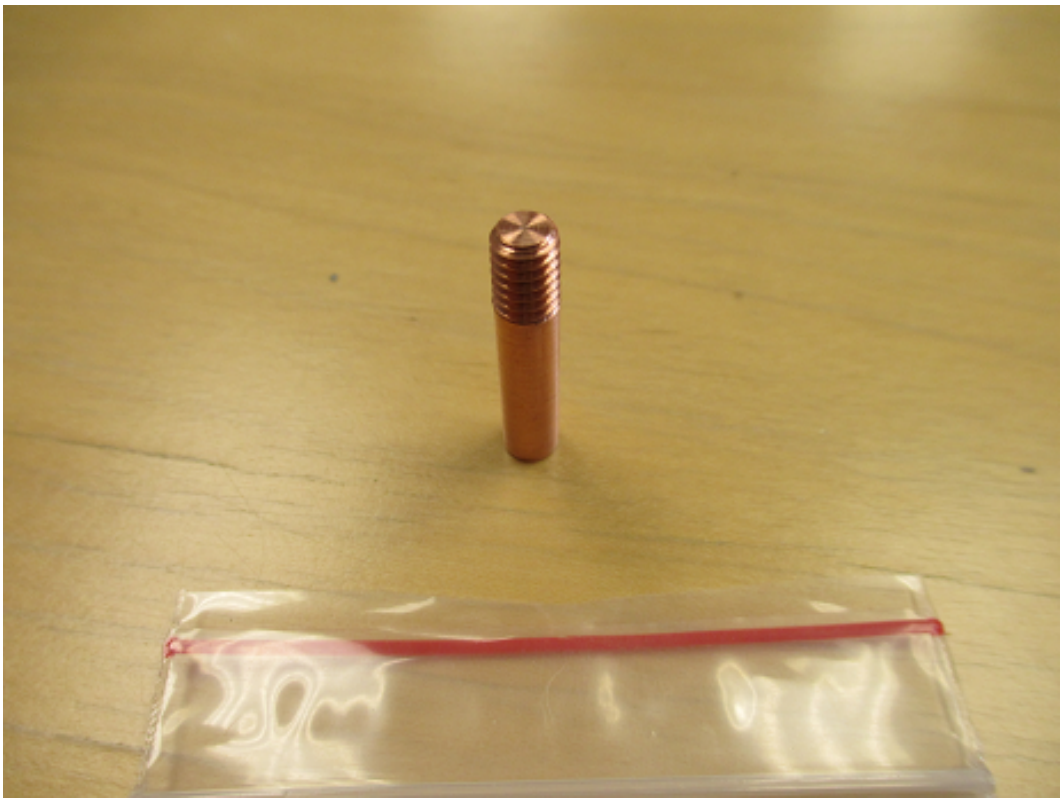

Figure 4.14: Copper support rod to serve as a guide pin and to maintain contact of the cold-head to the CCD during flight.

Figure 4.15: The machined parts for the rocket camera. On the left are the inverting board supports. The far right are the G10 materials that are provide thermal isolation of the cold surfaces from the neighboring components.

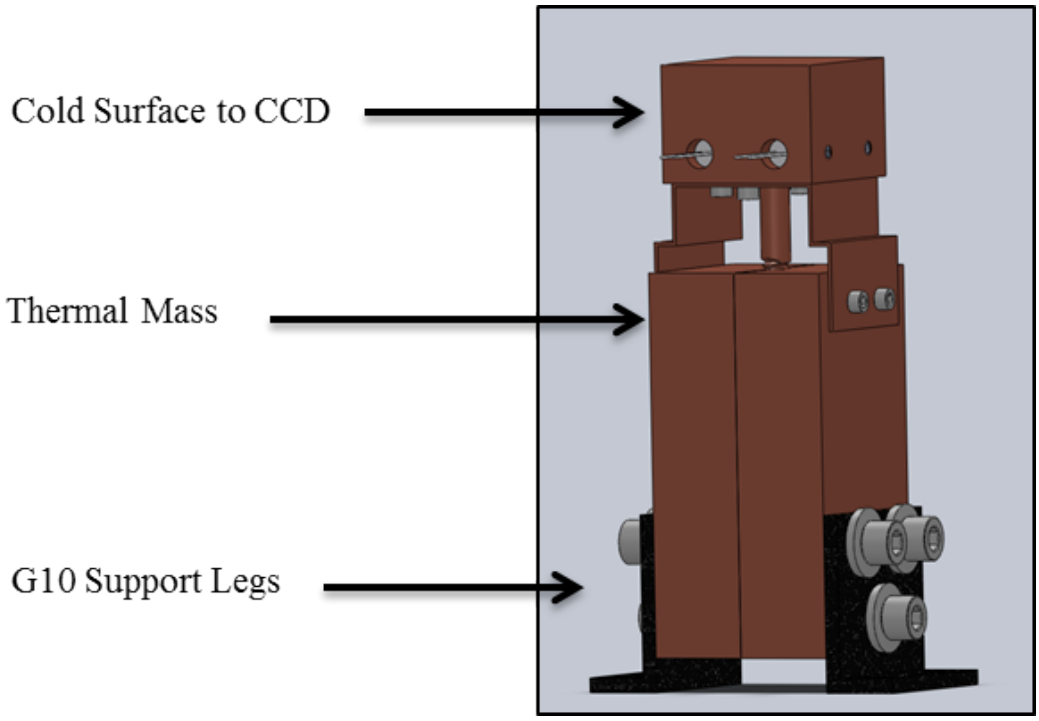

Figure 4.16: The cold bath is attached with G10 mounting feet for thermal isolation from the dewar wall.

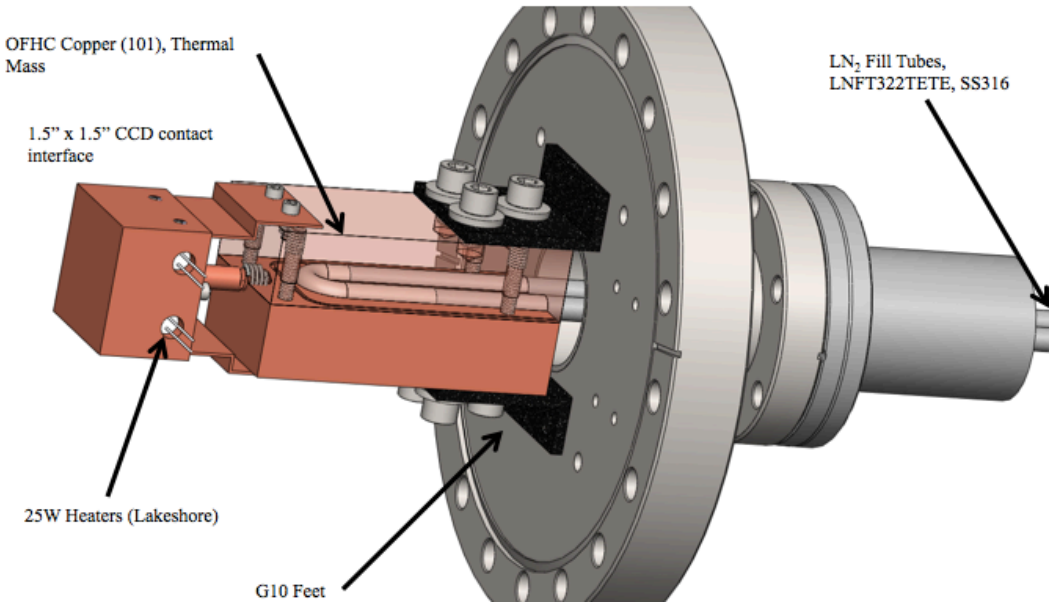

Figure 4.17: The liquid nitrogen cooling system can be seen clearly in this image. The LN_2 flows freely through the stainless inlet, cycles around the loop, and flows through the outlet. The system is designed for the flow LN_2 until launch.

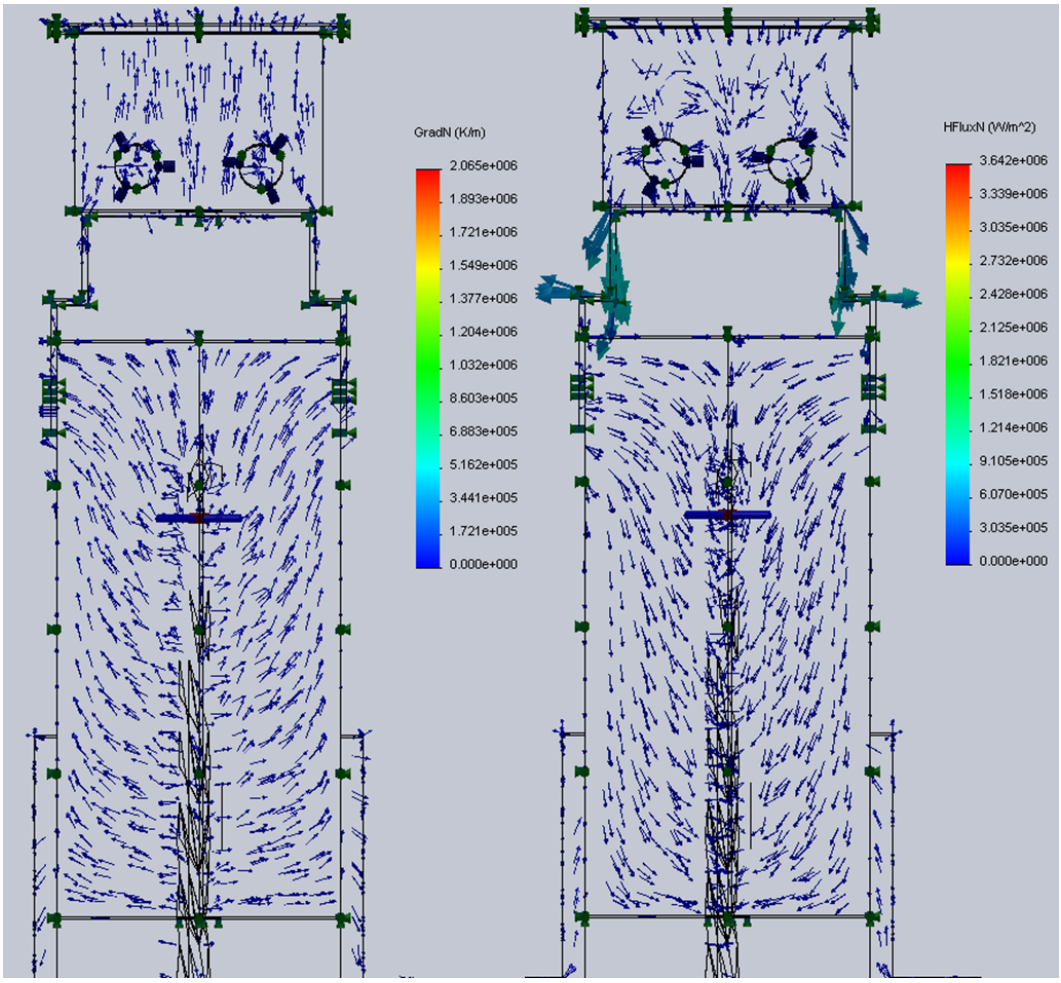

Figure 4.18: Snapshots of the thermal (K/m) and heat fluxes (W/m^2) within the cold finger as the system is cooling down. Notice the colder temperature flowing towards the CCD while the heat is being pulled away towards the stainless LN_2 fill tubes. The heat and thermal flux is also excluded from the G10 standoffs, supporting the claim of thermal isolation.

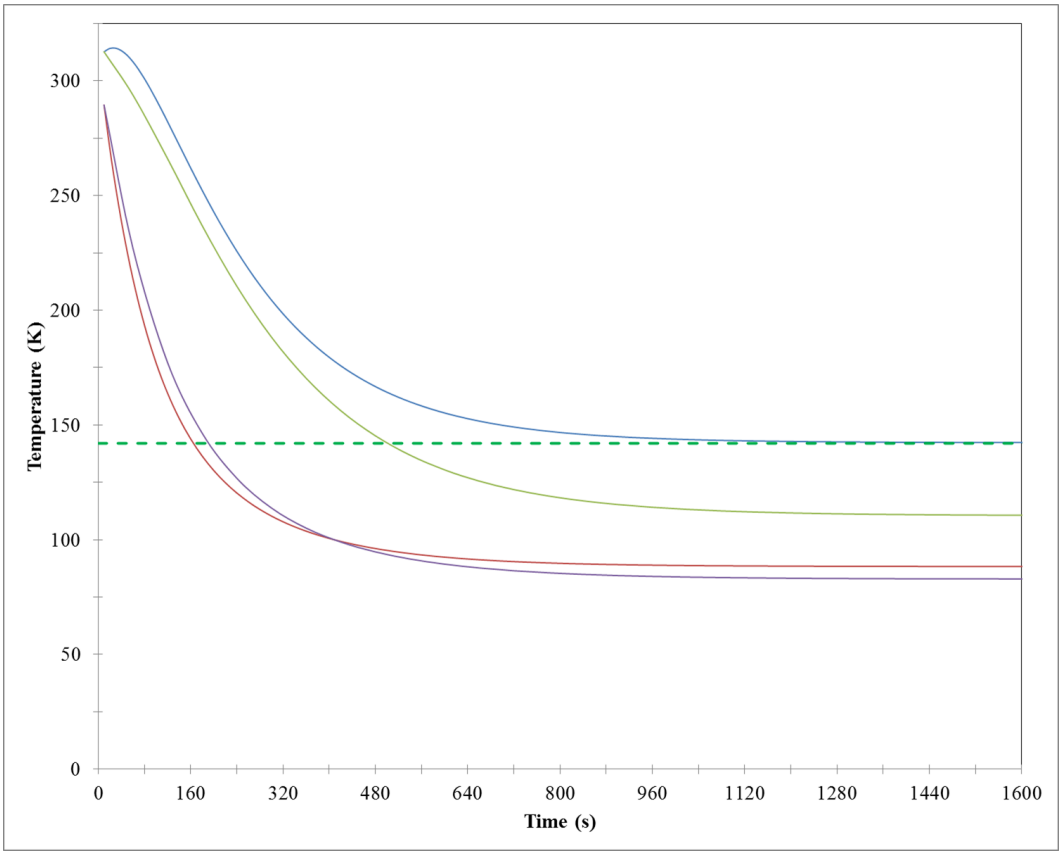

Figure 4.19: Simulated thermal cycle profile for cooling the CCD. The top two curves correspond to cooling of the cold-head at the surface of the CCD. The bottom two curves correspond to the cooling of the cold bath. The solid blue curve is the rate of cooling with both heaters in the cold-head at full power, 25 W, while cooling the system. The solid green is the rate with both heaters running at half power, or 12.5 W. The red curve corresponds to the cooling of the large thermal mass with both heaters on. The purple curve corresponds to cooling the large thermal mass with both heaters at half power. The dashed green demarcates the minimum safe temperature for CCD operation. The CCD cold-head reaches a steady state at $\sim$142 K, which is slightly lower than desired. The time to reach the steady state is $\sim$ 15 minutes.

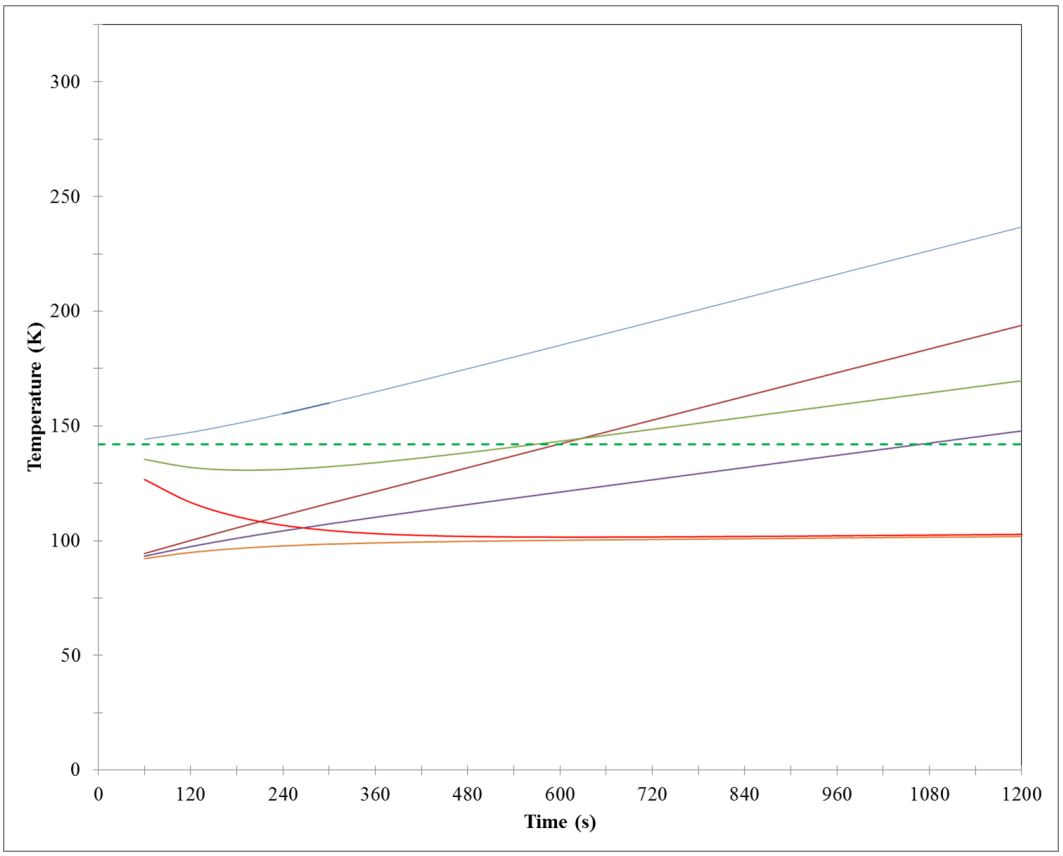

Figure 4.20: Simulated thermal cycle profile for warming of the CCD. The top blue, green and red curves correspond to heating at 25 W, 12.5 W, and 0 W, respectively, at the surface of the CCD. The maroon, purple, and orange curves are the heating profile for the copper cold bath with the heaters at 25 W, 12.5 W, and 0 W, respectively.

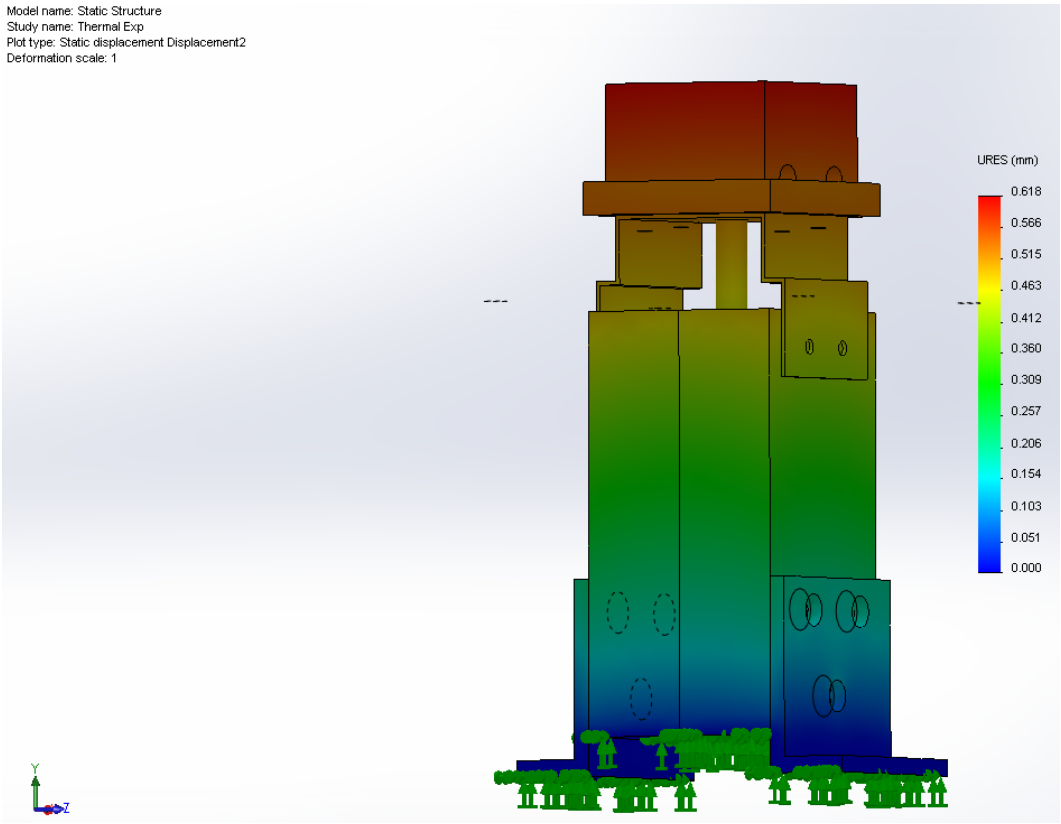

Figure 4.21: Shown is the SolidWorks simulated thermal contraction of the cooling system. The displacement at the CCD interface is ~ 0.6 mm towards the base. Mitigation of this will require the installation of Belleville washers at the base of the cold-head. The washers will provide a restoring force to counteract the contraction of the copper ensuring continuous thermal contact of the cold-head with the CCD during flight.

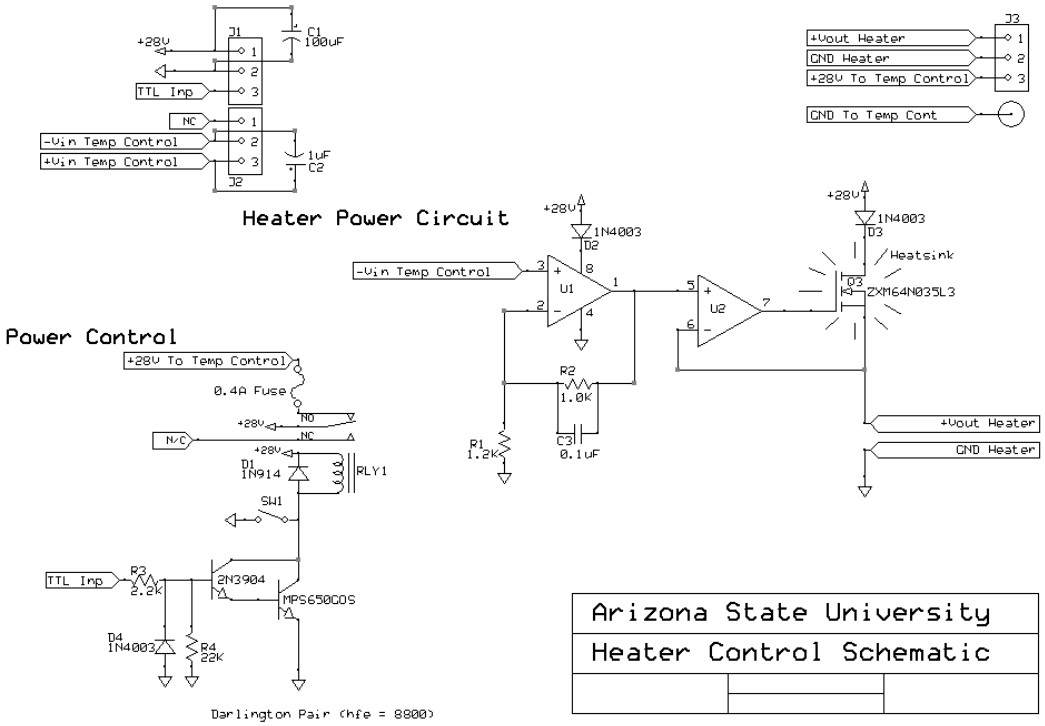

Figure 4.22: The schematic for the heater control circuit. The lower left hand circuit is for TTL power control and power switching to the Omega temperature controller.

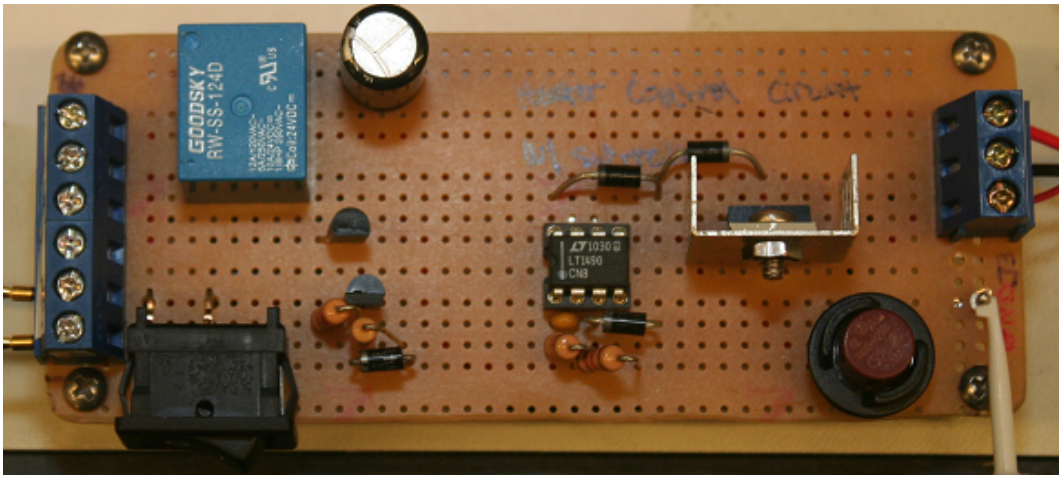

Figure 4.23: Thermal control circuit showing the MOSFET switch and heater element. The switch utilizes a reprocessed voltage from a thermocouple sensor to activate and deactivate the current flow to the heaters.

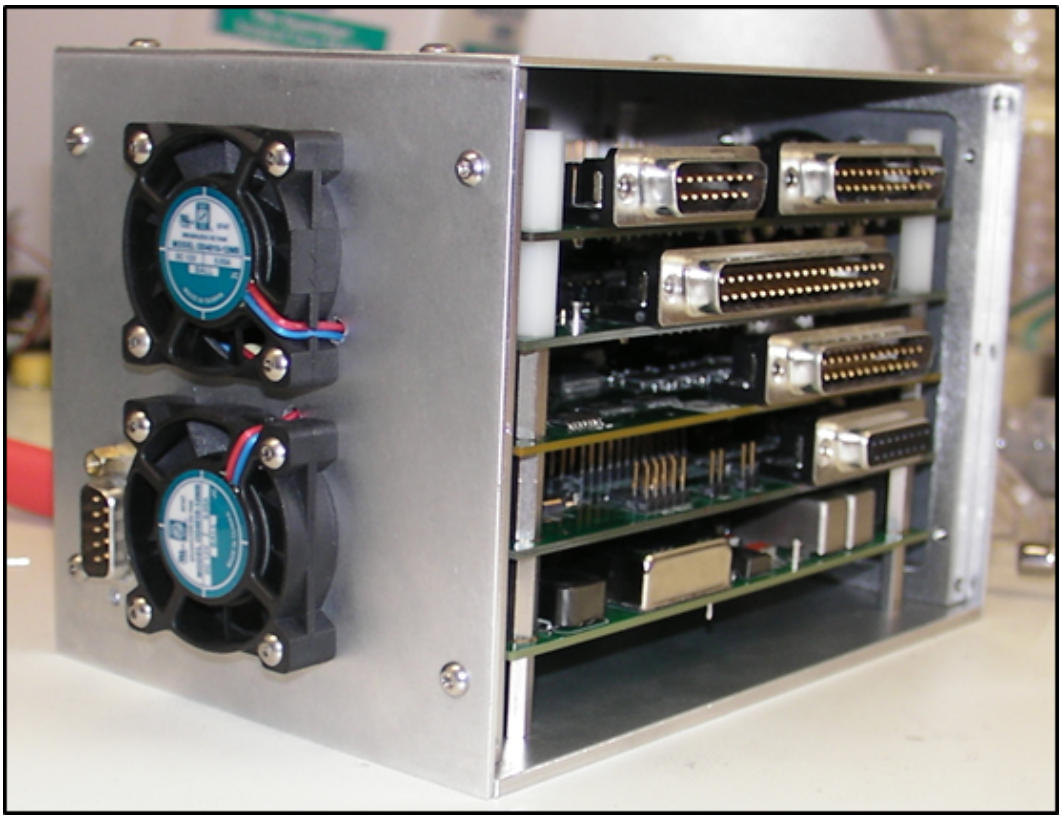

Figure 4.24: PCIe/104 Small-Cam imager controller from Astronomical Research Cameras, Inc. The fans on the side of the camera will not provide cooling during flight because forced air cooling is ineffective when there is a lack of air. A conductive cooling system will need to be developed in order to ensure the function of the Small-Cam in vacuo.

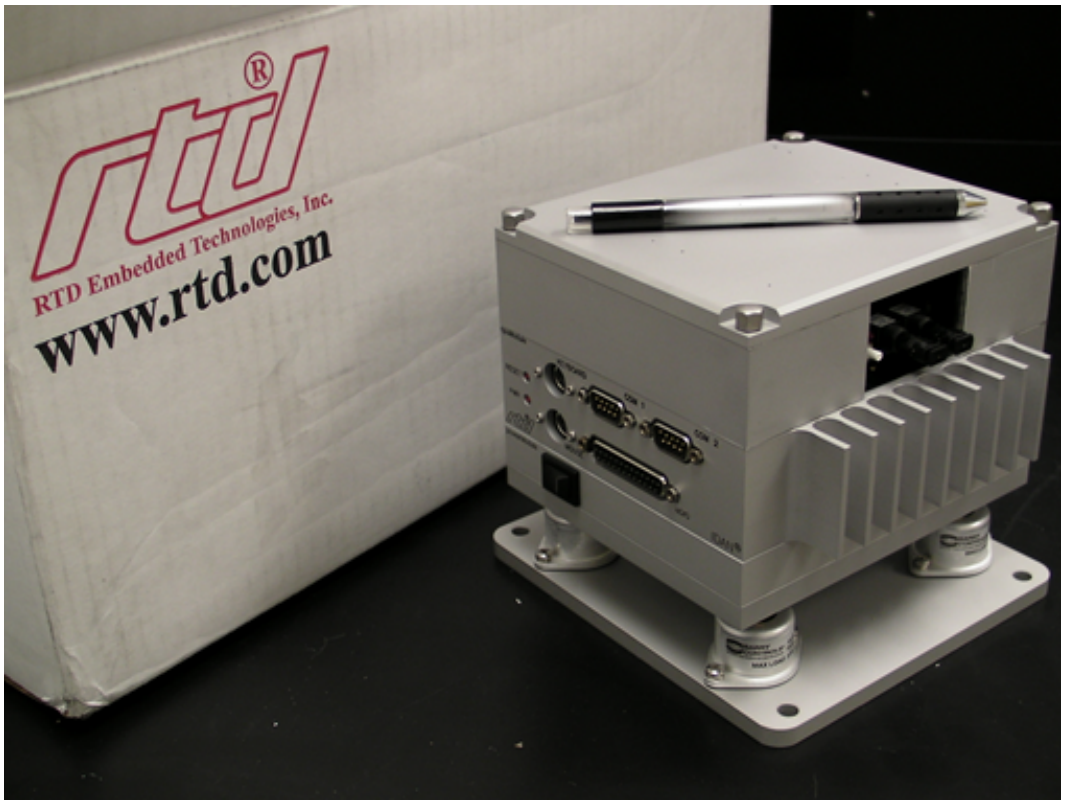

Figure 4.25: The instrument control computer (ICC) is an Intel Core 2 Duo 1.2 GHZ PC/104 embedded computer designed by RTD Technologies. Notice the cutout for Small-Cam PCIe/104 interface card.

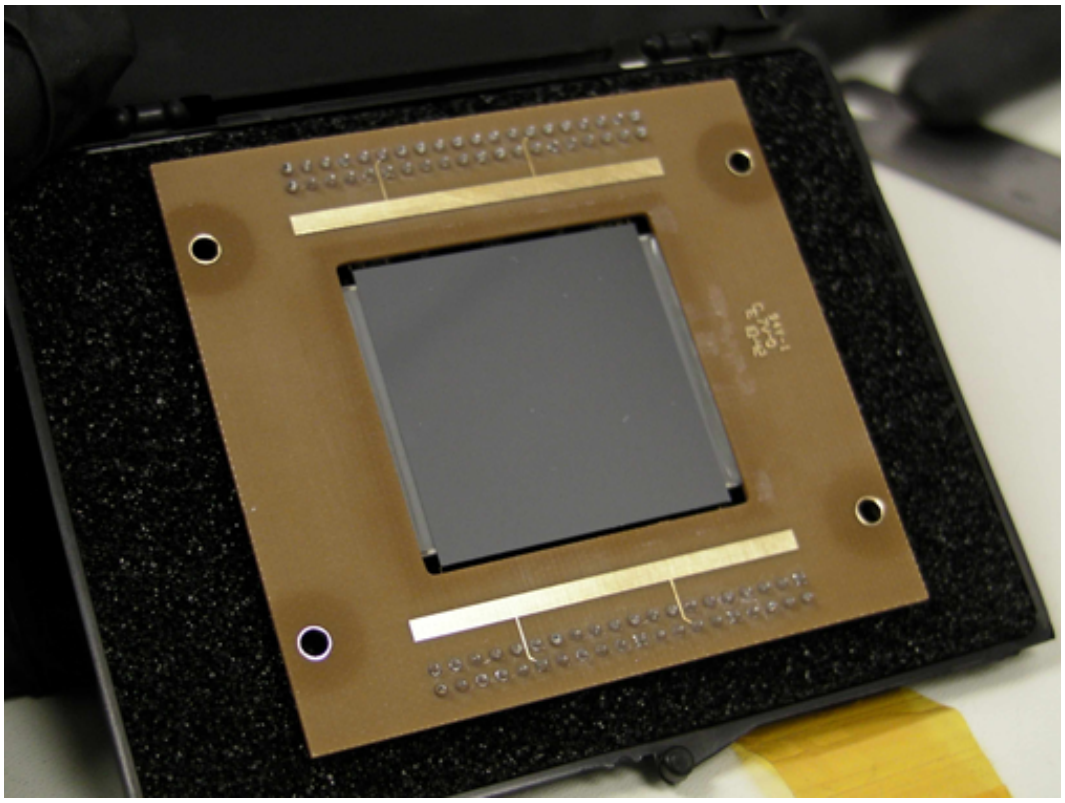

Figure 4.26: The delta-doped CCD in its picture frame packaging from JPL. The packaging prohibits the development of large focal plane arrays, but is sufficient for the operation of a single detector FPA.

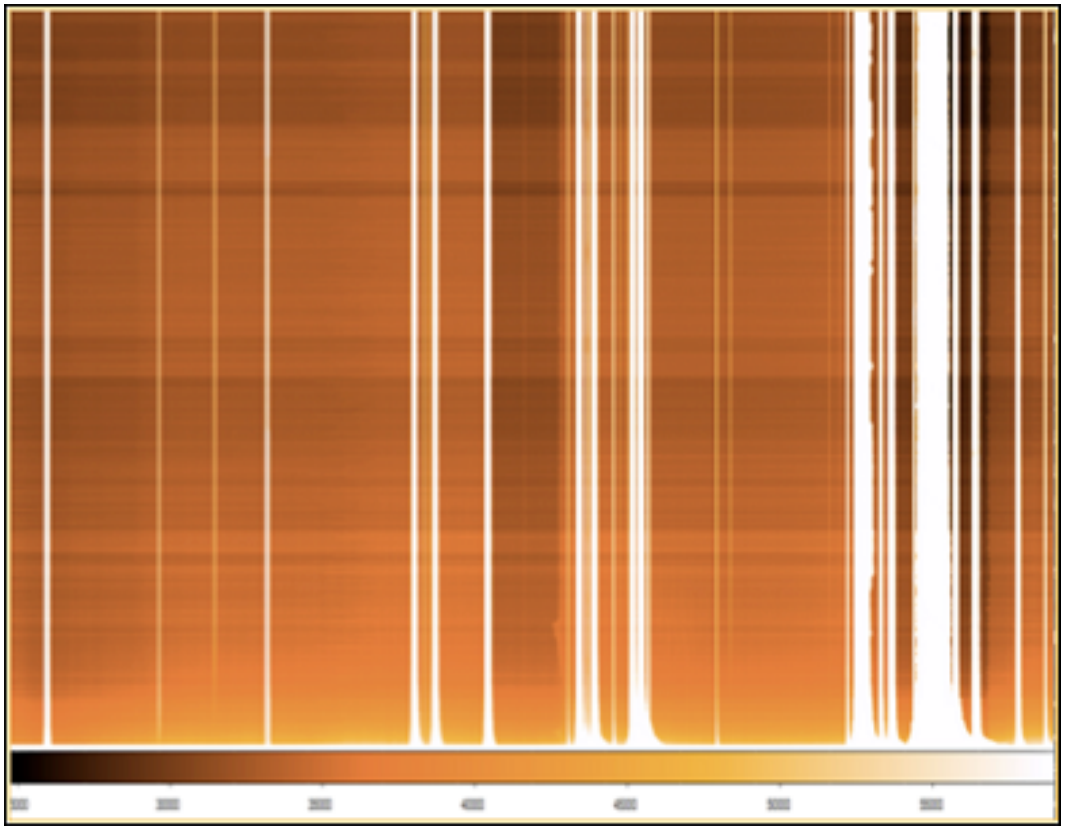

Figure 4.27: False color differential readout of a 10 s dark exposure for a 3.5k $\times$ 1.0k strip of the flight CCD. Only two of the four amplifiers were used. There is significant banding and streaking within the image, which can be corrected with changes to the clocking scheme or the development of a clock driver buffer board. Credit: Steve Monacos, JPL

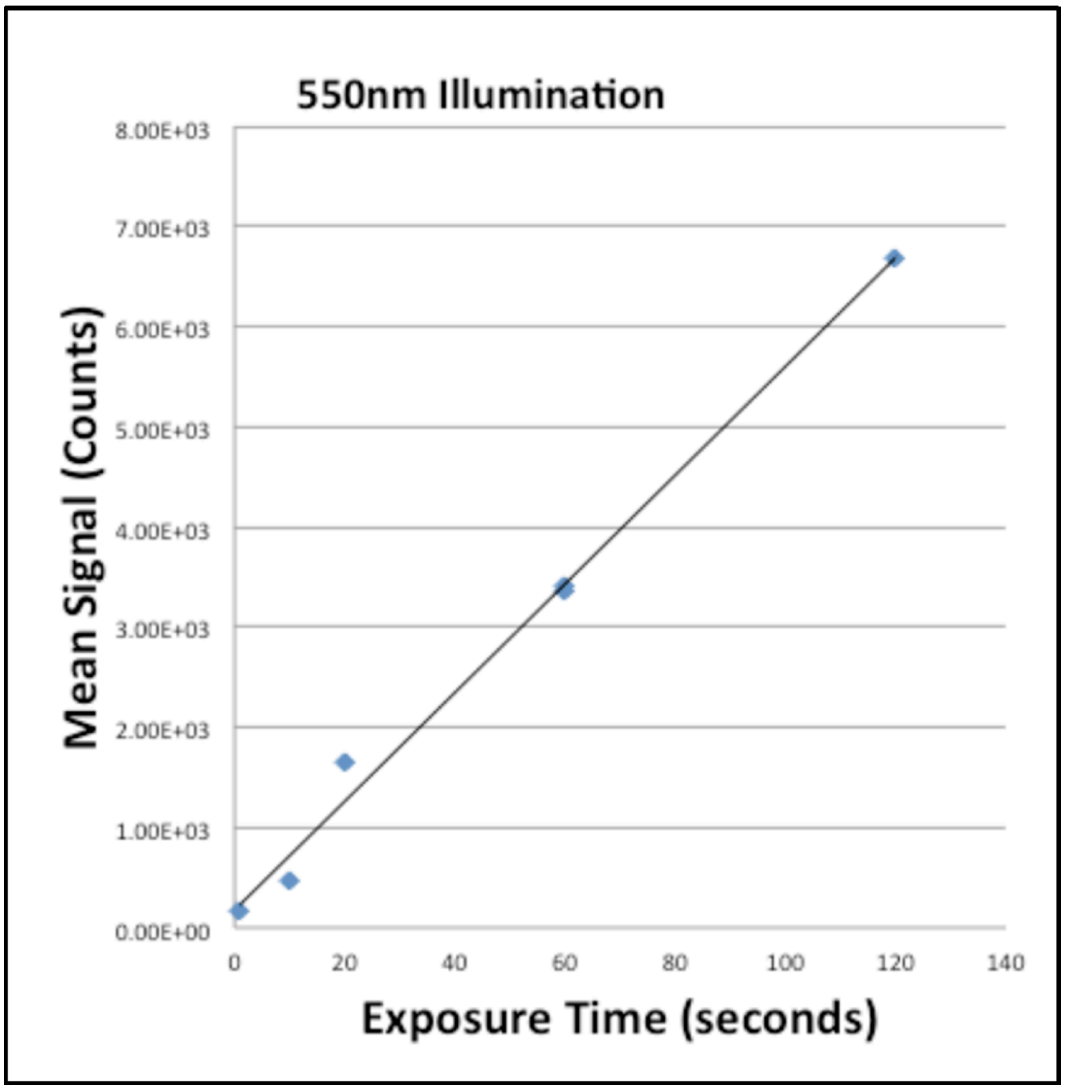

Figure 4.28: Readout of 1k $\times$ 1k lower-left quadrant of CCD without clock filtering. This image shows the device is linearly responsive to input radiation. Credit: Steve Monacos, JPL

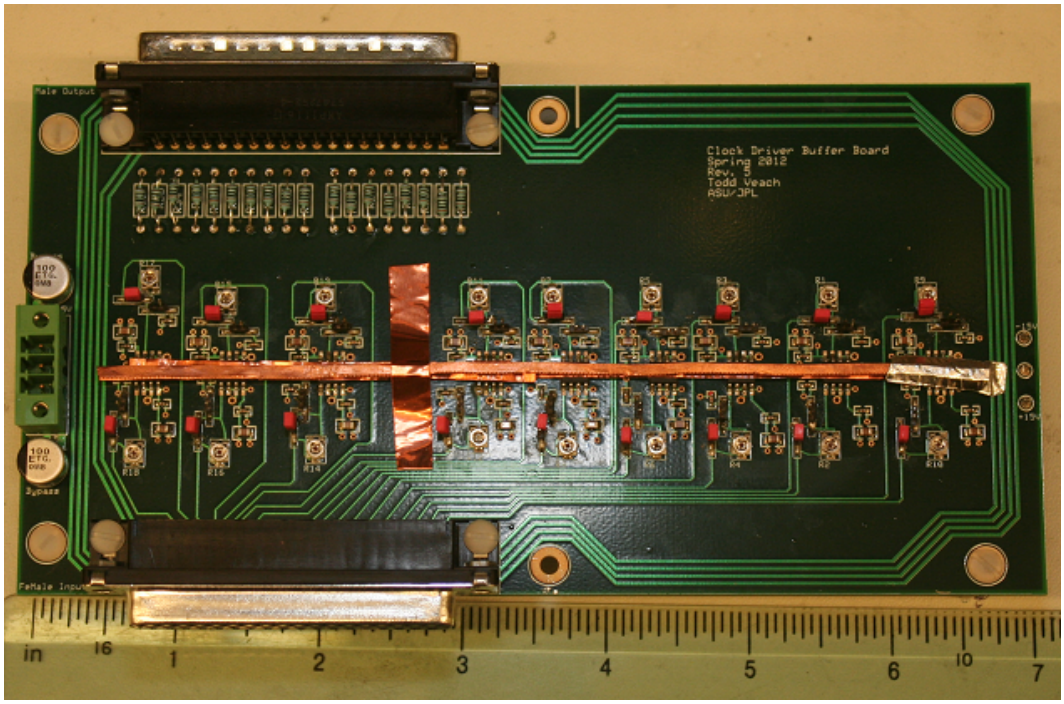

Figure 4.29: The clock driver buffer board fully assembled and heat sunk. The buffer board faithfully reproduces the clock signals for cable runs of up to 20 meters.

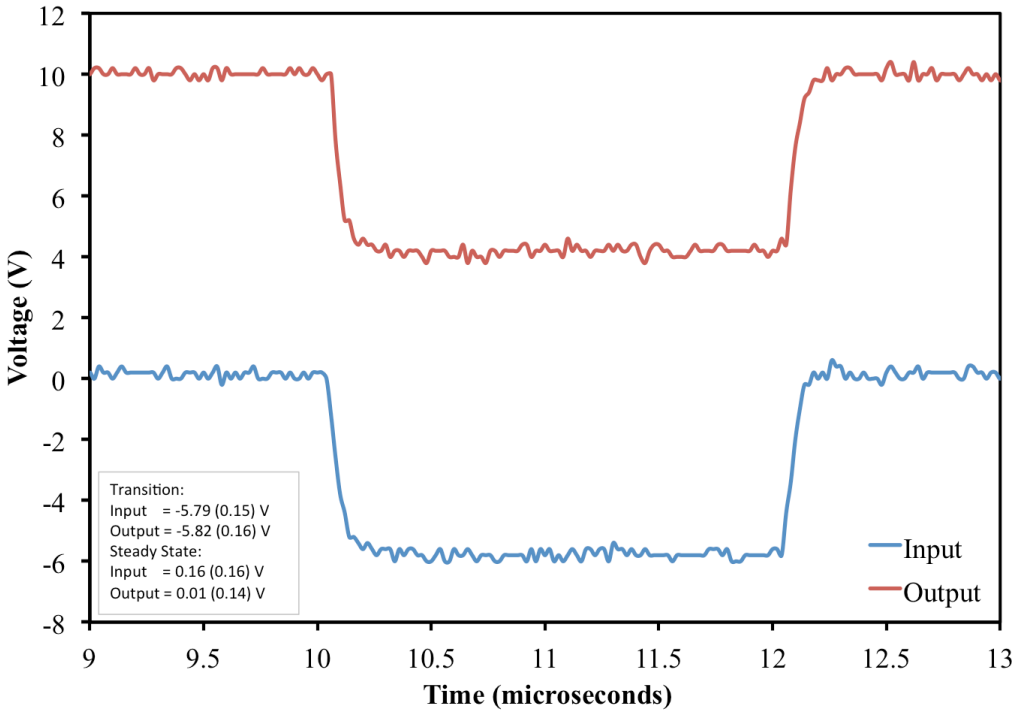

Figure 4.30: Shown is the faithful reproduction of the reset gate signal after a 20 m cable run from the Small-Cam. The blue line is the input to the buffer board and the red line is the output at the buffer board.

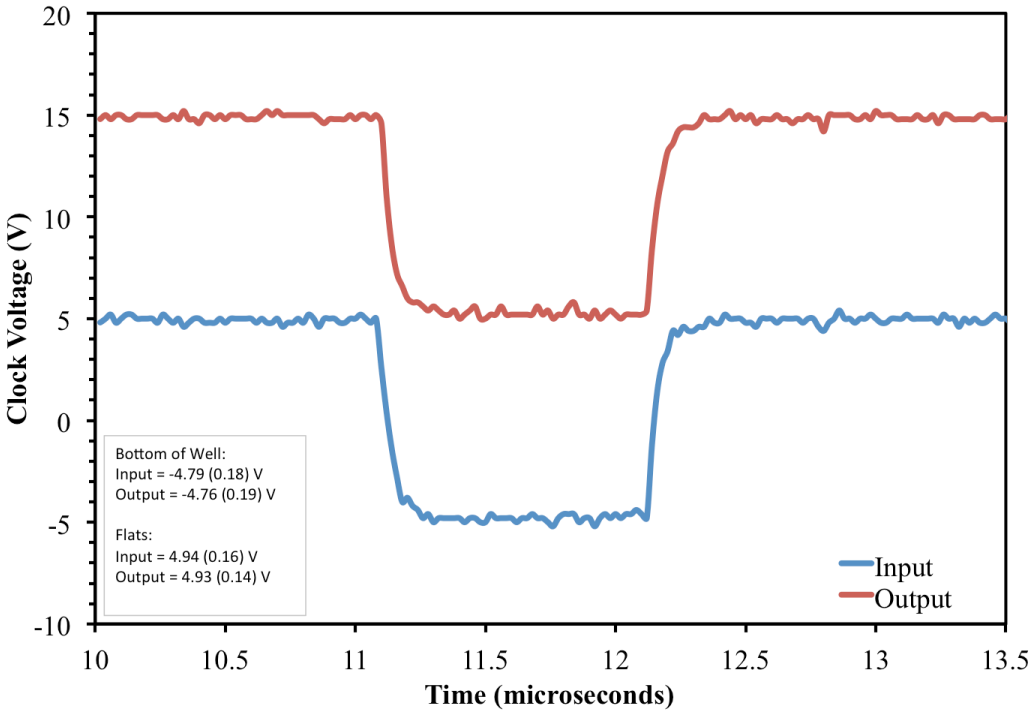

Figure 4.31: Shown is the faithful reproduction of the horizontal clocks after a 20 m cable run from the Small-Cam. The blue line is the input to the buffer board and the red line is the output at the buffer board.

Chapter 5

VIBRATIONALLY EXCITED HCN AROUND AFGL2591: A PROBE OF PROTOSTELLAR STRUCTURE

5.1 Introduction

Vibrationally excited molecules with sub-mm rotational transitions are potentially excellent probes of physical conditions in compact regions very near protostars. This study uses observations of the $v = 1$ and $v = 2$ ro-vibrational modes of HCN(4-3) to probe this environment. The presence or absence and relative strengths of these ro-vibrational lines probe the gas excitation mechanism and physical conditions in warm, dense material associated with protostellar disks. Pilot observations from the Heinrich Hertz Submillimeter Telescope (HHSMT) and followup observations from the Submillimeter Array (SMA) are presented here. All vibrationally excited HCN(4-3) $v = 0$, $v = 1$, and $v = 2$ lines were observed. All three of the $v = 2$ lines were observed to be of approximately equal brightness temperature, indicative of collisional excitation. Further, the line shapes of the $v = 2$ emission may suggest a Keplerian disk. The $v = 2c$ emission line has a component of excess emission, possibly indicative of a population inversion caused by a maser nearby to the compact embedded source or from emission from an expanding shell around the embedded source. The existence of the three $v = 2$ lines at approximately equal intensity suggests a density of greater than (10^{10} cm^{-3}) and a temperature of $>$ 1000K for the emitting gas. This warm, high density material should directly trace structures formed in the protostellar envelope and disk environment. This chapter demonstrates the utility of this technique which is of particular interest due to the ongoing commissioning of the the Atacama Large Millimeter Array (ALMA).

The vast majority of the molecular lines observed at millimeter wavelengths are associated with the lowest vibrational state ($v = 0$). However, several ro-vibrational molecular transitions have been detected in the ISM and towards hot molecular cloud cores (CS, H_2, SiO, HC_3N, CH_3CN, and HCN (Ziurys & Turner, 1986; Turner, 1987; Rolffs et al., 2011a,b)). For vibrational excitation to occur these molecules must be in regions of hot, dense gas (perhaps associated with a shock) and/or pumped by infrared radiation. Since these excitation requirements are expected to be fulfilled in only a very compact region close to an embedded source, they make vibrationally excited molecules with sub-mm/mm wave rotational transitions potentially excellent probes of the physical conditions very near embedded infrared sources. This is especially true for those sources which suffer so much extinction that they are unobservable in the infrared (Walker et al., 1994).

Initially, vibrationally excited HCN was used as a probe of physical conditions for astrochemistry studies (Morris et al., 1971; Wilson et al., 1973; Morris, 1975). In 1994, Walker et al. used the fact that the critical density and energy above ground for the $v = 1$ vibrationally excited state of CS $(7-6)$ and $(10-9)$ was quite high (n$\sim 10^8$ cm^{-3} and 2000 K respectively) in order to probe protostellar disk structure toward IRAS 16293, pioneering this technique. An excitation analysis of the vibrational lines suggests emission arising from shocks within a hot, dense circumstellar disk perhaps due to self-gravitating disk instabilities, e.g., Adams et al. (1989). Further, densities and temperatures that high are unlikely to be encountered in the infalling envelope or the outflow of a protostar, or even in a smooth, quiescent disk (Groppi, 2003). Since this hot, dense gas could be potentially associated with shocks and/or spiral density waves in a

protostellar accretion disk, vibrational molecular transitions could be used as a probe of disk structure and planet formation.

Observations of the $v = 0$, $v = 1$ and $v = 2$ vibrational modes of HCN(4-3) were made instead of CS. The critical densities of HCN are even higher than CS ($> 10^{10}\mathrm{cm}^{-3}$), but the excitation temperature of the $v = 1$ ro-vibrational transitions is ~ 1050 K, half that of CS. This could make HCN an even better probe of dense material in protostellar accretion disks, probing material farther from the protostellar object. For gas at the temperatures necessary to collisionally excite these ro-vibrational states, one would expect higher J levels are preferentially populated (Walker et al., 1994). Thus, the compromise between atmospheric transparency and line brightness makes HCN(4-3) the best choice for use as a probe of protostellar structure rather than lower lying rotational transitions.

The frequencies and selection rules governing the $v = 1$ and $v = 2$ modes also help with observing efficiency and interpretation. Emission from the (0, 2^{2c}, 0) and (0, 2^{2d}, 0) lines is expected to be absent due to $\Delta l = \pm 1$ selection rules if purely radiative excitation dominates (Figure 5.1) (Ziurys & Turner, 1986). If collisional excitation of the $v = 1$ and $v = 2$ lines dominates, one would expect to observe both $v = 1$ lines at approximately equal intensity, and all three $v = 2$ lines at approximately equal intensity. Furthermore, the extremely high critical density and temperature of these lines allow observation of emission that would ordinarily be contaminated by foreground and background emission within the beam (Walker et al., 1994). With contamination from the envelope removed, interpretation of the morphology and kinematics of protostellar sources should be simplified.

AFGL 2591 is a testbed of high-mass star formation that has unusually high HCN abundance ($\sim 10^{-6}$, Boonman et al. 2001). According to Benz et al. (2007) and references therein, it can be also be classified as a high mass

protostellar object (HMPO) or early "Hot Core." The HMPO are distinctive stages of star formation in which the sources are bright in the mid-infrared (10-12μm) and show a central density concentration. In this phase, the protostellar object is still deeply embedded in a collapsing dusty envelope. Thus, high energy radiation from UV photons or X-rays are unobservable directly, but the effects on the molecules within the surrounding environment can be observed in the submillimeter. van der Tak et al. (2006) provide interferometric observations of the $H_2^{18}0$ line at 203 GHz showing the existence of a rotating flattened structure, which could be evidence for an accretion disk (Ceccarelli et al., 2010). The central mass of AFGL 2591 is assumed to between $\sim 10-16$ $M_\odot$ (Marengo et al., 2000),(van der Tak et al., 2006), and the distance to AFGL 2591 is $1 \pm 1.0/0.5$ kpc (van der Tak et al., 1999). A distance of 1 kpc is adopted for all analyses.

This study makes use of submillimeter interferometric observations from the SMA to reduce the effects of beam dilution and increase sensitivity over single dish observations. The first goal of this study is to determine the excitation mechanism for the vibrational emission: collisional excitation or IR pumping. If the emission arises from collisional excitation, it should trace extremely dense, warm gas of the type expected in accretion disk structure. Furthermore, one would expect the emission region to be compact (i.e. unresolved) even at interferometric resolution if produced by dense gas tracing protostellar disk and/or envelope structure. The vastly expanded capabilities of the Atacama Large Millimeter Array (ALMA) will further increase spatial resolution and sensitivity to permit *imaging* of a wide variety of sources with greatly reduced integration time when compared to single-dish and other interferometric observatories. The observations of ALGL 2591 presented here demonstrate the utility of this technique, which will be even more effective and efficient when applied with ALMA.

5.2 Observations and Data Reduction

5.2.1 HHSMT HCN J=4→3 Observations

Observations of the $v = 0$ and $v = (0, 1^{1c}, 0)$ lines for AFGL 2591 were made at the HHSMT in February 2000 during priority observing time, with $\tau_{225} \leq 0.08$ for all observations. The receiver was tuned to 354.46033 GHz USB. The noise level and T_{sys} for this tuning were 0.010 K and 528 K, respectively and the time on source was 48 minutes. A second tuning covering the $v = (0, 1^{1d}, 0)$ and $v = 2$ lines was made in December 2002. The spectrometer was tuned to 356.25571 GHz. The noise level and T_{sys} for this tuning were 0.014 K and 1098 K, respectively and the time on source was 93 minutes. For both tunings, the facility MPIfR 345 GHz dual polarization SIS receiver was used, with 1 GHz bandwidth Acousto-Optical Spectrometers (AOS) spectrometers with 0.5 MHz (1.6 km/s) spectral resolution. Pointing was checked using planets and high flux continuum sources several times per observing session. Calibration was performed using the Hot-Sky-Cold method. The wobble switching observing mode was used with a $120''$ chopper throw, and a 50% duty cycle. Main beam efficiency of the HHSMT at 350 GHz is $\eta_{MB} \sim 0.45$ for unresolved sources. The beam size was $22.0''$ for both tunings. Linear fits to the baselines were subtracted for each spectrum, then co-added the spectra, weighted by RMS noise. Reductions were done using the GILDAS[1] software package (Groppi, 2003).

5.2.2 SMA HCN J=4→3 Observations

Observations of the vibrationally excited spectral lines of AFGL 2591 ($v = 0$, $v = (0, 1^{1c}, 0)$, (0, 1^{1d}, 0), and $v =$(0, 2^0, 0), (0, 2^{2c}, 0) and (0, 2^{2d}, 0) were observed in a single tuning (354.505476 GHz) of the SMA in the *subcompact*

[1] http://www.iram.fr/IRAMFR/GILDAS

configuration on September 8, 2008. The precipitable water vapor (PWV) during observations was less than 2.5 mm over the 7.2 hours of observations. This tuning was specifically chosen to place all six of the vibrationally excited HCN lines in the upper sideband (USB). The lower side band (LSB) also included CO(3→2) and $H^{13}CN$, but these spectral lines were not the focus of this study. The brightest calibrators closest to the source (mwc349a and 2015+371) were used as phase calibrators. Uranus served as flux calibrator, and the standard bright quasar 3c454.3 was used for passband calibration. Main beam efficiency of the SMA at 354 GHz is ∼0.74 for unresolved sources. The SMA primary beam is $36''$ at this frequency. The synthesized beam is $3.4'' \times 2.0''$ (3400×2000 AU, $\overline{D}_{mb} = 2700$ AU) with a position angle of 37.4°. Image reconstruction was done using the Multichannel Image Reconstruction, Image Analysis, and Display (MIRIAD) (Sault et al., 1995) software package with extensions for the SMA using the procedures outlined in Zhao (2009)(see Section 5.2.3).

The continuum data shown in Figure 5.3 were constructed using molecular line-free "chunks" of the correlator. After molecular line subtraction, the equivalent bandwidth for the continuum was 1.3 GHz. Using the MIRIAD INVERT task with uniform weighting, I generated a "dirty image" and performed a hybrid Hogbom/Clark CLEAN using a gain of 0.08 with 35000 iterations to produce output maps consisting of the clean components. The number of iterations used for cleaning was determined systematically by maximizing the map SNR (Figure 5.2). The hybrid Hogbom/Clark CLEAN algorithm is a form of deconvolution used on images containing one or more point sources. The algorithm iteratively finds the highest value in an "image" and subtracts a small gain convolved with the the point spread function, or dirty beam, until the highest value is smaller than some threshold, or the maximum number of iterations, has

been reached. The "dirty" maps were then RESTORed by convolution with a gaussian beam, producing the clean maps, which were then exported to IDL[2] for further analysis. The peak flux in the continuum image is 1.42 Jy beam^{-1} with an rms noise of 3.4 mJy beam^{-1}. The peak integrated intensity of the continuum is 0.55 ± 0.07 K km s^{-1}.

CLEANed three-dimensional image cubes, with a spectral resolution of 0.273 km/s, generated within MIRIAD, were exported to IDL for spectral line extraction. The spectral line extraction region is defined by a two-dimensional gaussian fit to the CLEANed continuum image, shown in Figure 5.3a as a white dashed ellipse. The FWHM of the extraction region is $4.0'' \times 2.6''$ with a 37.4° rotation angle east of north. No smoothing was applied to the v=0, v=(0,1^{1c},0), and v=(0,1^{1d},0) spectral lines. The v=(0,2^0,0), v=(0,2^{2c},0),v=(0,2^{2d},0) spectra were boxcar smoothed by 3. The spectra were weighted by RMS noise. The rms noise for the data cubes was 85 mJy beam^{-1}. The noise of the integrated intensity maps are 5.44, 0.92, 0.89, 0.81, 0.82, and 0.75 K km s^{-1} in order of the panels in Figure 5.3 from top left to bottom right. All of the HCN emission lines feature an $v_{lsr} = -5.3 \pm 0.7$ km/s velocity shift, consistent with observations made by van der Tak et al. (1999) and Benz et al. (2007).

5.2.3 MIRIAD Data Reduction

Following the procedures outlined in Zhao (2009), the data was calibrated and reduced to form continuum images for the upper and lower sidebands, along with data cubes corresponding to the relevant spectral features. This section explains, in detail, the analysis steps that were taken.

[2]IDL, ENVI, and Image Access Solutions (IAS) are trademarks of Exelis Corporation

The majority of data reduction regarding interferometric data involves corrections for noise introduced from atmospheric variability. According to Zhao (2009):

> A major concern at submillimeter wavelengths is the contribution to the noise by the atmosphere modulation in amplitude. The system temperature (T_{sys}) measurements determined by comparing the receiver output power from an ambient temperature load with that of the sky are essential to tracking noise variations of the receivers and therefore to calibration for the amplitude gains.

The raw *uv* data is loaded into MIRIAD and the system temperature for each telescope is inspected and flagged for bad values. The flagging removes the values from analysis, but doesn't remove them from the data set, allowing the user to redo the the system temperature analysis if unsatisfied. While inspecting the raw data, I found the system temperatures for antennas 1 and 7 to be corrupted with respect to the rest of the data. They were replaced with the uncorrupted system temperatures from antenna 3, which is standard procedure for interferometer data reduction with bad data.

The data from interferometers comes in the form of visibilities and correlations. In the reduction of the data, one can come across bad correlations and visibilities. In order to correct for this, I inspected the raw data for each source (gain calibrator, passband calibrator, flux calibrators, and source) within MIRIAD and flagged the bad data points using the task *smablflag*, which allows the user to interactively flag bad correlations and visibilities with the mouse.

After removing the bad correlations and visibilities, the data were corrected for bandpass, gain, and flux. Bandpass calibration corrects for the

frequency dependent response of the system and is typically done using a bright continuum source, for which the quasar 3c454.3 was used. The time-dependent response of the system, known as antenna gain, was corrected using targets nearby to AFGL 2591, mwc349a ($< 1°$) and 2015+371 ($< 4°$). These are point sources with flux densities of $\sim$2.38 and $\sim$1.73 Jy, respectively, at 340 GHz. The last step in calibration is for the absolute flux scale, which was done using Uranus as the calibrator. The final data products for analysis were the continuum image and spectral line extractions.

5.2.4 Spectral Line Extraction

Spectral data cubes were exported from MIRIAD UV format into FITS image format for subsequent analysis using IDL. Integral to the generation of the spectral data cubes in MIRIAD was to update the rest frequency information in the header to correspond to the rest frequency of the spectral line under investigation. This allowed for the "re-centering" of the data cubes such that the spectral line of interest was at or near 0 km/s in a plot of radial velocity versus intensity (see Figures 5.4,5.7,5.8). For example, in order to export the $v = 0$ spectral line, the header information was updated within MIRIAD to change the *restfreq* parameter to 354.505473 GHz using the MIRIAD command *puthd*.

In order to extract the spectral lines, a two-dimensional gaussian was "fit" using the IDL routine, GAUSS2DFIT, to an image made from the collapse of the appropriate spectral cube into an average image. The ellipse defined by the major and minor axes of the two-dimensional gaussian fit define the extraction region for the data cube. The functional form of the two-dimensional gaussian is given by:

$$F(x,y) = A_0 + A_1 e^{-\mathrm{U}/2} \tag{5.1}$$

$$\mathrm{U} = \left(\frac{x'}{\mathrm{a}}\right)^2 + \left(\frac{y'}{\mathrm{b}}\right)^2 \tag{5.2}$$

$$x' = (x-\mathrm{h})cos(\theta) - (y-\mathrm{k})sin(\theta) \tag{5.3}$$

$$y' = (x-\mathrm{h})sin(\theta) + (y-\mathrm{k})cos(\theta) \tag{5.4}$$

where A_0 and A_1 are fitting parameters. The center and rotation angle of the ellipse are defined by (h, k, θ). The axes are defined by $2a$ and $2b$. The gaussian fit parameters are shown in Table 5.1.

Pixel values within the gaussian ellipse centered on the brightest pixel were then summed and weighted by a two-dimensional gaussian to obtain the flux at each frequency slice. This mimics uniform weighting with some tapering, which gives a weight inversely proportional to the sampling density function. This form of weighting minimizes the sidelobe level. However the noise level can be a factor of two worse than natural weighting. According to the MIRIAD users guide “the optimum weighting for detecting a Gaussian source is to weight the visibility data by a gaussian”, which was done here (Zhao, 2009).

In order to build the spectra, I repeated this procedure for each frequency slice in the data cube. The spectra of flux density (Jansky/beam) versus slice were then converted to brightness temperature versus velocity for further analysis (see Figure 5.4).

The equation for brightness temperature used was derived by solving the Planck law for temperature, T, and converting the frequency, ν, to GHz:

$$S(Jy) = \frac{2h\nu^3}{c^2}\Omega_s \frac{1}{e^{h\nu/k\mathrm{T}} - 1} \tag{5.5}$$

$$T_B(\nu) = \frac{0.048\nu(GHz)}{ln[1 + (3.47 \times 10^{-8} \frac{\nu^3(GHz)}{S(Jy)}\theta_1\theta_2)]} \tag{5.6}$$

where $S(Jy)$ is the flux density, $\Omega_s = \theta_1\theta_2$ is the solid angle subtended by the beam.

The relevant spectral lines were interactively extracted using IDL. I plotted the brightness temperature for the full baseline subtracted spectra and overlaid a vertical line at the frequency of the interesting emission line (see Figure 5.4). Points on either side of the emission line, corresponding to slices in the data cube, were extracted by eye to include a small amount of of the baseline and the relevant spectral line. The "zoomed" spectral line was then plotted versus doppler corrected velocities in order to facilitate a more accurate selection of the extent of the spectral feature. The spectral line was extracted and a one-dimensional gaussian was "fit" using the IDL routine, GAUSSFIT, where the maximum value for the gaussian corresponded to the maximum brightness temperature and the FWHM the measurement for the velocity width of the spectral feature (see Table 5.3). The full procedure was repeated for all 6 HCN transitions within the bandpass.

5.3 Discussion

5.3.1 HHSMT Data

Spectra of AFGL2591 observed with the HHSMT are shown in Figures 5.5 and 5.6. I find a very bright $v = 0$ HCN(4-3) and strong HCN (4-3) v=(0,1^{1c},0) ($\sim$110 mK) emission. Given the strong infrared radiation field surrounding AFGL 2591, one might expect any detected vibrationally excited HCN emission to be

consistent with pumping through 14 μm absorption. Groppi (2003) found that the marginally detected $v = 1d$ line (1.5σ) was $5\times$ weaker than expected assuming excitation due to IR pumping (i.e. equal in intensity to the $v = 1c$ line). Furthermore, no $v = 2$ lines are found in the spectrum, which is unexpected for the unusually high HCN abundance of the source. In a recent SMA study, Benz et al. (2007) note that the HCN (4-3) $v = 1c$ line is preferentially emitted very close to the protostar ($\sim$600 AU) and, unlike other lines observed, its visibility diagram is not well described by models including far-UV and X-ray protostellar emission.

5.3.2 SMA Data

Figure 5.3 shows contours of integrated intensity of the HCN(4-3) emission lines overlaid on the background continuum. The $v = 0$ contours in Figure 5.3a show evidence for an extended source towards the northeast of the image, consistent with results from Benz et al. (2007). The contour levels of the v=(0,1^{1c},0) and v=(0,1^{1d},0) emission show a compact source of emission with some extended emission pointing towards the southwest. Contour levels of v = (0, 2^{0}, 0), (0, 2^{2c}, 0) and (0, 2^{2d}, 0) show extremely compact sources centered on the central density concentration and are unresolved. The calculated brightness temperatures derived from two-dimensional gaussian fits are given in Table 5.3. The spacings between the contour levels are defined as 10% of a gaussian fit to the peak integrated intensity of the spectral line. The blue ellipses in each panel correspond to the FWHM for each source determined from a Gaussian fit to the integrated intensity maps. The S/N, shown in the upper right corner of each panel in Figure 5.3, is defined here as (half the maximum value from a gaussian fit to the integrated intensity (HM))/(the background noise in the integrated intensity image).

Benz et al. (2007) have previously observed AFGL 2591 from 352.6 – 354.6 GHz at $0.6''$ spatial resolution in the extended array configuration. Their

observations cover the lowest vibrational state and the ($v_2 = 1$) rotational state of HCN. They measure a peak brightnesses of 2.3 Jy beam^{-1}and 3.1 Jy beam^{-1}, respectively. The measurements of 24.4 and 6.6 Jy beam^{-1} here are $\sim 11\times$ and $2.2\times$ larger than their measured values, respectively.

Since Benz et al. (2007) use a very different SMA configuration with much higher spatial resolution, comparison of the measured line fluxes is not straightforward. The large difference in measured flux for the $v = 0$ HCN line suggests the emission is relatively extended and resolved in the work of Benz et al. (2007). The larger beam recovers more of the extended flux. The difference between measurements of the $v = 1$ line fluxes is smaller. This suggests that some flux is still being resolved in Benz et al. (2007), but to a lesser degree. Both groups find a velocity offset of $v_{lsr} = -5.3 \pm 0.7$ km/s, consistent with the systemic velocity of the molecular cloud surrounding AFGL 2591 (van der Tak et al., 1999). Spatially, I see the same extended emission to the NW in the $v = 0$ transition images as van der Tak et al. (1999, 2006) and Benz et al. (2007); however, the angular resolution in the subcompact configuration is insufficient to resolve the two peaks as separate components.

Figure 5.7 shows the HCN(4-3) v=(0,1^{1c},0), and v=(0,1^{1d},0) spectra measured with the SMA. Table 5.3 shows the measured line strengths, FWHM, and v_{lsr} of the HCN transitions. The $v = 0$ transition is the brightest with a temperature of ~ 39 K. I observe the $v = 0$ and both $v = 1$ lines, but at brightness temperatures $\sim 80\times$ and $90\times$ greater than the HHSMT measurements. For both lines, this is consistent with the $\sim 70\times$ reduction in beam dilution provided by the SMA for a source unresolved by both telescopes. Furthermore, I observe the $v = 1d$ line to be of approximately equal brightness to the $v = 1c$ line. This supports the hypothesis that the emission results from collisional excitation.

In contrast to the HHSMT data, all three HCN (4-3) $v = 2$ lines are observed of approximately equal strength, but weaker than the $v = 1$ lines. Figure 5.8 shows the $v = (0, 2^{2c}, 0)$ emission line. This line is almost twice as strong as the other $v = 2$ lines, with excess emission primarily concentrated in a velocity component at -7.5 km/s. This excess emission could be caused by postulated maser activity (Trinidad et al., 2003) in the system. Another possibility is the system being shock heated by the FUV/X-ray emission escaping the central source, enhancing the v=(0,2^{2c},0) transition in the surrounding material (Bruderer et al., 2009). This lends further credence to collisional excitation because a possible source for the X-rays is interaction of an accretion disk with circumstellar material. Excepting the $v = (0, 2^{2c}, 0)$ excess emission at -7.5 km/s, all three $v = 2$ lines have approximately the same line strength, which is expected for collisional excitation of the material in a dense environment.

5.3.3 Line Ratio Analysis

The ratio of the measured brightness temperatures (Table 5.3) of the three $v = 2$ transitions to the two $v = 1$ transitions can be used to estimate the excitation temperature of the gas in the optically thin limit. The ratio of the upper and lower state brightness temperatures are related to the excitation energy and excitation temperature for a linear molecule by:

$$\frac{T_{\mathrm{MB},i}}{T_{\mathrm{MB},l}} = \frac{\mathrm{A}_i}{\mathrm{A}_l}\left(\frac{\nu_i}{\nu_l}\right)^2 \frac{g_i}{g_l} e^{-E_{il}/T_{\mathrm{ex},il}} \tag{5.7}$$

where $T_{\mathrm{MB}_{i,l}}$ are the brightness temperatures (K) of the upper and lower states, $\mathrm{A}_{i,l}$ are the Einstein coefficients, $\nu_{i,l}$ are the upper and lower frequencies, $\mathrm{g}_{i,l}$ are the upper and lower state degeneracies, E_{il} is the excitation energy, and $\mathrm{T}_{ex,il}$ is the excitation temperature. Table 5.4 lists the appropriate constants and results for the excitation temperature calculations. Averaging the excitation temperatures from all

six $i = 2$ to $l = 1$ line ratios, we obtain an estimate of the excitation temperature to be 1050 ± 243 K, which is not necessarily the kinetic temperature of the gas.

By assuming an optically thin transition, one is able to assign a lower limit on the excitation temperature. However, a more rigorous interpretation would require full radiative transfer calculations taking into account optical depth as measured using HI column density measurements.

5.4 Origin of Ro-Vibrational HCN Emission

5.4.1 Double Peaked Emission

Figure 5.8 shows the three $v = 2$ emission lines. Both the (0, 2^0, 0) and (0, 2^{2d}, 0) spectra appear to have double peaked emission which could be a possible signature of a Keplerian disk. The noise level of the spectra $\sigma_{\mathrm{T}} = 0.123$K. The signal-to-noise, defined as the $\frac{HM}{\sigma_{\mathrm{T}}}$, is ~ 8. Figure 5.9 shows a zoomed in view of the (0, 2^{2d}, 0) spectral line. The red and blue curves correspond to gaussian fits to each spectral peak. I measured the separation between peaks of both the v=(0, 2^0, 0) and (0, 2^{2d}, 0) lines to be ~ 2.7 km/s.

In order to determine if a Keplerian disk is consistent with observations, I assume a circular orbit with a constant orbital velocity, at an inclination angle, α, calculate the period, P, and sub into the following equation:

$$\mathrm{p} = \frac{2\pi\ r sin\alpha}{v} \tag{5.8}$$

$$\mathrm{p}^2 = \frac{4\pi^2}{\mathrm{G}(M+m)}\mathrm{r}^3 \tag{5.9}$$

where r is the orbital radius (m), or in this case, the radius of disk that has a rotational velocity equal to the separation in the in the double peaked emission of the (0, 2^{2d}, 0) line. Using Kepler's third law, assuming the central mass of AFGL 2591 to be $\sim 10 - 16$ $\mathrm{M}_{\odot}$, and a disk inclination angle of $26 \pm 3^{\circ}$ (van der Tak

et al., 2006), I estimate $\sim 1000 - 1800$ AU as the diameter of the disk. This estimation comparable to the results of van der Tak et al. (2006) who estimate the source size morphologically from continuum emission with a synthesized beam an order of magnitude smaller than presented here. The possibility also exists that this feature is self-absorption in the emission line, similar to the self absorption in the $v = 0$ line reported by Benz et al. (2007), or result from other kinematic effects like infall. Observation the $v = 2$ HCN(4-3) lines from this source with improved spatial resolution and sensitivity (i.e. with ALMA) will be able to clearly prove or disprove the Keplarian disk hypothesis by imaging the kinematic structure of the source.

5.4.2 Filling Factor

The filling factor describes how much of the emission is contained within the beam. A filling factor equal to one corresponds to the emission filling the beam. I have calculated the filling factor (see Table 5.3) of the SMA beam (ff_{mb}) by dividing the maximum brightness temperature (see Table 5.3) of a gaussian fit to the spectral lines by the excitation temperature for the spectral feature (see Table 5.2).

$$\mathrm{ff}_{mb} = \frac{T_{mb}}{T_{ex}} \tag{5.10}$$

This assumes the brightness temperature of the emission region is $\sim T_{ex}$, which is true if those regions are optically thick. The excitation temperature of the $v = 0$ transition is 42.5 K[3]. The brightness temperature presented in Table 5.3 for the same transition is ~ 39 K, leading the the value of 0.9164 for the filling factor. See Table 5.3 for the rest of the values.

The range of filling factors is as expected, with the $v = 0$ line the largest and the $v = 2$ lines the smallest. I find the $v = 0$ emission to approximately fill the

[3]http://splatalogue.net/

beam. The filling factors of the $v = 1$ lines are significantly larger than the $v = 2$ lines, possibly due to shock heating of the outer envelope of HCN surrounding AFGL 2591 (Bruderer et al., 2009). The filling factors associated with the $v = 2$ lines are approximately equal and very small, suggesting the emission is from compact unresolved sources within the beam. The filling factor of $v = (0, 2^{2c}, 0)$ is higher than expected due to the increased emission in the line, as previously discussed in section 5.3.2.

Assuming an annular disk where the inner disk radius is $1/2$ the radius of the outer disk, I can estimate filling factor of the disk to the beam size.

$$\mathrm{ff}_{disk} = \frac{R_{Outer}^2 - (0.5R_{Outer})^2}{(\overline{D}_{mb}/2)^2} \tag{5.11}$$

With a disk of diameter $\sim$1000 – 1800 AU as calculated using the $v = 2$ lines, and a beam size $\sim$2700 AU, I estimate the filling factor of the disk (ff_{disk}) within the beam by comparing the areal extent and find the a range of $\sim$.14 - .44.

Using this information, I can calculate an upper limit for the fraction of disk surface area (D_{AF}) over which the $v = 1$ and $v = 2$ emission is emitted. The calculations were done by multiplying the filling factor of the spectral line calculated from the brightness temperature and the excitation temperature by the ratio of disk fraction to beam.

$$D_{AF} = (\mathrm{ff}_{disk} \times \mathrm{ff}_{mb}) \times 100\% \tag{5.12}$$

The $v = 1$ fraction is 0.3% and $v = 2$ is 0.03%. The ratios are both less than 1.0% of the total disk surface area, consistent with the idea that the emitting regions are highlighting high density, warm structure in the disk and envelope. A plausible source for such emission is from shocks arising from self-gravitating instabilities in the disk, such as the eccentric $m = 1$ instability discussed by Adams et al. (1989). Such instabilities are expected to occur most frequently in system where

the disk to star mass ratio is high or in multiple systems where the stellar companions gravitationally perturb the disk.

5.5 Summary

I have demonstrated the feasibility of a novel technique for the study of protostellar accretion disks through the use vibrationally excited HCN (4-3). I observed AFGL 2591 with the HHSMT and the SMA at 350 GHz. Selection rules for $v = 1$ and $v = 2$ HCN emission allow us to determine the excitation mechanism independent of any other observations or assumptions and allows us to estimate the excitation temperature of the gas. In AFGL 2591, the vibrationally excited HCN emission appears to be collisionally excited. The very high densities and temperatures required for collisional excitation of these transitions show that the emitting gas likely traces structure in the protostellar envelope and/or disk surrounding the source. The line shapes of the $v = 2$ lines suggest the possibility of of an unresolved, rotating Keplerian disk. Future followup with ALMA will be able to observe AFGL2591 in the HCN (4-3) $v = 2$ lines with sufficient sensitivity and spatial resolution to clearly detect or rule out the Keplerian disk that is suggested. In addition, these lines are promising probes of protostellar disk and envelope structure in general. The increased sensitivity and spatial resolution offered by ALMA will allow these tracers to be applied to a variety of protostellar sources, and should offer an improved way to isolate and study the very high density, warm regions around protostellar objects.

5.6 Future Work

This work is currently in review for publication in the Astrophysical Journals Letters. I have applied for time on the ALMA to make similar observations of the same spectral feature for other high and low mass observational targets.

Table 5.1: Gaussian fit parameters for spectral line extraction. The width and center terms are given in pixels and the rotation angle is given in radians clockwise from the x-axis. The spectral extraction region is shown in Figure 5.3 as the dashed line.

Constant Term	0
Scale Factor	0.8351
Width (x)	2.6201
Width (y)	2.5031
Center (x)	256.3289
Center (y)	253.7847
Rotation Angle (θ)	-0.5499

Table 5.2: Energies and critical densities for the $v = 0$, $v = 1$ and $v = 2$ bending modes of HCN(4-3)

Transition	Energy above ground (K)
(0,1^{1c},0)	1066.9030
(0,0,0)	42.5347
(0,2^{2c},0)	2095.1770
(0,2^{2d},0)	2095.1790
(0,1^{1d},0)	1067.1190
(0,2^{0},0)	2073.4490

Table 5.3: Results (errors) calculated from gaussian fit to the HCN spectral lines.

Transition	Frequency GHz	Peak T_B SMA K	FWHM km/s	V_{lsr} km/s	Filling Factor
(SMA)					
$(0,1^{1c},0)$	354.460433 (1.30E-05)	10.5240 (0.0305)	5.1201 (0.0114)	-5.1294 (0.0073)	0.0099 (2.8587E-05)
(0,0,0)	354.505473 (1.00E-06)	38.9784 (0.1511)	6.6230 (0.0198)	-4.8467 (0.0126)	0.9164 (3.5524E-03)
$(0,2^{2c},0)$	356.135347 (5.00E-06)	1.9676 (0.0197)	5.4246 (0.0414)	-6.4622 (0.0263)	0.0009 (9.4025E-06)
$(0,2^{2d},0)$	356.162751 (5.00E-06)	0.8718 (0.0128)	6.6584 (0.0754)	-5.6232 (0.0477)	0.0004 (6.1093E-06)
$(0,1^{1d},0)$	356.255566 (1.30E-05)	12.2621 (0.0336)	5.1016 (0.0108)	-5.2010 (0.0079)	0.0115 (3.1487E-05)
$(0,2^{0},0)$	356.301176 (6.00E-06)	1.0692 (0.0149)	7.6095 (0.0847)	-4.4490 (0.0530)	0.0005 (7.1861E-06)
(HHSMT)					
$(0,1^{1c},0)$	354.460433 (1.30E-05)	0.1080 (0.0150)	3.7000 (6.4000)	-5.3000 (3.0000)	–
(0,0,0)	354.505473 (1.00E-06)	2.0300 (0.0150)	5.0000 (0.0700)	-5.6000 (0.0300)	–
$(0,2^{2c},0)$	356.135347 (5.00E-06)	< 0.0110	–	–	–
$(0,2^{2d},0)$	356.162751 (5.00E-06)	< 0.0110	–	–	–
$(0,1^{1d},0)$	356.255566 (1.30E-05)	0.017 (0.0140)	8.3000 (4.2000)	11.4000 (2.5500)	–
$(0,2^{0},0)$	356.301176 (6.00E-06)	< 0.0110	–	–	–

Table 5.4: Data for Line Ratio calculations.

Transition	Frequency (GHz)	$\mathrm{Log}_{10}(\mathrm{A}_{ij})$	E_U (K)	g_u	T_{ex}(K)
(0,1^{1c},0)	354.46043	-2.70345	1066.90383	8.5	883
(0,0,0)	354.50547	-3.16455	42.53436	9	838
(0,2^{2c},0)	356.13535	-2.72272	2095.17722	7	1447
(0,2^{2d},0)	356.16275	-2.72262	2095.17853	7	1330
(0,1^{1d},0)	356.25557	-2.69687	1067.11804	8.5	926
(0,2^{0},0)	356.30118	-2.70632	2073.44826	9	877

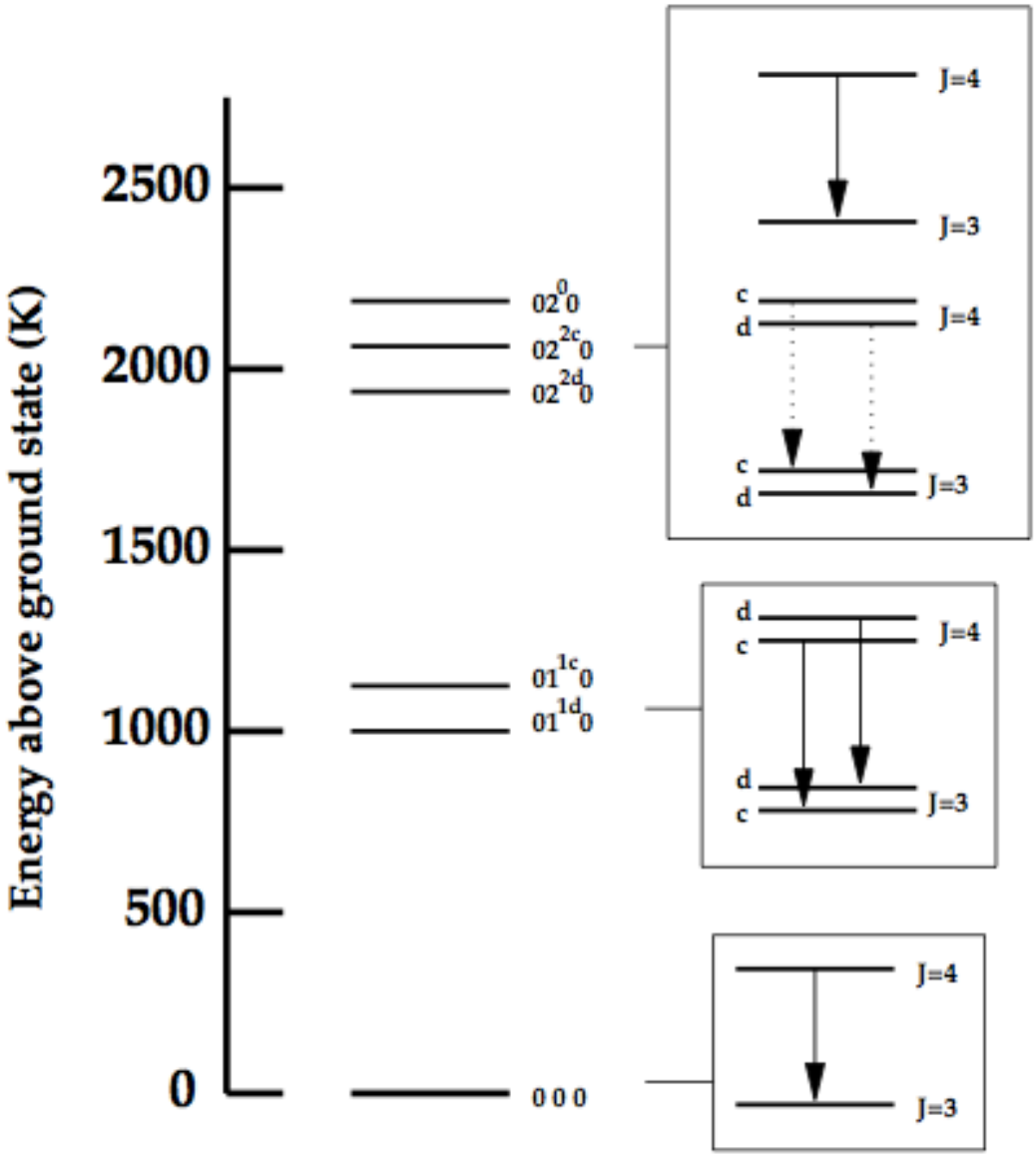

Figure 5.1: An energy level diagram for two ro-vibrational transitions of HCN(4-3). The v=(0,1^{1c},0), and v=(0,1^{1d},0) modes are a modest 1050 K above ground, compared to the $v = 2$ modes. The panels on the right show the selection rules for the transitions. The v=(0,2^{2c},0) and v=(0,2^{2d},0) transitions are not permitted for the radiative pumping excitation mechanism. (Ziurys & Turner, 1986; Groppi, 2003)

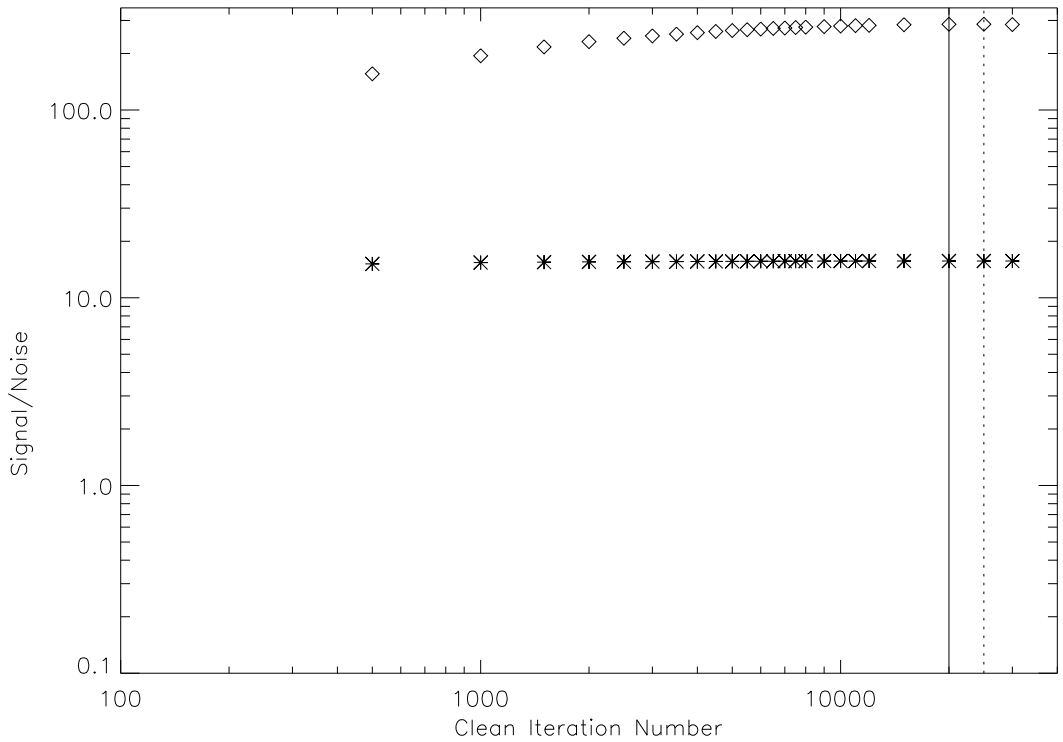

Figure 5.2: This plot shows the signal/noise of the various iterations on the creation of the upper side band continuum image. The diamonds correspond to $S(\text{source})/N(\text{background})$. The crosses correspond to the $S(\text{source})/N(\text{source})$. The solid vertical line corresponds to the maximum value for the $S(\text{source})/N(\text{source})$. The dotted line corresponds to the maximum value for the $S(\text{source})/N(\text{background})$. As I increased the iterations during the CLEAN procedure past the maximum value for $S(\text{source})/N(\text{background})$, I found the maximum value serves as an asymptote. The process was repeated for the lower side band.This process is analogous to aperture photometry in optical data reduction.

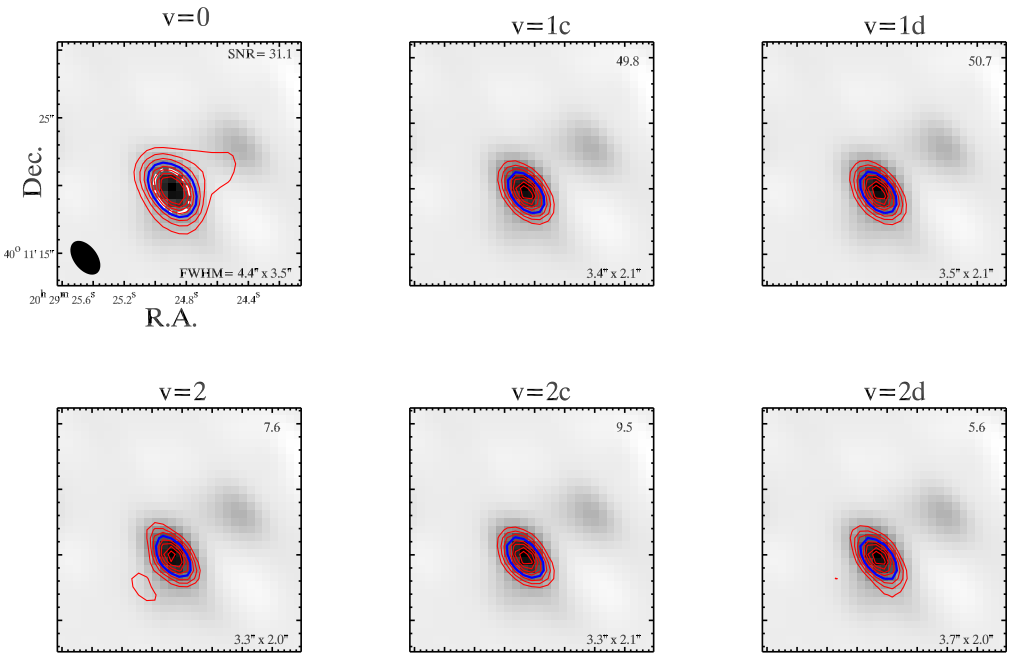

Figure 5.3: Integrated intensity contours of HCN emission overlaid on the continuum. The *red* contour levels are spaced at 10% intervals of a gaussian fit to the peak of the integrated intensity map. The lower right hand corner of each panel shows the size of the FWHM fit to the integrated intensity. The top right of each panel is the SNR of the integrated intensity maps. The spectra were extracted from the *white* dashed ellipse shown in the upper left panel. The $3.4'' \times 2.0''$ synthesized beam is the solid ellipse. The *blue* contour is the FWHM of the integrated intensity.

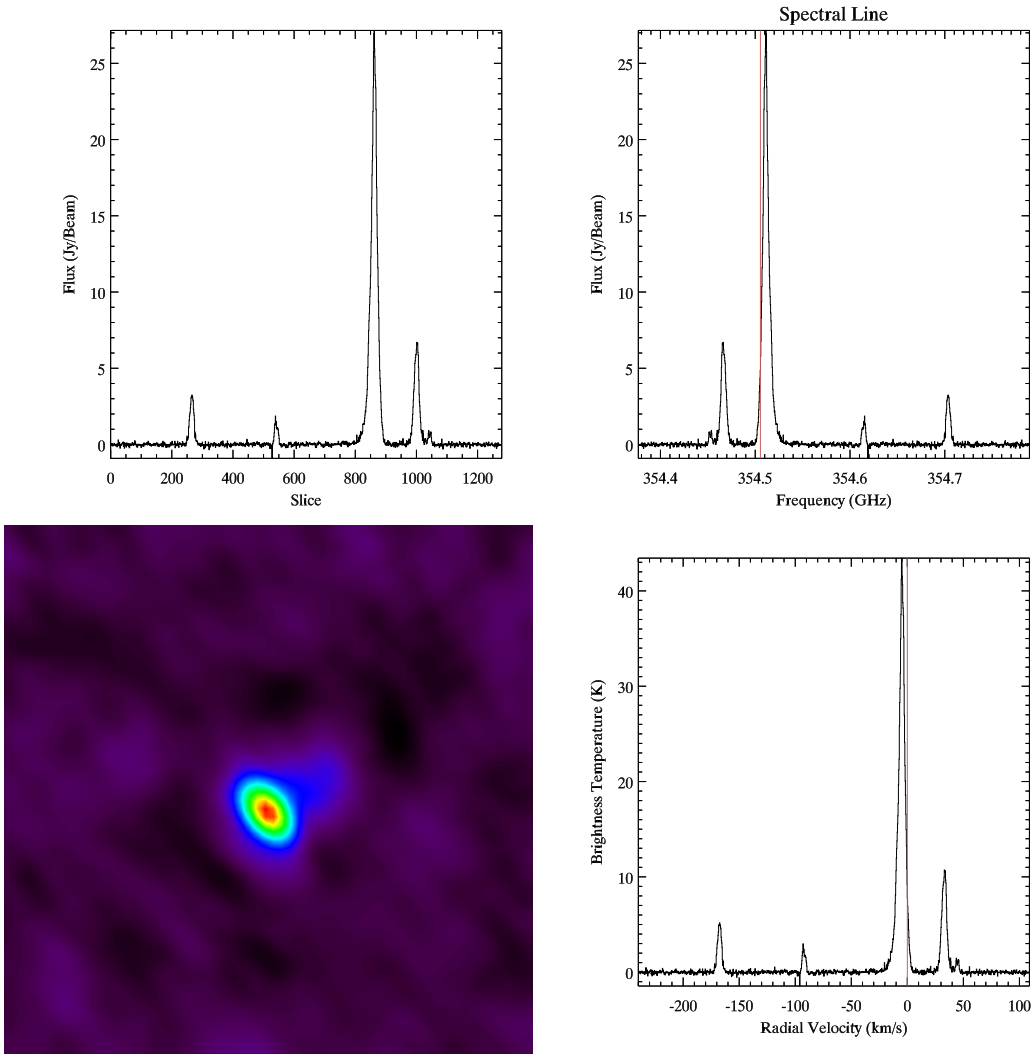

Figure 5.4: The upper left corner is the raw flux(Jy/beam) versus slice in the data cube. The upper right is the flux versus the frequency with the red line corresponding the interesting spectral feature, here corresponding to the v=0 line. The lower left is a zoom on the source. The lower right is the brightness temperature versus radial velocity offset from the spectral feature.

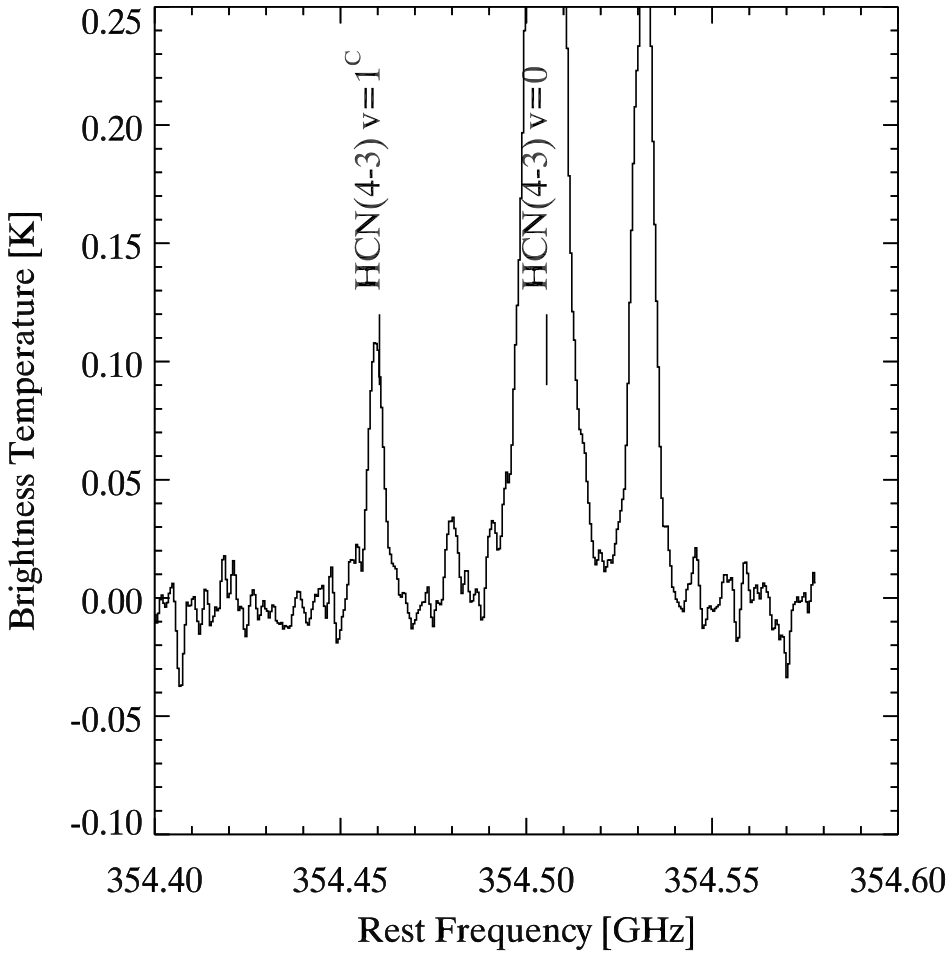

Figure 5.5: Spectra of AFGL 2591 observed with the HHSMT. Groppi (2003) found a very bright HCN(4-3) $v = 0$ line accompanied by exceptionally strong $v = 1c$ emission ($\sim$110 mK). No $v = 2$ lines were detected. Surprisingly, the $v = 1d$ line was marginally detected (1.5σ) and the upper limit is $5\times$ fainter than would be expected if excitation due to radiative pumping dominates the emission mechanism.

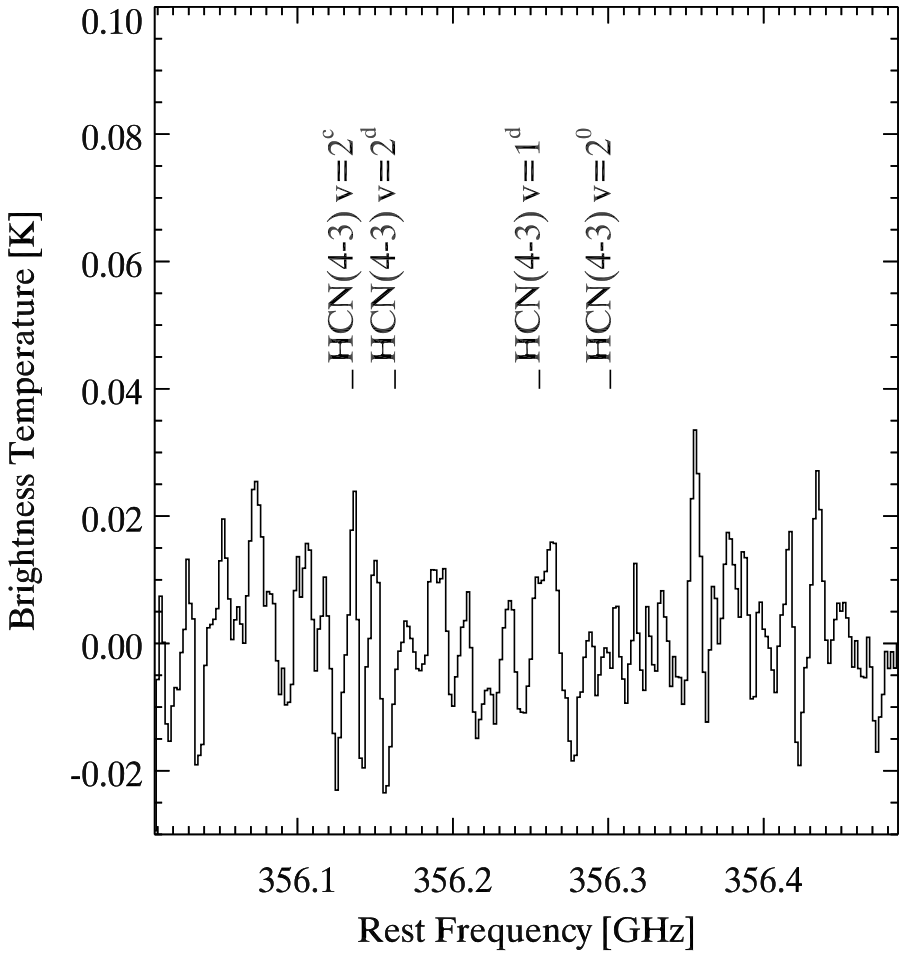

Figure 5.6: Spectra of AFGL 2591 observed with the HHSMT. Groppi (2003) found a very bright HCN(4-3) $v = 0$ line accompanied by exceptionally strong $v = 1c$ emission ($\sim$110 mK). No $v = 2$ lines were detected. Surprisingly, the $v = 1d$ line was marginally detected (1.5σ) and the upper limit is $5\times$ fainter than would be expected if excitation due to radiative pumping dominates the emission mechanism.

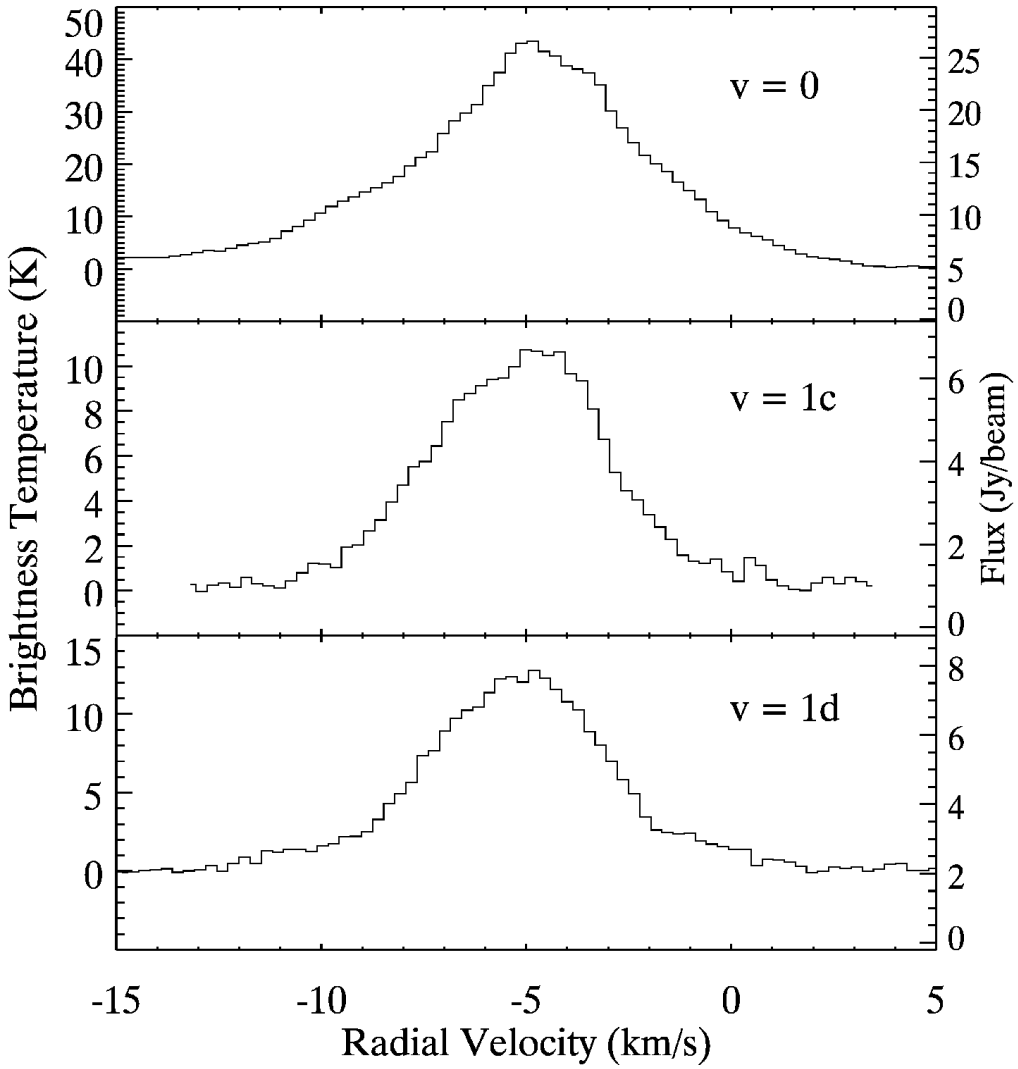

Figure 5.7: HCN v=0, v=(0,1^{1c},0), and v=(0,1^{1d},0) lines. Velocity channel widths are 0.273 km/s. All three molecular lines feature the v_{lsr} = -5.25 km/s velocity shift consistent with the emission coming from the expanding shell. (van der Tak et al., 1999)

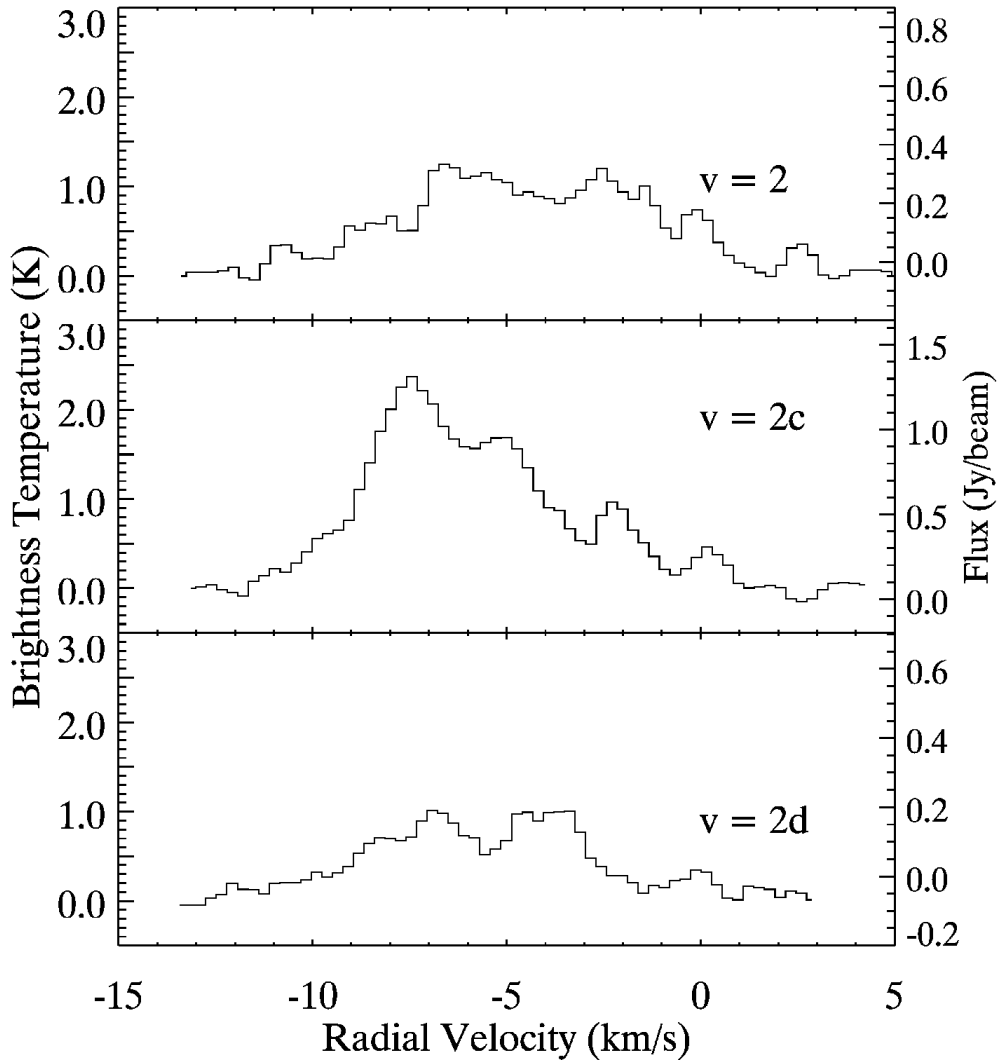

Figure 5.8: HCN v=(0,2^0,0), v=(0,2^{2c},0),v=(0,2^{2d},0). These data have been boxcar smoothed by a factor of n = 3 to a channel width of 0.82 km/s.

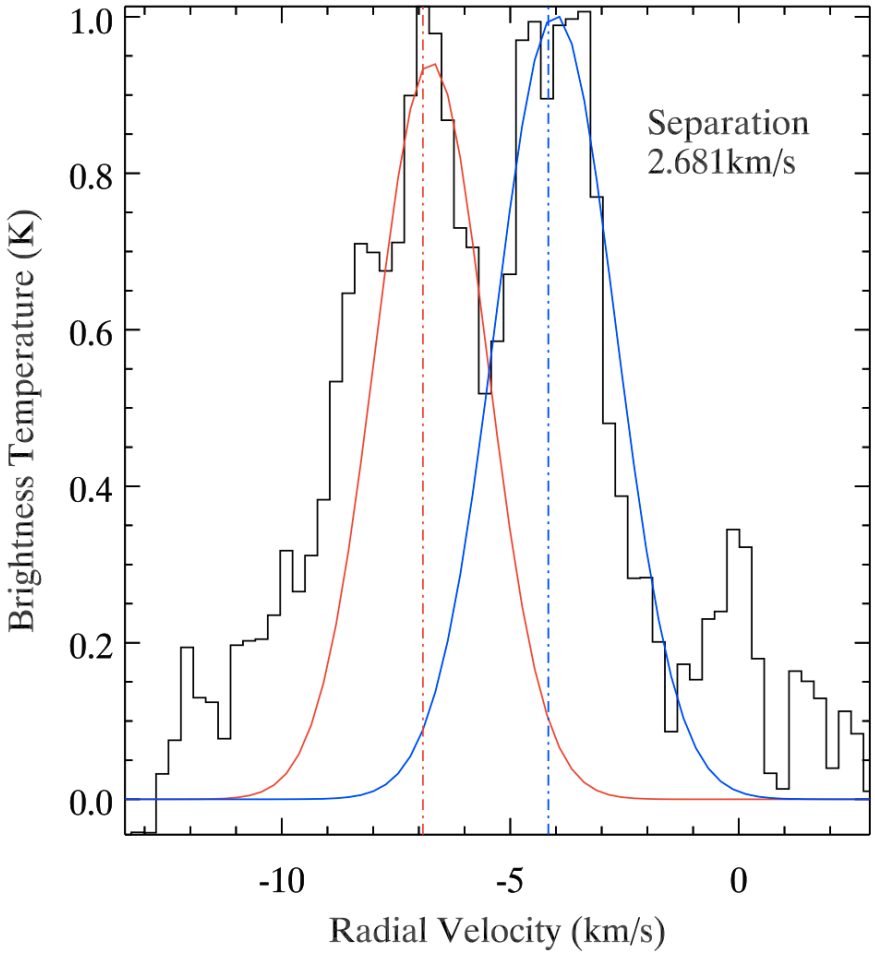

Figure 5.9: HCN v=(0,2^{2d},0). The blue and red lines correspond to gaussian fits to the spectral peaks. The separation between the peaks is ∼2.7 km/s. Assuming the velocity difference is due to rotational motion, we can calculate the radius of a Keplerian disk with this rotational velocity to be ∼1000 - 1800 AU.

Chapter 6

CONCLUSION

In this dissertation I presented the design and implementation of a development facility for large-format CCDs, the development of an innovative large-format CCD readout architecture, and the development of an imaging system for an FUV sounding rocket experiment. The development of these technologies will facilitate the design and implementation of future large focal plane arrays for space missions. Finally, I also presented a science case regarding the application of submillimeter observations of a high mass protostellar object.

6.1 Summary

I developed an experimental calibration facility for the characterization of UV/ optical/ NIR delta-doped detectors in a thermally controlled cryogenic (LN_2) and vacuum (10^{-6} torr) environment. A Leach (Leach, 1994) controller provided CCD power, clock level translation, and correlated-double sampling video acquisition. The optical train, including a monochromator, collimator, and various transfer optics are isolated within an enclosure I designed to eliminate stray light and allow for an N_2 purge. A novel approach introduced in this experiment is the co-location of the detector with a calibrated UV photodiode, which decreases the calibration time by half. Within the LASI facility, the calibration of dark current, read noise, linearity, full well depth, quantum efficiency, and various other operational parameters associated with the subject CCD are quickly and efficiently performed.

The large format delta-doped CCDs are a feasible choice for use in the next generation large focal plane arrays, but several issues must be addressed before large scale integration can be implemented. The thick p-channel delta-doped devices suffer from extreme irregularity from device-to-device. Operational clocks and voltages have been seen to wildly vary during calibration runs. Intrinsic to all

thick large format detectors is an inability to rapidly clock the charge out of the detector using conventional techniques. The average readout time for the full 3.5k detector is on the order of tens of seconds to a minute, depending on the number of output amplifiers used for readout. This is not a prohibitive readout duration for a single detector camera. However, if this were translated to a large focal plane array comprised of the number of devices proposed by SFC (Scowen et al., 2009d), the readout time would be on the order of more than half an hour, which would severely compromise the observatory's observational efficiency and subsequent scientific discovery potential. Finally, the LBNL detectors are extremely sensitive to over-illumination, creating an intrinsic limit to the brightness of observable targets. If thick delta-doped p-channel CCDs are to be the flagship detectors for the development of future large FPAs, then the technology must be significantly advanced enough to achieve scientific return worthy of the financial investment.

I developed a prototype modular imager cell for use on a sounding rocket flight and presented the design and testing results. The MIC is low power, low mass, and provides rigid mechanical support for the detector. I found the MIC to provide an amplification of the video signal of $\sim$2.6 with only a slight decrease in the SNR. The MIC also provided signal conditioning and presented an accurate reproduction of the clock signals to the detector. Overall, the MIC was successfully designed, fabricated, and tested as an amplifier and signal conditioner.

The development of large FPAs may hinge on the design and construction of an MIC using embedded controllers to ameliorate the power, mass, and cost associated with current FPA architectures. The MIC can provide a robust, low-risk high-reward solution that will mitigate possible mission failures by providing a way to assemble large FPAs using a modular "plug and play" solution. By placing the detector and the associated readout electronics on a single module, one can

easily remove and replace any single module without adversely affecting other detectors in the FPA. The assembling of large FPAs using MICs provides a reliable and robust method to create a wide field of view with extremely fine pixel scales, provided the mirror is of adequate match to the FPA. A wide field of view with extremely fine pixels scales will aid tremendously in the study of protostellar evolution by increasing the observational efficiency in the search for locations of star formation. Efficient discovery of sites of star formation over a wide field of view can lead to a better understanding of the global properties associated with stellar evolution.

I presented the design and system calibration results from the fabrication of a CCD based imaging system designed using a modular imager cell for use in an ultraviolet sounding rocket mission. The heart of the imaging system is the MIC, which provides the video pre-amplifier circuitry and CCD clock level filtering. The detector is a delta-doped 3.5k $\times$ 3.5k LBNL p-channel CCD with enhanced QE over unprocessed CCDs from 110 - 160 nm. The recently released Small-Cam from ARC provides for control and readout of the detector. The Small-Cam system has the same capabilities as its larger PCI brethren, but in a smaller form factor, which makes it ideally suited for sub-orbital ballistic missions. The overall control is then accomplished using a PCIe/104 computer from RTD. This work was pursued in collaboration with the University of Colorado Boulder and the JPL.

I have demonstrated the feasibility of a novel technique for the study of protostellar accretion disks through the use vibrationally excited HCN (4-3). We observed AFGL2591 with the HHSMT and the SMA at 350 GHz. Selection rules for $v = 1$ and $v = 2$ HCN emission allows for the determination the excitation mechanism independent of any other observations or assumptions and allows us to estimate the excitation temperature of the gas. In AFGL2591, the vibrationally

excited HCN emission appears to be collisionally excited. The very high densities and temperatures required for collisional excitation of these transitions show that the emitting gas likely traces structure in the protostellar envelope and/or disk surrounding the source. The line shapes of the $v = 2$ lines suggest the possibility of of an unresolved, rotating Keplerian disk. Future followup with ALMA will be able to observe AFGL2591 in the HCN (4-3) $v = 2$ lines with sufficient sensitivity and spatial resolution to clearly detect or rule out the Keplerian disk we suggest. In addition, these lines are promising probes of protostellar disk and envelope structure in general. The increased sensitivity and spatial resolution offered by ALMA will allow these tracers to be applied to a variety of protostellar sources, and should offer an improved way to isolate and study the very high density, warm regions around protostellar objects.

6.2 Toward Large Modular FPA Mass Production Implementation

The development of the large focal plane arrays discussed throughout this dissertation is currently cost-prohibitive for mass production. In order to mitigate the cost barriers that are currently inhibiting the development of large FPAs, the technology needs to be developed in order to:

- Increase observational efficiency of CCDs in the FUV either through delta-doping or the development of a new detector substrate.
- Increase the yield rate of delta-doped back-illuminated detector fabrication.
- Construct the modular imager cell for a low-cost while still meeting the requirements of the large FPA architecture. This includes physically smaller electronics that function at cryogenic temperatures, such as with an Application Specific Integrated Circuit (ASIC). With discrete components, such as those described in Chapter 3, the MIC is still too large for use in the

construction of Large FPAs. Furthermore, the power requirements are still prohibitive for successful implementation of mass production.

- Construct the Large FPAs using modular packaging architectures that can enable easy placement/test/removal/replacement of the modules during FPA integration (Scowen et al., 2009b).

- Construct large FPAs with minimal seams between the detectors using the modular architecture.

- Maintain stability of the large FPAs against thermal and vibrational shock.

- Maintain the detectors that populate the large FPAs at cryogenic temperatures. A possible solution proposed by Scowen et al. (2009b) is the use of variable conductance heat pipes (VCHPs) that will transport heat from the FPAs to a cryogenic radiator.

- Decrease the lead time involved with calibrating the detectors that will populate the large focal plane arrays.

- Accommodate terabytes of data transmission and storage that large space based FPAs will generate.

6.3 Looking Towards the Future

The development of innovative and revolutionary technologies are essential to the growth of research, especially within the astronomical community. It can safely be said that the development of new technologies have spurred every significant advance in scientific understanding. Within the astronomical community, the development of technologies enabling space-based observatories led to the mapping of the Cosmic Microwave Background (CMB) radiation that was first discovered by Penzias & Wilson (1965). The Hubble Space Telescope has also

enabled numerous scientific discoveries in all fields of astronomy that would otherwise have been impossible.

During my time in graduate school I was also involved in the Stratospheric Terahertz Observatory mission to observe the structure of the interstellar medium, the life cycle of interstellar clouds, and their relationship to star formation at 158 and 205 μm. Observations at these two wavelengths would not have been possible without the development of the appropriate detector technology. Furthermore, these wavelengths are inaccessible from the ground and require supra-atmospheric observations, which were accomplished from the Antarctic launch of a high-altitude ballon flight which would have been impossible without the development of new technologies.

We are rapidly approaching a state in the astronomical community where scientific discovery space is going to be hampered by the lack of access to truly revolutionary technologies. All four of NASA's Great Observatories (Spitzer, Chandra, Hubble, and Compton), which provided revolutionary and unprecedented scientific discovery, have either passed their operational lifetimes or are either nearing the end. The next great observatory, the James Webb Space Telescope, is still years away, leaving this author to question what will happen during the interim and how will we mitigate the inevitable void left when the Great Observatories cease to fulfill their designed purpose.

I suggest the development of an intermediate space mission comprised of a 2 to 4 meter mirror and a large focal plane array to provide access to a heretofore unprecedented scientific discovery space. The large focal plane array in combination with the mirror will provide a large field of view with Hubble-class resolution, allowing us to address the fundamental questions that govern the baryonic and non-baryonic evolution of matter in the Universe. Using the modular

imager cell concept developed here with the delta-doped detectors that I have discussed, it will be possible to address the spectral regime where emission from ionized atoms and molecules is abundant. Also, by addressing this spectral regime, we can gain access to statically complete samples of objects whose variability and population is as of yet unmeasured. Furthermore, serendipitous discovery, such as the observation of an exploding supernovae, increases greatly with an increased field of view and high resolution.

The upcoming decade in astronomy is a trepidatious time. The astronomy community cannot survive under the current fiscal model. Research money should be evenly distributed between many smaller projects instead of one or two large projects receiving the bulk. There should also be increased financial and governmental support for smaller mission programs, such as the University Class Explorer (UNEX[1]), Small Explorer (SMEX[2]), Medium-Class Explorer (MIDEX[3]), and Explorer (EX[4]) programs, which have been impossible to fund in recent years due to the current fiscal crisis gripping the nation. Financial support for these smaller projects allows for technological discovery that could eventually support the larger Flagship[5] class projects, which have also been shelved from the tightening of the budgetary belt. Furthermore, smaller projects allow for the development of the next generation of scientists and engineers in an environment where failure will not necessarily destroy an entire research community. I am in exceedingly in favor of large projects, having been the lead design engineer for the focal plane array of a multi-million dollar instrument, that are well run and well managed such that the project does not start siphoning money from the smaller

[1] explorers.gsfc.nasa.gov/missions.html
[2] explorers.larc.nasa.gov/SMEX/archives/SMEX-07/smexacq.html
[3] explorers.larc.nasa.gov/MIDEX/midexacq.html
[4] explorers.larc.nasa.gov/EX/ex_index.html
[5] solarsystem.nasa.gov/missions/future-mars2.cfm

projects, possibly threatening the viability of the field as a whole. Ultimately, it is an untenable and dangerous model to hinge the success of an entire field on one or two large projects.

One of the fundamental questions of human existence deals with the possibility of life existing elsewhere in the universe. As a species possessing intelligent thought, we question our place in the Universe and if life can truly exist beyond the confines of this pale blue dot. The vastness of the cosmos presents a fundamental challenge to answering this question. Statistically, the answer could be reasonably argued to be yes. The sheer volume of space and unfathomable number of planetary bodies that exist can lead only to the conclusion that somewhere there must be biological signatures of life that we can observe. Observations have already been made of Earth analog planetary bodies lying within the Habitable Zone of their parent star (Borucki et al., 2012). We need only the resolution capable of discerning biological signatures throughout the expanse of space to determine if this planet, and future planetary discoveries, harbor life. Without the development of innovative and revolutionary technologies, the answer to fundamental questions of human existence may elude us forever.

Adams, F. C., Ruden, S. P., & Shu, F. H. 1989, ApJ, 347, 959

Agilent. 2008, Mini-Task AG81, Agilent Technologies

Barsony, M. 1994, in Astronomical Society of the Pacific Conference Series, Vol. 65, Clouds, Cores, and Low Mass Stars, ed. D. P. Clemens & R. Barvainis, 197

Bebek, C. 2006, SNAP Imager CCD Technical Manual, Lawrence Berkeley National Laboratory, 1 Cyclotron Road Berkeley, CA 94720

Benz, A. O., Stäuber, P., Bourke, T. L., et al. 2007, A&A, 475, 549, 0709.0215

Blake, K. 2003, Microchip Application Notes, AN884

Borucki, W. J., Koch, D. G., Batalha, N., et al. 2012, ApJ, 745, 120, 1112.1640

Boyle, W., & Smith, G. 1970, The Bell System Technical Journal, 587

Bruderer, S., Benz, A. O., Bourke, T. L., & Doty, S. D. 2009, A&A, 503, L13

Bushouse, H., Baggett, S., Gilliland, R., Noeske, K., & Petro, L. 2011, WFC3/UVIS Charge Injection Behavior: Results of an Initial Test, Tech. rep., Space Telescope Science Insitute

Campbell, W. A., & Marriott, R. S. 1987, Outgassing Data for Selecting Spacecraft Materials (August 1, 1987), Tech. rep., Goddard Space Flight Center

Carroll, B. W., & Ostlie, D. A. 1996, Modern Astrophysics (Addison-Wesley Publishing Company Inc)

Ceccarelli, C., Bacmann, A., Boogert, A., et al. 2010, A&A, 521, L22+

Daly, P. N., & Buchholz, N. C. 2004, in Society of Photo-Optical Instrumentation Engineers (SPIE) Conference Series, Vol. 5496, Society of Photo-Optical Instrumentation Engineers (SPIE) Conference Series, ed. H. Lewis & G. Raffi, 373–381

Dressel, L. 2011, Wide Field Camera 3 Instrument Handbook, Version 4.0, STScI, Baltimore, MD

Einstein, A. 1905, Annalen der Physik, 322, 132

Evans, II, N. J. 1999, ARA&A, 37, 311, arXiv:astro-ph/9905050

Giavalisco, M. 2003, Minimizing CTE losses in the WFC3 CCDS: Post Flash vs. Charge Injection, Tech. rep., Space Telescope Science Institute

Groppi, C. E. 2003, PhD thesis, University of Arizona

Gunn, J. E., Carr, M., Rockosi, C., et al. 1998, AJ, 116, 3040, arXiv:astro-ph/9809085

Hoenk, M. E., Grunthaner, P. J., Grunthaner, F. J., et al. 1992, Applied Physics Letters, 61, 1084

Hopkinson, G., Goodman, T., & Prince, S. 2004, A Guide To The Use And Calibration Of Detector Array Equipment, Press Monographs (SPIE Press)

Horowitz, P., & Hill, W. 1989, The Art of Electronics (New York, NY, USA: Cambridge University Press)

Howell, S. B. 2006, Handbook of CCD astronomy, second edition edn., Cambridge Observing Handbooks for Research Astronomers (Cambridge University Press), 208

IRLabs. 2004, Infrared Laboratories ND-5 Series User Manual, Infrared Laboratories, 1808 East 17th St Tucson, AZ 85719-6505 USA

Jacquot, B. C., Monacos, S. P., Hoenk, M. E., et al. 2011, Review of Scientific Instruments, 82, 043102, 1102.2242

Janesick, J. R. 2001, Scientific Charge Coupled Devices (SPIE Press)

—. 2007, Photon Transfer (Bellingham, WA: SPIE Press)

Jansen, R. A. 2006, Astronomy with Charge Coupled Devices, AST 598 Instrumentation and Data Reduction course, ASU (ASU)

Jansen, R. A., Windhorst, R., Rhoads, J., et al. 2009a, in Astronomy, Vol. 2010, astro2010: The Astronomy and Astrophysics Decadal Survey, 139, 0904.2032

Jansen, R. A., Scowen, P., Beasley, M., et al. 2009b, ArXiv e-prints, 0904.2021

Johnson, H. L. 1963, Photometric Systems (the University of Chicago Press), 204

JPL. 2005, Electrostatic Discharge (ESD) Control, Jet Propulsion Laboratory, Pasadena, CA

K. France, e. a. 2012, in Society of Photo-Optical Instrumentation Engineers (SPIE) Conference Series, Vol. 8443.05, International Society for Optical Engineering

Keithley. 2001, Model 6485 Picoammeter Instruction Manual, 1st edn., Keithley Instruments, Inc., Cleveland, OH

Kitchin, C. R. 2003, Astrophysical Techniques, 4th edn. (Institue of Physics Publishing), 493

LakeShore. 2004, Model 321 Autotuning Temperature Controller User's Manual, 1st edn., LakeShore Cryotronics, 575 McCorkle Blvd., Westerville, Ohio 43082-8888

Leach, R. W. 1994, in Astronomical Society of the Pacific Conference Series, Vol. 55, Optical Astronomy from the Earth and Moon, ed. D. M. Pyper & R. J. Angione, 113

Leach, R. W. 1995, in IAU Symposium, Vol. 167, New Developments in Array Technology and Applications, ed. A. G. D. Philip, K. Janes, & A. R. Upgren, 49

Li, J. Z., & Hu, J. Y. 1998, A&AS, 132, 173

LSST Science Collaboration, Abell, P. A., Allison, J., et al. 2009, ArXiv e-prints, 0912.0201

Mackay, C. 1986, Annual Review of Astronomy and Astrophysics, 24, 255

Marengo, M., Jayawardhana, R., Fazio, G. G., et al. 2000, ApJ, 541, L63, arXiv:astro-ph/0008052

Moore, Davis, K. 2009, Building Scientific Apparatus, 4th edn. (New York: Cambridge), 647

Morris, M. 1975, ApJ, 197, 603

Morris, M., Zuckerman, B., Palmer, P., & Turner, B. E. 1971, ApJ, 170, L109

Motorola, I. S. P. S. D. D. 1996, Motorola DSP Assembler Reference Manual (6501 William Cannon Drive West Austin, TX, 78735-8598: Motorola Digitial Signal Processing Development Software)

Nikzad, S., Jones, T. J., Cunningham, T. J., Deelman, P. W., & Elliot, S. T. 2000, in JPL TRS +, Space Astrophysics Detectors and Detector Technology Workshop, Baltimore, Maryland, USA

Pedichini, F., Giallongo, E., Ragazzoni, R., et al. 2003, in Society of Photo-Optical Instrumentation Engineers (SPIE) Conference Series, Vol. 4841, Society of Photo-Optical Instrumentation Engineers (SPIE) Conference Series, ed. M. Iye & A. F. M. Moorwood, 815–826

Penzias, A. A., & Wilson, R. W. 1965, ApJ, 142, 419

Philbrick, R., Geary, J., Dunham, E., & Koch, D. 2004, in Astrophysics and Space Science Library, Vol. 300, Scientific Detectors for Astronomy, ed. P. Amico, J. Beletic, & J. Beletic (Springer Netherlands), 581–590

PIActon. 2003, Operating Instructions Acton Series SP-2150i, 4th edn., Princton Instruments, 15 Discovery Way, Acton, MA 01720

Recom. 2010, 3 Watt SIP8 Isolated Single and Dual Output, Recom-international

Rolffs, R., Schilke, P., Wyrowski, F., et al. 2011a, A&A, 529, A76, 1103.2088

Rolffs, R., Schilke, P., Zhang, Q., & Zapata, L. 2011b, A&A, 536, A33

Sault, R. J., Teuben, P. J., & Wright, M. C. H. 1995, in Astronomical Society of the Pacific Conference Series, Vol. 77, Astronomical Data Analysis Software and Systems IV, ed. R. A. Shaw, H. E. Payne, & J. J. E. Hayes, 433, arXiv:astro-ph/0612759

Schweiker, H., Howell, S., & Sawyer, D. 2011, KPNO MOSAIC-1.1 Imager User Manual

Scowen, P. A., Jansen, R., Beasley, M., et al. 2008, Proc. SPIE 7010, Space Telescopes and Instrumentation 2008: Optical, Infrared, and Millimeter, 70103Z

Scowen, P. A., Jansen, R., Beasley, M., et al. 2009a, in Astronomy, Vol. 2010, astro2010: The Astronomy and Astrophysics Decadal Survey, 268–+, 0904.2003

Scowen, P. A., Nikzad, S., Hoenk, M., et al. 2009b, in ArXiv Astrophysics e-prints, Vol. 2010, astro2010: The Astronomy and Astrophysics Decadal Survey, 30–+, 0904.1991

Scowen, P. A., Jansen, R., Beasley, M., et al. 2009c, in Astronomy, Vol. 2010, astro2010: The Astronomy and Astrophysics Decadal Survey, 266–+, 0904.1987

Scowen, P. A., Jansen, R., Beasley, M., et al. 2009d, ArXiv e-prints, 0904.1992

Scowen, P. A., Jansen, R., Beasley, M., et al. 2009e, in Astronomy, Vol. 2010, astro2010: The Astronomy and Astrophysics Decadal Survey, 267–+, 0904.2002

Scowen, P. A., Beasley, M., Cooke, B., et al. 2010, in Bulletin of the American Astronomical Society, Vol. 42, American Astronomical Society Meeting Abstracts #215, 481.06

Sridharan, T. K., Beuther, H., Schilke, P., Menten, K. M., & Wyrowski, F. 2002, ApJ, 566, 931, arXiv:astro-ph/0110363

Stiavelli, M., Hill, R. J., & Polidan, E. 2001, On the possible on-orbit use of charge injection for WFC3 : Preliminary assessment, Tech. rep., Space Telescope Science Institute

Trinidad, M. A., Curiel, S., Cantó, J., et al. 2003, ApJ, 589, 386

Turner, B. E. 1987, A&A, 182, L15

van der Tak, F. F. S., van Dishoeck, E. F., Evans, II, N. J., Bakker, E. J., & Blake, G. A. 1999, ApJ, 522, 991, arXiv:astro-ph/9905035

van der Tak, F. F. S., Walmsley, C. M., Herpin, F., & Ceccarelli, C. 2006, A&A, 447, 1011, arXiv:astro-ph/0510640

Walker, C. K., Maloney, P. R., & Serabyn, E. 1994, ApJ, 437, L127

Wells, D. C., Greisen, E. W., & Harten, R. H. 1981, A&AS, 44, 363

Wilson, W. J., Schwartz, P. R., & Epstein, E. E. 1973, ApJ, 183, 871

Zanella, G. 2002, ArXiv Physics e-prints, arXiv:physics/0211112

Zhao, J. H. 2009, MIRIAD Users Guide for the Reduction of SMA Data (Smithsonian Astrophysical Observatory)

Ziurys, L. M., & Turner, B. E. 1986, ApJ, 300, L19

APPENDIX A

PHYSICAL CONSTANTS

Table A.1: Physical constant according to NIST and USNO Astronomical Almanac Online

Name	Symbol	Number	CGS Units
Speed of light in a vacuum	c	$2.99792458 \times 10^{10}$	cm s^{-1}
Planck constant	h	$6.6260755(40) \times 10^{-27}$	erg s
	$\hbar$	$1.05457266(63) \times 10^{-27}$	erg s
Gravitational constant	G	$6.67259(85) \times 10^{-8}$	$cm^3g^{-1}s^{-2}$
Electron charge	e^-	$4.8032068(14) \times 10^{-10}$	esu
Mass of electron	m_e	$9.1093897(54) \times 10^{-28}$	g
Mass of proton	m_p	$1.6726231(10) \times 10^{-24}$	g
Mass of neutron	m_n	$1.6749286(10) \times 10^{-24}$	g
Mass of hydrogen	m_h	1.6733×10^{-24}	g
Atomic mass unit	amu	$1.6605402(10) \times 10^{-24}$	g
Avagadro's number	N_A	$6.0221367(36) \times 10^{23}$	
Boltzmann constant	k_B	$1.380658(12) \times 10^{-16}$	erg K^{-1}
Electron volt	eV	$1.6021772(50) \times 10^{-12}$	erg
Stefan-Boltzmann constant	σ	$5.67051(19) \times 10^{-5}$	erg $cm^{-2}K^{-4}s^{-1}$
Rydberg constant	R	$2.1798741(13) \times 10^{-11}$	erg
Mass of Sun	$M_\odot$	$1.9884(2) \times 10^{33}$	g

APPENDIX B

MODULAR IMAGER CELL SCHEMATICS

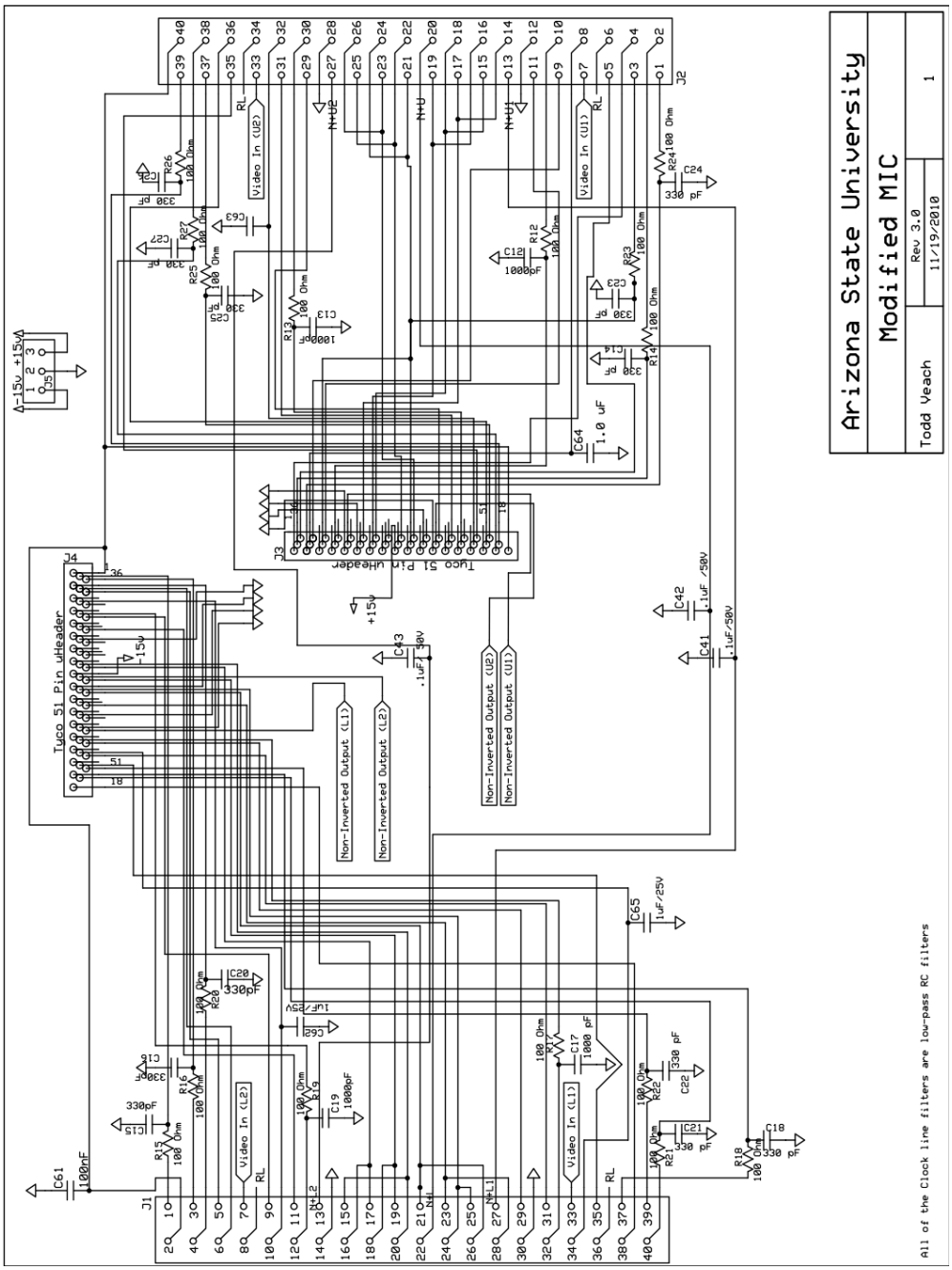

Figure B.1: MIC Schematic Page 1

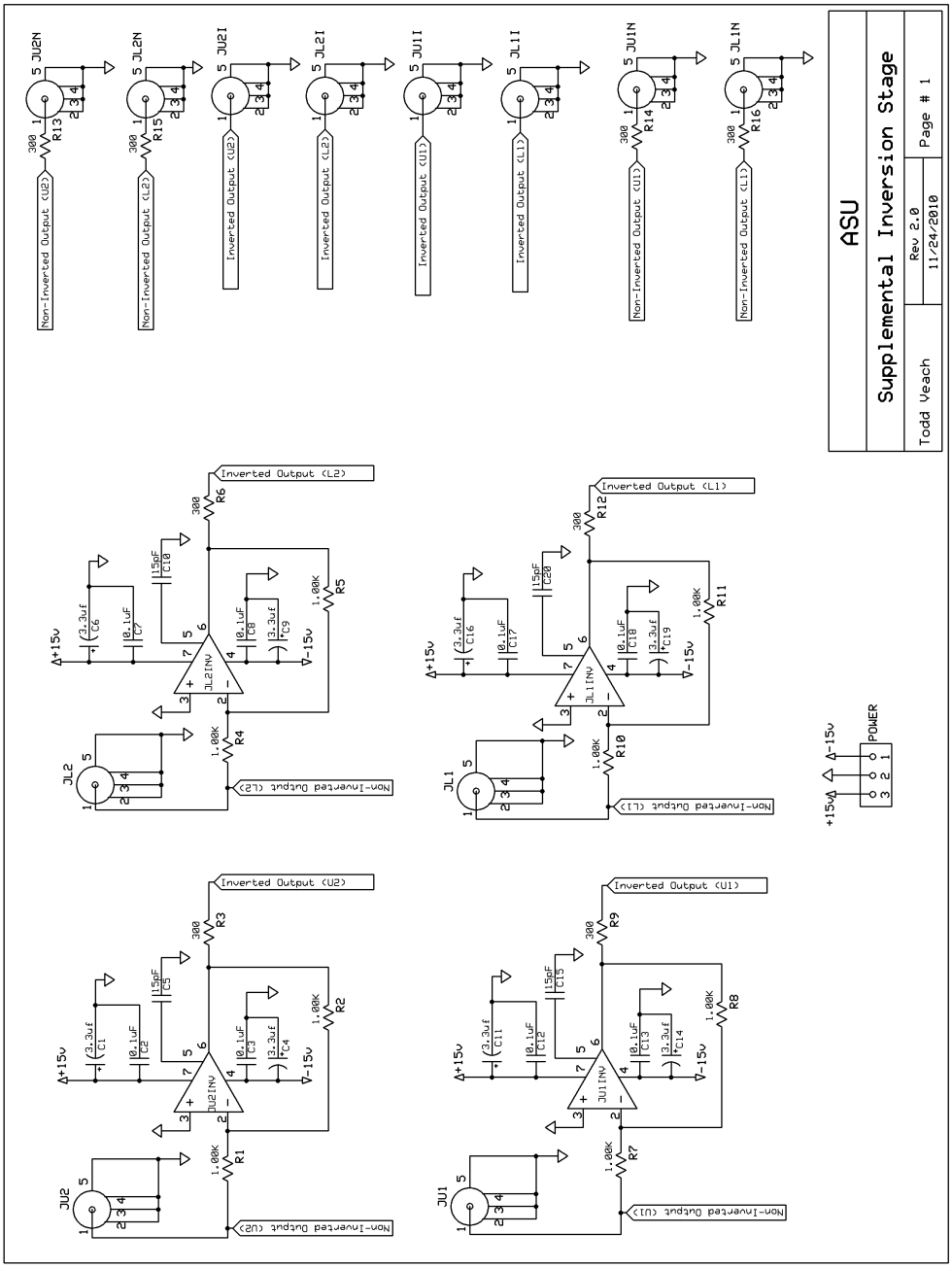

Figure B.2: MIC Schematic Page 2

APPENDIX C

CLOCK DRIVER BUFFER BOARD SCHEMATICS

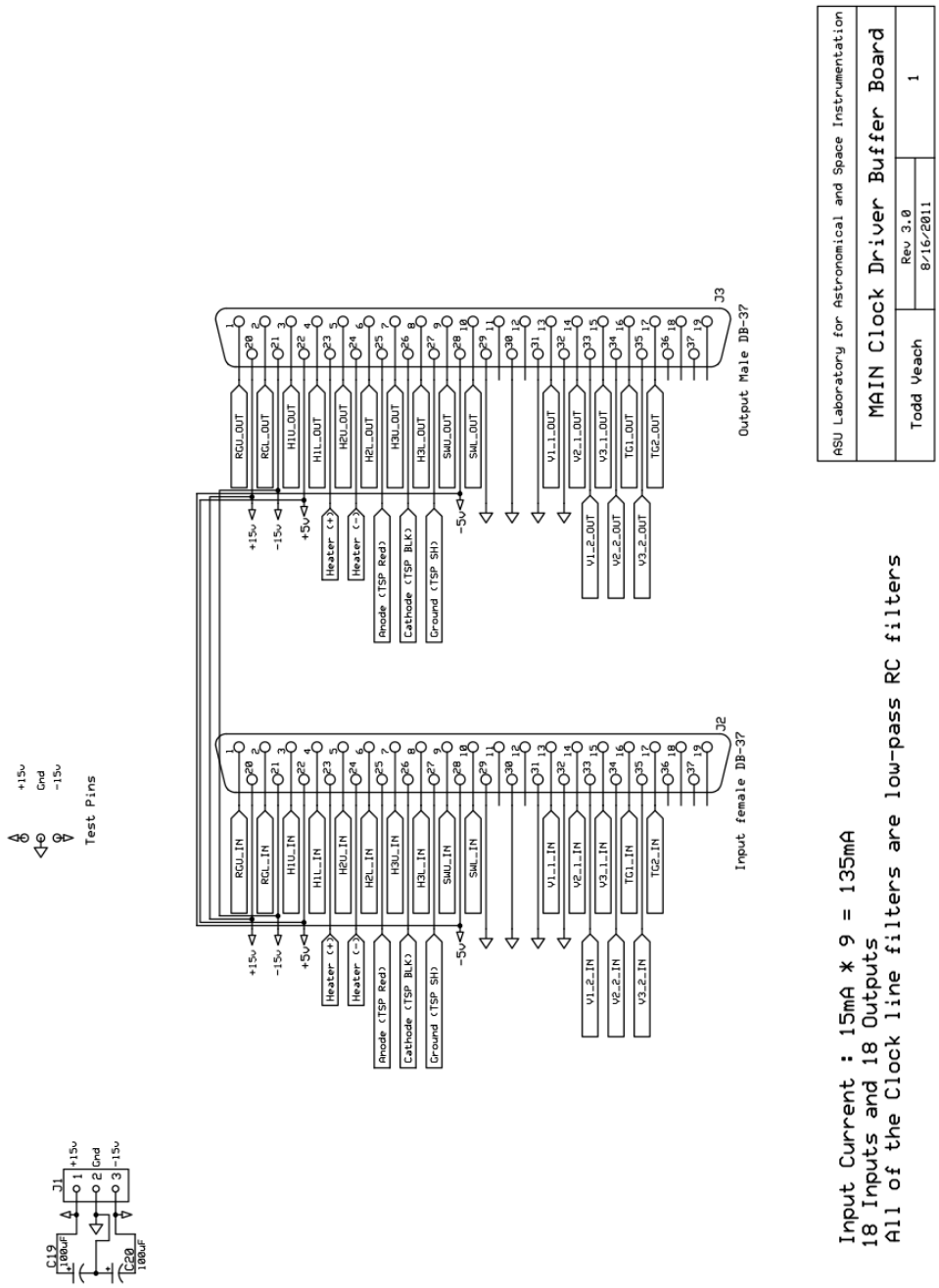

Figure C.1: Buffer Board Schematic Page 1

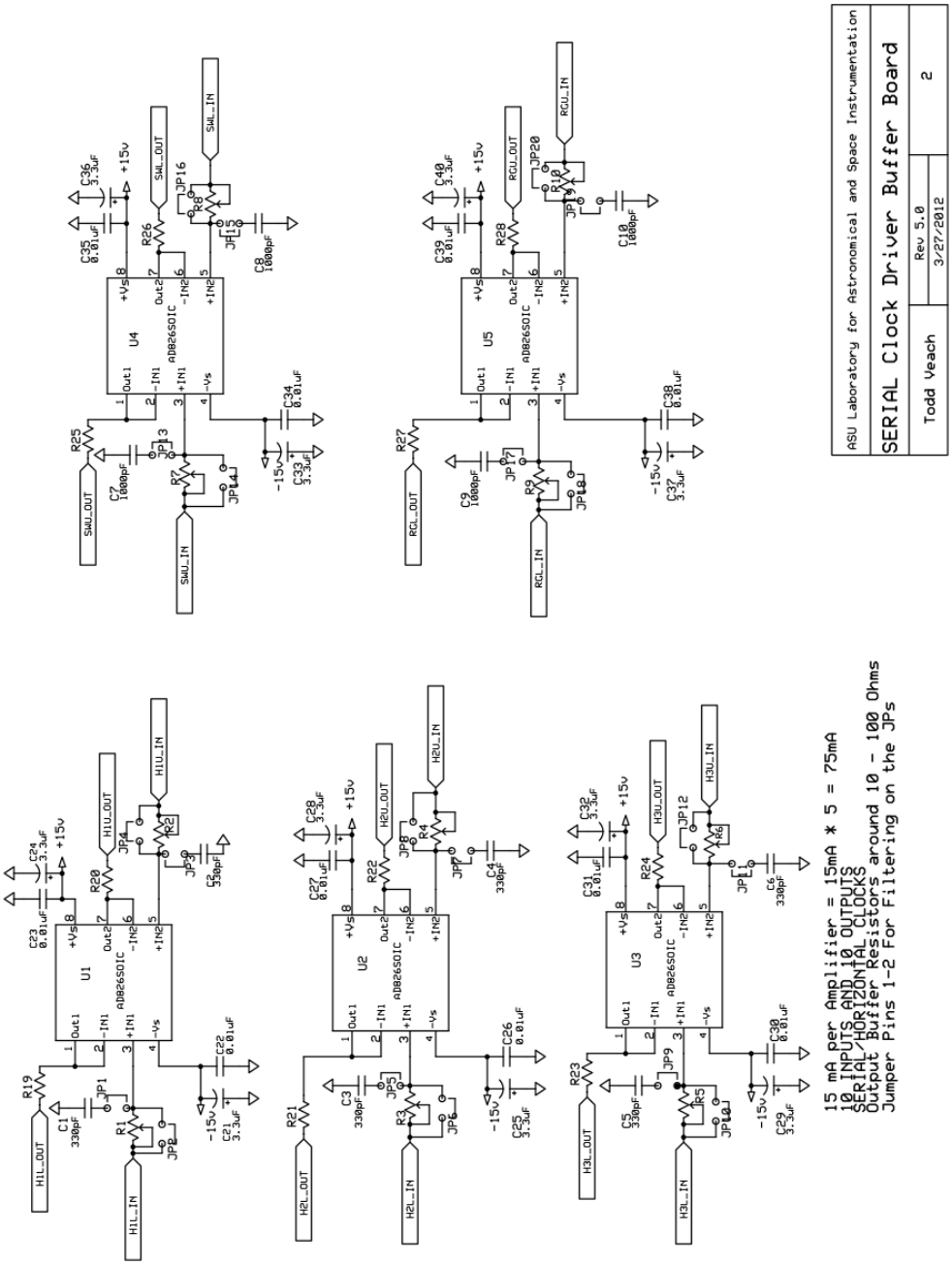

Figure C.2: Buffer Board Schematic Part 2

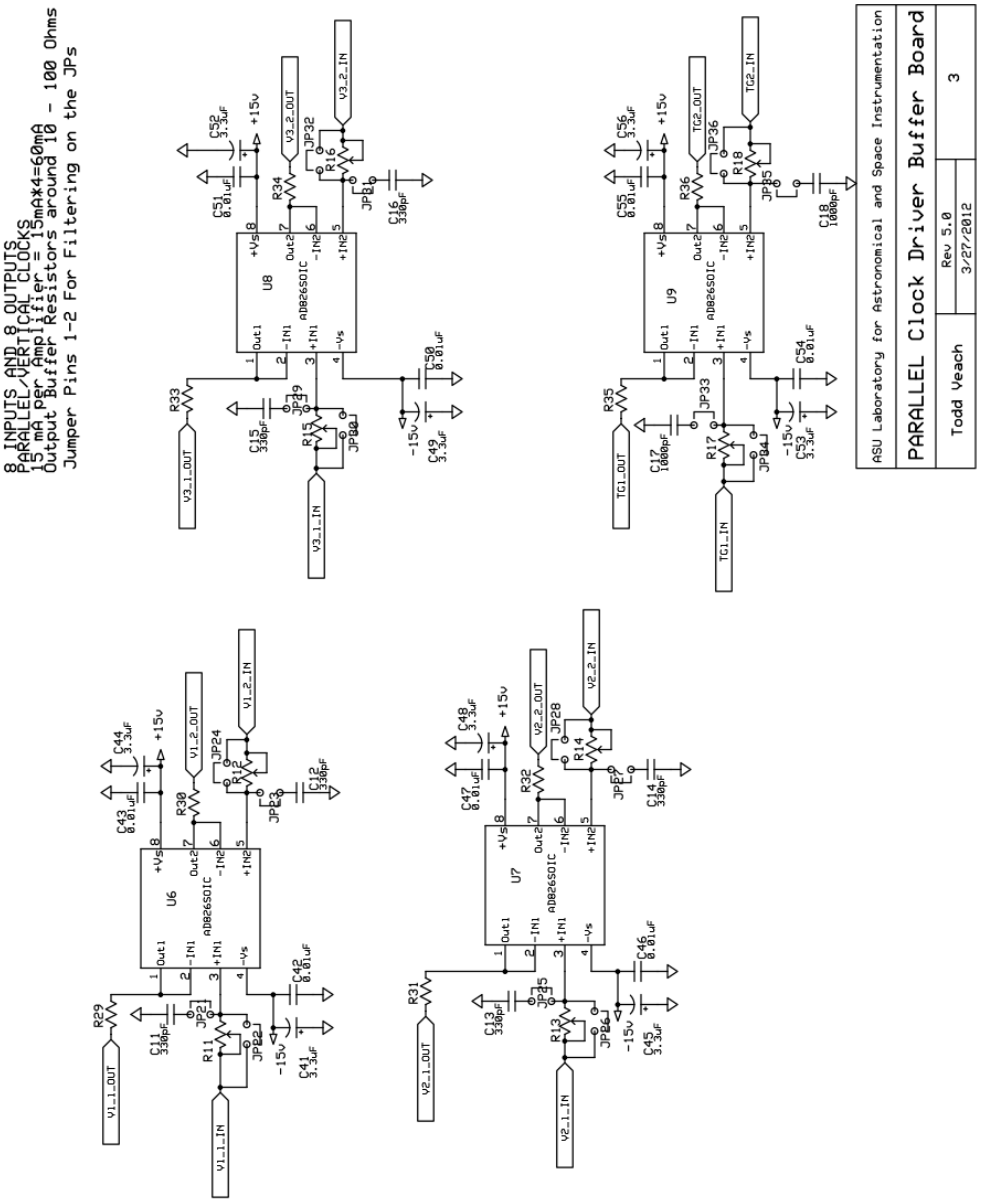

Figure C.3: Buffer Board Schematic Part 3